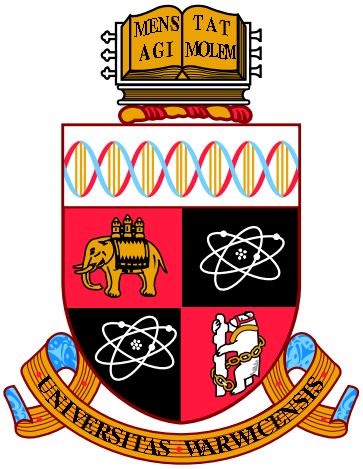

Biological imaging for adaptive bladder radiotherapy

by

Jane Ann Rogers

Thesis

Submitted to the University of Warwick

for the degree of

Doctor of Philosophy in Physics

THE UNIVERSITY OF WARWICK

Department of Physics

November 2019

Contents

List of Tables **iv**

List of Figures **v**

Acknowledgments **x**

Declarations **xiii**

Abstract **xx**

Chapter 1 Introduction **1**

1.1 Motivation underlying this thesis 2

1.2 Overview of the chapters 2

Chapter 2 Radiotherapy and imaging **4**

2.1 The use of radiation for medical treatment 4

2.1.1 Historical context 4

2.1.2 Radiation - production and interactions 6

2.1.3 Cellular responses to radiation and TCP 10

2.1.4 Overview of radiotherapy treatments 15

2.1.5 Complications and limitations of radiotherapy treatments . . 16

2.2 Use of imaging within radiotherapy 17

2.2.1 Computed tomography 17

2.2.2 Magnetic resonance imaging 22

2.2.3 Biological imaging: DW-MRI 27

2.2.4 Image registration for radiotherapy treatment planning . . . 35

2.2.5 Direct radiotherapy treatment planning on MRI 37

2.3 Adaptive radiotherapy and personalised medicine 37

Chapter 3 Bladder cancer treatment **39**
3.1 Overview of bladder cancer 39
3.1.1 Incidence and development 39
3.1.2 Diagnosis, treatment modalities and outcomes 41
3.1.3 Prognosis 42
3.2 Radiotherapy treatment of bladder cancer 45
3.2.1 Current techniques and their limitations 45
3.2.2 Current clinical trials: RAIDER and BladderPath 46
3.2.3 Potential developments in bladder cancer radiotherapy 50
3.3 Developing the use of DW-MRI as biolological imaging for adaptive bladder radiotherapy 53
3.3.1 Project sections 53
3.3.2 Project summary 54

Chapter 4 Investigations of distortion in DW-MRI for radiotherapy treatment of bladder tumours **56**
4.1 Introduction 56
4.1.1 Commercial MRI phantoms 57
4.2 Bespoke bladder phantom for quantification of distortion 59
4.2.1 Phantom design 59
4.2.2 Phantom materials 59
4.2.3 Phantom I construction 60
4.2.4 Phantom I imaging, processing and registration methods . . . 63
4.2.5 Phantom I: Results and discussion 66
4.2.6 Requirements for a second phantom 74
4.2.7 Phantom II design and construction 75
4.2.8 Phantom II imaging, processing and registration methods . . 77
4.2.9 Phantom II: Results and discussion 80
4.3 Summary and conclusions 84

Chapter 5 Modelling tumour control probability for bladder cancer **86**
5.1 TCP models 86
5.1.1 TCP model requirements for this project 87
5.1.2 Plataniotis and Dale's logistic model 88
5.1.3 Poisson Model 93
5.2 Fitting the Poisson model to TCP data 96
5.2.1 Fitting methodology 97
5.2.2 Estimation of model uncertainties 99

5.3 Results and discussion: Fitting the Poisson model to TCP data . . . 100
5.3.1 Fit of Poisson model to RT-only data . . . 100
5.3.2 Fit of Poisson model to RCT data . . . 101
5.3.3 Confidence in the models . . . 103
5.3.4 Use of these models to calculate TCP . . . 104
5.4 Summary and conclusions . . . 105

Chapter 6 Isotoxic dose escalation of simulated tumours 106
6.1 Introduction . . . 106
6.2 Development of a method to simulate tumours . . . 107
6.3 Radiotherapy treatment planning of simulated tumours . . . 110
6.4 Results and discussion . . . 114
6.4.1 Dose escalation for simulated tumours with 10 mm margins and RT-only TCP calculations . . . 115
6.4.2 Dose escalation for simulated tumours with 7 mm margins and RT-only TCP calculations . . . 126
6.4.3 TCP calculations using the RCT Poisson model . . . 129
6.4.4 Toxicity . . . 134
6.5 Summary and conclusions . . . 135

Chapter 7 Clinical verification and feasibility study 136
7.1 Introduction . . . 136
7.2 Calculation of accrued doses on CBCTs . . . 136
7.3 Methods of data extraction and analysis . . . 138
7.4 Results and discussion . . . 139
7.4.1 Standard plan - 64 Gy to whole bladder . . . 139
7.4.2 Superior tumour - 70 Gy . . . 148
7.4.3 Inferior tumour - 78 Gy . . . 151
7.4.4 Posterior tumour with 7 mm margins - 73 Gy . . . 153
7.4.5 Limitations of this method . . . 154
7.5 Summary and conclusions . . . 156

Chapter 8 Summary and Vision 157
8.1 Summary of the work . . . 158
8.2 Vision . . . 159
8.3 Future work . . . 160

List of Tables

3.1 Standard fractionation schemes for MIBC used in the UK. 45

4.1 Construction of phantom I 63
4.2 Settings used for T2W- and DW-MRI of phantom I. 64
4.3 Registrations applied to ADC maps 65
4.4 Dice similarity coefficients for all image registrations between CT and ADC maps. 68
4.5 Construction of phantom II 78
4.6 Settings used for T2W- and DW-MRI of phantom II. 79

5.1 Points calculated for 95 % confidence interval (CI) curves to pass through for RT-only and RCT data. 99

6.1 OAR dose constraints for RAIDER. 111
6.2 RAIDER expansion margins. 112
6.3 RAIDER target dose objectives. 113
6.4 Maximum dose escalation of tumours whilst meeting mandatory clinical goals and corresponding TCP using RT-only Poisson model. . . 125
6.5 Maximum dose escalation of tumours whilst meeting mandatory clinical goals and corresponding TCP using both models. 133

7.1 Expected and 'delivered' TCPs according to the RT-only and RCT models. 151

List of Figures

2.1 Picture of a modern Elekta linac. 5
2.2 Spectrum of a nominal 6 MV linac. 7
2.3 Variation of absorbed dose with depth for a nominal 6 MV x-ray beam produced by a medical linear accelerator. The variation of dose with depth is shown for an idealised beam with no attenuation and a realistic beam in which dose beyond the depth of dose maximum decreases approximately exponentially. 8
2.4 Schematic showing a linac and patient positioning system. 9
2.5 Schematic showing a cross-section through a patient and varying intensity of radiation beams. 10
2.6 Probability of tumour control and normal tissue complication against dose. 11
2.7 Schematic cell survival curves. 12
2.8 Example of a CT scanner. 18
2.9 Schematic of a CT acquisition, showing the movement of the patient along the axis of rotation of the x-ray source. 19
2.10 Schematic showing the relationship between the gross tumour volume (GTV), clinical target volume (CTV), internal target volume (ITV), and planning target volume (PTV) 21
2.11 Diagram showing movement of M_0 into the transverse plane 25
2.12 An example MR scanner showing the various typical axes and directions, and the location of the different parts of the scanner. 26
2.13 Schematic showing the application of RF pulses and diffusion sensitizing gradients to generate a DW-MRI signal. 28
2.14 Cross-sectional imaging of the bladder and internal tumour 29
2.15 Illustration of the calculation of ADC maps from multiple DW-MRIs of the same volume. 31

2.16 Representation of the effect of EPI readout of k-space on distortion in images. 33
2.17 Dice similarity coefficient. 36

3.1 Diagram showing the bladder and its location within the body. . . . 40
3.2 Diagram showing the development and stages of muscle-invasive bladder cancer. 41
3.3 Diagram showing schematic of trans-urethral resection for bladder tumours (TURBT). 42
3.4 Graph showing the net survival adjusted for age and sex for each cancer in 2010-11, and absolute change since 1971, all adults in England 5 years after diagnosis. 43
3.5 Graph showing the 5 year age-adjusted net survival after diagnosis for bladder cancer in England. 44
3.6 Diagram showing the radiotherapy treatment in the standard arm (arm (i)) of the RAIDER clinical trial. 47
3.7 Diagram showing the radiotherapy treatment in the trial arms of the RAIDER trial. 48
3.8 Schematic showing the differences in patient pathway being tested within the BladderPath Clinical Trial. 50

4.1 (a) Photograph of the ACR phantom and (b) schematic of the 2-D grid contained within the phantom. 57
4.2 Cross-sectional 2-D images of the grid section of an ACR phantom as it appears using (a) CT, (b) DW-MRI, and (c) following rigid registration of CT and DW-MRI. 58
4.3 Phantom I: first main phantom designed and constructed to model a bladder and internal tumour. 61
4.4 Imaged phantom I showing cross-sectional images with CT and T2W-MRI. 66
4.5 Imaged phantom I showing cross-sectional images with DW-MRI and ADC map. 66
4.6 Delineations of bladder wall and tumour after rigid registration only. 67
4.7 Diagram showing intersections of bladder and tumour volumes visualised on ADC maps and CT using rigid registration (RR) and deformable registration (DR) respectively. 69

4.8 Mean and standard deviation of positional differences between expected and actual positions of POIs following registrations of ADC maps to CT of phantom I. 70
4.9 Maximum positional differences between expected and actual positions of POIs following registrations of ADC maps to CT of phantom I. 71
4.10 Images showing CT and ADC maps following (a) rigid registration and (b) deformable registration. 73
4.11 Phantom II - second phantom designed and constructed to model a bladder and internal tumour. 76
4.12 Cross-sectional images of phantom II using CT and T2W-MRI. . . . 80
4.13 ADC maps where (a) 'blip up' and (b) 'blip down' refer to k-space readout direction; (c) ADC (FSL) map and (d) T2W-MRI for comparison. 81
4.14 Mean and standard deviation of positional differences between expected and actual positions of POIs following registrations of T2W-MRI and ADC maps to CT of phantom II. 82
4.15 Maximum positional differences between expected and actual positions of POIs following registrations of T2W-MRI and ADC maps to CT of phantom II. 83

5.1 RT-only observed complete response rates (RCR) against equivalent dose in 2 Gy fractions. 89
5.2 RT-only and radiochemotherapy (RCT) observed complete response rates against equivalent dose in 2 Gy fractions. 90
5.3 RCT observed complete response rates against equivalent dose in 2 Gy fractions (EQD2) and best fit using a fixed chemotherapy-alone contribution to complete response. 91
5.4 RCT observed complete response rates against EQD2 and best fit using a fixed degree of chemotherapy-induced radiosensitization. . . 92
5.5 Tumour control probability (TCP) as a function of dose. 94
5.6 How changing α_{mean} and σ_α affects the root mean square error when fitting RT-only trials data with the Poisson model. 97
5.7 How changing α_{mean} and σ_α affects the root mean square error when fitting radiochemotherapy data with the Poisson model. 98
5.8 RT-only trials data and logistic fit, along with the best fit using the Poisson model. 100

5.9 RCT trials data and both logistic fits, along with the best fit using the Poisson model. 102
5.10 Graph showing all trials data and all fits. 103

6.1 Schematic showing the coronal view of a simulation of an inferior post-TURBT (10 cm^3) tumour. 108
6.2 Schematic showing the sagittal view of a simulation of a posterior large (30 cm^3) tumour. 109
6.3 Effect of tumour (GTV) location within the bladder upon maximum achievable dose escalation. 115
6.4 Effect of tumour volume on TCP using the standard technique of uniform irradiation of the whole bladder to 64 Gy in 32 fractions. . . 116
6.5 Effect of reducing dose to the bladder wall (BW) to 48 Gy (dashed lines), with dose to tumour maintained at 64 Gy. 118
6.6 Effect of reducing dose to the bladder wall (BW) to 48, 52 or 56 Gy respectively, with dose to tumour maintained at 64 Gy. 119
6.7 Effect of increase in tumour dose to 68 Gy compared with the 64 Gy plans. 120
6.8 Tumour dose escalations of 64, 68 and 78 Gy. 121
6.9 Mean predicted TCP using the RT-only Poisson model for small, medium and large tumours for the range of doses with EQD2 of 61.5 - 78.3 Gy. 122
6.10 The location of a superior tumour close to the bowel results in lower achievable maximum dose escalations than for tumours in other locations within the bladder. 124
6.11 Location of high dose gradients in 84 Gy dose distributions. 127
6.12 Comparison of dose distributions for inferior tumour plans. 128
6.13 Left tumour shown re-simulated with reduced superior extent. 129
6.14 Effect of reducing bladder wall dose to 48, 52 or 56 Gy respectively, with dose to tumour maintained at 64 Gy using the RCT TCP model for calculation. 130
6.15 Effect of increase in tumour dose from 64 to 68 and 78 Gy compared with the standard plan (64 Gy) using the RCT TCP model for calculation. 131
6.16 Mean TCP predicted using the RT-only and RCT Poisson models. . 132

7.1 Original planned dose distribution calculated on the planning CT for a single (2 Gy) fraction using the standard 64 Gy plan. 140

7.2 Re-calculated dose distribution on the CBCT for a single (2 Gy) fraction using the standard 64 Gy plan. 141
7.3 Differences between original planned dose distribution and the dose distributions which would have been delivered using the standard 64 Gy plan, based on re-calculation on a CBCT image. 142
7.4 Differences between original planned dose distribution and the dose distributions which would have been delivered using the standard 64 Gy plan, doses mapped back onto planning CT using DR. 143
7.5 Deformable registration (DR) mapping vectors between CBCT and CT shown overlaid upon the planning CT. 144
7.6 CBCT delineated volumes overlaid from the original planning CT. . 145
7.7 CBCT delineated volumes including manual alterations. 146
7.8 Cumulative dose volume histograms for standard (64 Gy) plan. . . . 147
7.9 'Delivered' dose distributions using the 70 Gy to superior GTV plan, based on re-calculation on a CBCT. 149
7.10 Cumulative dose volume histograms for 70 Gy plan to superior GTV. 150
7.11 'Delivered' dose distributions using the 78 Gy to inferior GTV plan, based on re-calculation on a CBCT. 151
7.12 Cumulative dose volume histograms for 78 Gy to inferior GTV. . . . 152
7.13 'Delivered' dose distribution for 73 Gy plan to superior GTV. 153
7.14 Cumulative dose volume histograms for 73 Gy to posterior GTV. . . 154

Acknowledgments

So many people to thank, it's hard to know where to start...

Firstly thank you to my supervisors: **Jon Duffy** for your patience and help in understanding what I needed to do to produce a PhD and getting the thesis together, **Spyros Manolopoulos** for your ideas and support during the PhD, and **Tom Hase** for the criticism - no really! Many thanks also to **Prof Nick James** for your time and interest despite not officially being a supervisor, as well as the idea behind the project and clinical perspective.

Thanks to **Sam Manger** for all the coffee and general commiserations throughout it all - it was a lot more lonely before you started and after you finished, I'm glad you were around for most of it. (That does make it sound like you must've got yours done in about 2.5 years, doesn't it!)

Thank you to so many at Cov for help throughout - I can't name you all in case I miss someone out and this will be even longer than it already is, but I must mention **Sarah Wayte** and **Andy Weedall** for all your time and help with the MRI work and your patient explanations; **Vicky Sherwood** for your MRI support as well as the more general encouragement - and for continuing to help long after it was any part of your job. Thanks to **Jo Hamilton** for clinical perspective and information, **Weibing Xu** for RayStation and MATLAB help, **Matt Craddock** and **Matt Jones** for more RayStation support (not to mention **Kate Robertson** at RaySearch and the various other people there for answering my many questions and queries), as well as to **Pete Mulholland** and **Ryan Gilder** for making and altering the phantoms and **John Sage** and **Gareth Baugh** for 'getting it' and letting me continue to work on the thesis after starting work - and particularly for

reading the thesis at short notice.

A very big thank you to **Jo Hales** for the MATLAB help, I might still be writing the code for DVH processing without you... and to **Dan Kirby** for finding and anonymising bladder patients and scans.

Thank you to **Ruth Wyatt** for your radiobiology help and **Geoff Heyes** for your encouragement that what I was doing made some sort of sense - I miss sharing the office with you both!

Thanks to **Jen** and **Jon Rogers** for the long-term loan of your monitor - it's been so useful and saved me so many trips up and down the A46!

Thank you to **Sophie**, **Isaac** and **Mike Rogers** for putting up with mum's endless whinging about her PhD and never complaining or asking why she's bothering anyway, and to **Lucy Rogers** for your interest in Bob and the rainbows (that's the RayStation orientation man and isodose colours for anyone who's wondering).

Lastly - and definitely not least - a massive thank you to **Chris Rogers**, for all the support and encouragement to finally do it, even though you knew what it would entail. Hopefully we can finally have some time together in the evenings and weekends now!

This thesis was typeset with LaTeX 2$_\varepsilon$[1] by the author.

[1] LaTeX 2$_\varepsilon$ is an extension of LaTeX. LaTeX is a collection of macros for TeX. TeX is a trademark of the American Mathematical Society. The style package *warwickthesis* was used.

This thesis is dedicated to the memory of Edmond Levi Rogers.

Declarations

I declare that this thesis has been composed solely by myself and that it has not been submitted, in whole or in part, in any previous application for a degree. Except where stated otherwise by reference or acknowledgment, the work presented is entirely my own.

Glossary

Apparent diffusion coefficient (ADC) map A parametric map in which the intensity of each pixel of the image contains information which originates from multiple diffusion-weighted MR images. 30

Biologically Effective Dose (BED) Dosimetric quantity which indicates how much damage a particular dose fractionation scheme will do. The BED is the total dose which if given in infinitely small fractions is equivalent to the actual fractionation scheme with finite doses per fraction. 13

CE marking A certification mark which indicates conformity with health, safety and environmental protection standards for products sold within the European Economic Area. 34

Clinical target volume (CTV) The volume of tissue that contains a GTV and/or subclinical microscopic disease that must be eradicated for achievement of local control of disease. 20

Clonogens Cells which have the potential to proliferate and give rise to a colony of cells. 11

Computed tomography (CT) 3-D image set produced using an x-ray set rotated around the patient and reconstructed into axial slices. 15

Cone beam CT (CBCT) Similar to conventional CT but using a cone beam of x-rays resulting in 3D images of the patient from a single rotation. Images are noisier due to increased scatter but these devices are sufficient to allow rapid imaging (and positional correction) of a patient prior to radiotherapy treatment delivery. 22

Cystectomy Surgical removal of the whole bladder. 41

Deformable registration (DR) Geometrical alignment of two or more image datasets to a common coordinate system in which a point-to-point transformation of the spatial correspondence between image datasets is found. 35

Dice similarity coefficient (DSC) A simple method for quantifying the similarity of volumes and the degree to which they overlay. 36

Diffusion-weighted MRI (DW-MRI) A type of MRI in which image contrast depends on diffusion of water molecules and which is therefore sensitive to the high cellularity within tumours. 27

Digital Imaging and Communications in Medicine (DICOM) International standard to transmit, store, retrieve, print, process and display medical imaging information and related data. 34

Dose volume histogram (DVH) A histogram of the volumes of organs receiving specific doses. Often plotted in cumulative form, but can be used in differential form (i.e. dDVH). 104

Dose-escalated Adaptive Radiotherapy (DART) Trial arm of the RAIDER clinical trial in which an escalated radiotherapy dose is prescribed using an adaptive radiotherapy technique. 46

Echo-planar imaging (EPI) A rapid method of reading out MR signal in a raster pattern. 32

Echo time (TE) Time between excitation pulse and MR signal sampling. 26

Equivalent dose in 2 Gy fractions (EQD2) The dose which is biologically equivalent if delivered in fractions of 2 Gy. 13

Field of view (FOV) Cross-sectional area over which images are acquired. 22

Fractionation The practice of splitting radiotherapy delivery over the course of days or weeks. 13

Functional Magnetic Resonance of the Brain Software Library (FSL) A library of analysis tools for MRI. 34

Gray (Gy) Unit used for quantifying absorbed dose (i.e. energy absorbed per unit mass), where 1 Gy = 1 J/kg. 6

Gross tumour volume (GTV) The gross palpable, visible, or demonstrable position and extent of malignant growth. 20

Hounsfield units (HU) Units used in CT images in which the displayed greyscale of a pixel varies depending upon the inferred x-ray absorption coefficient of that pixel. 19

Intensity modulated radiotherapy (IMRT) Radiotherapy treatment in which beams of radiation are varied in intensity often using MLCs and enabling conformality of isodoses to concave tumours. 5

Internal target volume (ITV) The volume formed to accommodate the variation in relative position of the CTV owing to variations in anatomical changes from breathing or other organ motion. 20

International Commission on Radiation Units and Measurements International Commission on Radiation Units and Measurements. 20

Isotoxic Of equal toxicity. 16

Large bladder (LB) Large model bladder used in MRI phantom I in Chapter 4. 60

Linacs Linear accelerators used to produce x-rays or electrons for radiotherapy treatments. 6

Magnetic susceptibility A measure of how magnetized a material will become in an applied magnetic field. 32

Magnetic resonance imaging (MRI) Imaging modality using high magnetic field and radiofrequency pulses which generates good contrast between different soft tissues. 22

MR-linac Linear accelerator incorporating an MRI which can be used prior to or during radiotherapy treatment delivery. 23

MR-sim Use of MRI for radiotherapy treatment simulation, i.e. imaging used for the design of the radiotherapy dose distributions is MR-based rather than CT-based. 23

Multi leaf collimators (MLCs) Multiple narrow pieces of metal used on a linear accelerator to shape the treatment beam. 5

Multiparametric MRI (mpMRI) When multiple types of MR images are acquired in a single imaging session. 27

Muscle-invasive bladder cancer (MIBC) Later stages of bladder cancer in which the tumour has invaded the detrusor muscle. 40

Neuroimaging Informatics Technology Initiative (NIfTI) Format of images introduced by the Neuroimaging Informatics Technology Initiative. 34

Non muscle-invasive bladder cancer (NMIBC) Earlier stages of bladder cancer in which the tumour has not invaded the detrusor muscle. 40

Normal tissue complication probability (NTCP) Probability of complications arising as a result of treatment (e.g. bowel stenosis). 10

Number of excitations (NEX) Number of excitations used in an MR sequence. 26

Organs at risk (OARs) Organs within the body which may limit the dose delivery owing to potential toxicity. 20

Planning target volume (PTV) A geometrical definition of a volume used for radiotherapy treatment planning such that the GTV and/or CTV will receive the prescription dose with an acceptably high probability. 20

Planning CT The CT used to calculate dose distributions for the purpose of radiotherapy treatment, which is usually performed within a radiotherapy department in addition to any diagnostic imaging. 15

Points of interest (POIs) Marked points within the radiotherapy treatment planning system imaging frames of reference at which data may be required, such as dose received. 36

Polyvinyl alcohol (PVA) Cryogel used in phantoms for MRI. 59

Radiochemotherapy (RCT) Treatments using ionising radiation and chemotherapy drugs. 88

Radiofrequency (RF) Electromagnetic radiation in the range 9 kHz - 300 GHz. 23

Radiosensitivity Sensitivity of cells to radiation. 10

Radiotherapy (RT) Treatments using ionising radiation. 88

Radiotherapy treatment planning system (TPS) See TPS. 34

Radiotherapy treatment planning The design and calculation of dose distributions for the purpose of radiotherapy treatment. 15

RAIDER A Randomised phase II trial for Adaptive Image guided standard or Dose Escalated tumour boost Radiotherapy in the treatment of the bladder cancer. 46

Regions of interest (ROIs) Regions or volumes defined within the radiotherapy treatment planning system imaging frames of reference within which data may be required, such as dose. 36

Relaxation time (TR) Time between two excitation RF pulses. 26

Rigid registration (RR) Geometrical alignment of two or more image datasets to a common coordinate system in which only one global transformation for translations and/or rotations of all points in one dataset with respect to the other are performed. 35

Small bladder (SB) Small model bladder used in MRI phantom I in Chapter 4. 60

Standard Adaptive Radiotherapy (SART) Trial arm of the RAIDER clinical trial in which a standard radiotherapy dose is prescribed using an adaptive radiotherapy technique. 46

Survival fraction (SF) The fractions of cells which survive irradiation. 12

$\boldsymbol{T}_1$ Relaxation process in MRI often referred to as longitudinal or spin-lattice relaxation in which the net magnetization returns to its initial maximum value. 25

$\boldsymbol{T}_2$ Relaxation process in MRI often referred to as transverse or spin-spin relaxation in which the transverse components of magnetization dephase. 25

Theragnostic imaging The use of molecular and functional imaging to prescribe the distribution of radiation in 4 dimensions. 51

Trans-urethral resection of bladder tumour (TURBT) Piecemeal removal of bladder tumour via the urethra; used as primary treatment in non-muscle invasive bladder cancer and as diagnosis of muscle-invasive bladder cancer. 41

Treatment planning system (TPS) Radiotherapy treatment planning system, usually commercial software used to delineate tumour and other volumes usually on CT imaging and calculate dose ditributions for radiotherapy treatments. 35

Tumour control probability (TCP) Probability of achieving local control of the tumour. Can be defined in terms of a specific endpoint over a certain number of years (i.e. control at 2 years may be higher than at 5 years). 10

Volumetric modulated arc therapy (VMAT) A method of delivering IMRT treatment with one or more rotations of a linac gantry. 5

Whole bladder radiotherapy (WBRT) Radiotherapy treatment in which the whole bladder is prescribed a single uniform dose. 46

Abstract

Outcomes for muscle-invasive bladder cancer (MIBC) have changed little over recent decades, with long term survival remaining around 50 % [1]. Standard radiotherapy treatment for MIBC involves resection of tumour followed by uniform radiotherapy to the whole bladder, as the residual tumour is not readily visible on conventional computed tomography (CT) imaging. This thesis investigates the use of diffusion-weighted MRI (DW-MRI) to enable a dose-escalated radiotherapy treatment, aiming to improve local control of MIBC.

Geometrical distortion in DW-MRI was investigated via bladder-mimicking phantoms, and positional differences were quantified between DW-MRI, standard T2-weighted MRI, and CT. Deformable registration within a commercial radiotherapy treatment planning system was tested to see whether it could mitigate distortion. All markers were located within a maximum discrepancy of 5 mm (mean 3 mm). Open-source software designed to correct geometric distortion in DW-MRI was tested and produced improved results with a maximum of 1.8 mm (mean 1.3 mm).

Tumours were simulated in 6 locations within the bladder on a CT dataset of a previously-treated MIBC patient. Expansions producing planning target volumes incorporated the findings from the phantom investigations, aiming to mimic the use of DW-MRI registered to CT. Escalated dose distributions were compared against the standard, using established dose-constraints for nearby sensitive organs. Maximum dose-escalations to 70 - 78 Gy were possible depending on tumour location.

Poisson-based tumour control probability (TCP) models were fitted to MIBC trials data for radiotherapy-only and radio-chemotherapy treatments, and used to calculate TCP for all dose distributions. TCP increased 9.0 - 19.2 % depending on tumour location and model used. The feasibility of delivery of the dose distributions was assessed via dose-accumulation using cone beam CT.

This work showed that the use of DW-MRI for planning and pre-treatment imaging of MIBC patients could isotoxically improve local control of MIBC.

Chapter 1

Introduction

This thesis presents a series of investigations into a potential improvement of radiotherapy treatment for bladder cancer. The work involved assessing a specific type of magnetic resonance imaging (MRI) called diffusion-weighted MRI (DW-MRI), which provides additional information to conventional imaging methods regarding tumour cell density. DW-MRI would be used within the design of radiotherapy treatments to enable an increased dose to areas of tumour highlighted by the images to contain tumour, rather than basing treatment on standard computed tomography (CT) imaging in which the whole bladder is targeted as the tumour is not consistently visible. DW-MRI is already in clinical use for the diagnosis of some cancers, but is not yet used within the design of radiotherapy treatments. The assessment of the use of DW-MRI within the design of radiotherapy treatments for bladder cancer was performed by developing models to quantify the probability of control of bladder tumours. The models were then used to compare a standard radiotherapy technique with the proposed new technique, quantifying the expected increase in probability of tumour control. A range of scenarios were tested, and the feasibility of delivering the technique in clinical practice was also assessed. The aim was to provide a basis upon which a future clinical trial could be developed.

Section 1.1 explains the motivation underlying the work described in this thesis, and begins with a brief background to bladder cancer and its treatment using radiotherapy, to provide a context for the subsequent outline of the different sections of work. An overview is given in section 1.2 of the contents of each chapter.

1.1 Motivation underlying this thesis

Bladder cancer is the 4th most common cancer in males in the UK [2] and is associated with poor survival, with around 50 % surviving for 5 years post diagnosis [3]. It is the most expensive cancer to care for from diagnosis to death [4]. The historical standard treatment is the surgical removal of the whole bladder (cystectomy) to control disease spread [5], however this obviously causes significant long-term morbidity in patients, even if their cancer is cured. Relatively little improvement in outcomes has been seen for patients with bladder cancer in recent decades, unlike for several other cancer sites such as breast or prostate [6]. Some clinical trials of alternative treatments to cystectomy have shown similar outcomes for patients who received combined therapies including tumour resection, radiotherapy and chemotherapy [7, 8]. Current trials are investigating ways to maximise the effectiveness of such bladder-conserving treatments via the use of either technical improvements in the delivery of radiotherapy [9] or improved imaging within the diagnostic pathway [10]. The work presented in this thesis fits within this context of the use of technical developments within radiotherapy and related imaging to improve outcomes and reduce morbidity for patients with bladder cancer.

1.2 Overview of the chapters

The current chapter provides an introduction and overview of the thesis as a whole, including the main aims and sections of work. Chapter 2 introduces background information regarding radiotherapy treatments and the types of imaging used within the radiotherapy process, and which is required for the context of this project to be understood. This includes the effects of radiation on cells and how they are exploited in the design of radiotherapy treatments. An overview of radiotherapy treatment design and the relevant imaging modalities used within the process is presented. Finally, in section 2.3, the limitations of radiotherapy treatment are discussed in order to underpin the efforts to overcome or mitigate these problems later in the thesis.

Chapter 3 provides background information on bladder cancer, including its incidence and diagnosis as well as common treatment techniques, with particular reference to radiotherapy and patient outcomes. Some important previous clinical trials and their impact upon current standard treatments are presented, as well as some current clinical trials. This leads on to the aims of the current work and the rationale for this investigation.

The first set of results are presented in Chapter 4, which covers the work performed in designing, producing and imaging two model bladders using DW-MRI. The purpose of this work was to quantify the effects of distortion seen in DW-MRI, as this is a known issue and potential limitation to the ability to use this imaging method within radiotherapy treatment design. The aim of this section of work was to provide a 'worst case' but realistic prediction of the amount of geometric distortion which could be seen in DW-MRI of the bladder, in order to be able to assess the clinical effect of such distortions within the later work in this thesis.

The next section of work is presented in Chapter 5, in which two models are developed to fit clinical trials data of bladder cancer radiotherapy. These models can therefore be used to predict the probability of tumour control. One of the models follows a standard method, using Poisson statistics to fit data in which patients were only treated using radiotherapy. The second model is not a standard approach, but builds upon the previous model and aims to provide an additional, 'best estimate' of the effects of treating patients with chemotherapy as well as radiotherapy. Both models were designed to be used to enable comparison of the likely effects of a standard bladder radiotherapy treatment with a variety of alternatives based upon the use of DW-MRI within their design.

The central results of this thesis are presented in Chapter 6; this details the systematic investigation of increases in dose to simulated bladder tumours. In this study, tumours were simulated to mimic the range that might be seen using DW-MRI within the BladderPath Clinical Trial [10]. Standard radiotherapy treatments were compared with dose-escalated treatments, with a wide range of doses tested. The models produced in Chapter 5 were then used to predict the probability of control of the tumours using both the standard technique and the dose-escalated techniques. The resulting predicted increases in probability of tumour control from the dose-escalated treatment design based on DW-MRI are presented.

The feasibility of clinical delivery of the radiotherapy dose distributions discussed in Chapter 6 was assessed using daily imaging of a patient showing the day-to-day movement of the bladder and other anatomy. The results of this feasibility study are presented in Chapter 7.

Finally, Chapter 8 draws together the implications of the results seen in Chapters 4-7 and sets out a vision of how this change in radiotherapy treatment technique could be implemented, along with the future work required.

Chapter 2

Radiotherapy and imaging

This chapter introduces the concepts and background knowledge about radiotherapy and related imaging that is relevant for the chapters which follow. It begins with a brief history of the development of the use of ionising radiation for medical treatment, in order to set the context for this project. The methods of production and shaping of x-ray beams for radiotherapy treatments, and their interactions with cells and resultant effects are then discussed. This leads on to the introduction of tumour control probability (TCP), which is fundamental to the practice of radiotherapy, and which is investigated further in Chapter 5. Section 2.1.4 then provides an overview of the techniques used in current radiotherapy clinical practice, and section 2.1.5 presents the limitations of radiotherapy treatment including toxicity and treatment failure. Section 2.2 introduces the imaging methods currently required for accurate calculation and delivery of 3-D dose distributions to a patient, as well as other imaging of relevance to this thesis.

2.1 The use of radiation for medical treatment

The information presented within sections 2.1.1, 2.1.2 and 2.1.3 can be found in many radiotherapy physics textbooks; where not otherwise stated information was taken from The Handbook of Radiotherapy Physics [11] and Radiotherapy physics in practice [12].

2.1.1 Historical context

High energy x-rays have been routinely used for decades for the treatment of cancer, and remain one of the main forms of radiotherapy. A variety of techniques are used to image the patient prior to radiotherapy treatment in order to accurately

delineate the volume of tumour which requires irradiation. Over the last few decades, the imaging techniques used to determine the tumour volume, and the ability of radiotherapy treatment machines to deliver radiation accurately to these volumes have been refined and developed [13].

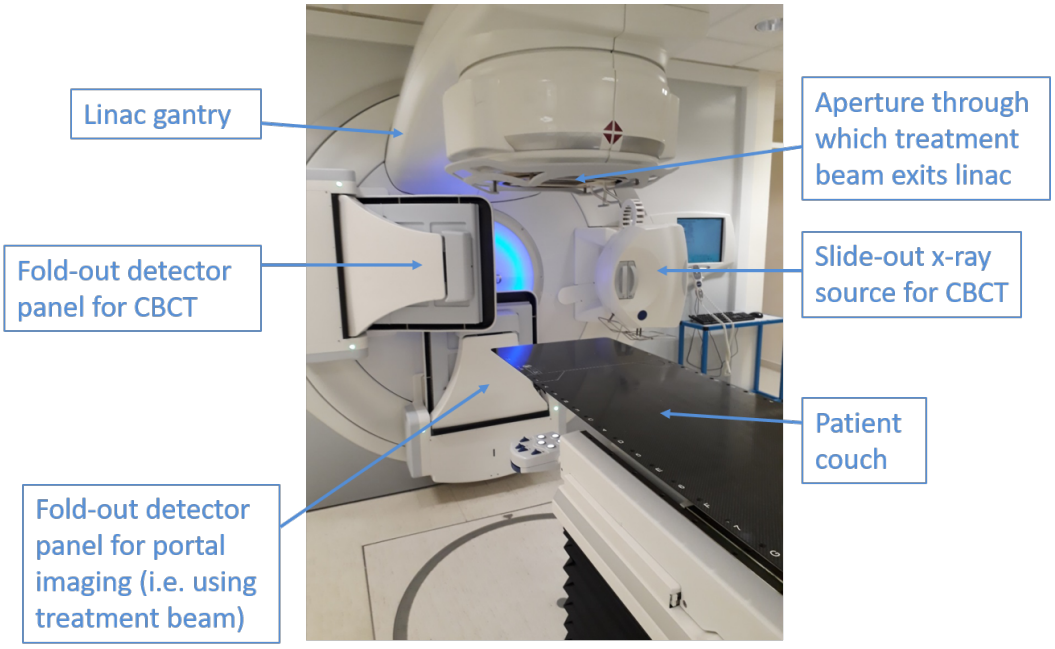

Figure 2.1: Picture of a modern Elekta linac.

Technological developments from the initial use of radioactive sources (particularly Cobalt-60) and cathode-ray x-ray generators, through to modern linear accelerators (linacs) have systematically improved the ability to deliver radiation doses more accurately, and with corresponding decreases in doses to healthy tissues. An example of a modern linac is shown in figure 2.1. These technological developments have led to improvements in both survival and patient quality of life following treatment, owing to the ability to deliver higher doses of radiation to tumours, with lower doses to nearby healthy organs. Improved conformality of regions of high dose to the desired volume have been possible via the development of multi leaf collimators (MLCs). These consist of multiple narrow pieces of high-Z metal such as tungsten which can be rapidly moved and interleaved to produce complex-shaped x-ray beams (for a schematic example, see figure 2.4). Developments in computer systems in conjunction with MLCs has enabled the calculation of sculpted radiation dose distributions and the treatment machines to accurately deliver them. The progression has developed from basic 2-D to 3-D and even 4-D radiation delivery, so that in the latter, the effects of positional changes with respiration can now be ac-

commodated. At the present time, there is widespread clinical use of 3-D sculpted dose distributions which are accurately calculated and delivered using such techniques as intensity modulated radiotherapy (IMRT) and volumetric modulated arc radiotherapy (VMAT). These techniques may also be gated to enable delivery at specific parts of the breathing cycle for greater accuracy of dose delivery to tumours in 4-D [13].

It could be argued that some of the current limitations of radiotherapy treatment are due to limitations in imaging capabilities, rather than dose delivery, and in the ability to accommodate patient anatomical variations at the time of treatment relative to the snapshot previously seen during initial imaging of their anatomy. Much current research and development aims to address these issues, particularly with regard to the use of MRI both prior to, and during the delivery of radiotherapy treatments, in order that radiation doses are conformed as closely as possible to the required volumes. As the technological developments discussed above enabled improvements to radiotherapy treatment delivery, it is anticipated that further technological advances incorporating developments in MRI could lead to future improvements in patient outcomes. This could be via enabling improved identification of tumour volumes and individualisation of treatments such as adaptations to response as evidenced by MRI during treatment.

2.1.2 Radiation - production and interactions

X-rays used for modern radiotherapy treatments are generally produced using linear accelerators (linacs), which produce a spectrum of energies in the megavoltage (MV) range. Figure 2.2 shows a nominal 6 MV spectrum, which may have a mean x-ray energy of around 2 MeV. This energy range exhibits the 'build-up' effect, as seen in figure 2.3, in which the absorbed dose is higher a short distance beneath the skin compared to the surface. The effect is due to a lack of electronic equilibrium, as it requires a short distance for the electrons generated (principally via the Compton effect) by the incident x-ray beam, and which tend to travel along the direction of the incident beam, to reach an equilibrium level. The range of secondary electrons produced via interactions in tissue will be around 16 mm [11], but the dose deposited will decrease after reaching electronic equilibrium as the beam is attenuated. Doses are usually measured in Gray (Gy) where 1 Gy is equivalent to 1 J/kg.

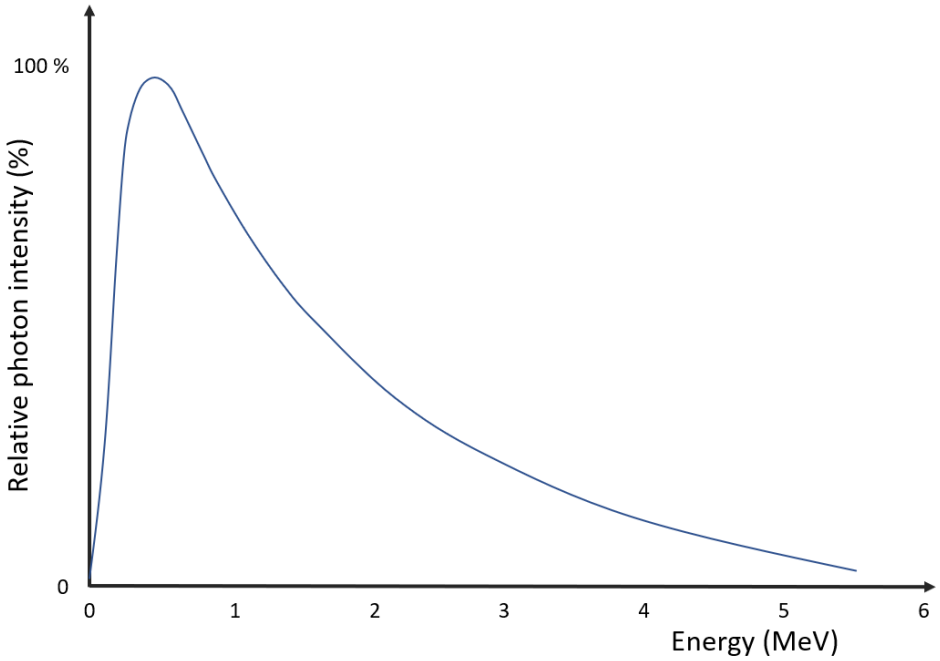

Figure 2.2: Spectrum of a nominal 6 MV linac.

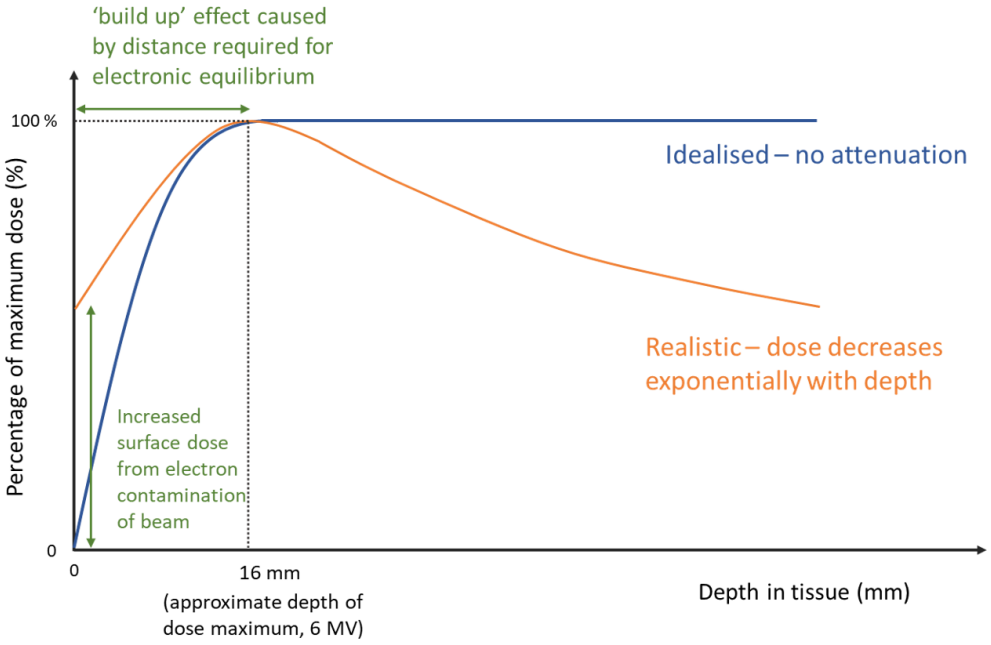

Figure 2.3: Variation of absorbed dose with depth for a nominal 6 MV x-ray beam produced by a medical linear accelerator. The variation of dose with depth is shown for an idealised beam with no attenuation and a realistic beam in which dose beyond the depth of dose maximum decreases approximately exponentially.

This 'build up' effect is exploited in radiotherapy treatments, as the dose to the skin would otherwise limit the achievable dose at depth. A schematic showing a linac and patient positioning system is shown in figure 2.4.

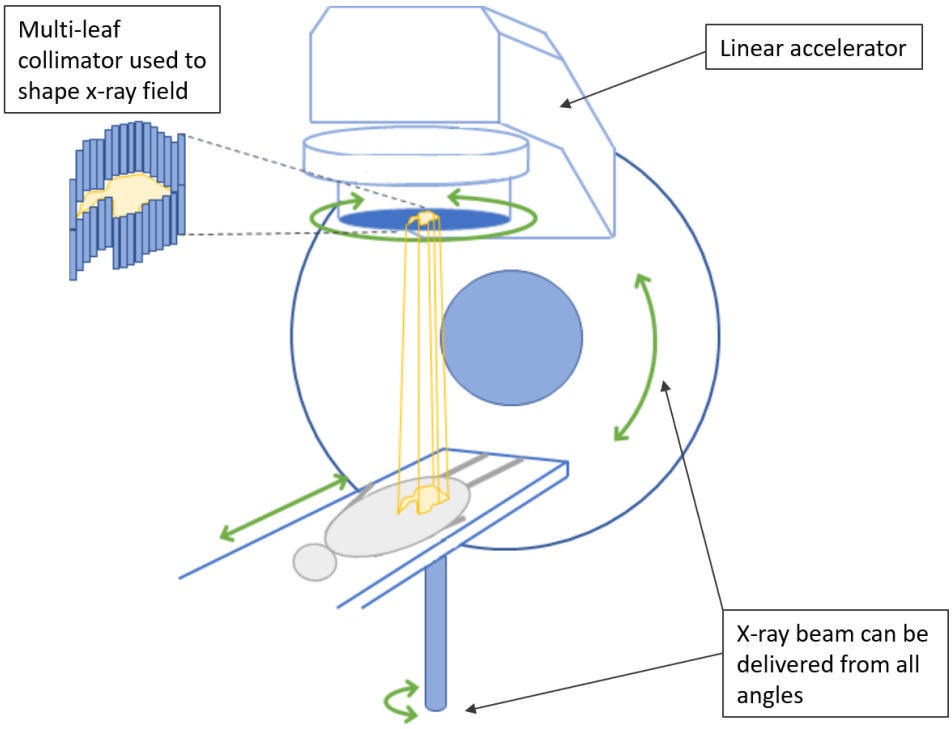

Figure 2.4: Schematic showing a linac and patient positioning system, allowing delivery of shaped beams of x-ray radiotherapy from all angles as required.

Medical linacs such as these are designed to enable x-ray beam delivery from all angles around a patient, allowing multiple beams to intersect at the desired location, and spreading out the radiation dose to healthy tissues. In the case of commonly-used VMAT treatments, the linac rotates continuously around the patient with positional adjustments to the MLC occurring whilst x-rays are delivered. Figure 2.5 shows a schematic of the effect of delivery of shaped beams of radiation of varying intensities from around the patient via a cross-sectional diagram through a patient. High dose gradients are achieved at the intersection of the beams (referred to as the 'isocentre'). This is usually chosen such that it is located within the tumour volume to be treated.

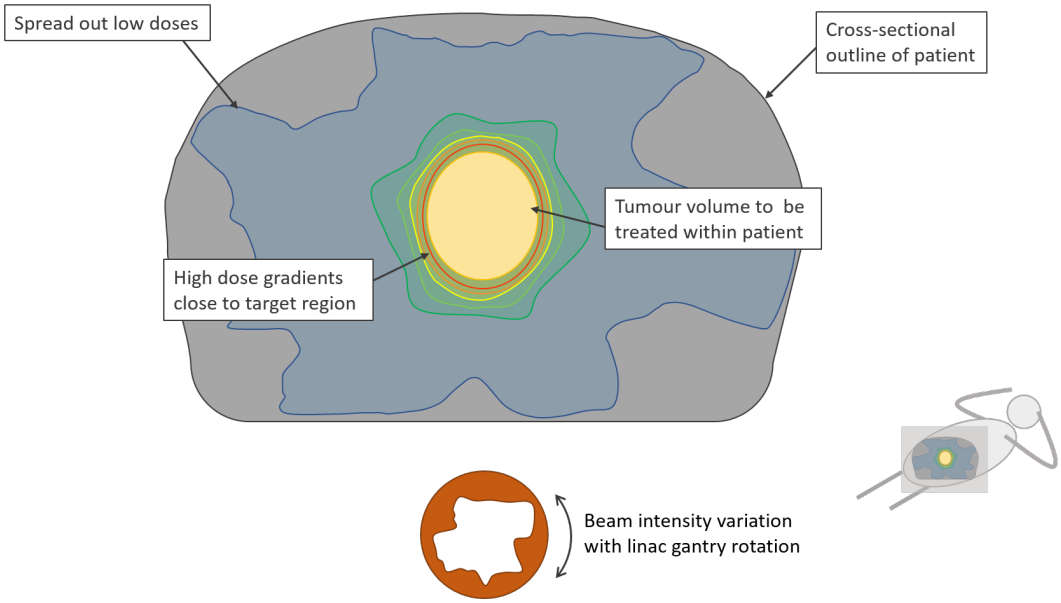

Figure 2.5: Schematic showing a cross-section through a patient and the intersection of beams of varying intensity from all angles around the patient. The variation of beam intensities with gantry rotation is indicated schematically below the patient cross-section.

2.1.3 Cellular responses to radiation and TCP

When radiotherapy is used to treat tumours, both tumour cells and healthy (normal) cells are exposed to ionising radiation. The proportion of cells killed depends on many factors including the sensitivity of the exposed cells to radiation (radiosensitivity). For each individual cell the likelihood of cell kill if exposed to a certain dose occurs with a particular probability, i.e. it is a stochastic process. However, for a large number of cells it is seen as a deterministic effect, and so there is a threshold below which no clinical effect is observed (and similarly a threshold above which an effect will always be observed). Figure 2.6 illustrates this; the curve on the left shows tumour control probability (TCP) i.e. the probability that the tumour will be controlled by that dose of radiation. The curve on the right shows normal tissue complication probability (NTCP), which is the probability that healthy tissue will experience a particular complication as a result of the radiation dose received. Successful radiotherapy treatment is more likely when the TCP curve lies far to the left relative to the NTCP curve, as it is possible to deliver a larger dose to the tumour and achieve a higher probability of tumour control with a lower probability of unacceptable side effects.

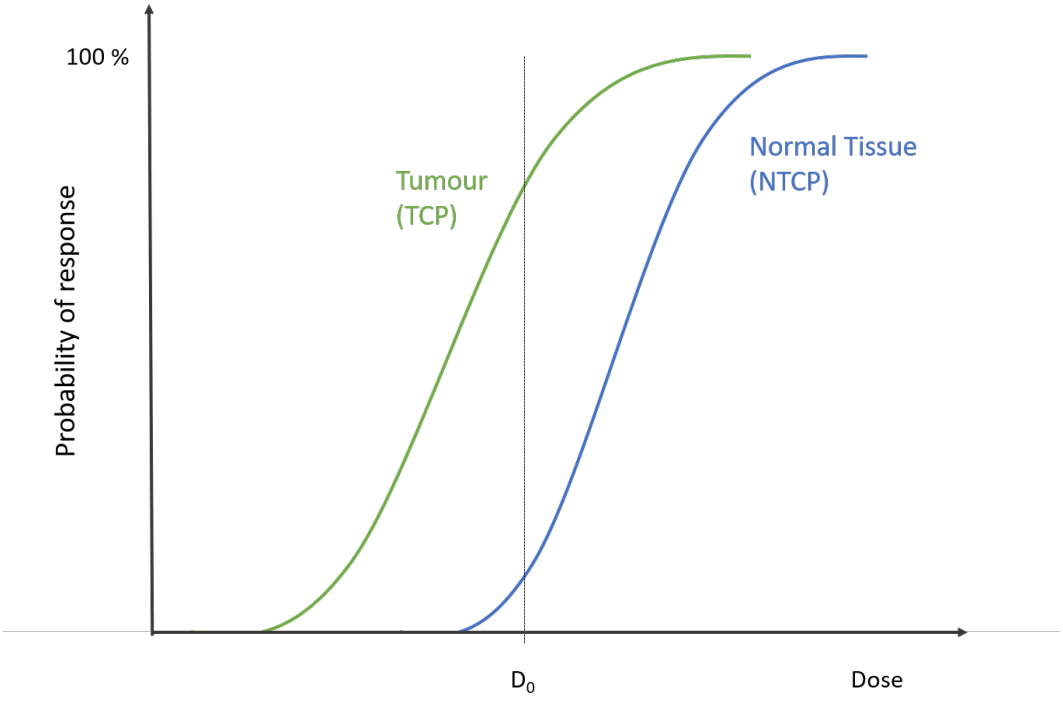

Figure 2.6: Probability of tumour control and normal tissue complication against dose. D_0 is the intended treatment dose. Adapted from Williams and Thwaites [12].

The tissues of the body retain their function via renewal of the cells within them, which occurs due to the ability of stem cells to reproduce. Tumours contain cells which reproduce rapidly, and can proliferate beyond the body's normal control mechanisms, leading to overgrowth and resultant complications. Not all cells within a tumour retain this ability to reproduce, however, and indeed many cells within a tumour remain normal functional cells. The intention of the use of radiation to treat a tumour is to 'kill' tumour cells whilst minimizing damage to normal, healthy cells nearby. Although the term 'kill' is often used when talking about the effects of radiation on cells, in fact it is not that the cells will necessarily immediately die, but that they lose the ability to reproduce and proliferate. Tumour stem cells can be detected via assays in which cells are placed in a growth medium, and those which are able to reproduce and form colonies are referred to as 'clonogenic', 'colony-forming' cells, or 'clonogens'. When clonogenic assays are performed, the proportion of surviving cells or colonies can be compared for variations in dose. The results from such experiments are often presented as cell survival curves, such as those seen in figure 2.7, which shows typical cell survival curves for irradiated cells.

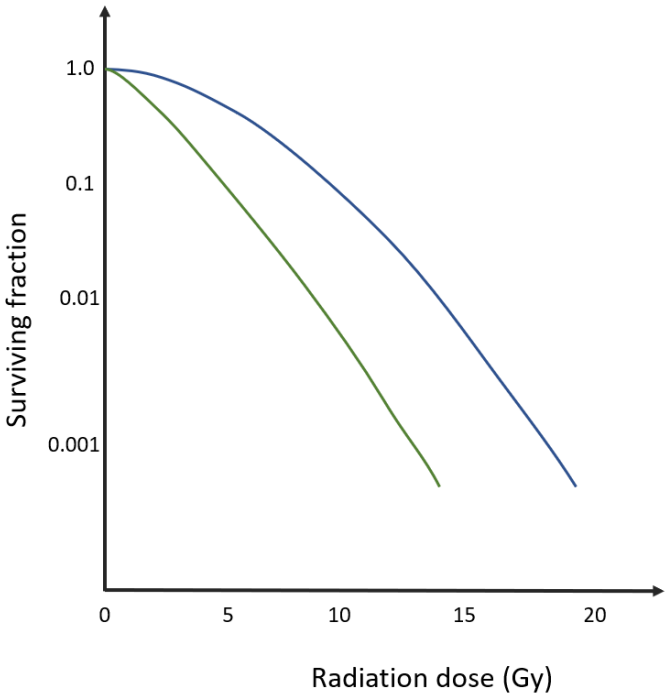

Figure 2.7: Schematic cell survival curves, plotted on a logarithmic scale. The green curve shows cells which are more radiosensitive and which would have a higher α/β ratio than those shown by the blue curve.

Study of cell survival curves has led to the development of the linear quadratic model, in which linear-quadratic curves are fitted to the survival data and are of the form

$$SF = e^{-\alpha d - \beta d^2}, \tag{2.1}$$

where the survival fraction (SF) is the fraction of cells which survive the irradiation, d is the radiation dose and α and β are parameters which determine the shape of the curve. Often, the shape of cell survival curves are referred to via a single parameter, the α/β ratio. The α value determines the initial slope of the curve, and the β value determines the degree of curvature. The curves in figure 2.7 illustrate the effect of variations in α/β, with the green curve having a higher α/β ratio than the blue curve. In general, tumours are thought to have high α/β ratios (e.g. $\sim$ 10 Gy) and normal tissues low α/β ratios (e.g. $\sim$ 3 Gy), although there is much variation between different tissue and tumour types, and some tumours have low α/β ratios.

For the purposes of comparing the effects of different types or doses of radi-

ation, it can be more appropriate to consider the effect (E) of radiation, instead of the surviving fraction of cells. In this case equation 2.1 becomes

$$E = \alpha d + \beta d^2, \tag{2.2}$$

i.e. here E = -ln(SF). Historical practice of radiotherapy led to the development of fractionation of treatments, that is, for the dose to be delivered in several equal portions, often with a portion given each day for 5 days over several weeks. This was found to produce a greater tumour response and reduce side effects to healthy tissue. The linear-quadratic model for n fractions is then

$$E = n\left(\alpha d + \beta d^2\right) = \alpha D + \beta d D, \tag{2.3}$$

where total dose D = number of fractions (n) $\times$ dose per fraction (d). This can be rearranged into the form

$$E/\alpha = D\left(1 + \frac{d}{\alpha/\beta}\right). \tag{2.4}$$

The quantity E/α is also known as the Biologically Effective Dose (BED), which indicates how much damage a particular fractionation scheme will do. This is the total dose which, if given in infinitely small fractions, is equivalent to the actual fractionation scheme with a dose per fraction of d and total dose D. The practice of fractionation can then be understood as the different α/β ratios between tumours and healthy tissues leading to the different effects of fractionation, where healthy cells tend to be less affected than tumours.

The BED is one way of comparing fractionation schedules; another commonly-used quantity for this purpose is to convert to the dose which if given in 2 Gy fractions is biologically equivalent (EQD2). This quantity is related to the BED via

$$EQD2 = \frac{BED}{1 + \frac{2}{(\alpha/\beta)}}. \tag{2.5}$$

Tumour control probability modelling

In theory, it should be possible to eradicate every clonogenic cell within a tumour, and if this were achieved, would enable control of the tumour. This is often referred to as 'local control', i.e. in the locality of the tumour the disease is controlled, although distant spread elsewhere (metastasization) may have ocurred and not yet be apparent.

However, total eradication of all clonogenic cells is difficult to achieve. Each

gram of a tumour may contain $\sim 10^9$ cells, of which only around 1 % will be clonogenic [11]. At the time of radiotherapy treatment, a tumour may be many grams and therefore the total number of clonogenic cells to be eradicated may be greater than 10^9. If, for example, a tumour contains 10^{10} clonogenic cells, then assuming a constant effect per fraction which results in a surviving fraction of around 0.5, then 30 fractions of 2 Gy will reduce the number of surviving clonogenic cells to around ten ($0.5^{30} \approx 10^{-9}$). However, although this number of surviving cells may not be visible on any imaging used to assess response, it does not necessarily mean that complete regression has been achieved.

From equation 2.1, and replacing SF by N_s/N_0, we can now write

$$N_s = N_0 \exp\left[-\alpha D\left(1 + \frac{\beta}{\alpha}d\right)\right] \tag{2.6}$$

where D is the total dose, d is the dose per fraction, N_0 is the initial number of clonogens, and N_s is the surviving number of clonogens.

Munro and Gilbert [14] originally modelled TCP using a combination of Poisson statistics and the linear-quadratic model of cell survival. They assumed that tumours are only controlled if there are no surviving clonogens at the end of treatment, and that for a population of identical tumours the number of surviving clonogens after irradiation has a Poisson distribution, i.e.

$$P(N, y) = \frac{e^{-N}N^y}{y!} \tag{2.7}$$

where P is the probability of the occurence of y events when the mean number of events is N. Therefore the probability of y = 0 (no clonogens survive) is

$$TCP = P(N, 0) = \exp(-N). \tag{2.8}$$

If an experiment were performed in which identical tumours were irradiated and there was, on average, a single clonogenic cell remaining then the probability of no clonogens remaining is 1/e (37%). Combining equations 2.1 and 2.8:

$$TCP = \exp\left[-N_0 \exp\left[\left(-\alpha d - \beta d^2\right)\right]\right] \tag{2.9}$$

where $N = N_s = N_0 SF$, for a single fraction. For n fractions of dose d and $D = nd$, this becomes

$$TCP = \exp\left[-N_0 \exp\left[-\alpha D\left(1 + \frac{\beta}{\alpha}d\right)\right]\right] \tag{2.10}$$

This approach to the modelling of TCP has been taken by many authors, and different models have aimed to incorporate the various effects of tumour cell radiosensitivity, changes in tumour volume, or inhomogeneities in dose distributions amongst other effects.

2.1.4 Overview of radiotherapy treatments

In general, a patient attending a radiotherapy department will have had diagnostic imaging to confirm cancer diagnosis, which will likely have included a computed tomography (CT) scan. In conventional radiotherapy treatment of most cancer sites, the patient will ordinarily have further CT imaging performed within the radiotherapy department which is often referred to as a 'planning CT', as it is used for planning and calculating the radiation dose distribution to the patient. Further details of CT scans are discussed in section 2.2.1, however in essence they are a 3-D image of the patient which shows good contrast between soft tissues (such as muscle) and bony anatomy. The image intensities within CT allow not only the visibility of many internal tumours and organs, but also the accurate calculation of radiation dose from x-ray beams. The dose calculation procedure is referred to as 'radiotherapy treatment planning', and may take place over the course of one or more days as it requires the input of several members of the radiotherapy team, in order to calculate and check all aspects. The radiotherapy treatment is then delivered over the course of several 'fractions' over several days, as discussed in section 2.1.3.

A difficulty which arises from planning treatments on a set of images from one snapshot of anatomy, and then fractionating treatment delivery, is that there will always be some changes in patient anatomy between the acquisition of the planning CT and delivery of each fraction. Some differences originate from the positioning of the patient, whilst others are due to internal changes such as variations in bladder filling. Where possible, all differences are minimised via the choice of reproducible patient positioning and assisted with immobilisation devices at the time of acquisition of planning CT. Nevertheless, dependent upon the anatomical treatment site and previous analysis of reproducibility of positioning, some imaging may be performed immediately prior to the delivery of radiotherapy. This is done with the aim of performing small shifts to the patient position so as to reproduce the original position as well as possible. The imaging used for this purpose is often cone beam CT (CBCT), which is very similar to standard CT but uses a cone beam of x-rays and a single rotation of the beam, and can be directly attached to the linac (see section 2.2.1).

2.1.5 Complications and limitations of radiotherapy treatments

Imaging limitations

Radiotherapy treatments can be limited by the visibility of tumour on the imaging used to determine the volume to be treated, There may be infiltration of nearby tissue by tumour which is not yet large enough to be visible owing to the limitations in resolution of any imaging method. There also may have already been metastasization of the tumour (distant spread around the body) which means that even if the local tumour is adequately treated, the disease elsewhere limits the long-term response of the patient. There is also the basic limitation of the anatomy located close to the tumour which limits the dose which may be prescribed to the tumour, as the proximity of other sensitive organs means doses must be limited for safety. This is a particular problem in mobile organs such as the bladder, where the margins required to ensure that tumour is treated are quite large and so nearby organs such as the bowel limit the dose that can be prescribed. Historical developments in both imaging and techniques to deliver radiation have enabled safe dose increases in some cases, or the reduction of side effects.

Side effects and toxicity

As tumours can infiltrate and also contain normal functioning tissue, the requirement to deliver a tumouricidal dose to volumes containing normal tissue means that side effects from radiotherapy treatment is to some extent unavoidable, even if the dose is highly conformed to the volume which requires treatment. Side effects of radiotherapy are very dependent upon the dose received and the tissue of the body receiving the dose. Some effects are short term 'acute' effects, which generally subside with time, and others can be long-term chronic or 'late' effects. Although the acute effects can be clinically significant as they may limit the deliverability of the treatment, the late effects are obviously also of concern as they are long-term and not necessarily reversible.

Side effects of particular relevance for bladder radiotherapy include those caused by irradiation of the bowel such as malabsorption, diarrhoea, ulceration and occasionally obstruction. The bladder itself can also be affected, with cystitis being the most common side effect but possible shrinkage or ulceration can occur [15]. This is not a complete list of the potential toxic effects of bladder radiotherapy but rather an indication of the many possible undesirable effects, most of which increase in likelihood with dose and the volume of tissue irradiated. The tolerance of the various different tissues can vary significantly, and in general the dose to the bowel

will be the limiting factor regarding the dose which is deliverable to the bladder owing to its proximity. These potential side effects can be generally referred to as the 'toxicity' of treatment. Technical developments in radiation delivery such as IMRT and VMAT have meant that doses have often been increased ('escalated') to small tumour volumes, whilst doses to nearby organs have been kept low. Sometimes this has been referred to as the development of 'isotoxic' dose escalation strategies, i.e. for tumour sites where there is an acceptable level of toxicity, the probability of local tumour control has been increased by a change in treatment technique, and clinical trials have compared the change against the standard technique with the aim of keeping the rates of toxicity constant.

Chemotherapy

Some tumours respond better when chemotherapy is given in addition to radiotherapy. It can be prescribed prior to (neoadjuvant) or during (concurrent) radiotherapy treatments. As chemotherapy agents are essentially toxic (although ideally preferentially affect tumour cells), the effects of chemotherapy can increase toxicity of radiotherapy treatments, as well as improving response.

2.2 Use of imaging within radiotherapy

Prior to the introduction of CT imaging, radiotherapy treatments were planned on the basis of external measurements of anatomy and 2-D (planar) x-rays of internal anatomy. Over recent decades, the use of CT to provide 3-D anatomical information about tumour and nearby organ locations has become ubiquitous. Current developments involve the use of other imaging modalities such as MRI and PET, which provide additional information regarding either improved soft tissue contrast or functional information. This section provides an overview of the imaging modalities relevant for radiotherapy treatments with respect to this thesis.

2.2.1 Computed tomography

The background information about computed tomography (CT) described here can be found in many textbooks on medical physics and imaging; unless otherwise stated this section refers to information from An Introduction to Medical Physics [16].

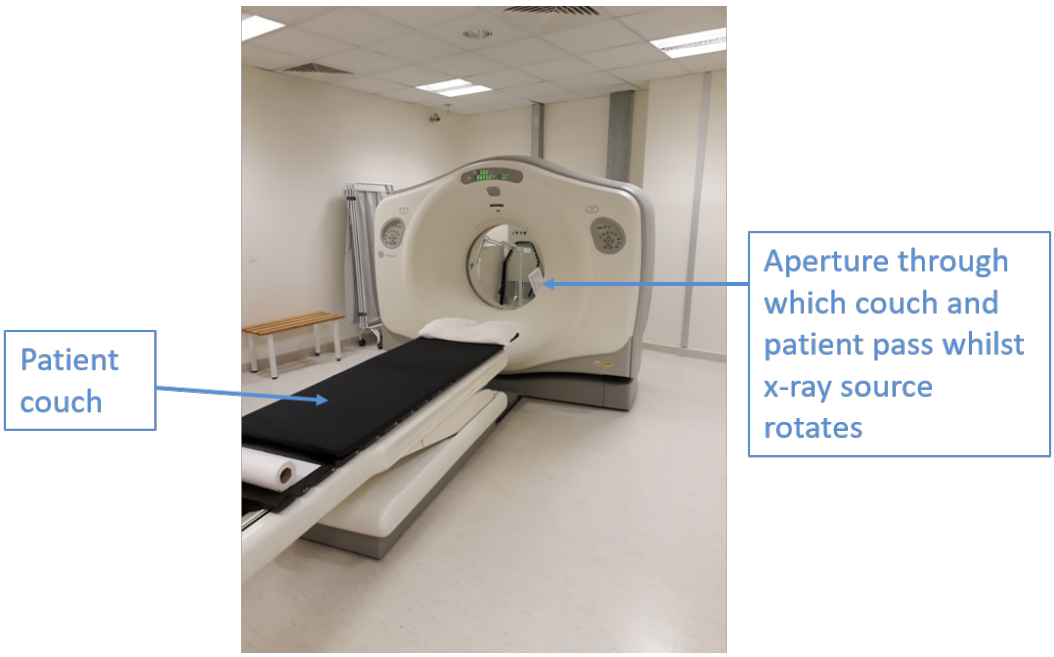

Figure 2.8: Example of a CT scanner.

Figure 2.8 shows an example of a CT scanner, with the patient couch and ring of detectors through which the couch is passed for image acquisition. A CT scanner produces cross-sectional images of the internal anatomy of a patient, via the use of a fan beam of x-rays which is rotated around the patient as they are moved along the axis of rotation (see figure 2.9 for a schematic). Detectors on the opposite side of the patient are used to detect the radiation which has passed through the patient. Images are then formed via back-projecting and reconstructing what must lay within each ray-path to have produced the images acquired.

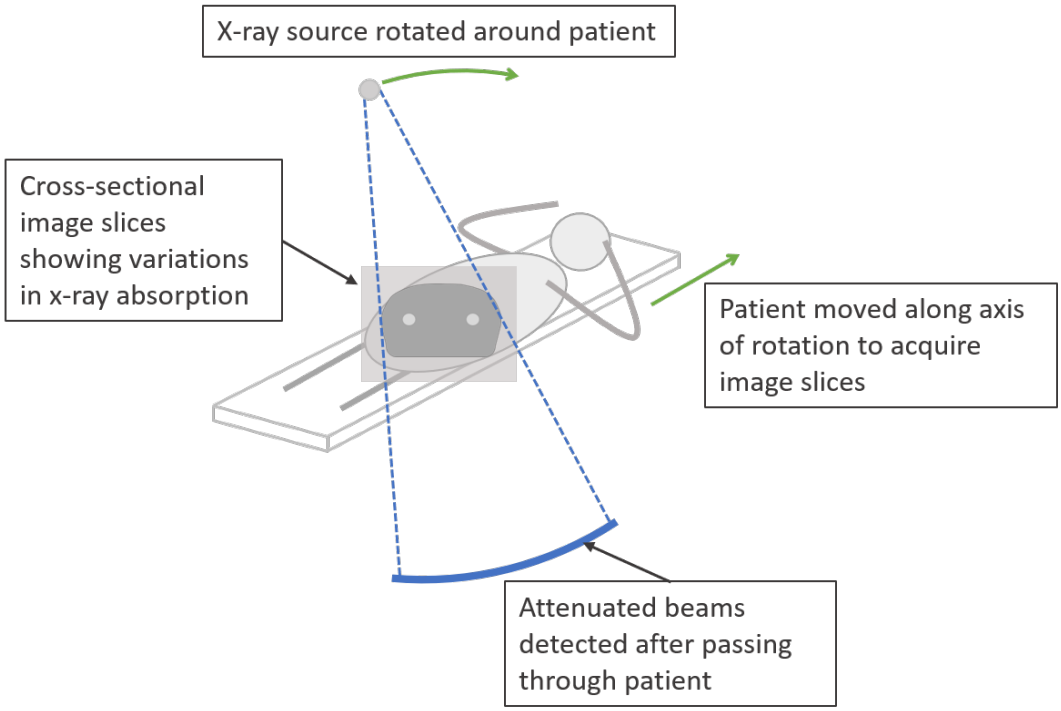

Figure 2.9: Schematic of a CT acquisition, showing the movement of the patient along the axis of rotation of the x-ray source and a simplified cross-sectional image slice with contrast between bones and the rest of the pelvis.

CT images are displayed as transaxial 'slices', i.e. a set of 2-D images each showing the cross-sectional view of internal anatomy. The display of these images is via an array of pixels (picture elements), the shade of which varies from white to black. The shade displayed varies according to the CT number, measured in Hounsfield units (HU), which depend upon the inferred x-ray absorption coefficient of that pixel. Figure 2.9 shows this idea with increased absorption shown in the cross-sectional view of the top of the femur (thigh bones) compared to the rest of the pelvis. As there is a stack of slices, each slice has a finite thickness, and therefore each pixel has an associated volume. This small volume element is called a voxel, and is often around 2 mm in each dimension [16].

Use of CT for radiotherapy treatment planning

CT is used for the dual purposes of delineation of tumours and nearby sensitive structures, as well as to allow accurate calculation of radiation doses. Patient geometry can be determined from CT due to good contrast between the various tissues of the body, and no geometric distortion of the reconstructed images. CT data is

readily converted from Hounsfield units to relative electron densities; this is useful as the x-rays used for radiotherapy treatments are of high energy (several MeV) and predominantly interact in the body via the Compton effect. Since the probability of Compton interaction is directly proportional to electron density, CT scans can therefore be used to calculate dose distributions which account for inhomogeneities in tissue [12].

Radiotherapy treatments require the delineation of the tumour volume, with subsequently reliable and accurate delivery of radiation to this tumour volume. This must be achieved by taking into account the various uncertainties in the process of imaging and repeatedly setting up the patient for multiple treatment fractions. The process is aided by the definition of specific 3-D volumes within the CT of the patient. These volumes are illustrated schematically in figure 2.10 and include the gross tumour volume (GTV), clinical target volume (CTV), internal target volume (ITV), planning target volume (PTV), and organs at risk (OARs). These volumes are defined by the International Commission on Radiation Units and Measurements (ICRU [17]).

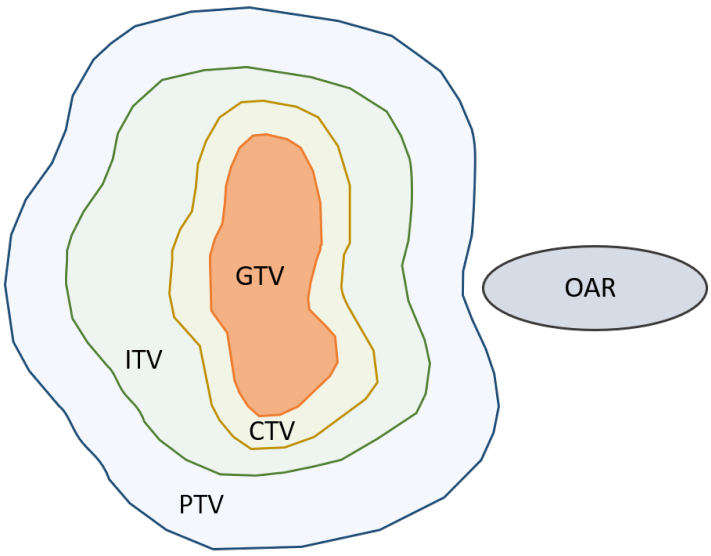

Figure 2.10: Schematic showing the relationship between the gross tumour volume (GTV), clinical target volume (CTV), internal target volume (ITV), and planning target volume (PTV) as defined by the International Commission on Radiation Units and Measurements (ICRU [17]). Note that the margins around each volume may be anisotropic, depending upon known positional variations and treatment techniques used. An organ at risk (OAR) is also shown for context.

The GTV is the gross palpable, visible or demonstrable position and extent of the malignant growth, and the CTV is the volume of tissue that contains the GTV and any subclinical microscopic disease (if there has been surgery to remove the GTV, there will remain a CTV but which no longer contains the GTV). This CTV is the entire volume which must be treated using radiotherapy in order for the local control of the disease to be achieved. An ITV may be produced in order to accommodate the internal motion of a CTV relative to bony anatomy of the patient. Variations in size and location of a CTV may occur due to breathing or other organ motion, and so is formed from the CTV plus a margin to accommodate the variations.

The PTV is a geometrical definition which is used for the purposes of treatment planning, and contains the CTV but with additional margins which vary in order to account for variations in daily positioning and motion-related uncertainties. The purpose of the PTV is to enable delivery of the prescribed radiation dose to the whole GTV/CTV with an acceptable (high) probability.

In the case of bladder cancer, the GTV is the tumour volume itself, but the CTV is usually the whole bladder, as there may be microscopic disease spread and distinguishing GTV from healthy bladder wall is not always possible using CT (and particularly CBCT). The PTV is therefore constructed via a margin around the outside of the whole bladder. The margins may be isotropic, or anisotropic in order to take into account the known variations in movements of the bladder in different directions (this is discussed in greater detail in Chapter 6, section 6.3).

Cone Beam CT

An imaging technique similar to CT is cone beam CT (CBCT), in which instead of using a fan beam of x-rays for imaging the patient whilst the patient is moved, a cone beam is used, and rotated around the patient a single time with the patient remaining stationary. Equipment which can be used to do this is often attached to the linear accelerator used to deliver the radiation treatment, enabling rapid imaging of the patient immediately prior to treatment delivery. Figure 2.1 in section 2.1.1 showed a linac with CBCT attached.

Small alterations in the patient position may be made on the basis of the acquired CBCT images which show internal anatomy, so that margins used to create the PTV can be minimized, resulting in minimisation of doses to OARs and the volume of healthy tissue irradiated around the tumour. CBCT produces images with poorer image quality than is possible with conventional CT, owing to the increased scatter from the use of the cone beam of x-rays, but is adequate for many tumour sites. The field of view (FOV, i.e. cross-sectional area in which images are acquired) of CBCT may also be smaller than for a conventional CT scan.

2.2.2 Magnetic resonance imaging

The background information about magnetic resonance imaging (MRI) described here can be found in many textbooks on medical physics and imaging; unless otherwise stated this section refers to information from An Introduction to Medical Physics [16] or MRI From Picture to Proton [18].

Whilst CT is the predominant imaging modality used within radiotherapy, other modalities can provide supplementary information. Sometimes contrast between different tissue types is insufficient using CT, or information about the functionality of the tissues rather than gross anatomic differences may be desirable. MRI is one of the most commonly-used of these other modalities. In general, where MRI is used within radiotherapy treatment planning, the images are acquired in addition

to the planning CT and fused with or registered to the CT, such that the visibility of anatomy can be compared between the two datasets [16]. This image registration means that the information from the MRI can be incorporated into the radiotherapy treatment planning, and dose calculation still performed using the CT dataset.

MRI can contain spatial distortions and other artefacts and so care must be taken when using this modality for the purposes of radiotherapy, as whilst these effects may not be significant when the same images are used purely for diagnosis, they could result in significant effects within the radiotherapy process. It is not straight-forward to use MRI for volumetric radiotherapy dose calculation, as the electron density information acquired from CT is not simple to infer from an MRI. However, this is an area of much research and is starting to be used clinically in some sites [19]. This use of MRI without fusion to CT is referred to as MR-simulation or MR-sim. The use of MRI for MR-sim and radiotherapy treatment planning is likely to be developed further in the future as MR-linacs become more widespread (MR-linacs are combined linacs and MRIs used for radiotherapy treatments with the MRI used to image patients prior to and even during delivery of radiation [20]).

Generation of an MR image

MRI involves putting the patient inside a strong magnetic field (usually 1.5 or 3.0 T) to induce a magnetic field within the patient. This field is then perturbed in a variety of ways by using radiofrequency (RF) pulses, and as the system returns to equilibrium by a process called 'relaxation', small RF signals are produced. The RF signals can be detected and converted into images using a fast Fourier transform (FFT) which converts the frequency information detected into positional information. The frequency information is referred to as 'k-space' and is essentially an array in which each cell contains information about how much of that particular signal frequency occurs in the image. The appearance of MR images can vary widely depending on the sequence of applied RF pulses and additional gradients in magnetic field used for its acquisition.

In the presence of an external magnetic field, protons will align either parallel or anti-parallel with this field, and precess around it. A slight excess of protons are aligned parallel with the field and so this results in a net induced magnetic field in the patient, in the direction of the applied field (usually referred to as the longitudinal direction). This net induced magnetization can be referred to as the net magnetization vector (M_0). The precession frequency ω_0 is described by the Larmor equation,

$$| \omega_0 | = | \gamma B_0 | \tag{2.11}$$

where γ is the gyromagnetic ratio which is a constant for each nuclear isotope and B_0 is the external magnetic field. When an RF pulse (B_1) is applied which has the same or very similar frequency as the precession frequency, the amount of longitudinal magnetization is decreased and the protons also become synchronized (i.e. begin to precess in phase with each other). We can say that

$$B_1 = | B_1 | cos(\omega_{RF} t + \phi), \tag{2.12}$$

where $| B_1 |$ is the magnitude of the RF signal, ω_{RF} is the frequency of the applied RF, t = time and ϕ is an arbitrary offset. The resonance offset, Ω, is the difference between the applied RF and the Larmor frequency, i.e.

$$\Omega = \omega_{RF} - \omega_0, \tag{2.13}$$

which must be sufficiently small for resonance to occur.

The application of the RF pulse results in a transverse component to the magnetic field (i.e. perpendicular to the original longitudinal direction of the magnetization). Figure 2.11 (a) illustrates this movement of M_0 from longitudinal (z) direction into the transverse (x-y) plane. This is often pictured via a rotating frame of reference, as can be seen in (b) where the frame of reference rotates at ω_{RF}. The angle through which M_0 is moved is often specified in terms of the RF pulse which caused it - e.g. a 90° pulse causes M_0 to be 'tipped' or 'flipped' such that it rotates in the x-y plane at ω_{RF}.

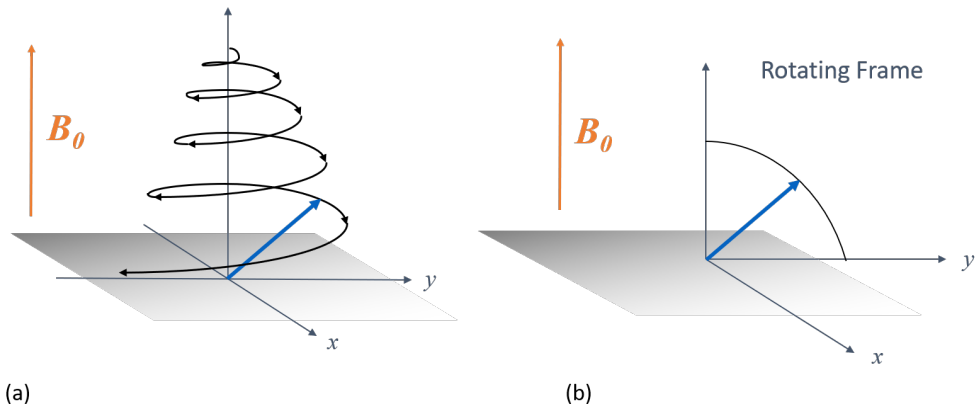

Figure 2.11: Diagram showing movement of M_0 into the transverse plane following application of an RF pulse at ω_{RF}. (a) shows the effect in the laboratory frame of reference, and (b) a frame of reference rotating at ω_{RF}.

If the RF pulse is switched off, the system begins to revert to the initial state, and the rates at which longitudinal magnetization is regained and transverse magnetization are lost are independent from each other. The former depends on energy exchange with the surroundings (or lattice, so this is sometimes referred to as 'spin-lattice' interactions) and are described by a time constant denoted T_1. The rate at which transverse signal is lost depends on the rate at which synchronicity in the phase of precession is lost, and this in turn depends on inhomogeneities in both the external magnetic field and in the local environment. This can therefore be referred to as 'spin-spin' interactions, and these are described by a time constant denoted T_2. Images acquired in which the timings of excitations and signal measurement are chosen so as to maximize either the contrast resulting from differences in T_1 or T_2 relaxation times are referred to as T_1 or T_2 'weighted' images (T_1W or T_2W respectively).

Sometimes the RF pulse used is referred to as 'tilting' the magnetization, as what can be seen on the macroscopic scale is a net shift in direction of magnetization, for example from longitudinal to transverse (which would be called a 90° pulse). Other RF pulses can be used, and are similarly named based on the angle through which the net magnetization is changed. Combinations of pulses can be used so as to maximise the differences in signals generated between tissue types, according to their relative relaxation times. For example, a 'spin-echo' pulse consists of a 90° pulse and one or more 180° pulses (for T_2 weighted imaging) and can be used to highlight differences in rates of loss of phase coherence between different tissue types [21].

Figure 2.12: An example MR scanner showing the various typical axes and directions, and the location of the different parts of the scanner.

Gradient fields are produced in MRI by the gradient coils, such that the strength of magnetic field varies linearly along the length of the scanner (figure 2.12 shows the location of the coils and the axial directions referred to here). The gradient fields allow positional information in terms of the 'slice' (or z-direction for axial slices) along the patient length to be selected. To determine positional information within a given slice, other gradients are applied; these are the 'phase encoding' and 'frequency encoding' gradients.

In order to fill k-space with sufficient data to form an image, these processes are repeated multiple times in quick succession. The repetition time, TR, is the time between two excitation RF pulses, and the echo time (TE) is the time between an excitation pulse and the MR signal sampling. The number of excitations (NEX) and echo train length (or number of echoes) may also be specified when describing a particular MR sequence. Whereas in CT scanning, the FOV of the scanner is generally fixed, this can be manually set for MR scans in order that the region of interest can be imaged with sufficient resolution in a reasonable time.

Conventional MR imaging produces images in which there is excellent contrast between various soft tissues of the body; this can be useful within radiotherapy both for delineation of tumours (GTVs) as well as for OARs. An advantage of an MR-linac is that this kind of imaging is then possible both immediately prior to and

even during treatment, with no additional radiation dose to the patient unlike with the use of CBCT. As there is improved soft tissue contrast, some tumours are much more visible against local soft tissues using MRI than with CT, and particularly with the reduced contrast seen in CBCT.

2.2.3 Biological imaging: DW-MRI

Biological imaging does not have a precise definition, but can broadly be divided into functional and molecular imaging (although there is no consensus on these definitions) [22]. Functional imaging can refer to imaging of physiological processes such as blood flow, and may be performed using MRI, CT and ultrasound. Molecular imaging generally refers to imaging of molecular and cellular processes and can be performed using positron emission tomography (PET), magnetic resonance spectroscopy and others.

Of interest for the purposes of this thesis is a particular type of biological imaging which can be performed using MRI, in which the sequences chosen produce images which are sensitive to the degree of diffusion of water molecules within the body called diffusion-weighted MRI (DW-MRI). In addition to the conventional forms of MRI discussed in section 2.2.2, an MR scanner can also be used to produce images in which contrast is produced between regions of high diffusion of water, and regions where diffusion is restricted. This provides information beyond pure anatomic information (indeed, the detailed anatomic information normally acquired in MRI is lost when using this technique). However, when multiple types of MR images are acquired in a single session they can provide a range of information about the relevant part of the patients' anatomy; this is often referred to as multiparametric imaging (mpMRI). DW-MRI is a form of biological imaging which is often one of the acquired datasets of mpMRI.

DW-MRI techniques show signal intensities that vary according to the average distance water molecules are displaced through diffusion. The signal decreases with increase in speed with which the water molecules travel in the direction of an applied gradient. Where the geometry of the environment on a cellular level prevents free movement of water, as in the proliferation of tumour cells, the diffusion is reduced.

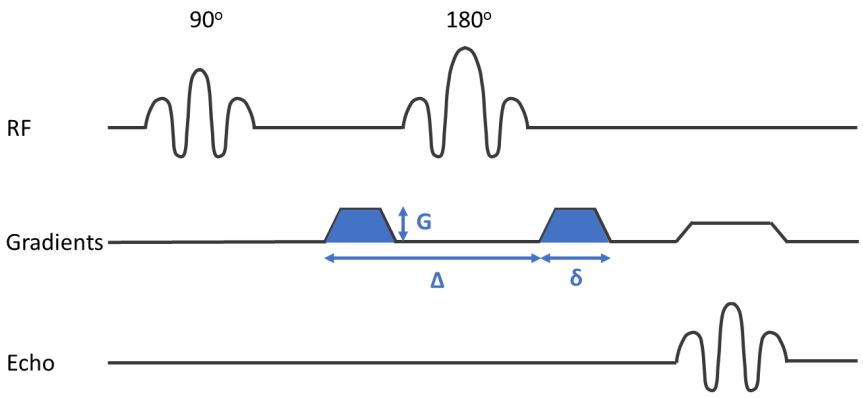

Figure 2.13: Schematic showing the application of RF pulses and diffusion sensitizing gradients to generate a DW-MRI signal.

In order to create an image in which the contrast is sensitive to the diffusion of water, a pair of (very high amplitude) gradients can be applied before and after the 180° RF pulse. This is illustrated schematically in figure 2.13, which shows an initial 90° RF pulse (which tips the signal from alignment with the applied magnetic field) followed by a later 180° pulse which is used to rephase the protons. The signal is then detected following the time allowed for rephasing. On either side of the 180° pulse are the applied diffusion gradients. The effect of this is essentially that if all protons were to remain stationary the effect of the applied gradients would cancel. However, if there is movement (due to the diffusion of the water containing the protons) then the protons will experience different magnetic fields and therefore there will be resulting signal loss. Hence there is greater signal where there is restricted diffusion, and reduced signal where there is a high rate of diffusion.

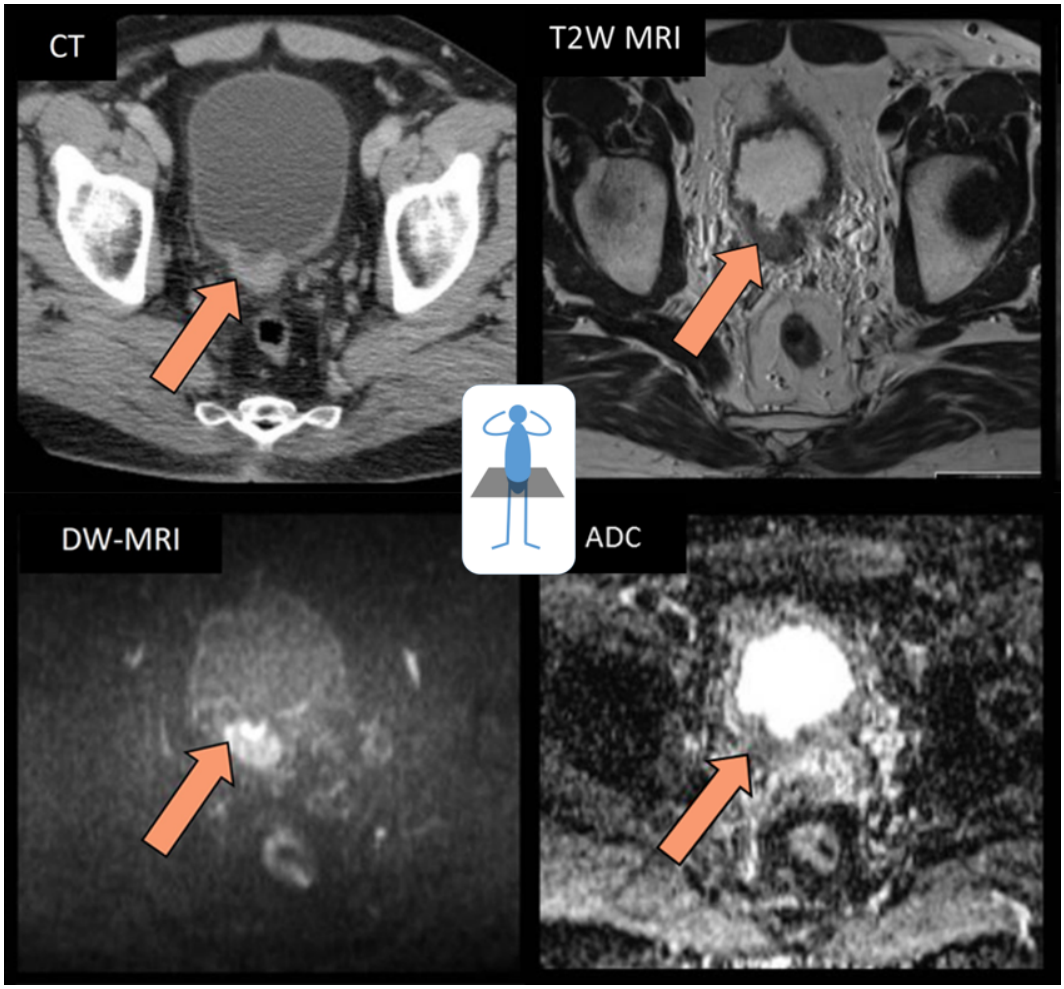

Figure 2.14: Cross-sectional imaging of the bladder and an internal tumour as shown using CT, T_2-weighted MRI (T_2W-MRI), Diffusion-weighted MRI (DW-MRI) and Apparent Diffusion Coefficient (ADC) mapping. Images reproduced from Maurer et al. [23], arrows added.

An example of the various types of imaging discussed can be seen in figure 2.14, which shows a cross-sectional image of a bladder and an internal tumour highlighted with an arrow as it appears on each image modality. The thickening of the bladder wall at the location of the tumour is visible on the CT image. Similarly on the T_2W-MRI, although there is improved contrast between the bladder wall and its contents, it remains difficult to clearly see the extent of the tumour. On the DW-MRI it can be seen that, although anatomic information is reduced, the tumour volume is highlighted clearly. This is because the proliferation of cells in a tumour restricts the diffusion of water molecules that would normally occur in the

intracelluar spaces, and so the information contained within the image shows what is occurring at the cellular level (although obviously the resolution is far less than this). From the perspective of the designing of radiotherapy dose distributions, it would be useful to be able to accurately overlay the information from all of these images, so as have knowledge of tumour proliferation (from the DW-MRI) as well as electron density (from the CT) and nearby soft tissues and organs at risk (from the T_2W-MRI).

Apparent Diffusion Coefficient (ADC) maps

The final image in figure 2.14 is an apparent diffusion coefficient (ADC) map, which is generated via the acquisition of multiple DW-MRIs of the same volume, but with different amounts of diffusion weighting applied each time (i.e. different gradient strengths or applied for different times). The different amounts of diffusion weighting are applied by altering the amplitude and duration of the gradients and are referred to as the 'b-value'. An ADC map is a parametric map, in which the greyscale of each pixel of the image is a display of the ADC value according to the equation

$$I = I_0 e^{-b.ADC}, \tag{2.14}$$

where I = intensity and b = b-value. The b-value depends on the strength and timing of the diffusion gradients applied - the higher the b-value, the stronger the diffusion effects. The value(s) of b can be chosen prior to imaging, and this choice controls the degree of observed diffusion weighting. Typical values available on MRI scanners range from 0 - 4000 s.mm^{-2}, although those used are generally in the range 0 - 1000 s.mm^{-2}. Using the original Stejskal-Tanner pulsed gradient method [24], the b-value is given by

$$b = \gamma^2 G^2 \delta^2 (\Delta - \delta/3), \tag{2.15}$$

where γ = gyromagnetic ratio, G = gradient amplitude, Δ = interval between gradient pulses and δ = duration of each pulse (and as illustrated schematically in figure 2.13).

Calculation of b varies, however, depending on the sequence used, and modern techniques often use trapezoidal or sinusoidal pulses rather than the rectangular Stejskal-Tanner technique. In any case, larger b-values are achieved by increasing the gradient amplitude (G) and/or duration (δ) and by widening the interval between gradient pulses (Δ).

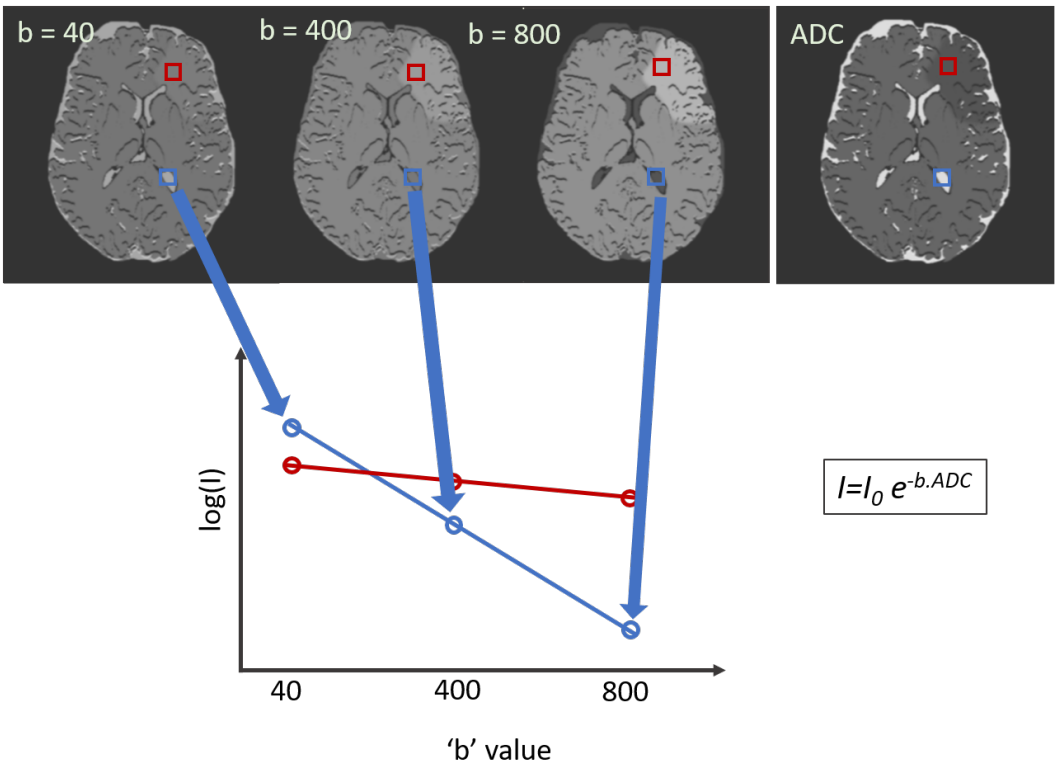

Figure 2.15: Illustration of the calculation of ADC maps from multiple DW-MRIs of the same volume. Highlighted blue and red volumes on each image correspond to the plotted blue and red circles. Images reproduced from http://xrayphysics.com/dwi.html.

Figure 2.15 illustrates how the parametric map is produced, with bright areas on the ADC map produced where the gradient of the log(intensity) against b-value curve is highest. Similarly, darker areas on the ADC map are produced from regions where the gradient of the graph is flatter. In theory, any two b-values could be used to fit the straight line in the b-value against log intensity graph. However, the behaviour of the curve can deviate from linearity, particularly at lower b-values as microcapillary perfusion effects can also cause changes in the apparent diffusion coefficient [25]. There may be optimal b-values to use to fit the ADC curve for a particular anatomic site [26], or a greater number of b-values than two may be used for acquisition.

The ADC map is a useful tool, as an individual DW-MR image may have 'T_2 shine-through', where a bright area of the image is not necessarily due to reduced diffusion but due to a long T_2 relaxation time. The ADC is independent of such

effects and shows only the change in response with diffusion weighting. Therefore it is quantitative, and ranges of expected ADC values can be measured for various tissues, either to note differences between patients or changes for a given patient over the course of time.

Unfortunately, the acquisition of DW-MRI and the resulting ADC maps can be strongly affected by geometric distortion, to a far greater extent than conventional MRI. One of the known main causes of this, is the way in which the signal is read out for this type of sequence. As the images must be acquired rapidly, in order that the effect of the diffusion of water is seen, the acquisition of all of the signal frequency information is performed for each cross-sectional slice much more rapidly than for conventional MRI.

A representation of the spatial frequencies acquired over the whole slice is referred to as the 'k-space' of that slice, and for conventional imaging this may be read out a line (of k-space) at a time. Echo-planar imaging (EPI), is a frequently-used method to rapidly read out the signal for DW-MRI and other techniques which require fast acquisition. In this technique, k-space is read out in a 'raster' pattern, as represented in figure 2.16 following a single 90° pulse. In this figure, the magnetic field map is illustrated as non-uniform owing to the distribution of magnetic susceptibility in the patient to be imaged within the bore of the MR scanner. (The magnetic susceptibility may be thought of as the readiness of a material to be magnetized, i.e. how magnetized a material will become in an applied magnetic field). Also illustrated is the way in which one direction of k-space is read out rapidly, and the other is read out more slowly (k_x and k_y respectively in 2.16). The interaction of this readout of k-space and the resulting potentially misplaced signal in k-space is what leads to distortions in physical space, and which occur predominantly in the 'slow' direction of k-space readout.

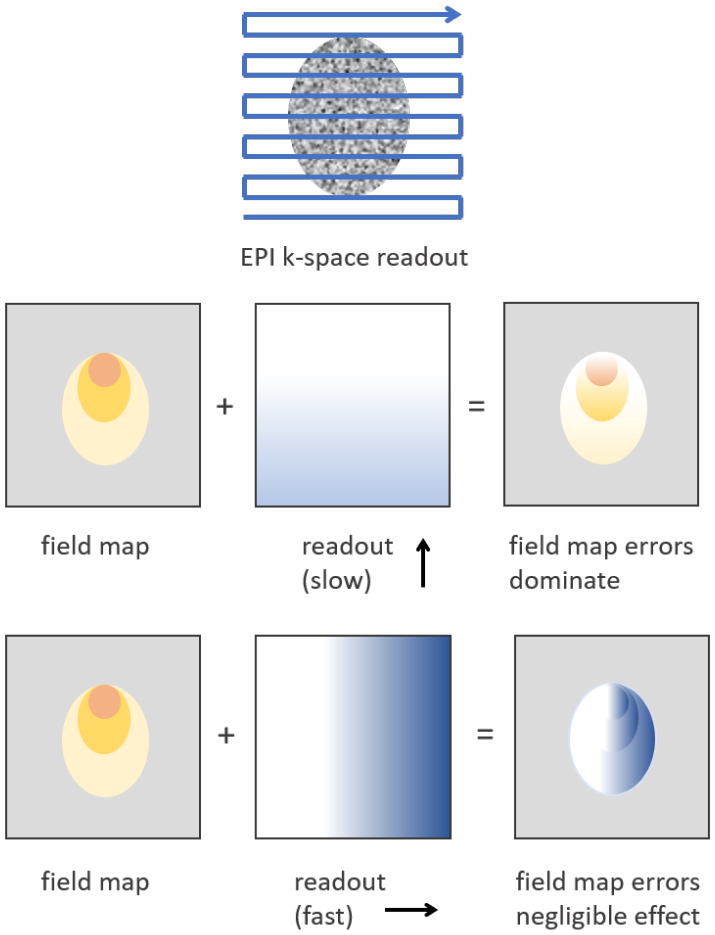

Figure 2.16: Representation of the effect of EPI readout of k-space on distortion in images. Images adapted from http:/users.fmrib.ox.ac.uk/∼mchiew/teaching/.

Figure 2.16 illustrates a 'blip up' image acquisition, in which the raster pattern of k-space readout is performed from bottom up - the image could also be acquired in a 'blip down' direction, i.e. with the acquisition of k-space from top-to-bottom. The effects of this change are discussed further in chapter 4 and particularly section 4.2.9.

The use of biological imaging within radiotherapy treatment design

Biological imaging modalities such as DW-MRI could provide important, additional information regarding the functionality of tissues and the changes in functionality over the course of treatment. Adaptations could then be made to treatments based on individual patient response as indicated using these types of imaging. Some stud-

ies have been performed investigating these possibilities, for example Shaverdian *et al.* [27] assessed the feasibility of the use of DW-MRI within an integrated MRI-radiotherapy system for response assessment in rectal cancer, and Yang *et al.* [28] reported their preliminary experience in the use of an MRI-guided cobalt 60 radiotherapy system for three head and neck and three sarcoma patients. The results of these studies showed the incorporation of DW-MRI into the radiotherapy treatment pathway is feasible, and that larger studies are warranted.

One major potential limitation to the use of DW-MRI within radiotherapy treatment design is the difficulties in acquiring geometrically accurate images, as discussed in the previous sections for DW-MRI and ADC. These effects are generally not important when the images are acquired for diagnostic purposes, as the distortions are unlikely to affect the visualisation of a tumour or other area for medical concern. However, they do pose a potential limitation to the use of this type of imaging within the workflow of radiotherapy treatments, as the geometric fidelity of images are paramount for accurate treatment delivery.

Methods of distortion correction in DW-MRI

There are established methods for distortion correction of DW-MRI, and an overview of a commonly used open-source toolkit to do so is included here as it is subsequently used for the work reported in Chapter 4.

The Functional MRI of the Brain Software Library (FSL) [29] is an open-source toolkit which, amongst other processing packages, implements a method described by Andersson *et al.* [30] to estimate and correct susceptibility-induced distortions in DW-MRI. Section 2.2.3 discussed the reasons for the increased distortion seen in DW-MRI and how these primarily originate from the interaction between the readout of the image slice and the field map (i.e. the non-uniform magnetic field in the patient caused by variations in the magnetic susceptibility within the patient). This is sometimes referred to as the susceptibility-induced off-resonance field, where the resonance offset Ω may be insufficiently small owing to the variations in ω_0 caused by the variations in magnetic susceptibility (see equation 2.13). The field map will be approximately constant for all acquired images, and the method used by FSL uses two acquisitions in which the distortions go in different directions. Typically this is referred to as the phase enoding blips having opposing polarities, and can be thought of as reading out the k-space in figure 2.16 in opposing raster patterns (the 'blips' being the steps between the horizontal line readouts in this diagram).

The typical use of this software is for diagnosis and the overlaying of mpMRI

information onto anatomic (T_1 or T_2W-MRI) images within a diagnostic setting. It is not CE marked (which would indicate conformity with health and safety standards for products sold within the European Economic Area), unlike the imaging/processing and treatment calculation software usually used within radiotherapy. There are also potential difficulties or short-comings in its use within a radiotherapy treatment pathway, as FSL requires input of Neuroimaging Informatics Technology Initiative (NIfTI) format images, rather than the Digital Imaging and Communications in Medicine (DICOM) format produced by MR scanners and required by a radiotherapy treatment planning system (TPS). Therefore any use of FSL requires image format conversion prior to use and then back to DICOM afterwards in order to proceed within the radiotherapy pathway. Hence there are possible practical and safety issues regarding image orientation for example which would require rigorous testing should it be used for clinical (rather than non-clinical, research-only) purposes.

2.2.4 Image registration for radiotherapy treatment planning

The design and calculation of radiotherapy dose distributions is usually performed using a CT dataset. However, sometimes it is useful to be able to overlay an imaging dataset acquired using another modality, in order to visualize the location of volumes which are visible on that imaging modality in relation to the dose distribution. This is usually done via the use of image registration algorithms. The most commonly used modalities for this purpose are conventional (T_1 or T_2-weighted) MRI, or PET.

Regardless of the care taken to set up the patient in the same position, the two different image datasets will have been acquired with the patient anatomy in slightly different positions. Therefore, whatever method is used to overlay the images, there will always be limitations in the accuracy with which the location of volumes visible on one dataset can be located within another dataset.

Rigid and Deformable Registration

Commercial radiotherapy treatment planning systems (TPS) commonly provide methods to geometrically register two (or more) image datasets to a common coordinate system (image registration). This can be done either by rigid registration (RR) methods where only one global transformation for translations and/or rotations of all points in one dataset with respect to the other are performed, or by deformable registration (DR) in which a point-to-point transformation of the spatial correspondence between image datasets is found [31]. Whichever method is

used, the result is the establishment of a common coordinate system that will be used for the subsequent radiotherapy treatment plan. Any remaining spatial errors due to the imaging methods, as well as the registration procedure will propagate through the radiotherapy treatment process and therefore must be understood and accounted for in the design of the radiotherapy dose distribution.

As well as a RR algorithm, the RayStation TPS (v.5.0.2.35, RaySearch Laboratories AB, Stockholm, Sweden) offers two DR algorithms: a hybrid DR and a structure-based DR. In the hybrid DR the registration is performed via a non-linear optimization and can use a combination of image intensity and anatomical information (regions of interest (ROIs) and points of interest (POIs) - both defined by the user). The structure-based DR requires an intermediate step to convert the delineated ROIs into triangular mesh structures. It allows the assignment of different linear elastic material properties to the structures associated with the images and registration is performed using a finite element method.

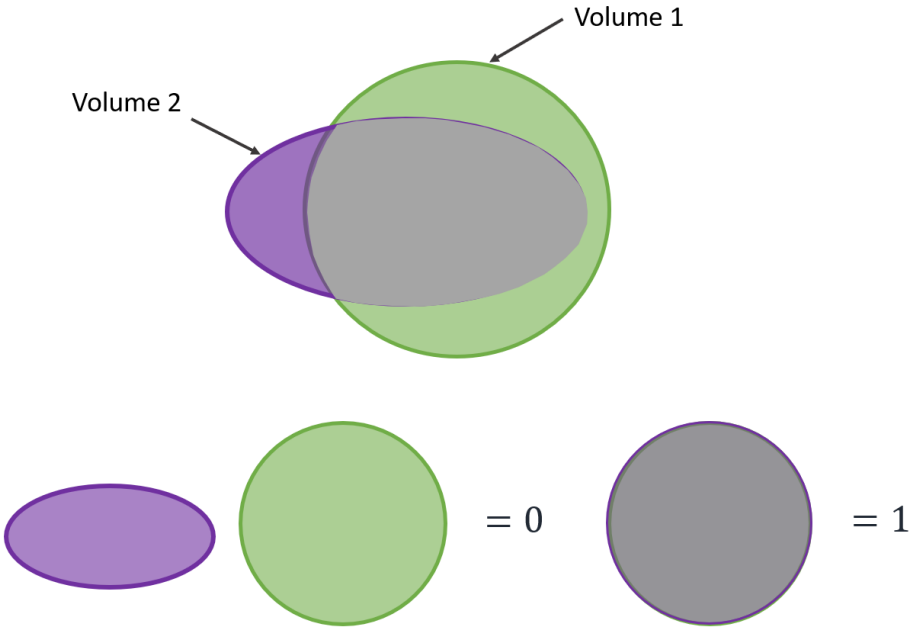

Figure 2.17: The Dice similarity coefficient (DSC), which varies between zero for no volume overlap and one where there is complete overlap of two volumes.

One common method for assessing the similarity of delineation of volumes used within radiotherapy is the Dice similarity coefficient (DSC) [32]. This is a simple method for quantifying the similarity of volumes and the degree to which they overlay, and can be useful either for assessing the variation in a given volume

over the course of sequential imaging sessions, or across different imaging modalities. The DSC is given by

$$DSC = \frac{2(V_1 \cap V_2)}{V_1 + V_2}, \tag{2.16}$$

where V_1 is the volume of volume 1 and V_2 is the volume of V_2. The DSC will therefore vary between zero (where there is no overlap) and 1 (where the two volumes overlap perfectly) as illustrated in figure 2.17.

2.2.5 Direct radiotherapy treatment planning on MRI

Although radiotherapy treatments are conventionally designed and calculated using the electron density information contained within CT images, there is a move towards the use of MR to replace CT within the pre-treatment workflow of radiotherapy. In such an 'MR-sim' workflow, the patient is imaged with MR in the required treatment position, with care taken to ensure the use of RF coils does not deform the patient anatomy. Additional checks are performed on an MR scanner used for this purpose to ensure potential distortion and other imaging parameters are within acceptable limits for radiotherapy purposes. The dose calculation in the MR-sim workflow will be performed either assuming bulk density information of water, bone or air from the MR images, or on a 'pseudo-CT'. These are image sets created from the MR(s) such that the image intensities are converted to what would have been produced by imaging the same anatomy using CT.

One potential advantage of the use of MR-sim may be that, as the various MR sequences can be acquired in a single patient imaging session, there will be less variation in patient positioning between the different image sets than there would currently be between a planning CT and additional (separately-acquired) MR image set. Therefore the errors which propagate through the system from image registration may be reduced.

It is anticipated that clinical use of MR-sim will increase and that direct MR-based radiotherapy treatment planning will become more widely used, particularly as the use of MR-linacs becomes more routine.

2.3 Adaptive radiotherapy and personalised medicine

The prescribed dose of radiotherapy treatment for a particular type of cancer may vary between centres for reasons of historical development or clinical differences in opinion. However, in general, the dose prescribed is standardized either locally or

nationally, and is not tailored to an individual patient. So far all discussion of radiotherapy treatment has also implied that the intended delivery of the radiation dose distribution remains constant throughout all fractions of a course of radiotherapy. However, there is increasing interest and research into ways of individually adapting radiotherapy treatment, both based on day-to-day variations in patient anatomy (for example the RAIDER clinical trial, discussed in section 3.2.2), and/or based on knowledge acquired about the individual patient's tumour (e.g. hypoxia, gene sequencing and radiosensitivity), or response as seen on imaging during the course of treatment. These developments are referred to as adaptive radiotherapy, i.e. radiotherapy in which the treatment is adapted in some way which is individualised to the patient.

Of particular interest for this thesis, is the use of imaging acquired prior to and during the course of radiotherapy treatment of the bladder. The development of MR-sim and MR-linacs means that it is becoming possible to image the bladder both prior to and at the time of radiotherapy treatment delivery. This would enable visualization of the internal tumour using various MR sequences, which at present is not possible using CT/CBCT. The use of such imaging may therefore enable the reduction of margins used for radiotherapy treatment of bladder cancer: currently margins are used around the bladder to facilitate delivery of a uniform dose to the whole bladder, as this is what is visible using CBCT prior to treatment. Multiparametric MRI, used prior to treatment delivery, could enable targeted treatment to the tumour itself, with smaller margins owing to the reduced uncertainty in tumour location. This could reduce complications from treatment, and/or enable an increase in dose delivered without unacceptable increase in side effects, i.e. widening the gap between the TCP and NTCP curves seen in figure 2.6. Further individual adaptations could be based on changes in these images seen through the course of therapy, either escalating or de-escalating doses prescribed to an individual patient based upon their response.

Chapter 3

Bladder cancer treatment

The previous chapter discussed the treatment of bladder cancer with radiotherapy, and the limitations and problems encountered within the radiotherapy process. This chapter provides relevant background information on bladder cancer, including an overview of its incidence, diagnosis and treatments (including placing the use of radiotherapy into context), and prognosis. Some previous and current clinical trials are discussed, before developing the questions which will then be addressed through the rest of this thesis. The aim of the work presented in this thesis was to facilitate improvements in prognosis for bladder cancer patients and quality of life following treatment with radiotherapy.

3.1 Overview of bladder cancer

3.1.1 Incidence and development

The urinary bladder is a hollow, muscular bag located in the pelvis, into which the ureters drain urine from the kidneys. Urine collects in the bladder before being excreted from the body via the urethra. Figure 3.1 shows a schematic of the bladder with an inset showing its location within the body. A healthy bladder can store up to ∼400 ml of urine [33] and has a bladder wall thickness of up to 3 mm depending on the volume of urine stored [34].

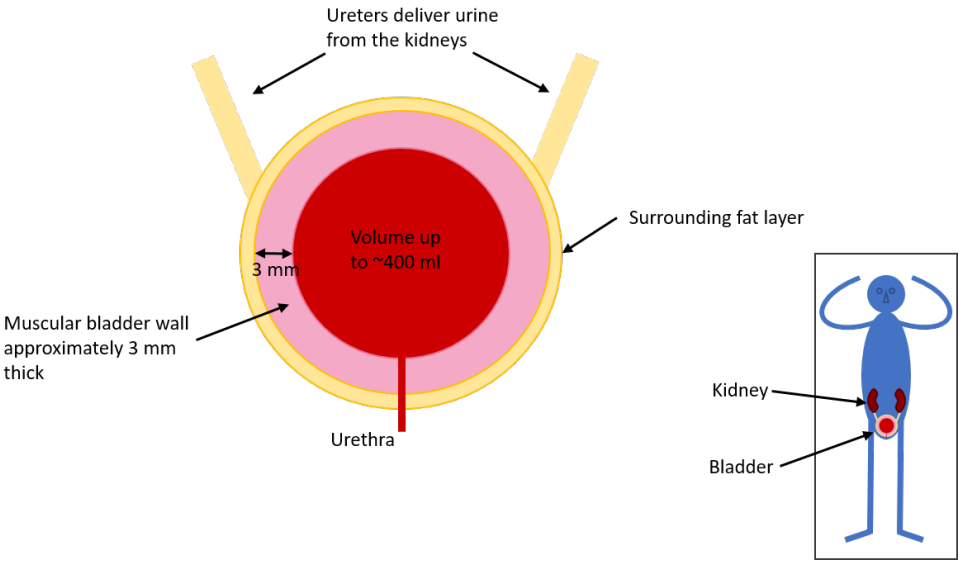

Figure 3.1: Diagram showing the bladder and its location within the body [33] (not to scale).

Basic stages of bladder cancer and its development are illustrated schematically in figure 3.2. The early stages of bladder cancer do not invade the muscular wall of the bladder, and are called non muscle-invasive bladder cancer (NMIBC). Around 75 % of bladder cancers are non muscle-invasive, and treatments are aimed at preventing further tumour development and muscle invasion [4].

Higher grade tumours are those which have begun to invade the bladder muscle and this is diagnosed as muscle-invasive bladder cancer (MIBC). MIBC accounts for around 25 % of bladder cancer diagnoses [4] and is associated with poor survival, with less than half of these surviving 5 years post diagnosis [3].

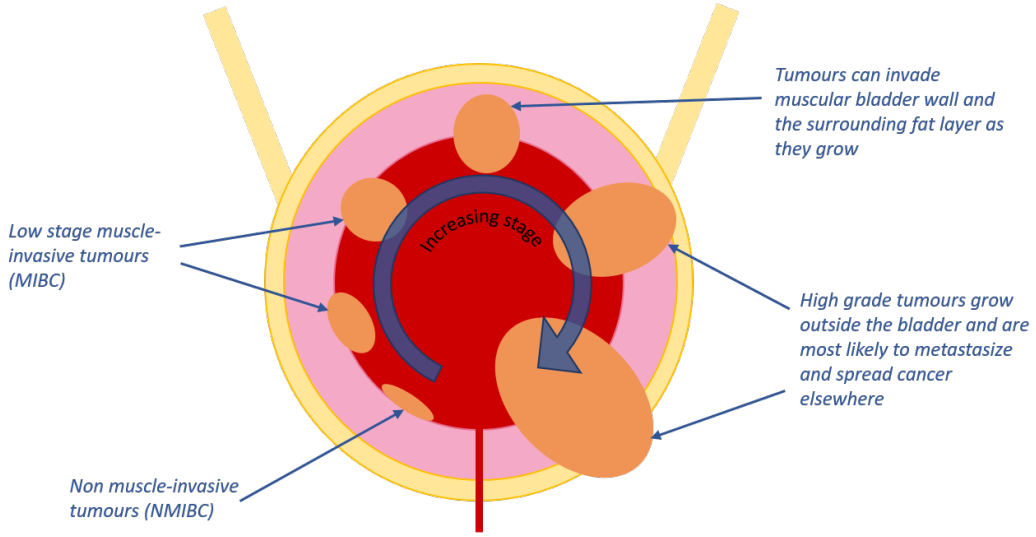

Figure 3.2: Diagram showing the development and stages of muscle-invasive bladder cancer [35].

3.1.2 Diagnosis, treatment modalities and outcomes

The required treatments and their prognoses differ considerably between NMIBC and MIBC, as well as the individual stage of progression. Therefore, the early ability to distinguish between the two is of great importance. Standard practice in the UK may involve, depending upon individual requirements, cytological testing (the assessment of cells from the inside of the bladder under a microscope), visualisation of the interior of the bladder via cystography, histological testing of biopsies taken from suspicious areas, CT imaging, and trans-urethral resection of bladder tumour (TURBT) [5]. TURBT is illustrated schematically in figure 3.3, which shows how for NMIBC, the procedure is a primary treatment as all visible tumour is removed (although further, adjuvant treatments may also be used to reduce the chance of recurrence). The diagnosis of muscle-invasion is strongly influenced by the findings of the TURBT procedure, but it is not a primary treatment in this case as gross tumour will still remain owing to the invasion of muscle (as shown in figure 3.3). For these patients, the TURBT will be followed by cystectomy, chemotherapy and/or radiotherapy depending upon various factors including staging and other patient-specific factors [35].

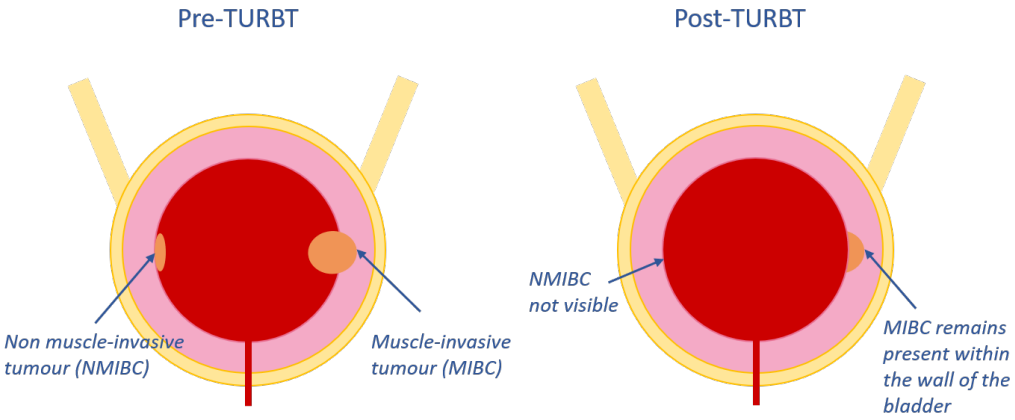

Figure 3.3: Diagram showing schematic of trans-urethral resection for bladder tumours (TURBT).

Historically, the standard treatment of MIBC is surgical removal of the whole bladder (cystectomy) to control disease spread [5]. This obviously causes significant long-term morbidity in patients, even if their cancer is cured. An alternative treatment is TURBT followed by chemotherapy and/or radiotherapy to the whole bladder. Although there has not been a randomised controlled trial directly comparing cystectomy with combined TURBT, radiotherapy and chemotherapy treatments, the BC2001 trial demonstrated that modern treatments with TURBT followed by both chemotherapy drugs and radiation can achieve outcomes comparable to cystectomy whilst preserving bladder function [7]. It is possible that developments in techniques could lead to this bladder-preserving approach replacing surgical removal as the gold standard, as has been seen in other sites such as breast cancer [35].

3.1.3 Prognosis

In a recent paper in the Lancet, patient cancer outcomes in England and Wales were analysed by cancer site for trends over the 40-year period from 1971-2011 [6]. The authors showed that survival at 1, 5 and 10 years post diagnosis had increased for both men and women across all cancers, but that there was great variation between cancer sites. They divided the sites into 3 broad clusters: firstly those cancers with high survival in 2010-11 and for which the absolute increase in survival since 1971-72 was progressively larger for survival at 1, 5 and 10 years. This cluster includes breast, prostate and testicular cancers. The second cluster was those cancers with a moderate level of survival in 2010-11 and generally smaller increases since 1971-72. This cluster includes bladder cancer, as well as cervix, ovary and colon. The final

cluster is those cancers for which survival for patients who were diagnosed in 2010-11 was low and for which there has been little improvement since 1971-72. This group includes pancreatic and oesophageal cancers.

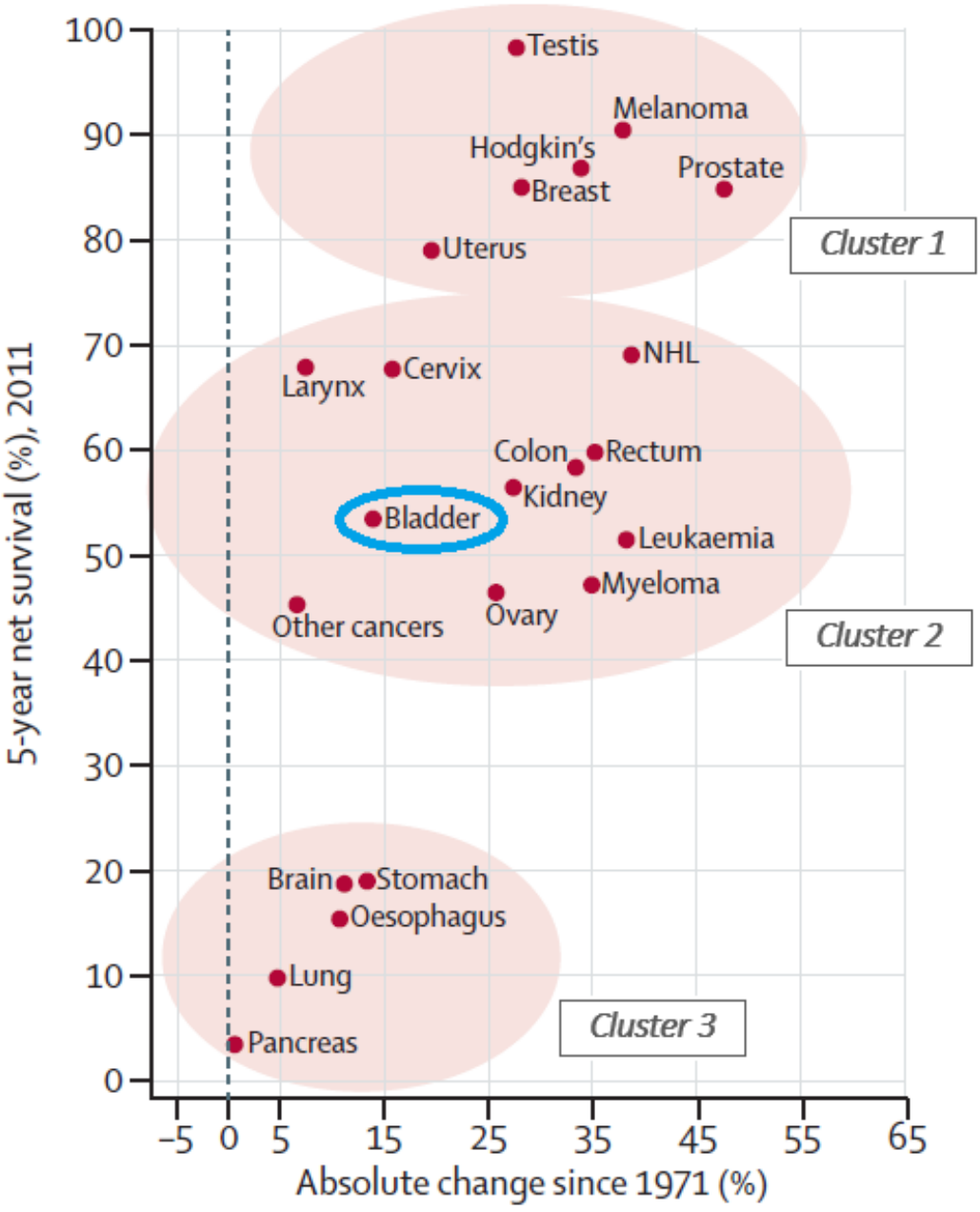

Figure 3.4: Graph showing the net survival adjusted for age and sex for each cancer in 2010-11, and absolute change since 1971, all adults in England 5 years after diagnosis. Reproduced from Quaresma *et al.* [6].

Figure 3.4 shows a reproduction from Quaresma *et al.*'s paper illustrating the three clusters for 5-year net survival, with bladder cancer highlighted. This illustrates well the way in which bladder cancer outcomes are better than some of those cancers with the poorest prognoses, but still much poorer than the cancers with the best prognoses. Bladder cancer's position towards the left of the graph shows that the improvements in outcomes since 1971 are lower than many other cancer sites.

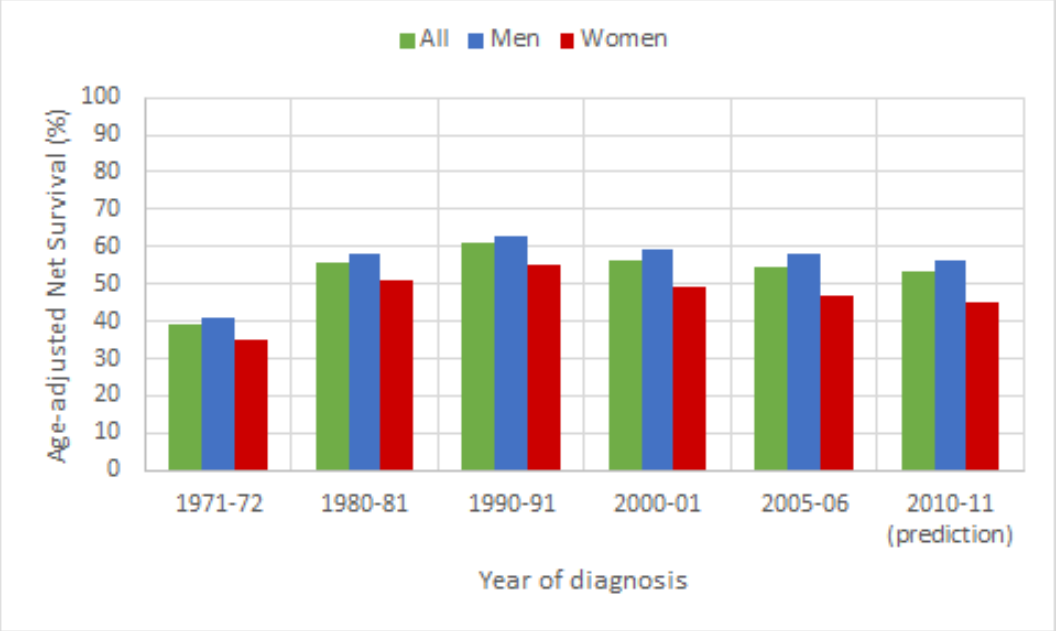

Figure 3.5: Graph showing the 5 year age-adjusted net survival after diagnosis for bladder cancer in England [6].

Figure 3.5 shows the trend in 5 year age-adjusted net survival after diagnosis for bladder cancer in England, as tabulated by Quaresma *et al.* A similar trend is seen also for the equivalent data regarding 1- and 10-year net survival respectively (presented in the Quaresma *et al.* paper but not shown here). In all cases, there is an increase in survival between patients diagnosed in the 1970s and 1980s, but this improvement does not continue beyond the 1990s. The subsequent apparent slight decrease in survival is likely due to changes in the definitions of bladder cancer (the staging definitions changed from the Jewett-Marshall-Strong classification system following the introduction of the TNM sysytem in 1983 [36]).

In their discussion of the three clusters of cancer sites, Quaresma *et al.* recommend that *"...for the cancers in [the second] cluster that have shown no evidence of improvement, efforts should be made to achieve earlier diagnosis, and to focus on*

stricter guidelines for improved treatment, such as increased use of surgery, radiotherapy with curative intent, neoadjuvant therapies, or a combination of the three." Bladder cancer can be considered to fall in this category, as although there has been some improvement it has been limited, as is readily seen in figure 3.5.

3.2 Radiotherapy treatment of bladder cancer

3.2.1 Current techniques and their limitations

Standard radiotherapy treatments for MIBC usually use one of two dose fractionation schemes, as shown in table 3.1. The BC2001 trial showed that these schemes were equivalent in terms of both local tumour control and toxicity [7].

Table 3.1: Standard fractionation schemes for MIBC used in the UK [7].

Prescription dose (Gy)	No. of fractions
55	20
64	32

In both standard fractionation schemes the dose is delivered as a uniform treatment to the whole bladder. This is partly because there is the expectancy that there will be some degree of microscopic spread of tumour which is not visible on imaging. However, it is also because the residual tumour remaining within the bladder wall is not readily visible on the planning CTs used to design radiotherapy dose distributions, and visiblity is poor on the daily CBCT used for pre-treatment positioning of the patient. As the amount of bladder filling, shape of the bladder and therefore the exact location of the tumour will vary from one fraction to another, this lack of visibility means there is greater uncertainty in the tumour location. For these reasons, a uniform dose is prescribed to the whole bladder and large margins are generally used to expand the CTV (outer bladder wall) to create the PTV used for radiotherapy treatment planning. This is illustrated in figure 3.6 which shows a schematic of a bladder and surrounding PTV along with residual tumour following TURBT.

The size of the margins used to create the bladder PTV limits the maximum dose that can be prescribed, due to the proximity of radiosensitive OARs such as the bowel. Radiation doses prescribed for bladder cancer are therefore lower than for other cancers such as the prostate [37], and improvements in tumour control are thought to be possible should dose be increased (escalated) [7].

If imaging of the bladder could be achieved with better visibility of residual (post-TURBT) tumour volume to be treated, doses could be escalated to the tumour alone rather than to the whole bladder. Indeed, it would also no longer be necessary to deliver the current standard dose to the rest of the bladder (as there would be increased confidence that the volume did not contain tumour). Therefore, with improved imaging, better outcomes could potentially be delivered with a similar toxicity to that currently accepted. One current clinical trial called RAIDER [9] is investigating the potential of dose escalation of the residual tumour, whilst decreasing the dose prescribed to the rest of the bladder (see section 3.2.2). A question which arises from this approach to dose escalation is the degree of microscopic spread and therefore the dose to which the rest of the bladder should be treated. The BC2001 trial provided some encouragement that a reduction of dose to the bladder wall to 75-80 % of the planned tumour dose did not reduce the effectiveness of the treatment [38].

Various MRI techniques allow excellent visualisation of bladder tumours, and there has been considerable work showing that it may improve diagnosis of MIBC compared with TURBT [39, 40]. Another current clinical trial called BladderPath [10] (see section 3.2.2) is aiming to show that the use of multi-parametric MRI, including T_2-weighted and DW-MRI can be used in place of TURBT to more accurately and rapidly diagnose MIBC.

3.2.2 Current clinical trials: RAIDER and BladderPath

The two MIBC clinical trials most relevant to this thesis are RAIDER [9] and BladderPath [10], which are described here.

RAIDER

RAIDER is a Randomised phase II trial for Adaptive Image guided standard or Dose Escalated tumour boost Radiotherapy in the treatment of the bladder cancer [9]. The objective of RAIDER is to define a feasible and safe adaptive dose-escalated tumour boost radiotherapy schedule for MIBC. It is investigating the ability to deliver daily adaptive bladder radiotherapy and will assess the impact of doing so. Patients are randomised (1:1:2) between (i) standard whole bladder radiotherapy (WBRT) which is the control arm of the study, (ii) adaptive standard dose tumour-focused radiotherapy (SART), and (iii) adaptive dose-escalated tumour boost radiotherapy (DART). All groups are permitted to receive chemotherapy, and both standard fractionation schemes of 55 Gy in 20 fractions and 64 Gy in 32 fractions are permitted

within the trial, although only the latter is referred to in this thesis for clarity and relevence to later work. All RAIDER patients are treated with radiotherapy following performance of the TURBT procedure.

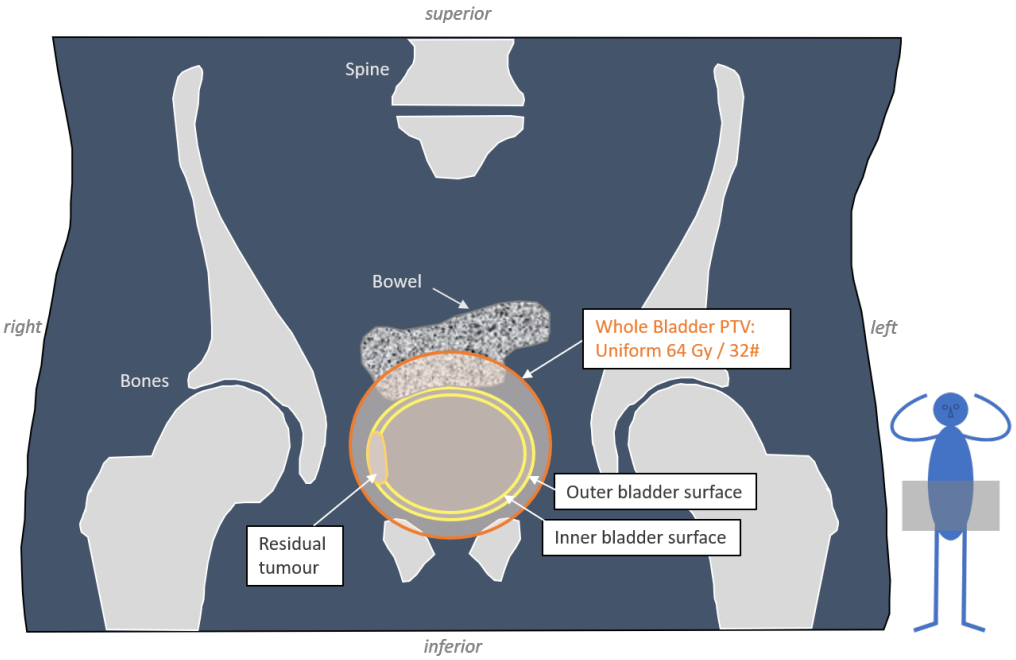

Figure 3.6: Diagram showing the radiotherapy treatment in the standard arm (arm (i)) of the RAIDER clinical trial. In the case illustrated the whole bladder receives 64 Gy in 32 fractions.

In arm (i) of the trial, the whole bladder is delineated on a CT scan which is performed after patient voiding of the bladder, and treatments will also be delivered following patient voiding. This arm is illustrated diagrammatically in figure 3.6.

In arms (ii) and (iii) of the trial the bladder is partially-full, with patients following a specified drinking programme prior to the performance of the CT and all radiotherapy treatments. This means the bladder is partially distended, moving OARs such as the bowel away from some of the bladder and, owing to the stretching of the bladder wall, reducing the volume of bladder wall contained within the high dose treatment volume. The variability in bladder filling is accommodated via the production of 3 radiotherapy plans which are generated for each patient, with small, medium and larger versions. On each day of treatment the smallest plan will be used which adequately covers the required bladder/tumour volumes. Figure 3.7 illustrates arms (ii) and (iii) of the trial. In arm (ii), the dose to the tumour volume remains at the standard dose (i.e. 64 Gy for the 32 fraction scheme), whilst the

dose to the whole bladder is reduced to 52 Gy. In arm (iii) of the trial the dose prescribed to the tumour is escalated to 70 Gy (for the 32 fraction scheme) and the dose to the bladder is again reduced to 52 Gy.

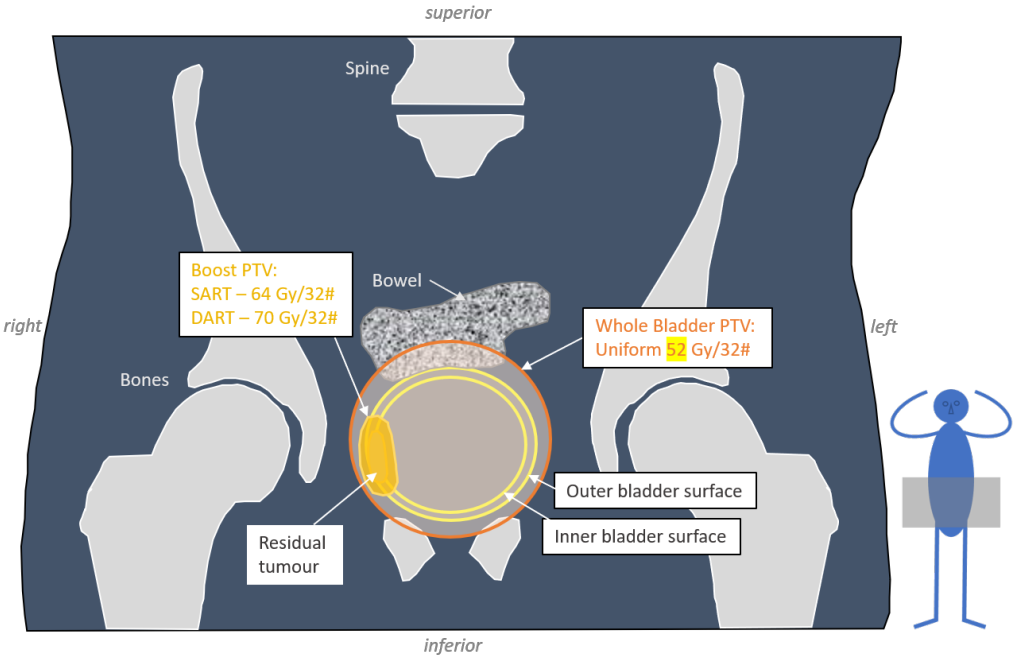

Figure 3.7: Diagram showing the radiotherapy treatment in the trial arms of the RAIDER trial, where in arm (ii) the whole bladder receives 52 Gy and boost volume receives 64 Gy and in arm (iii) the whole bladder receives 52 Gy and the boost volume receives 70 Gy (both for the 32 fraction scheme).

It is hoped that the RAIDER trial will show that adapting radiotherapy to the daily imaged position and volume of the bladder is feasible, as well as that the reduction in dose to the low risk volume of the bladder and increased dose to the tumour results in improved control of the tumour without increased toxicity.

BladderPath

Another current clinical trial of relevance to the later work presented in this thesis is the BladderPath trial. BladderPath is the image-directed redesign of Bladder cancer treatment Pathways [10]. Rather than changing the treatment received by patients, it instead seeks to test how a change in the clinical pathway for patients with suspected MIBC affects outcomes by expediting their route to definitive treatment. At present, the requirement for the TURBT procedure for the diagnosis of

muscle-invasion can cause a delay between patient presentation with symptoms at a haematuria clinic, and their receipt of treatment with the aim of cure (radiotherapy, chemotherapy and/or surgery). Often clinics can need to refer to a different hospital for the TURBT procedure, and then afterwards a further referral for treatment is required. BladderPath is intended to improve staging, accelerate treatment and reduce tumour spread for MIBC patients by avoiding TURBT, ultimately improving clinical outcomes.

A schematic showing the intended differences in patient pathway being tested in the BladderPath trial is shown in figure 3.8. The MRI step highlighted in red in the new pathway replaces the TURBT procedure with multi-parametric MRI including DW-MRI for patients with suspected MIBC. This trial does not change the other aspects of the patient treatments; therefore, once diagnosed the patients will proceed to treatments with radiotherapy, chemotherapy and/or surgery as would ordinarily be the case. MRI can accurately diagnose bladder cancer [39, 40, 41] and whilst not yet widely used in the UK for this purpose, it is routinely used for other cancer sites.

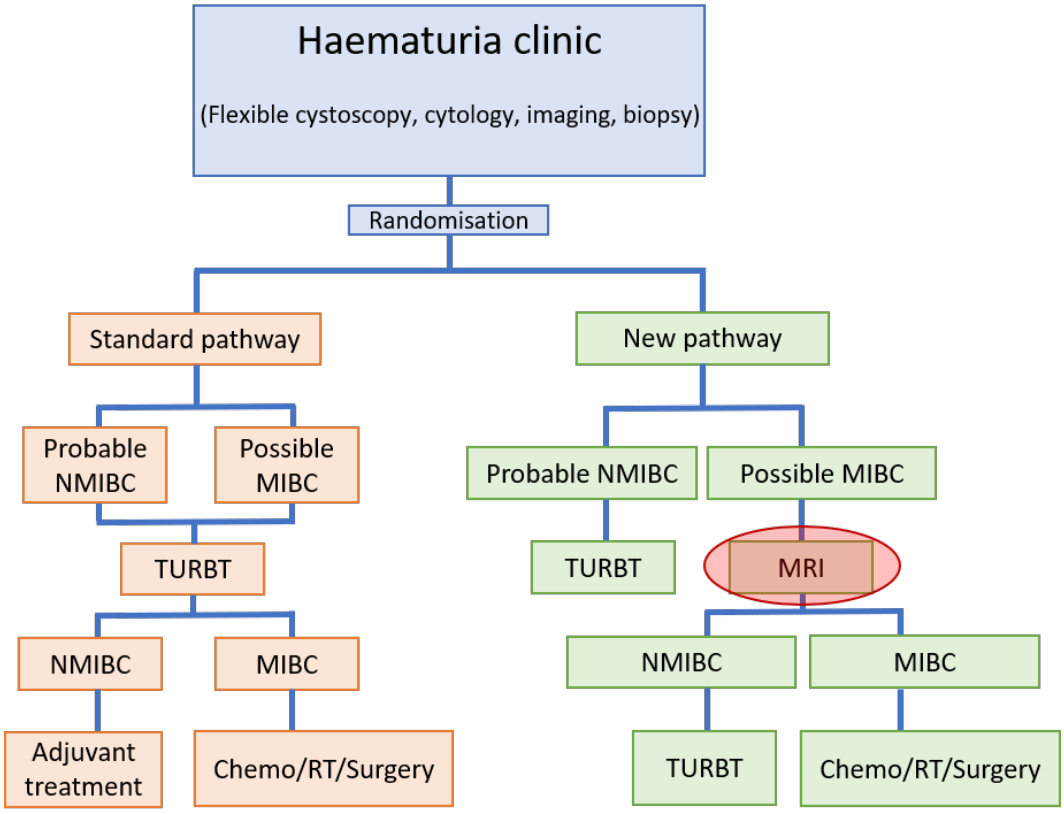

Figure 3.8: Schematic showing the differences in patient pathway being tested within the BladderPath Clinical Trial. The highlighted MRI step tests the use of multi-parametric MRI including DW-MRI to more rapidly diagnose MIBC, removing the requirement for TURBT for patients with suspected MIBC.

3.2.3 Potential developments in bladder cancer radiotherapy

Developments and improvements in imaging have the potential to enable better stratification of patients and personalisation of treatments. Along with the ability to better target radiotherapy treatment delivery using modern intensity modulation techniques, these developments could lead to improvements in outcome for some patients with bladder cancer. The technical difficulties which would need to be overcome include the significant mobility of the bladder and poor visibility of (in particular post-TURBT) tumours on pre-treatment CBCT.

The excellent soft tissue contrast afforded by MRI is becoming more widely available for radiotherapy simulation and treatment planning, and is starting to become available at the time of treatment delivery via the use of MR-linacs. This means that the possibility is raised of addressing the difficulties in visualisation of

residual bladder tumour at the time of both radiotherapy treatment design and its delivery. The use of an MR-linac potentially allows real-time information of cellular function to be acquired, enabling treatment not only of conventional, anatomically-defined tumour volumes, but also 'biological' tumour volumes. These 'biological' tumour volumes (BTVs) could have associated prescriptions which could vary in intensity over the volume itself, and/or over the course of treatment based on response.

This possibility of biologically-adaptive radiotherapy (sometimes called theragnostic imaging), has potential to transform the way radiotherapy is delivered to patients. The current 'one-size fits all' approach would become one in which treatments are individually adapted based on patient response to treatment, during the course of treatment.

Theragnostic imaging and biologically-adaptive radiotherapy

Theragnostic imaging within radiation oncology is the use of molecular or functional imaging (i.e. imaging which provides underlying biological information rather than purely structural, anatomical information) to prescribe radiotherapy which varies in intensity in 3-D, and also varies over time. It was highlighted by Bentzen [42] as the upcoming revolution in radiotherapy, owing to its ability to visualize cellular or biochemical processes by various imaging methods and enable treatments to be individually tailored from this information, minimizing radiation damage to nearby healthy tissue. As Fowler noted [43], the use of ionizing radiation for this purpose has the virtue over drug or gene-based therapies that it unambiguously reaches the cells that the physical radiotherapy plan encompasses.

There is increasing interest in the use of multi-parametric MRI including DW-MRI and resulting ADC maps for informing radiotherapy treatment and assessing tumour burden or response [44, 45]. The next step in the use of this modality is to assess the feasibility of using the information it conveys to directly influence radiotherapy planning, i.e. acting as theragnostic, rather than purely diagnostic imaging. This has also been referred to as biologically-adaptive radiotherapy (BART) or biology-guided adaptive radiotherapy (BiGART) [46]. In all of these approaches to radiotherapy treatment, the tumour volume to be treated is not purely informed by the anatomic tumour volume but by some biological (or functional) information, which may also be adjusted or adapted during the course of treatment based on response.

As discussed in section 2.2.3, DW-MRI is able to highlight areas of restricted diffusion which occur in regions of increased cellularity including tumours, and has

also been recommended for testing in clinical trials as a biomarker for cancer [47]. Its use to generate ADC maps allows the quantification of the degree of diffusion, and has been investigated for the ability to predict clinical aggressiveness in bladder cancer [48]. This ability to produce images which quantify the degree of diffusion could potentially enable a 'dose painting' technique [42, 49], allowing the radiotherapy treatment to be intensified or focussed where the tumour burden is higher. Moreover, changes in ADC values during treatment could be used as a means to assess response and predict efficacy. This would enable individualised adaptations of radiotherapy treatments, and enter the realm of personalised medicine. However, these approaches would be limited by any geometrical distortion present in the ADC maps, particularly if this is greater than the spatial uncertainties associated with the CT scan that is used for radiotherapy treatment planning.

Use of DW-MRI in radiotherapy treatment planning

Imaging that is used within radiotherapy requires stringent quality control, which may differ from that required for diagnostic purposes. In particular, any geometric distortion in images used for determination of treatment volumes could have significant impact on achievable accuracy in delivery of the required radiation dose to the appropriate volume, whereas this level of distortion may be of less significance if the same images were used for diagnosis alone.

As discussed in section 2.2.1, CT is conventionally used for treatment planning - both for delineation of all relevant anatomical volumes and for calculation of dose distributions using the electron density information contained within the CT images. Investigations into the use of MRI-based treatment planning have been ongoing for many years [50, 51, 52], and some centres now use MRI to produce pseudo-CT images and calculate dose distributions directly upon these images, although this practice is still not yet widespread. Multi-parametric MRI, and other imaging modalities such as PET, if used at all within the radiotherapy pathway, tend to be used to provide supplementary information regarding the tumour. However, the prescription of dose and delineation of volumes is conventionally confined to planning CT (or MRI pseudo-CT) images only.

Progressing the use of DW-MRI from use within diagnosis alone to use for directly informing tumour volume and even dose prescription, would rely upon the ability to produce images of the required quality for radiotherapy purposes. If this were shown to be possible, then DW-MRI could be used either via registration with a conventional planning CT, or via the acquisition of other MR sequences within the same image acquisition session as DW-MRI to produce a pseudo-CT for use in

dose calculations and delineation of OARs. This second method would have the advantage of reduced differences in patient positioning between image acquisitions.

This project aimed to investigate the possibilities of using DW-MRI and resultant ADC maps within the treatment pathway for MIBC.

3.3 Developing the use of DW-MRI as biolological imaging for adaptive bladder radiotherapy

This project used data from a previously treated MIBC patient to simulate the possibilities regarding the adaptation of radiotherapy treatments using DW-MRI information in conjunction with standard planning CTs. The aim was to mimic what would be achievable with additional bladder imaging information similar to that acquired through the BladderPath trial, but with dose escalation strategies similar to those used within the RAIDER trial. The overall aim of this project was to investigate and predict the effect on patient outcomes from escalation of absorbed dose to bladder tumours treated with radiotherapy.

3.3.1 Project sections

There were 4 main sections within this project:

1. The magnitude and effect of distortion in DW-MRI was assessed with respect to its effect upon tumour definition within radiotherapy;

2. Models were developed which could be used to predict TCP when escalating the dose to bladder tumours, and which allowed the effect of variations in both tumour volume and dose to tumour and bladder wall to be taken into consideration;

3. Tumours were simulated and dose distributions calculated to mimic the clinical situation if DW-MRI were used to inform tumour volume, with standard and escalated dose levels used to enable comparison. The TCP models previously developed were used to assess the expected effect of dose escalation;

4. The feasibility of delivery of the radiotherapy treatment plans was assessed via accumulation of dose on pre-treatment CBCTs which were acquired for the patient at the time of treatment. The doses which would have been received were summed and compared to the original planned doses.

Firstly, in order to assess the magnitude of distortion in DW-MRI under conditions similar to those for clinical images of a bladder, a phantom (i.e. model) was designed and constructed to mimic the bladder and a tumour. This enabled imaging to be performed under reproducible conditions with DW-MRI, conventional T2W-MRI, and CT. Geometric distortion was measured via reference markers within the bladder and tumour across the imaging modalities. Potential mitigation strategies to correct distortion were tested, and estimates made of additional margins required for creation of PTVs using this strategy.

The second section of work involved the development of two models to predict TCP when provided with the doses received by bladder tumours. The models were based on published work which used a logistic model, but were refitted with a Poisson model so that tumour volume could be explicitly controlled. One model was fitted to clinical trials data involving treatment with radiotherapy alone, and the other used data in which patients received both radiotherapy and chemotherapy.

The third section of the project required the development of a method for simulating tumours on a previously-treated patient CT, in which tumour location and volume was varied. Once tumour volumes were simulated, margins used to produce PTVs were informed by the first section of work. This was intended to simulate a situation where the tumour volume had originated from an ADC map which was registered to the planning CT. Prescription doses to tumours and the rest of the bladder were systematically varied, along similar lines to the RAIDER trial, but with a wider range of doses tested. The dose distributions produced were used to calculate TCP with each of the two models which had been developed.

Finally, the feasibility of delivery of the calculated dose distributions in practice was assessed by recalculating the dose on the daily CBCTs of the previously-treated patient, as if these treatment plans had been delivered instead. The dose accumulated over the course of treatment was summed and compared with the original planned dose. These recalculated dose distributions were then used to predict TCP as before, and compared with the original predicted TCP.

3.3.2 Project summary

The central aim of this project was to systematically investigate the increase of radiation dose to bladder tumours, and determine the expected effect this should have on the probability of tumour control. Tumour positional information from ADC maps was quantitatively assessed for accuracy relative to current methods. These results were used within the simulation of tumour target volumes and the calculation of dose distributions for radiotherapy treatments. Previously acquired

patient images were used to quantatively assess the feasibility of delivery of the calculated dose distributions, and the effect of variations in day-to-day volume and location of the bladder upon TCP.

Chapter 4

Investigations of distortion in DW-MRI for radiotherapy treatment of bladder tumours

4.1 Introduction

This chapter reports on work done to assess the magnitude of distortion in DW-MRI under conditions similar to those used for clinical imaging of the bladder within the BladderPath clinical trial. This work was designed in particular to determine the margins which might be required should DW-MRI of the bladder be used for tumour volume (GTV) delineation if these images were registered with a planning CT, although it would also be relevant if MR-sim were used instead of CT.

Clinical images of patients suffer from limitations in the reproducibility of patient position between different image acquisitions, and this is particularly significant for imaging of the bladder due to temporal variations in bladder filling. Therefore, this research required the design and construction of a model bladder to mimic what would be seen when imaging a patient bladder so that any changes between image acquisitions would be due only to differences between CT and DW-MRI rendering of the images rather than changes in the ground truth between acquisitions. Such a model or phantom should be appropriately constructed to produce adequate visibility of landmarks across all imaging modalities to enable measurement of distances and quantify geometrical uncertainties in and between the associated images.

4.1.1 Commercial MRI phantoms

The American College of Radiology (ACR) MRI phantom is commonly used to assess the magnitude of distortion in MRI using a 2-D grid. Figure 4.1 shows a photograph of the phantom and MR image of the 2-D grid contained within it.

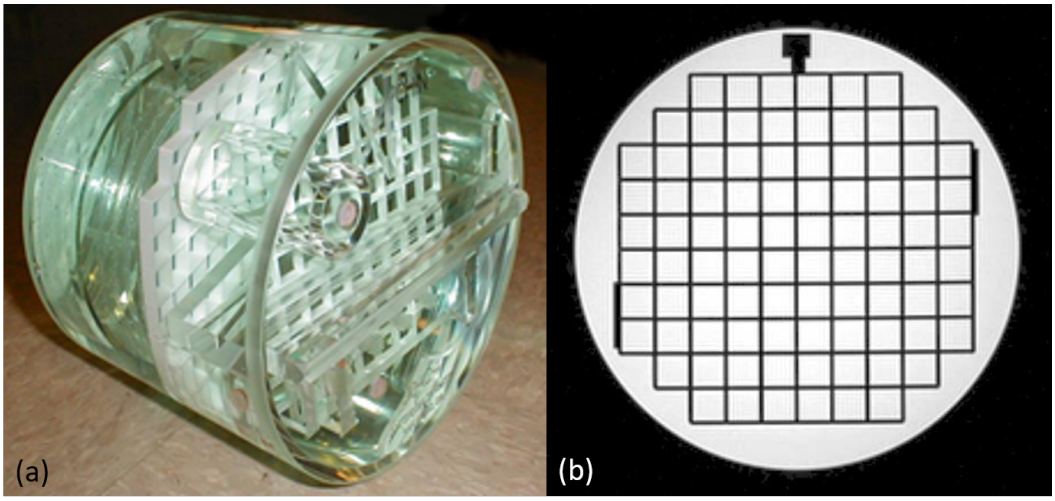

Figure 4.1: (a) Photograph of the ACR phantom and (b) MR image of the 2-D grid contained within the phantom [53].

Figure 4.2 shows transverse images of an ACR phantom as it appears when imaged using (a) CT, (b) DW-MRI and (c) following rigid registration of the CT and DW-MRI (i.e. these images are overlaid). The extent of the distortion that can be present in DW-MRI is apparent by comparison with the undistorted CT image, and the schematic of the grid shown in figure 4.1 (b).

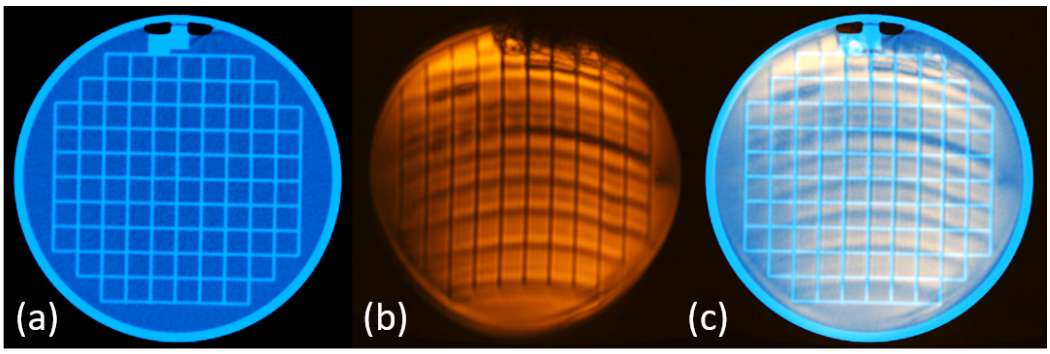

Figure 4.2: Cross-sectional 2-D images of the grid section of an ACR phantom as it appears using (a) CT, (b) DW-MRI (with a b-value of 300 s.mm^{-2}), and (c) following rigid registration of CT and DW-MRI.

The ACR phantom is not representative of any relevant anatomy, and its 1 cm thick grid for evaluation of distortions in 2-D is of limited use for the volumetric evaluation of distortions required here. There are also other commercially-available phantoms, some of which allow quantification in 3-D such as the QUASAR MRID (Modus Medical Devices Inc., Ontario, Canada). However, in common with the ACR phantom, these have a uniform pattern of objects which are often aimed at testing aspects of image quality within MRI, usually T1W- or T2W-MRI rather than DW-MRI. Publications regarding in-house design of phantoms for testing DW-MRI image quality exist [54, 55, 56] but these are generally aimed at testing ADC value consistency with time or between scanners, rather than geometric distortions, as these are the parameters of greater relevance in diagnostic use of DW-MRI.

Testing of geometric distortions within DW-MRI for the purposes required in this thesis, would be best achieved in a phantom which mimics the anatomy of the bladder rather than a generic phantom, as the distortions generated will be affected by the construction of the phantom itself and the inhomogeneities contained within it. Ideally, therefore, this work would use a phantom which mimics the situations of tumours within the bladder. Such a phantom could also have the advantage that it could be constructed so as to enable visibility of both tumour and bladder on all imaging modalities, unlike the clinical situation where tumour is not readily visible on CT.

4.2 Bespoke bladder phantom for quantification of distortion

4.2.1 Phantom design

A phantom designed for the purposes of assessing distortion in DW-MRI of bladder tumours would need to:

1. Be constructed using synthetic (non-metallic) components with a geometrical shape that approximates a urinary bladder containing an internal tumour,
2. Produce sufficient contrast on all relevant image modalities to allow the delineation of volumes of clinical interest,
3. Contain positional markers for spatial reference,
4. Allow production of artefact free images,
5. Produce no additional distortion beyond that expected for similar clinical bladder images.
6. Ideally enable the investigation of different sizes and shapes of bladder/tumour.

Construction of a phantom using non-metallic components is important for use within MRI, as any metal will cause loss of signal and artefacts. The production of adequate contrast across all modalities is difficult to achieve, however, particularly whilst also trying to ensure that there is limited distortion created within the DW-MRI. The following section discusses the types of materials investigated for these purposes.

4.2.2 Phantom materials

Within the clinical use of CT and MRI, it is common to produce in-house phantoms for the purposes of testing specific situations relevant to the local use of the equipment. Often materials used for the construction of phantoms used for CT include water, acrylic, wood and air. For MRI these may typically involve the use of water or oils, and perhaps the addition of clinically-administered contrast agents such as gadolinium in order to alter the T_1 or T_2 relaxation times of the solution, and depending upon the specific parameters to be tested. Air is not usually used but if present in the phantom will produce regions of minimal signal. If DW-MRI is to be tested, however, it is less straightforward to produce a phantom which will have adequate contrast between different components, particularly if there must also be

good contrast on other imaging modalities as well. In particular, if there are even small volumes of air (such as bubbles), this can produce significant distortion in the DW images. One compound which is frequently used within MRI phantoms is a cryogel called polyvinyl alcohol (PVA), as it is a non-toxic, stable compound which is simple to produce and handle within the hospital environment [57].

Cryogels

Cryogels are substances which can be dissolved in water and then the process of cycling through freezing and thawing changes the properties of the material. PVA is a commonly-used cryogel in MRI, which is used as a tissue-mimicking material and which becomes more solid as it is subjected to more freeze-thaw cycles. This change also affects the degree to which the water molecules are able to diffuse within the material, and therefore the signal produced when imaged using DW-MRI is also changed [57]. In this way it is possible to produce contrast within DW-MRI, particularly if other materials with differing degrees of diffusion are included - e.g. water, which has high rates of diffusion and solids such as wood or plastics (which will produce little or no signal if imaged using DW-MRI).

4.2.3 Phantom I construction

The process of development and construction of a phantom which would achieve all of the purposes listed in section 4.2.1 was iterative. Therefore, this section of work details the first main phantom ('phantom I') developed and tested, in order to show the various issues encountered, and section 4.2.7 discusses the developments and alterations made based upon findings from this phantom.

Figure 4.3 shows (a) a photograph of phantom I produced to model a urinary bladder with internal tumour and (b) and (c) schematic diagrams of the cross-sections of the phantom construction. Information regarding the materials used are reported in table 4.1. Two bladder inserts were constructed for this phantom, with cross-sections of diameter 5.5 cm and 6.5 cm, which are later referred to as the small bladder (SB) and larger bladder (LB), respectively.

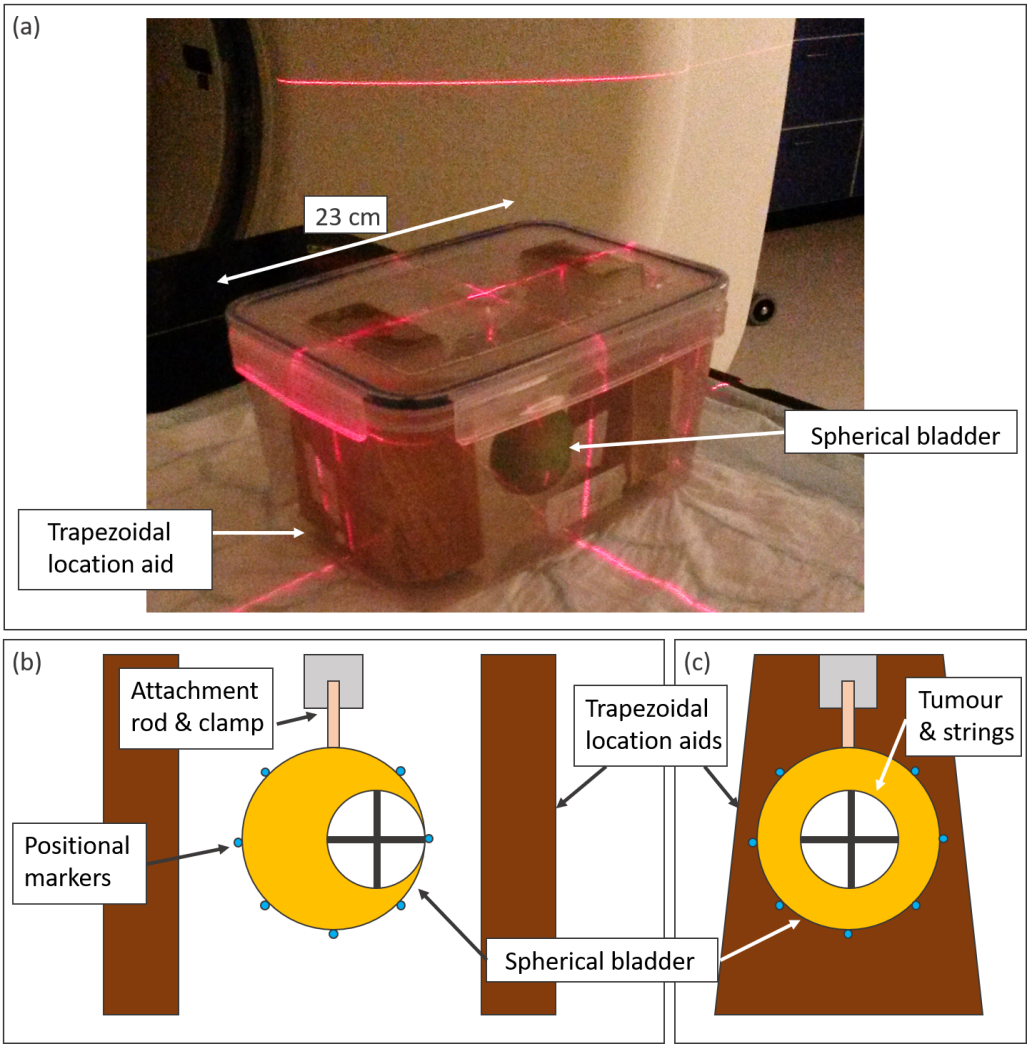

Figure 4.3: Phantom I: first main phantom designed and constructed to model a bladder and internal tumour shown in (a) photograph, and (b) and (c) schematic cross-sectional diagrams of the phantom internal construction.

Features of the construction of phantom I were:

- The main phantom volume was filled with water.
- Two bladder volumes were produced to mimic post-micturition (SB) and partially-full bladder (LB) containing internal spherical tumours of the same size. No attempt was made to replicate a full bladder as it is not typical practice for radiotherapy treatments.
- The bladders were made of hollow plastic spheres containing solidified gelatine

solution. Seventeen markers were positioned on the outside of each of the bladder spheres.

- The tumours were solid spheres made from polyvinyl alcohol (PVA) gel, held in position inside the bladder by the solid gelatine solution.
- Care was taken during construction of the bladder and tumour to ensure no air bubbles were introduced as they would cause additional distortion when imaged using DW-MRI.
- Each bladder was suspended inside the container using a wooden dowel glued to the bladder and clamped at the other end by an acrylic attachment inside the phantom.
- Strings saturated with gelatine solution (to ensure no introduction of air) had been passed through each tumour in three perpendicular directions prior to fixation within the bladder. This enabled identification of 6 points of intersection of string with the tumour surface.
- Wooden location aids were affixed on either side of the bladder. Their trapezoidal shape enabled accurate registration between image modalities in 3 orthogonal directions as well as 3 axes of rotation. They also prevented the generation of dielectric artefacts on MRI.

Table 4.1: Construction of phantom I

Item	Material	Size	Comments
Small Bladder (SB)	Polyethylene (PE) sphere	5.5 cm diameter, wall 1 mm thick	Sphere 87.1 cm^3
Large Bladder (LB)	PE sphere	6.5 cm diameter, wall 1 mm thick	Sphere 143.8 cm^3
Tumour	PVA gel with gadolinium (Gd) contrast agent	3.5 cm diameter	10 % PVA cryogel solution with Gd was cast into spherical mould; 3 freeze-thaw cycles completed
Bladder filling solution	Water and gelatine		(enabled fixation of tumour within bladder)
Markers	Low density polyethylene (LDPE)	2 x 2 x 2 mm	
Attachment rod	Wood	0.8 x 0.8 x 4 cm	
Localisation aids	Wood	Upper end 7.0 x 3.8 cm; lower end 9.3 x 3.8 cm	The tapering shape of these wooden blocks enabled accurate RR between CT and MRI
Container	Polypropylene	23 x 16 x 13 cm	
Main filling liquid	Water		

4.2.4 Phantom I imaging, processing and registration methods

Phantom I was imaged using CT, T2W-MRI and DW-MRI with each bladder remaining in position for all imaging modalities. CT was performed using a GE HiSpeed CT scanner (GE Inc., New York, USA) with a 2.5 mm slice width. Multiparametric MRI was performed using a GE 3T Discovery MR750w scanner (GE Inc., New York, USA) with the settings as shown in table 4.2. An axial DWI Focus sequence was used for the DW-MRI, and ADC map generation was performed automatically using the scanner software. These imaging parameters were chosen as

they are those used clinically for imaging of the prostate at the centre at which this work was performed.

Table 4.2: Settings used for T2W- and DW-MRI of phantom I.

Parameters	**T2W-MRI**	**DW-MRI**
Repetition time (TR) (ms)	6237	2851
Echo time (TE) (ms)	120.4	65.9
Slice thickness (mm)	2.5	2.5
Slice gap (mm)	0	0
Matrix size	352 x 288	140 x 70
Field of view (FOV) (cm)	24 x 24	24 x 24
Echo train length	19	-
No. of excitations (NEX) & b-values[†]	-	b = 50, NEX = 1 b = 300, NEX = 2 b = 700, NEX = 4 b = 1000, NEX = 6

[†]b-value is calculated using equation 2.14.

All DICOM image sets were transferred to the RayStation TPS (v. 5.0.2.35, RaySearch Laboratories AB, Stockholm, Sweden). The bladder outer surface, tumour, location aids, positional markers and string were manually delineated on the CT, T2W-MRI, and ADC maps. The locations of the centres of the bladder positional markers were projected to the inner surface of the plastic sphere (of approximately 1 mm thickness) and marked with points of interest (POIs). The delineation of the outer bladder surface as a region of interest (ROI) and the placement of POIs on its internal surface ensured all POIs were inside the bladder ROI for consistency, as this contour was used to control all subsequent deformable registrations (DR). POIs were also placed at the intersection of the tumour surface with the strings (6 points).

Phantom I - Rigid and deformable image registrations

Rigid and deformable registrations (RR and DR, respectively) were introduced in section 2.2.4. For both bladder sizes, RR of the T2W-MRI to CT was performed manually using the trapezoidal location aids to position accurately in 3 orthogonal directions and with respect to 3 axes of rotation. The same transformation was then applied to the ADC map resulting in RR of the ADC map to CT. DRs between ADC

map and CT were then performed with this underlying RR and using the bladder delineation alone to control the algorithm. This mimics the clinical situation in which tumour would not be adequately visible on CT.

Table 4.3: Registrations applied to ADC maps

Name	**Registration type**	**Algorithm used**	**DR settings**
RR	Rigid	-	-
DR1	Deformable	Hybrid	Image intensities not used
DR2	Deformable	Hybrid	As DR1; ROI focus set to bladder and IL setting[†] applied
DR3	Deformable	Hybrid	As DR1; ROI focus set to bladder
DR4	Deformable	Structure based	Structure based, 'fixed' setting
DR5	Deformable	Structure based	As DR4; 'sliding' setting

[†]IL setting is usually used for internal lung to accommodate changes in lung volume between image sets.

Five different DRs were produced, as detailed in table 4.3. These DRs correspond to the available default settings in the TPS, although the intensity-based information was not utilized as this is designed for registration of CT-CT datasets. Only the default settings of linear elastic properties were investigated (i.e. the default value of 0.48 for Poissons ratio in linear elasticity was used for the bladder).

The three default settings of the hybrid DR algorithm were tested: all used the bladder delineation to control the registration, two also used the bladder as a focus region (DR2 & 3). The two default settings of the structure-based algorithm were tested: fixed, in which vertex-to-vertex correspondence of the triangular mesh structures was required between the reference (CT) and target (ADC map) datasets (DR4), and sliding, in which some latitude or slippage was permitted in the mapping of vertices from one dataset to the corresponding vertices on the other dataset (DR5).

The positions of pairs of POIs which had been identified on CT and ADC maps were compared. The expected position was taken to be that on the CT dataset, and the actual position was that identified on the ADC map. The distances between the two locations were recorded. The delineated volumes were compared via their Dice similarity coefficients (DSC), which were calculated according to

$$DSC = \frac{2(V_{CT} \cap V_{ADC})}{V_{CT} + V_{ADC}}, \tag{4.1}$$

where V_{CT} is the volume of the ROI delineated on CT and V_{ADC} is the correspond-

ing volume delineated on the ADC map (as discussed in section 2.2.4).

4.2.5 Phantom I: Results and discussion

Images of phantom I

Representative transaxial CT and T2W-MR images of phantom I are shown in figure 4.4 for corresponding central slices. These images both show minimal distortion and good contrast between the relevant parts of the phantom.

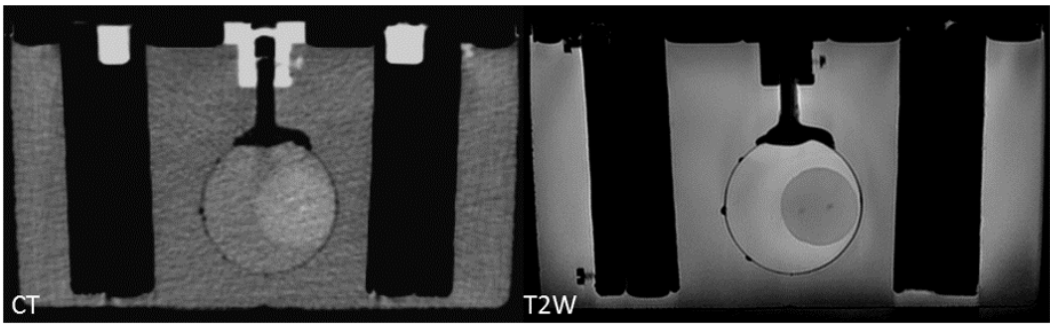

Figure 4.4: Imaged phantom I showing cross-sectional images with CT and T2W-MRI.

Figure 4.5 shows the equivalent slices as shown in figure 4.4 but from the DW-MRI (with b=300) and ADC maps. The distortions in these images relative to CT and T2W-MRI are apparent, but the various phantom parts are still visible across all modalities, enabling delineation of the various ROIs and positioning of POIs for quantification of the distortions.

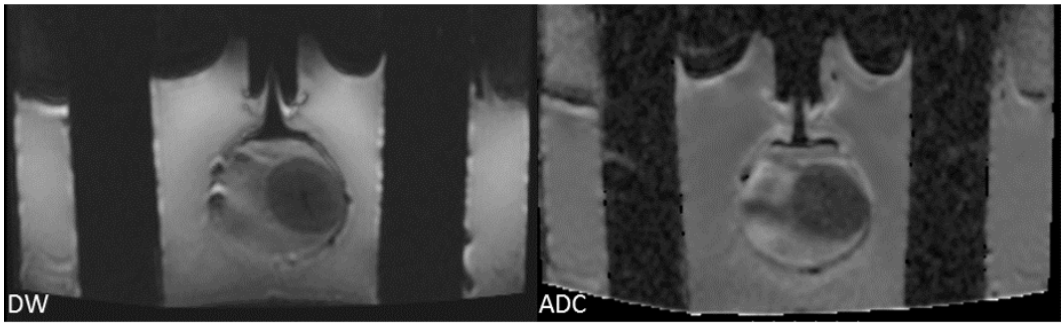

Figure 4.5: Imaged phantom I showing cross-sectional images with DW-MRI (b=300) and ADC map.

Delineated images of phantom I

Greater distortion was noted in the ADC maps of the small bladder (prior to DR) compared to those for the larger bladder; this effect is shown in figure 4.6. This figure shows the delineation of a central slice of the SB and LB following RR only (i.e. the images are simply overlaid with no DR performed) to allow comparison of the CT (solid line) and ADC map (dotted line) delineations of bladder (yellow) and tumour (green). Note that a representative distance between ADC bladder delineation and that on the CT is 1.1 cm for the small bladder and 0.8 cm in a similar location for the larger bladder. This indicates that the subsequent use of the DR had to deform the ADC maps further for the small bladder images than for the larger bladder images.

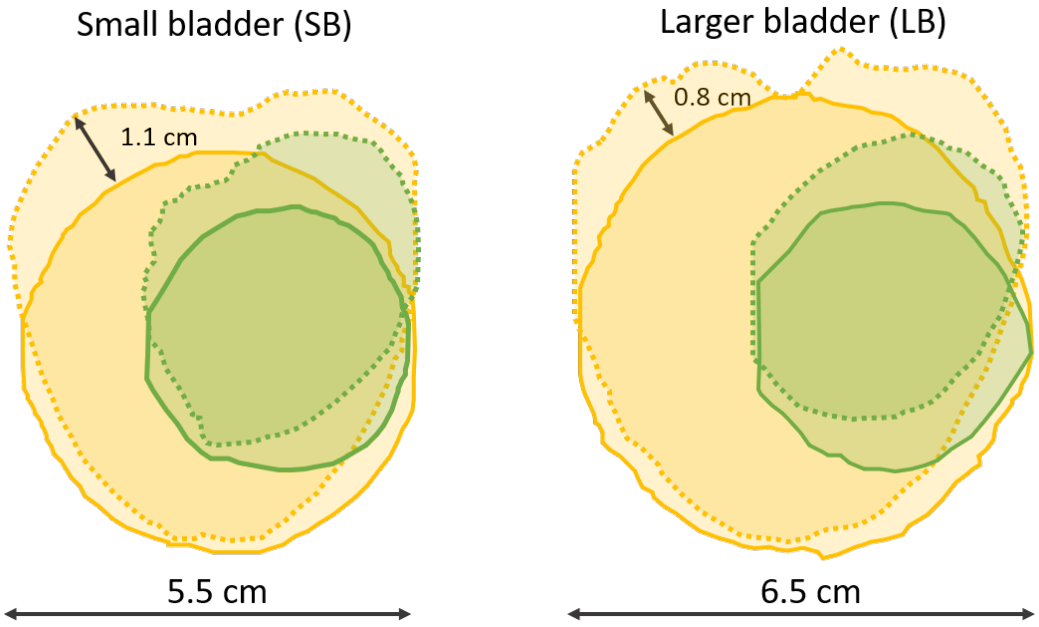

Figure 4.6: Delineations of bladder wall (yellow) and tumour (green) after RR only. Images show small and large bladder, from CT (solid lines) and ADC (dotted lines).

Dice similarity coefficients

Dice similarity coefficients (DSCs) were calculated according to equation 4.1 for each registration for both bladders and their tumours as shown in table 4.4.

Table 4.4: Dice similarity coefficients for all image registrations between CT and ADC maps.

	Dice similarity coefficient:						
	RR	**DR1**	**DR2**	**DR3**	**DR4**	**DR5**	**DR (mean)**
SB	0.81	0.99	0.99	0.99	0.96	0.96	0.98
Tumour	0.67	0.92	0.92	0.93	0.92	0.92	0.92
LB	0.85	0.99	0.99	0.99	0.97	0.97	0.98
Tumour	0.67	0.90	0.90	0.91	0.89	0.89	0.90

The application of all of the DRs reduced the distortion seen in the ADC maps significantly, with all algorithms producing similar results. After RR alone, DSCs were 0.81 and 0.85 for SB and LB respectively, whereas after DR, the DSCs ranged from 0.96 - 0.99 for both bladder sizes. Similarly, after RR alone DSCs were 0.67 for both tumours, which improved to 0.89 - 0.93 after DR. As DSCs would be expected to vary between 0 if there were no overlap, and 1 if there were perfect overlap of the volumes (as shown in figure 2.17), these results indicate good agreement following the DRs. The DSC was higher after DR for bladder (mean 0.98 for both bladder sizes) than tumours (mean 0.92 and 0.90 for SB and LB respectively). This is further illustrated in figure 4.7, which shows the intersectional volumes for the small bladder and tumour shown on ADC maps and CT respectively, for both RR and DR3. In this case the DSC of 0.81 for the bladder following RR increases to 0.99 following DR3; for the tumour these values are 0.67 and 0.93, respectively.

Both visually and numerically, these results show that the use of DR produces good agreement in the volume of both bladder and tumour. However, the use of the DSC as a metric does not provide any information regarding the location of individual points within either the bladder or tumour volumes. The following section addresses this via the measurement of positional markers and their locations within each image dataset.

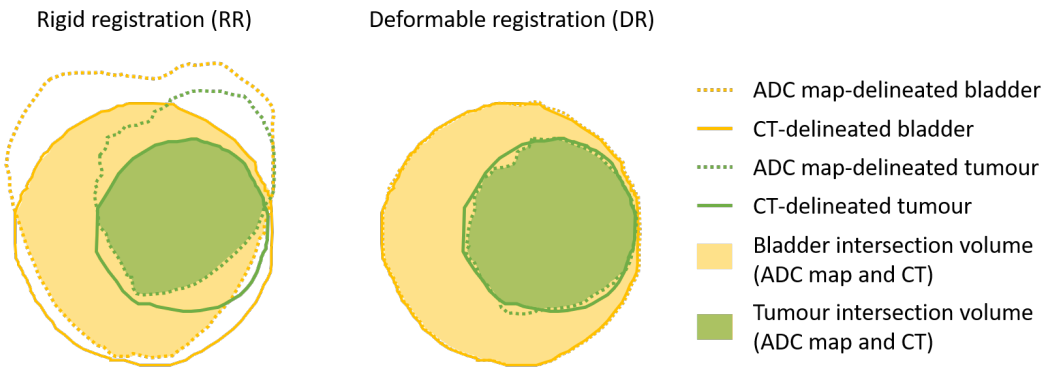

Figure 4.7: Diagram showing intersections of bladder and tumour volumes for the small bladder (SB) visualised on ADC maps and CT using rigid registration (RR) and deformable registration (DR), respectively. Bladder and tumour are shown in yellow and green, respectively. ADC map and CT delineations are shown with dashed and solid lines, respectively. Intersections between ADC maps and CT volumes are shown shaded in yellow (bladder) and green (tumour). These diagrams illustrate the SB results in table 4.4 where RR produced a DSC of 0.81 for the bladder and 0.67 for the tumour, and DR3 produced a DSC of 0.99 (bladder) and 0.93 (tumour), respectively.

Differences between locations of positional markers

The locations of the 17 bladder positional markers and 6 tumour markers had been denoted with POIs for each bladder size as described in section 4.2.4. The mean and one standard deviation in differences between expected positions of POIs and their actual positions were recorded for each registration, and are shown in figure 4.8. The values were recorded in mm for all POIs and are shown as the mean and range of 17 POIs for each bladder size and 6 for each tumour.

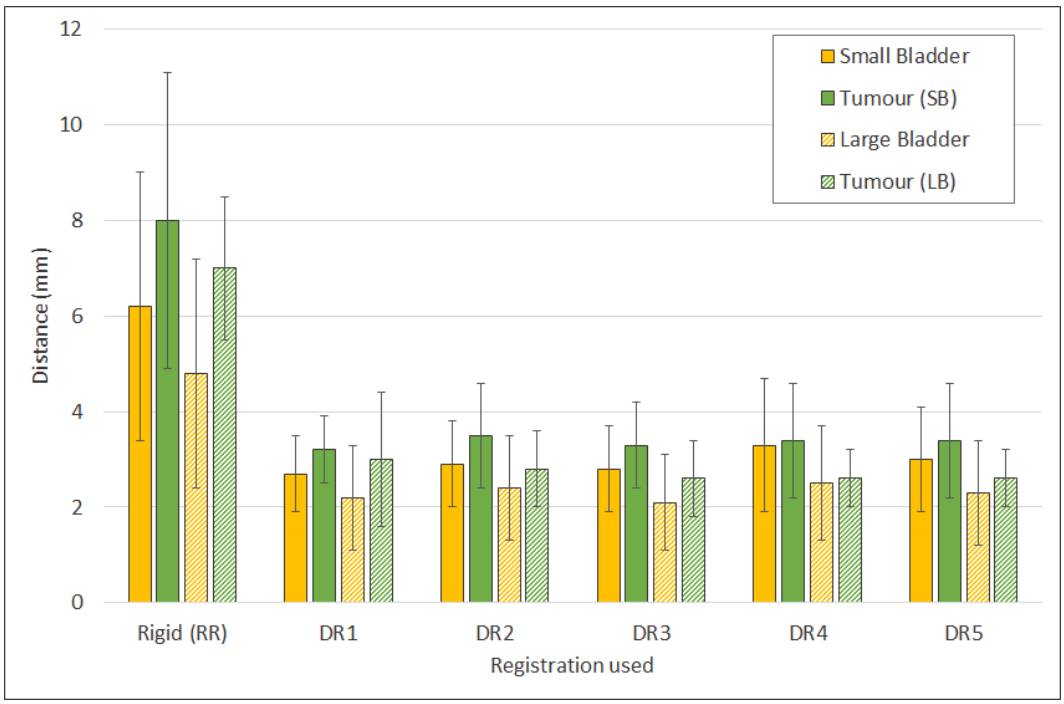

Figure 4.8: Mean and standard deviation of positional differences between expected and actual positions of POIs following registrations of ADC maps to CT of phantom I, for small bladder (solid colours) and larger bladder (hashed colours).

The mean differences between expected and actual bladder POIs were reduced by approximately 50 % using DR rather than RR alone (6.2 to 2.9 mm and 4.8 to 2.8 mm for SB and LB respectively). The spread in differences between expected and actual POIs was similarly reduced with the maximum decreasing from 12.4 to 5.9 mm and from 10.1 to 5.2 mm (SB and LB respectively). The mean differences between expected and actual bladder POIs were slightly lower than those for the tumour POIs (2.9 and 2.3 mm for bladder compared to 3.4 and 2.7 mm for tumours for SB and LB respectively). These results might be expected as the delineation of the bladder was used by the TPS to control all DRs, and so POIs close to this delineation (i.e. bladder POIs) would be more likely to be correctly mapped than POIs further from the controlling structure.

More importantly, for the purposes of estimating the realistic worst case scenario of positional information transfer from DW-MRI to CT, are the results shown in figure 4.9, which shows the maximum positional error for each method of registration.

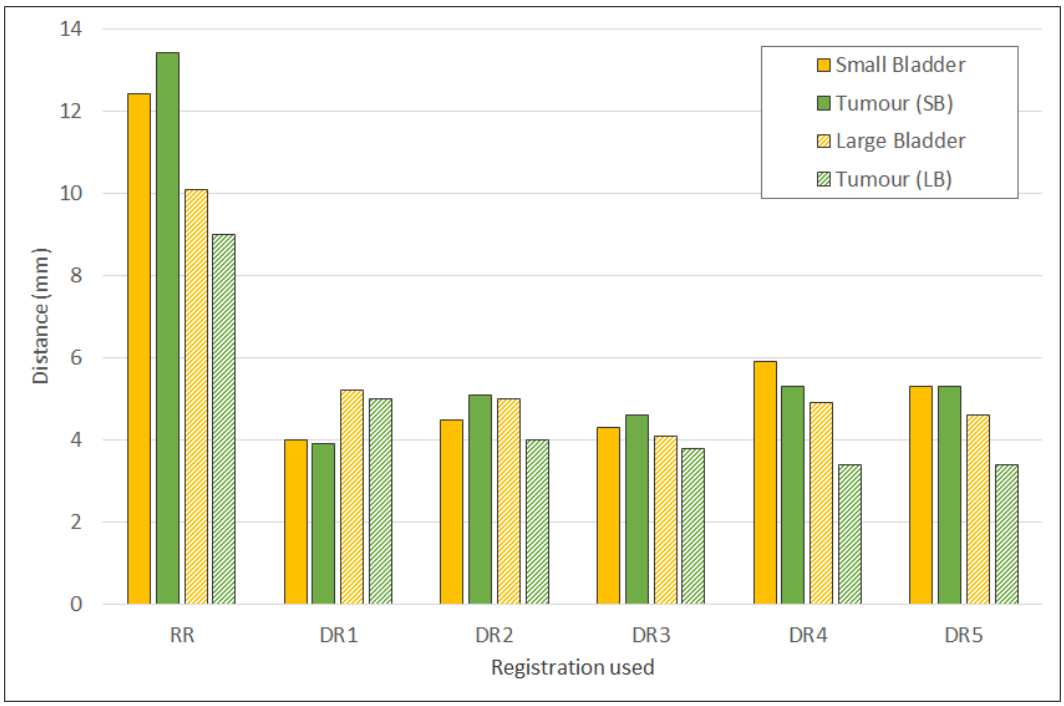

Figure 4.9: Maximum positional differences between expected and actual positions of POIs following registrations of ADC maps to CT of phantom I, for small bladder (solid colours) and larger bladder (hashed colours).

General discussion and implications

For all five DR settings the mean, standard deviation and range of the differences between expected and actual POIs were consistently lower for the LB data. For example, the mean post-DR POI differences were only 2.3 and 2.7 mm for the LB and tumour respectively, but 2.9 and 3.4 mm respectively for the SB. This was probably due to greater distortion prior to DR in the SB ADC maps compared to those for LB, which is shown in figure 4.6. These images show the delineation of a central slice of the SB and the LB following RR only to allow comparison of the CT (solid line) and ADC map (dotted line) delineations of bladder (yellow) and tumour (green) prior to DR. The distortion seen in the SB was visibly greater than for the LB, as indicated by the arrows. This is also indicated by the lower DSC of 0.81 compared to 0.85 for the RRs of SB and LB respectively. There was no obvious cause for this difference in distortion as the MRI scans of the two bladders were acquired under the same conditions.

It was noted that the differences between expected and actual positions of bladder POIs following DR tended to lie along the bladder surface itself, that is

to say that the high DSC values seen in table 4.4 imply a greater improvement in distortion than the results in figure 4.9 indicate. This is visually illustrated by figure 4.10 which shows the bladder ADC map ROI (dotted yellow) closely matching the bladder CT ROI (solid yellow), but an example POI shown (dotted crosshair = ADC map and solid crosshair = CT) indicates positional differences of approximately 3 mm, with both points lying along the bladder surface. This difference highlights a limitation that the DR algorithm may not correctly map the target bladder voxels onto the reference bladder voxels, although visually the ROIs appear correct. This is due to the way in which the DR algorithm works, as the use of the hybrid algorithm in RayStation without the intensity information (as this is designed for CT-CBCT or MR-MR registrations) uses only a chamfer-matching technique. In this technique, the system is looking at nearest points and minimizing distances between the two delineations of the bladder. When the delineations are overlaid by the algorithm, there is no further information or calculation within the algorithm to drive any further deformation of the bladder. For dose painting approaches to radiotherapy this limitation is potentially significant, otherwise the original benefit referred to by Fowler [43] (and highlighted in Chapter 3) - that the use of ionizing radiation has the virtue over drug or gene-based therapies that it reaches the cells that the physical plan encompasses - may therefore not be achieved.

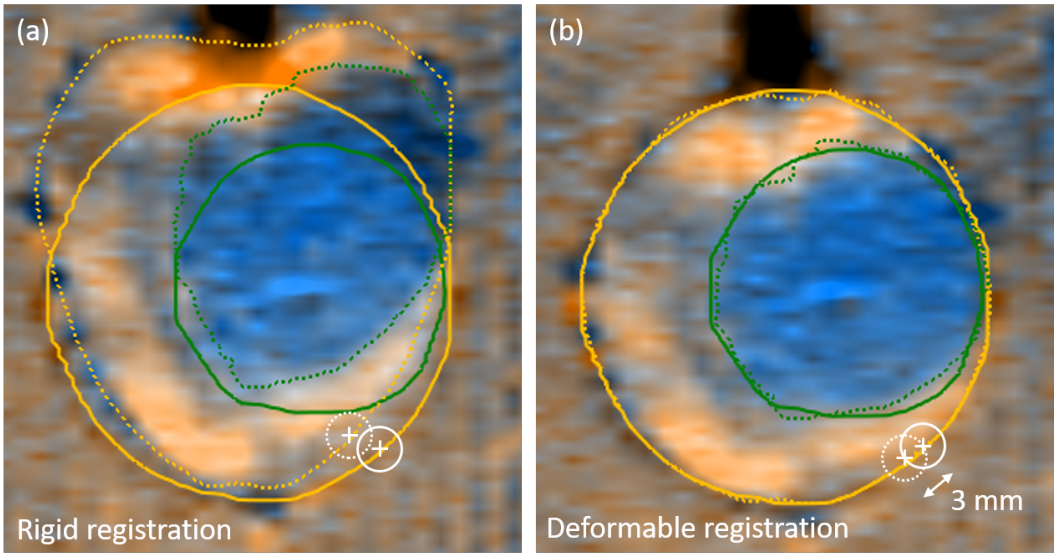

Figure 4.10: Images showing CT (blue) and ADC maps (orange) following (a) rigid registration (i.e. the original images are overlaid) and (b) deformable registration. Bladder delineations are shown in yellow and tumour in green with CT delineation indicated by solid lines and ADC by dotted lines. An example of POI differences along the bladder surface is indicated with white cross-hairs. Note that whilst contours closely align following DR, there remains a 3 mm difference along the bladder surface.

In practice, tumours are likely to be visible on T2W-MRI as well as ADC maps, and therefore some correction for the effect in figure 4.10 might be possible in terms of correlating tumour delineation with the T2W (less-distorted) image set. However, one of the purposes of investigating the use of ADC maps to directly inform a radiotherapy treatment plan was as a first step in investigation of the utilization of a dose painting strategy based upon ADC image intensities. If incorrect positioning remains following mapping of the ADC to CT, this would mean that the clinically visible volume will not have the same representation as with CT or T2W images and so dose painting techniques would not be possible.

When using data from ADC maps to inform radiotherapy treatment planning using the more standard method of dose prescriptions to delineated tumour volumes, the values of most interest would be the maximum difference between expected and actual POIs, as this information will allow a conservative estimation of the size of additional (planning) margin which would be required to mitigate against target positional uncertainties. In this case, the results from DR3, which used the hybrid DR algorithm and the ROI focus set to the bladder, are the most promising. The

maximum positional difference was 4.6 mm for DR3 and was the lowest across all registrations. Using this DR, a margin of 5 mm could therefore be appropriate to account for the positional uncertainties introduced by the use of DW-MRI. It would be expected that this margin would be in addition to any others required in order to account for bladder filling, changes in patient position and anatomy and other uncertainties. It would therefore form an additional part of the gross tumour volume/clinical target volume to planning target volume expansion. Note that these results were obtained using a 3 T scanner, whereas MR-sim would usually be performed using a 1.5 T scanner, and therefore this value is likely to represent a conservative estimation of the required margin as distortions would be expected to be greater using a 3 T scanner.

As the results found using phantom I showed distortions which remained larger than desired for radiotherapy purposes, a further phantom was developed, and a different method of correcting the distortions in DW-MRI was tested. Further alterations were made to the phantom, in order to improve the design including construction of a more realistic (non-spherical) bladder shape. The use of plastic for bladder wall and fiducial markers was swapped for PVA and string respectively. This served to make the bladder more tissue-equivalent and to minimise artefacts from small air bubbles which had tended to lodge inside the plastic markers used in phantom I. The work using phantom II is discussed in section 4.2.7.

4.2.6 Requirements for a second phantom

The aim of designing, constructing and imaging a new phantom was to test whether a different method of correcting distortion in DW-MRI would produce improved results. The method that had been used for phantom I relied upon deformable registration software available within the TPS which is used for radiotherapy dose distribution calculation. Therefore this software was CE-marked and known to be robust with respect to its handling of images and attached patient information. The method of distortion-correction which was intended to be tested via the use of phantom II, however, does not form part of the software ordinarily used within the pathway of radiotherapy treatments. It is an established method within research and clinical diagnostic use of DW-MRI in some centres (as discussed in section 4.2.8), but is not commonly used within routine clinical analysis of diagnostic images as diagnosis is usually possible without distortion correction. For example, no distortion correction software is used by the centre at which this work was performed when DW-MRI is used clinically for diagnosis of prostate cancer. Therefore, although the software used is established, it is not as well-designed for use within the path-

way required for radiotherapy treatment design, and there are some difficulties and limitations associated with this; these will be discussed in 4.2.9.

As a second set of results was to be obtained, it was an opportunity to also include a more realistic shape of bladder than the spheres previously used (these changes will be discussed in section 4.2.7).

Distortion correction methods

The method of distortion correction used here was introduced in Chapter 2, section 2.2.3. The FSL software (FMRIB Analysis Group, Oxford, UK) was downloaded from the FMRIB Software Library and installed and tested on an iMac (OS X 10.9.5). The functionality of 'topup' within FSL was used, in which the 'blip up' and 'blip down' images acquired with b = 0 are used to calculate a field map. This field map was then used via 'applytopup' to correct the other diffusion-weighted images with different b-values. These calculations produced distortion-corrected images for each b-value used. The distortion-corrected images were generated by the FSL software in NIfTI format, and were processed in MATLAB (v. 2016a, MathWorks, Natick, NA, USA) to produce ADC maps according to the mathematical methods presented in Chapter 2 section 2.2.3. These distortion-corrected ADC maps are referred to as ADC (FSL) in this thesis. In order that the ADC (FSL) files could be used within the radiotherapy TPS, these files were then converted back into DICOM format, again using MATLAB. This required stripping the header information from the NIfTI ADC (FSL) files and re-attaching the DICOM header from the uncorrected 'blip up' ADC maps which had been automatically produced on the scanner. This step would not be robust enough as currently implemented for clinical patient images, but was sufficient for testing the work using a phantom.

4.2.7 Phantom II design and construction

Phantom II was designed and constructed as shown in figure 4.11. This figure shows (a) a photograph and (b) and (c) cross-sectional diagrams of the design of a second phantom to model a urinary bladder with internal tumour. Information regarding the materials used are reported in table 4.5; these are similar to those used for phantom I except that the bladder wall as well as the tumour was constructed using PVA gel. This meant that the bladder wall material was more tissue-mimicking than plastic, there could be a bladder wall of finite thickness (rather than 1 mm as previously) such that POIs could be located on the internal and external bladder wall surfaces, and the shape of the bladder could be made more similar to that of a

human bladder. The acrylic block used originally to clamp the attachment rod of the bladder in phantom I was retained, as it had been seen to result in slightly increased distortion towards the top of phantom I and so could provide some indication of the effect of nearby anatomical inhomogeneities such as bowel gas or bone.

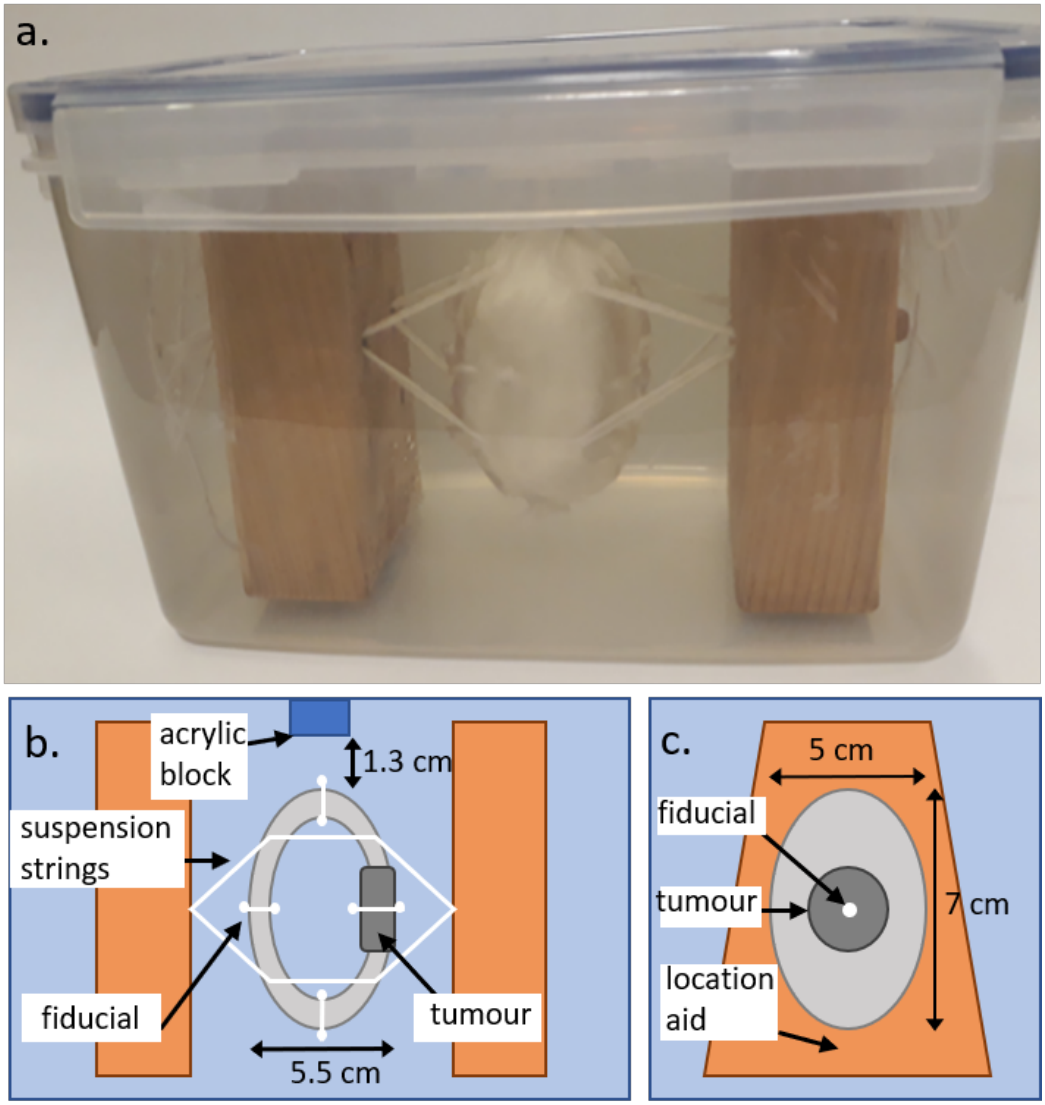

Figure 4.11: Phantom II - second phantom designed and constructed to model a bladder and internal tumour shown in (a) photograph and (b) and (c) cross-sectional diagrams.

Features of the construction of phantom II were:

- The main phantom volume was filled with water.

- The bladder was cast in two parts using PVA gel, with approximate dimensions taken from the CT of a patient previously treated for MIBC (7.0 x 5.5 x 5.0 cm); the thickness of the bladder wall was as required for adequate rigidity (0.5 - 1.0 cm) and therefore greater than that of a patient bladder (typically 0.3 cm [34]).
- The tumour was also PVA gel but with added Gadolinium contrast agent. The volume of 10 cm^3 was chosen such that it was similar to that expected for a post-resection MIBC tumour as used by Wright *et al.* [58].
- Assembly of the bladder and tumour was performed using wet string to ensure no air bubbles were introduced as they would cause additional distortion when imaged using DW-MRI.
- Wooden location aids were affixed on either side of the bladder as for Phantom I.
- The assembled bladder and tumour was suspended inside the container using wet string attached to the wooden location aids.
- Intersections of string with bladder/tumour surfaces were used as fiducial/positional markers for comparison across the imaging modalities. Five fiducials were in cardinal positions on the inner and outer bladder wall surfaces, and four within the tumour.

4.2.8 Phantom II imaging, processing and registration methods

Phantom II was imaged using CT, T2W-MRI and DW-MRI as for phantom I; CT was performed using the same scanner and settings as for phantom I, but the MRI scans were performed with slightly different settings (see table 4.6). These changes (in particular the NEX values) were made in order that the required images to use the distortion correction algorithm could be acquired - using firstly the clinical mode of the scanner ('blip up' images) and also the research mode, in order to acquire the 'blip down' images. The 'blip down' images could only be acquired with NEX = 1, and therefore all images were acquired with NEX = 1. This time the scans were also performed using both 3.0 T (GE 3T Discovery MR750w scanner as previously) and 1.5 T (GE 1.5T Optima MR450w scanner) MR scanners and so the images acquired using the 1.5 T scanner required slightly different settings. As previously, all settings were based upon those in clinical use at this centre for imaging of the prostate. Axial DWI Focus setting with 3-D geometry correction was used in both

Table 4.5: Construction of phantom II

Item	**Material**	**Size**	**Comments**
Container	Polypropylene (PE) sphere	23 x 16 x 16 cm	
Main filling liquid	Water		
Bladder wall	PVA gel	7.0 x 5.5 x 5.0 cm	10 % PVA cryogel solution with Gd cast into 2 moulds; 3 freeze-thaw cycles completed. Thickness 0.5-1.0 cm for rigidity
Tumour	PVA gel, Gd contrast agent	10 cm^3	10 % PVA cryogel solution containing Gd cast into cylindrical mould; 5 freeze-thaw cycles completed
Localisation aids	Wood	Upper end 7.0 x 3.8 cm, lower end 9.3 x 3.8 cm	The trapezoidal shape of these wooden blocks enabled accurate RR between CT and MRI
Fiducials	String		
Inhomogeneity	Acrylic	2 cm diameter, minimum 1.3 cm from bladder wall	An acrylic block located close to bladder enabled testing of the effect of a nearby inhomogeneity

cases, and ADC map generation was performed automatically using the scanner software for the generation of ADC 'blip up' and 'blip down' images.

Table 4.6: Settings used for T2W- and DW-MRI of phantom II.

	1.5 T		**3.0 T**	
Parameters	**T2W-MRI**	**DW-MRI**	**T2W-MRI**	**DW-MRI**
TR (ms)	6433	4000	6604	2081
TE (ms)	102.3	70.5	120.3	66
Slice thickness (mm)	2.5	2.5	2.5	2.5
Slice gap (mm)	0	0	0	0
Matrix size	256 x 224	140 x 70	352 x 288	140 x 70
FOV (cm)	24 x 24	24 x 24	24 x 24	24 x 24
Echo train length	21	-	19	
		b = 0		b = 0
		b = 50		b = 50
b-values†	-	b = 300	-	b = 300
		b = 700		b = 700
		b = 1000		b = 1000

†b-value is calculated using equation 2.14.

The operation of the scanners in the two modes, i.e. clinical mode and research mode enabled acquisition of images with reversed phase-encode blips and resulted in pairs of diffusion-weighted images with distortions going in opposite directions, as can be seen in figure 4.13 (a) and (b). The DW images which had been used by the scanner to produce these ADC maps were converted from DICOM into NIfTI format using MRIcroGL10 [59] software for processing in FSL. The paired DW images were imported into FSL, and the susceptibility-induced off-resonance field was estimated using a method similar to that described by Andersson *et al.* [30] as implemented in FSL and previously introduced in Chapter 2 section 2.2.3. The two sets of DW images were thereby combined into a single distortion-corrected one. This was done for each set of DW-MRIs (i.e. each b-value used) and then the corrected images imported into MATLAB. A new ADC map was then created manually within MATLAB following the methodology outlined in Chapter 2 section 2.2.3. An example distortion-corrected ADC map is shown in figure 4.13 (c), with the equivalent 'blip up' and 'blip down' ADC maps shown in (a) and (b) for comparison. MATLAB was then also used to convert the ADC (FSL) NIfTI image files back into

DICOM format so that they could then be imported into RayStation TPS.

The CT, T2W-MRI and 'blip up' ADC maps were imported directly into RayStation TPS from the scanners without further processing. The bladder outer surface, tumour, location aids, positional markers and string were delineated on the CT, T2W-MRI, and both 'blip up' and 'FSL' ADC maps. The locations of the fiducial markers were marked with points of interest (POIs) at the intersection of the string with the relevant bladder wall or tumour surface.

Rigid registration of the T2W-MRI to CT was performed manually using the location aids to position accurately in three orthogonal directions and with respect to three axes of rotation. This transformation was then applied to both ADC maps resulting in the same rigid registration of each ADC map to CT.

4.2.9 Phantom II: Results and discussion

Representative cross-sectional images of phantom II on CT and T2W-MRI are shown in figure 4.12, in which the bladder wall, tumour and string fiducials are visible along with location aids. Figure 4.13 shows similar representative cross-sectional slices to those in figure 4.12, but of the three different ADC maps generated ((a) 'blip up', (b) 'blip down' and (c) 'FSL', i.e. distortion-corrected with (d) T2W-MRI for comparison). The distortions, particularly at the interface between water and acrylic block or air at the top of the images are displaced in opposite directions between the blip up and blip down ADC maps. It is less noticeable, but still visible that the bladder itself appears shorter in the vertical direction in the 'blip down' image than in the 'blip up' image. The distortion in the 'ADC (FSL)' image shown in (c) is visibly reduced.

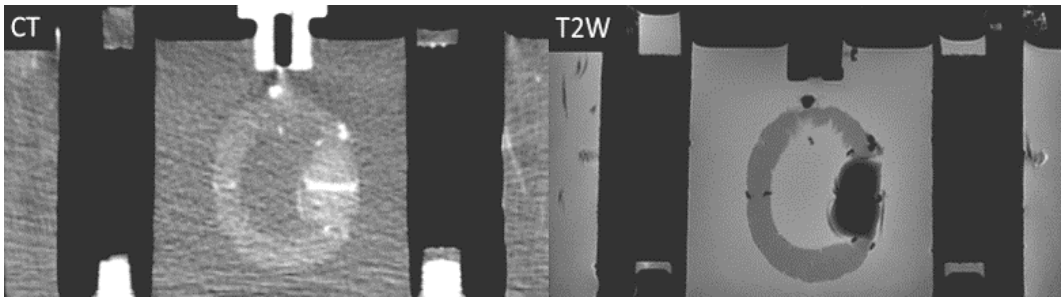

Figure 4.12: Cross-sectional images of phantom II using CT and T2W-MRI.

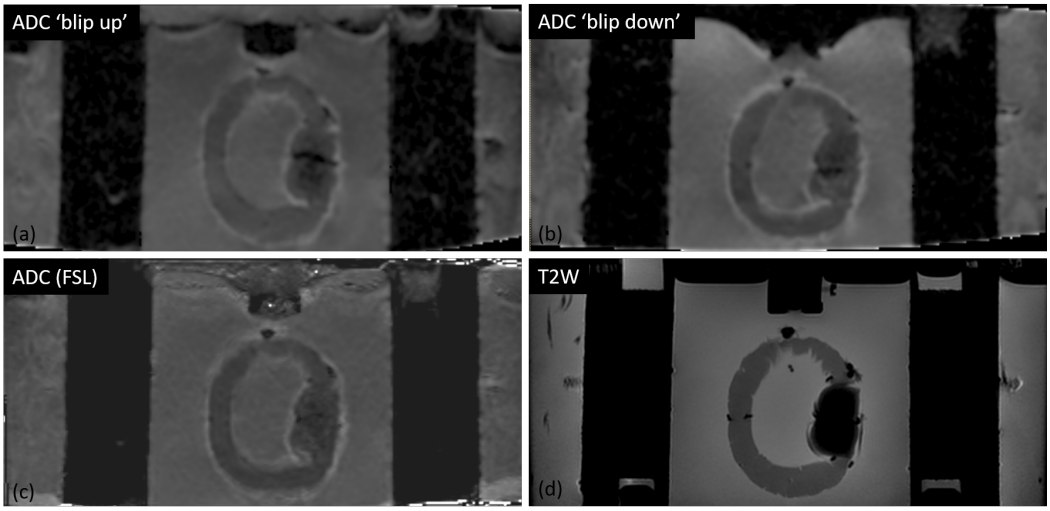

Figure 4.13: ADC maps where (a) 'blip up' and (b) 'blip down' refer to k-space readout direction showing distortion primarily in the relevant readout direction; (c) the ADC (FSL) map was recalculated following distortion-correction of acquired DW-MRIs using FSL and (d) T2W-MRI for comparison.

Following rigid registration of the ADC image sets to CT, the location of 14 POIs marking fiducial locations were compared between the modalities. This information is summarised in figure 4.14 which shows the mean and one standard deviation distances between POIs located on the labelled image set compared to their locations on CT.

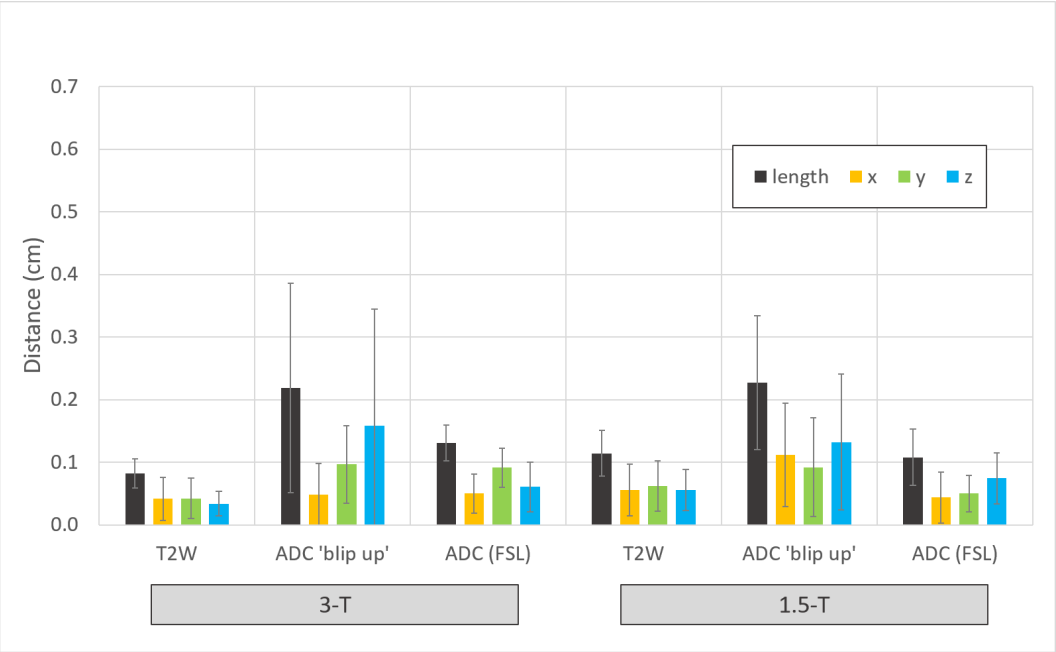

Figure 4.14: Mean and standard deviation of positional differences between expected and actual positions of POIs following registrations of T2W-MRI and ADC maps to CT of phantom II.

Of greater importance than the mean and spread of location agreement of POIs for the purposes of radiotherapy, is the maximum disagreement in location of the POIs. Figure 4.15 is a graph showing these maximum differences between POI locations on CT and T2W-MRI, and CT and ADC maps.

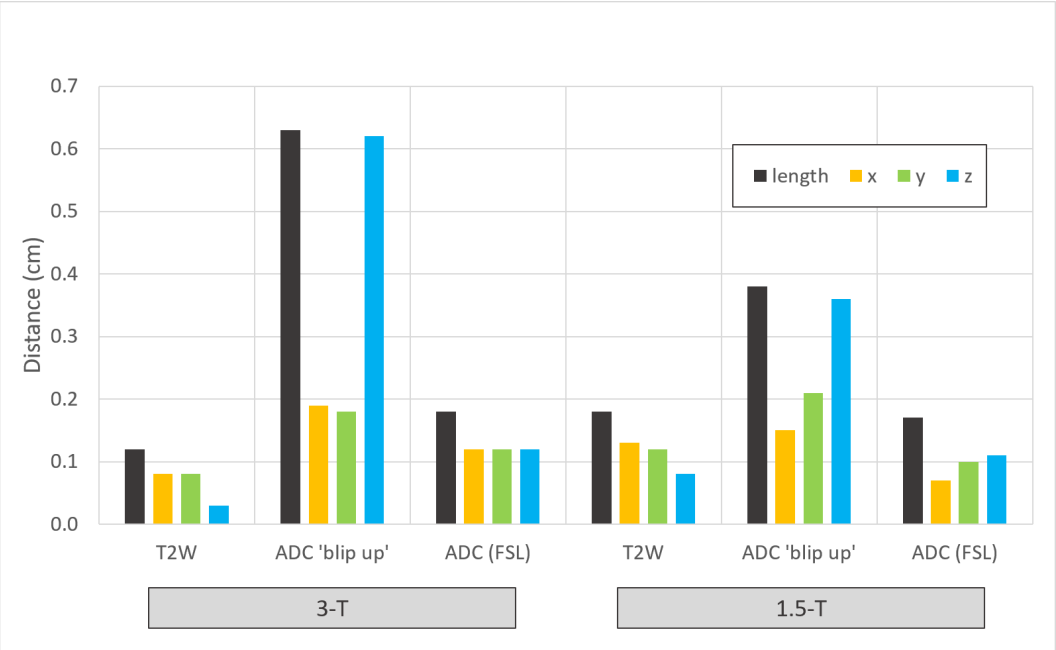

Figure 4.15: Maximum positional differences between expected and actual positions of POIs following registrations of T2W-MRI and ADC maps to CT of phantom II.

The results in figures 4.14 and 4.15 show that for the T2W images at 3 T the discrepancy in POI location is less than 1 mm on average, and only 1.2 mm maximum. Similarly, at 1.5 T these results were 1.1 mm (mean) and 1.8 mm (maximum) respectively. However, the equivalent results for 'blip up' ADC maps show that whilst the mean location discrepancy is 2.2 mm, the maximum exceeded 6 mm at 3 T. At 1.5 T these results were 2.3 mm on average and 3.8 mm maximum. Therefore, at both 3 T and 1.5 T the distortion seen in distortion-uncorrected ('blip up') ADC maps would be unacceptable for the purposes of tumour delineation and subsequent dose escalation in radiotherapy.

At 3 T, the locations showing poorest agreement corresponded to the fiducials located at the furthest superior and inferior extremes of the bladder. A possible reason for this could be that the centre of the scanned volume is positioned at the centre of the bore longitudinally, and therefore any field inhomogeneities would be worse for slices further from the centre of the phantom. One of these POIs also shows the worst agreement at 1.5 T, although there are also several other points with similar disagreement at 1.5 T (unlike at 3 T where all other points lie within 2.5 mm). At both 3 T and 1.5 T, the discrepancy occurs predominantly in the z-direction, which is the direction in which positional information is encoded using the phase of precession. This effect was more pronounced for the 3 T images, as

would be expected. For the 1.5 T images, there are several points with 2 - 4 mm discrepancy between POI locations, and more of these discrepancies lie in the x or y-direction. It may be that these points were more difficult to accurately ascertain as there was poorer contrast in the images acquired at 1.5 T, although this would require further investigation to confirm.

Following distortion-correction of the DW-MRIs using the FSL software and subsequent recalculation of ADC maps as discussed in section 4.2.8, the mean (and maximum) discrepancies in fiducial locations were 1.3 mm (1.8 mm) at 3 T and 1.1 mm (1.7 mm) at 1.5 T respectively. These results are similar to those found for the T2W images, and certainly below 2 mm in all directions. Therefore, using this method to correct the distortion of DW-MRI and ADC maps for radiotherapy delineation and dose escalation purposes appears feasible, providing the route of image processing required could be made more robust to potential errors.

The acrylic block at the top of the phantom was located a distance from the bladder similar to that expected for potential air/gas in patient rectum or bowel. This was 1.3 cm from the bladder wall and nearest external bladder wall fiducial marker, and 2 cm from the nearest internal bladder wall marker. Both points show improvement in agreement in fiducial location following distortion correction, with maximum discrepancies being 2.5 mm (uncorrected) reduced to 1.8 mm (post-correction) at 3 T and 3.3 mm reduced to 1.5 mm at 1.5 T (both for the internal marker, I1).

4.3 Summary and conclusions

Two phantoms were designed and constructed to determine the effect of distortions in ADC maps of the positional information in cases of muscle-invasive bladder cancer (MIBC). Imaging at 3 T of phantom I and processing using a commercially available deformable registration software found that ADC maps were produced from DW-MRI and transferred to a CT frame-of-reference with a 4.6 mm spatial accuracy. This was a significant improvement compared to the initial accuracy of over 13 mm using rigid registration, but is still large for radiotherapy treatment planning purposes.

Similar imaging at both 3 T and 1.5 T of phantom II found that ADC maps produced directly from DW-MRI on the scanner and transferred to a CT frame-of-reference reproduced location within up to 6.3 mm. However, when the DW-MRIs were processed and corrected for distortion using FSL software before production of ADC maps, the location of fiducials was reproduced within 1.8 mm for both 3 T

and 1.5 T MRI scanners. This is similar to the reproducibility accepted clinically for standard MRI techniques such as T2W-MRI. However, the workflow required for this technique is not currently possible within a clinical framework as much offline processing of images was required in order to produce the distortion-corrected images and import into the TPS.

Work in later chapters of this thesis investigating the potential impacts of the use of DW-MRI of bladder tumours for delineation of tumour (GTV) volumes will therefore use both the initial results from phantom I (using deformable registration) and phantom II (using offline distortion corrections) to accommodate uncertainties in location originating from the use of DW-MRI. This means a conservative margin of 5 mm will be used initially, and a less conservative margin of 2 mm will also be tested. This work will be discussed in Chapter 6.

Chapter 5

Modelling tumour control probability for bladder cancer

The response of cells to radiation, and the resulting probability of local control of a tumour (TCP) was introduced in Chapter 2 (section 2.1.3). This chapter develops TCP models for MIBC to enable the subsequent comparison of dose distributions in chapter 6.

5.1 TCP models

Several different mathematical functions have been used to model the probability of tumour control given the delivered radiation dose. A useful introduction is provided in a paper by Bentzen and Tucker [60], in which they describe how dose-incidence data for a specific radiation effect (i.e. endpoint) follows a sigmoid curve. They present the three most frequently used mathematical models: Poisson, logistic and probit respectively. The work in this thesis builds upon a logistic model described by Plataniotis and Dale [61] and refits their data using the Poisson model, for reasons discussed later in this chapter.

All TCP models are limited in their ability to accurately predict TCP, for two main reasons. Firstly, the clinical data on which the model is based will be several years old in order to have the follow-up time to determine outcome data. Therefore, the techniques and technology in use at the time of treatment delivery may be different from those in current use, and it is difficult to know how important these differences may be. For example, at the time of the BC2001 clinical trial [7] the delivery techniques used did not routinely include daily CBCT for patient set up, but such techniques are now in widespread use. Therefore, the partial bladder

boost incorporated in the trial could potentially lead to better outcomes if performed using current equipment as targeting of the boost volume would now arguably be more accurate.

A second limitation of TCP models is that, historically, only the effect of radiotherapy is taken into consideration [58, 62, 63, 64]. It is much less common for TCP models to attempt to assess the effects of combined treatments such as those including chemotherapy. This is a difficulty for many tumour sites, as often the prediction of TCP will therefore be based on data acquired from clinical trials which used only radiation therapy. However, in subsequent clinical practice patients may also receive chemotherapy. Assessing the impacts of combined treatments is not straight-forward [65].

There are also other limitations and difficulties involved in modelling TCP including the inability to measure the ideal data points systematically such as would be done for other experiments (i.e. varying dose across the possible range) as it would obviously be unethical to do so outside cellular (laboratory) studies.

5.1.1 TCP model requirements for this project

The aim of this project was to investigate the effects of dose escalation on TCP for simulated tumours akin to those expected to be found within the BladderPath trial. To be used for this purpose, the TCP model must be able to account for differences in tumour volume because the BladderPath trial omits the TURBT procedure, but uses neoadjuvant chemotherapy, followed by radiotherapy (or other treatments including surgery, although these treatments are not relevant to this project). The tumour volume at the time of radiotherapy treatment under the BladderPath trial will presumably be smaller than seen at diagnosis, owing to response to the chemotherapy, but may not be as small as post-TURBT tumours. It is not yet known what a representative tumour volume should be, and so it is pragmatic to model a range of volumes and assess the effect of tumour volume as well as dose upon the resulting TCP.

As BladderPath will include multimodality treatments, i.e. both radiotherapy and chemotherapy, it is also desirable to be able to estimate the additional effect of the chemotherapy as well as the effect of radiotherapy dose escalation upon TCP. As noted above, this is not simple to achieve and there have been several approaches to the solution of this problem. A detailed review is given by Grassberger and Paganetti [65], but there is currently no established method. In general, work has assessed the potential impact of radiotherapy dose escalation using radiotherapy data alone when investigating various adaptive radiotherapy treatment techniques

for MIBC (for example Wright *et al.* [58], whose work is discussed in section 5.1.3). Ideally, this project would follow this approach of using radiotherapy data alone, as it is most established, but also incorporate an estimate of the additional effect of chemotherapy.

5.1.2 Plataniotis and Dale's logistic model

One paper which attempts to accommodate the effects of chemotherapy in addition to radiotherapy for MIBC is that by Plataniotis and Dale [61], using the logistic model. This model is frequently used in statistical applications and came into widespread use in radiobiology following work by Suit *et al.* in 1965 [66]. In the logistic model, the probability of an event x is given by

$$P(x) = \frac{\exp(u)}{1 + \exp(u)}. \tag{5.1}$$

In this equation, $u = a_0 + a_1 D + a_2 Dd$ and d = dose per fraction, D = total dose and a_n are constants.

In Plataniotis and Dale's paper this standard approach was used to fit data from radiotherapy-only (RT-only) trials and then used as a platform to quantify the chemotherapy contribution in single-phase radiochemotherapy (RCT) trials. The radiation-induced complete response (RCR) at 2 years post-treatment was the endpoint investigated, as it is reported most commonly by clinical trials. Complete response is the disappearance of all signs of the tumour in response to treatment, and is more readily measurable than other endpoints such as overall survival. RCR was associated with a given dose, which may have been delivered using various fractionation schemes across the different clinical trials. These differences were accommodated via the use of the biologically effective dose (BED) formula and converted to equivalent dose in 2 Gy fractions (EQD2), where

$$BED = n \times d \left[1 + \frac{d}{\alpha/\beta}\right] - k(T - T_k). \tag{5.2}$$

and

$$EQD2 = \frac{BED}{1 + \frac{2}{(\alpha/\beta)}}. \tag{5.3}$$

Equation 5.2 is similar to equation 2.4 in which BED was originally defined in chapter 2, but now explicitly includes the dose per fraction (d) and number of fractions (n), as well as a factor $k(T - T_k)$ to take account of potential repopulation of tumour cells if delivery of dose is prolonged. In this factor, T is the overall

treatment time in days, and T_k is the delay time in days before fast repopulation of the cells in the tumour is thought to occur, and was taken to be 28 days by Plataniotis and Dale. The factor k was taken to be 0.2 Gy.day^{-1} and the α/β ratio was assumed to be 10 Gy.

The radiotherapy-only studies were analysed using the formula

$$RCR = \frac{1}{1 + \exp\left(4\gamma_{50}\left(1 - \left(\frac{EQD2}{D_{50}}\right)\right)\right)} \tag{5.4}$$

where RCR = radiation-induced complete response at 2 years associated with a given equivalent dose in 2 Gy fractions (EQD2), D_{50} is the dose in 2 Gy fractions required for a 50% response and γ_{50} is the slope of the response curve (percentage increase in response corresponding to a 1% increase in dose) at 50% response.

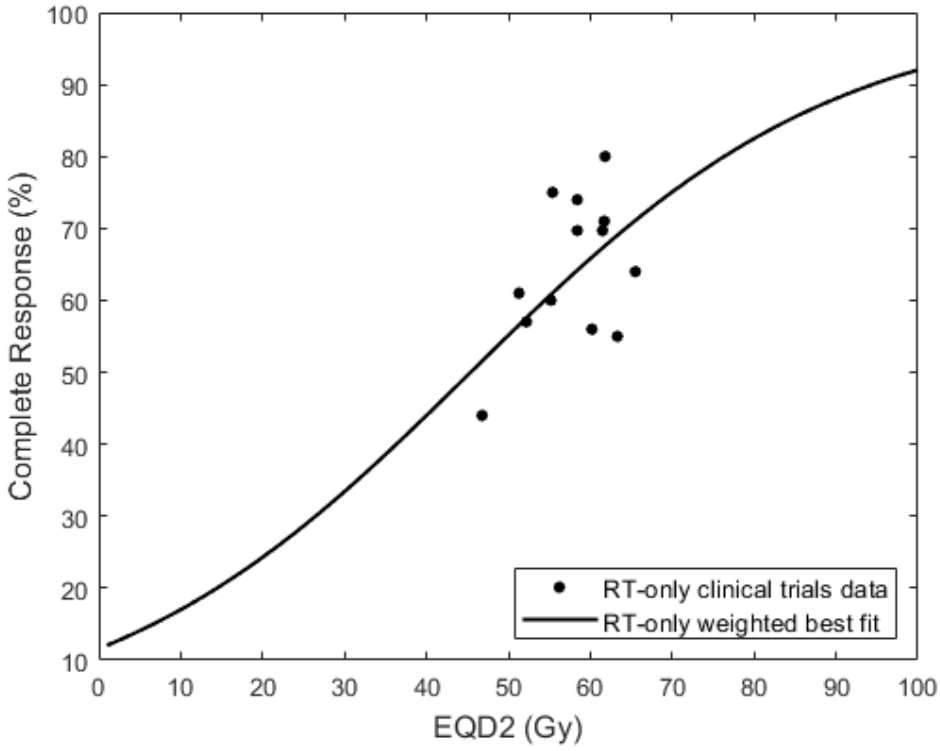

Figure 5.1: Scatterplot of RT-only observed complete response rates (RCR) against equivalent dose in 2 Gy fractions (EQD2), together with the weighted best fit response curve. Reproduced from figure 1 of Plataniotis and Dale [61].

Figure 5.1 is a reproduction of figure 1 from Plataniotis and Dale's paper in which a scatterplot of the RT-only observed complete response (CR) rates against

EQD2 is shown, together with the best fit response curve which was weighted according to the number of patients in each clinical trial. Figure 5.2 shows the same data and fit, but with the clinical trials data in which patients received chemotherapy as well as radiotherapy (radiochemotherapy, RCT). It can be clearly seen that this data shows a trend of improvement in complete response, although there is a wide spread thought to be due at least in part to the variations in chemotherapy regimens used.

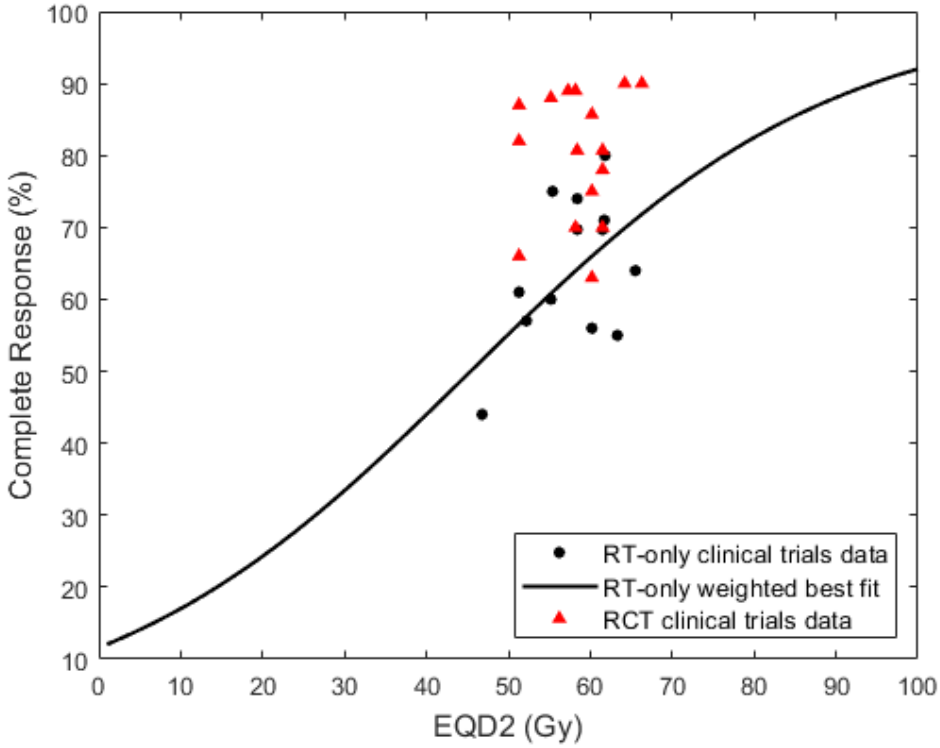

Figure 5.2: Scatterplot of RT-only (black circles) and RCT (red triangles) observed complete response rates against equivalent dose in 2 Gy fractions (EQD2), together with the weighted best fit to the RT-only data (black line). Reproduced from figures 1 and 2 of Plataniotis and Dale [61].

Plataniotis and Dale considered two alternative modes of operation for the incorporation of chemotherapy into response: (a) a fixed chemotherapy-alone contribution to complete response, or (b) a fixed degree of chemotherapy-induced radiosensitization. The corresponding graphs are shown in figures 5.3 and 5.4 respectively.

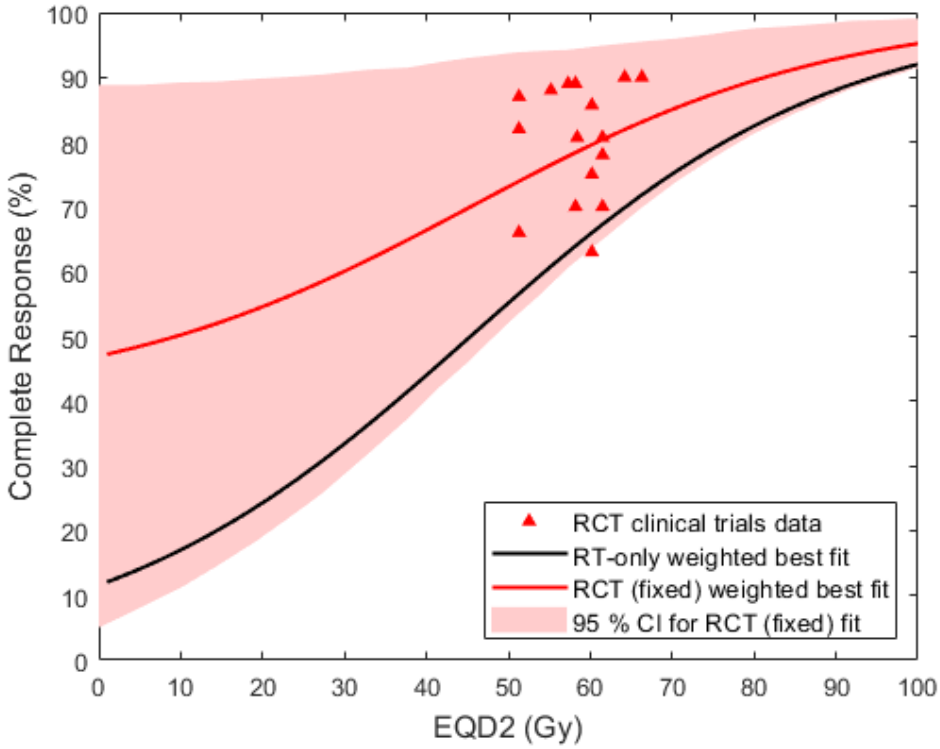

Figure 5.3: Scatterplot of radiochemotherapy (RCT) observed complete response rates (red triangles) against equivalent dose in 2 Gy fractions (EQD2), together with the weighted best fit using a fixed chemotherapy-alone contribution to complete response (red solid line). The 95% confidence interval of the fit is shown by shading, and the RT-only fit from figure 5.1 is shown for comparison (black line). Reproduced from figures 1 - 3 of Plataniotis and Dale [61].

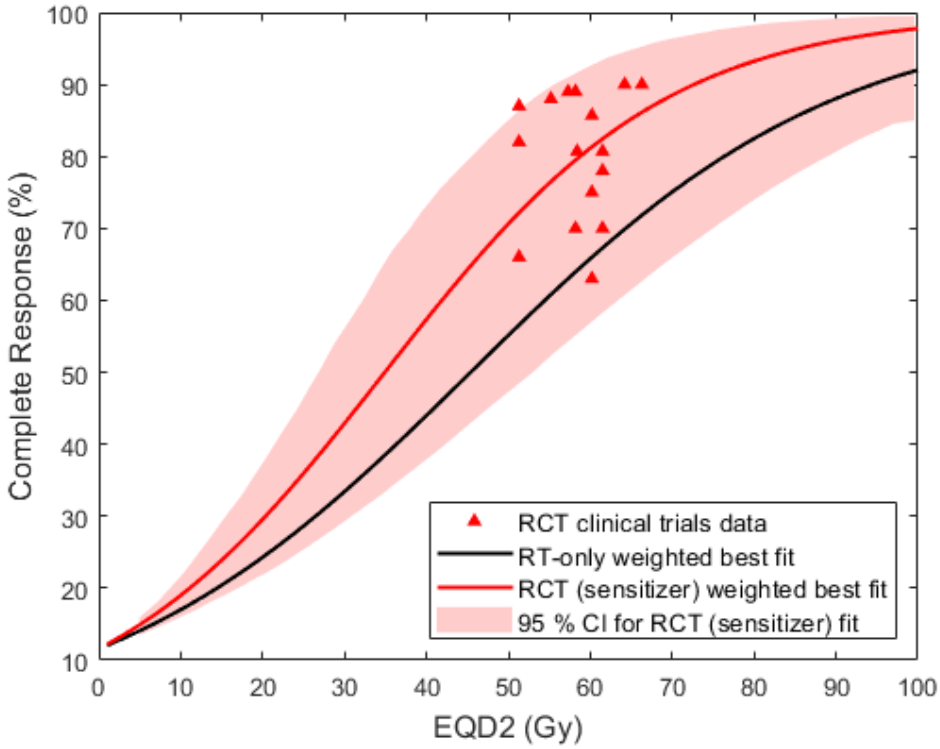

Figure 5.4: Scatterplot of radiochemotherapy (RCT) observed complete response rates (red triangles) against equivalent dose in 2 Gy fractions (EQD2), together with the weighted best fit using a fixed degree of chemotherapy-induced radiosensitization (red solid line). The 95% confidence interval of the fit is shown by shading, and the RT-only fit from figure 5.1 is shown for comparison (black line). Reproduced from figures 1 - 4 of Plataniotis and Dale [61].

In mode (i), chemotherapy provides a response rate independently of radiotherapy and complete response (CR) was calculated from

$$CR = CCR + RCR(1 - CCR) \tag{5.5}$$

where CCR = chemotherapy complete response and RCR is given by equation 5.4 and can therefore be combined as

$$CR = 1 + \frac{CCR \exp\left(4\gamma_{50}\left(1 - \frac{EQD2}{D_{50}}\right)\right)}{\left(1 + \exp\left(4\gamma_{50}\left(1 - \frac{EQD2}{D_{50}}\right)\right)\right)}. \tag{5.6}$$

In the second possible mode of operation, Plataniotis and Dale postulated

that chemotherapy may act purely as a radiation dose sensitizer and therefore the CR would be modified as

$$RCR = \frac{1}{\left(1 + \exp\left(4\gamma_{50}\left(1 - \left(s\frac{EQD2}{D_{50}}\right)\right)\right)\right)} \tag{5.7}$$

where s is the dose sensitization coefficient and all other parameters are as previously stated.

The resulting graphs produced from these two approaches (of incorporating chemotherapy effects as having a fixed contribution or as a sensitizing agent) are reproduced in figures 5.3 and 5.4 respectively. These figures show large differences in fit at low doses, however the predicted response at these doses are not clinically relevant (as treatment doses are in the range of the clinical trials data points).

The analysis by Plataniotis and Dale is novel in the way it attempts to incorporate the effects of chemotherapy as well as radiotherapy within the TCP models for MIBC, and ideally this approach would be incorporated within any assessment of the effect of dose escalation upon MIBC. Unfortunately, however, as there are no parameters in the logistic model to enable direct control of the tumour volume, it is not possible to use this model to assess the potential impact of dose escalation within a BladderPath-based study. This is because it is not known whether tumour volumes at the time of radiotherapy treatment in this study will be similar to those for standard treatments, as tumours within the BladderPath treatment pathway will not have undergone the TURBT procedure but will have been treated with neoadjuvant chemotherapy. In this situation, the Poisson model would be useful, as it contains parameters which enable the direct manipulation of tumour volume and so investigations across a range of potential tumour volumes is possible.

5.1.3 Poisson Model

A detailed introduction to this model is given in The Handbook of Radiotherapy [11], and the background discussed in this section can be found there unless otherwise stated.

In Chapter 2 equation 2.10 we saw that

$$TCP = \exp\left[-N_0 \exp\left[-\alpha D\left(1 + \frac{\beta}{\alpha}d\right)\right]\right], \tag{5.8}$$

where N_0 is the initial number of clonogens, d is the dose per fraction, D is the total dose and α and β are the fitting parameters which affect the shape of the curve. This model produces sigmoidal curves, with very steep slopes, as seen in the dashed curve

in figure 5.5. As these slopes are steeper than those found in practice, the model has been developed to incorporate inter-patient variation, where it is assumed that α is distributed normally amongst the patient population with a standard deviation σ_α. Figure 5.5 shows the effect of varying σ_α, with the two curves both having an α of 0.35 Gy^{-1}. Where the standard deviation in α is zero, i.e. $\sigma_\alpha = 0.00$ Gy^{-1} the steep (dashed) curve is produced, and when $\sigma_\alpha = 0.08$ Gy^{-1} the shallower (solid) curve is produced.

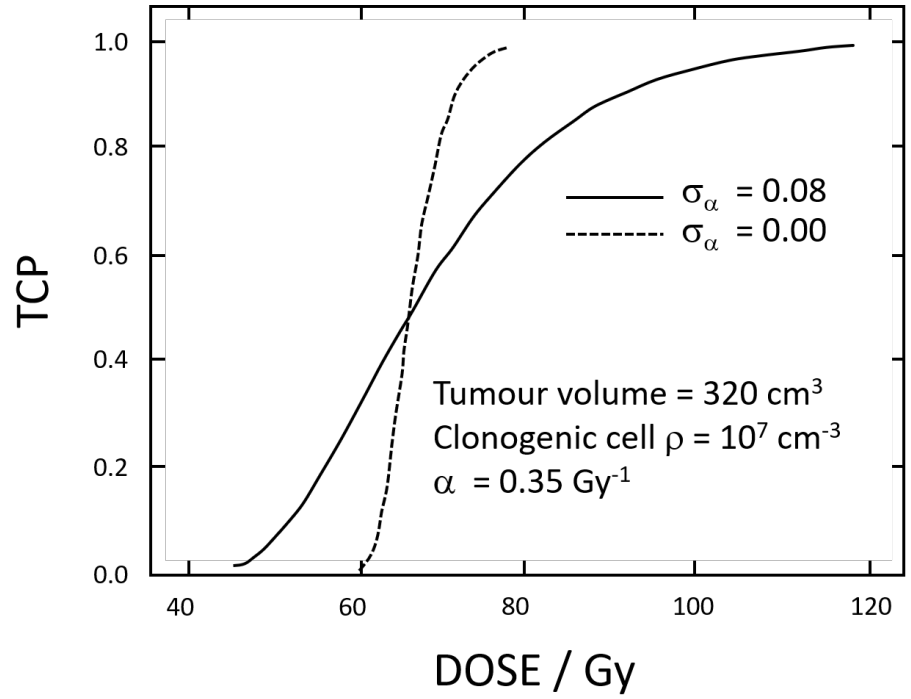

Figure 5.5: Tumour control probability (TCP) as a function of dose, adapted from [67]. Both curves are calculated with $\alpha = 0.35$ Gy^{-1}, but with a standard deviation $\sigma_\alpha = 0.00$ Gy^{-1} (dashed line) or 0.08 Gy^{-1} (solid line) respectively.

Wright *et al.* [58] have used the Poisson model in this way to fit a set of MIBC clinical trials data, which they subsequently used to assess the effectiveness of different adaptive bladder radiotherapy techniques. In chapter 2 (equation 2.1) we saw that the survival fraction (SF) of cells is given by

$$SF = e^{-\alpha d - \beta d^2}. \tag{5.9}$$

In their paper, Wright *et al.* assumed that the survival fraction over all volume elements (voxels, i) and all fractions (j) are given by

$$SF_i = \prod_{j=1}^{30} SF_{i,j} = \exp\left(-\sum_{j=1}^{30}\left(\alpha d_{i,j} + \beta d_{i,j}^2\right)\right). \tag{5.10}$$

The probability of no surviving clonogens in a voxel (the voxel control probability, VCP) is then given by

$$VCP_i = \exp\left(-V_{vox}\rho_i SF_i\right) \tag{5.11}$$

where V_{vox} is the voxel volume and ρ_i is the density of clonogenic cells in the i^{th} voxel. The overall TCP is therefore given by the product of all VCPs, i.e.

$$TCP = \prod_i VCP_i = \exp\left(-V_{vox}\sum_i \rho_i SF_i\right). \tag{5.12}$$

To include inter-patient variations in radiosensitivity, as discussed above, Wright *et al.* assumed α followed a normal distribution with standard deviation σ_α as presented originally by Nahum and Tait [67]. The α/β ratio was assumed to remain constant with a value of 13 Gy (based on Pos *et al.*'s findings [62]). Hence they used the equation

$$TCP = \int_0^\infty \exp\left(V_{vox}\sum_i \rho_i SF_i\right) g(\alpha)d\alpha, \tag{5.13}$$

where $g(\alpha)$ is a Gaussian distribution. In the case of bladder cancer, the target volume to be treated with radiation contains both primary tumour and the bladder wall, as both may contain some clonogenic cells. The density of clonogenic cells will be higher in the tumour volume than in the bladder wall, and incorporating both into equation 5.13 results in

$$TCP_{bladder} = \int_0^\infty e^{\left(-V_{vox}\rho_{tumour}\sum_i SF_i\right)} e^{\left(-V_{vox}\rho_{wall}\sum_{k\neq i} SF_k\right)} g(\alpha)d\alpha. \tag{5.14}$$

Wright *et al.* used equation 5.14 to fit a set of MIBC clinical trials data from Pos *et al.* [62]. These trials were RT-only and used an endpoint of 3 year local control. In fitting the data, Wright *et al.* assumed a post-TURBT tumour volume of 10 cm^3 as being representative of an average volume, and a clonogenic cell density within the tumour of 10^7 clonogens/cm^3 as suggested by Webb and Nahum [68]. They kept constant the total number of clonogenic cells in the whole (bladder wall plus tumour) volume, whilst varying the relative density (i.e. greater

or lesser proportions between the bladder wall and tumour itself. As stated, an α/β ratio of 13 Gy was used from the Pos *et al.* paper, and constraints of 0% at 30 Gy and 95% at 100 Gy were used with a restricted nonlinear least square fit. The work was then used by Wright *et al.* to compare different adaptive strategies for radiotherapy of MIBC.

The combination of the work done by Plataniotis and Dale using the logistic model, and by Wright *et al.* using the Poisson model gave rise to the approach taken in this thesis. That is, the use of the Poisson model (in order to have explicit control of the effects of tumour volume and clonogenic cell density), but also a separate, additional attempt to incorporate the effects of chemotherapy upon TCP.

5.2 Fitting the Poisson model to TCP data

The aim of the work in this chapter was to refit the data used by Plataniotis and Dale in their paper using the technique described by Wright *et al.* This would result in a standard Poisson-based TCP model to predict outcomes from RT-only treatments. The same methodology was then used to fit to the radiochemotherapy (RCT) data fitted by Plataniotis and Dale. The intention of this was to be used as an adjunct to the standard RT-only model in order to be able to better predict outcomes using a dose escalatation technique which would include the use of chemotherapy and require the ability to directly control for variations in tumour volume.

A MATLAB script was written which emulated the approach of Wright *et al.*, and was tested on the dataset used by Wright *et al.* and shown to reproduce the results in Figure 1 of their paper [58]. All assumptions made within the MATLAB code were based on those used by Wright *et al.*, i.e. a post-TURBT average tumour volume of 10 cm^3, clonogenic cell density of 10^7 cm^3 and constraints of 0% at 30 Gy and 95% at 100 Gy were used with a restricted nonlinear least square fit and α/β = 13 Gy. The output of the code was designed to find the value of α_{mean} and σ_α which would best fit the input trials data.

Following validation by reproduction of Wright *et al.*'s results, the α/β ratio used by the code for fitting the (Plataniotis and Dale) data was altered to 10 Gy, in order to be in keeping with the values used by Plataniotis and Dale in their fitting using the logistic model and previously presented in figures 5.1 - 5.4. A review of dose and fractionation schemes in the literature by Pos *et al.* [62] found that any value for α/β in the range 10 - 15 Gy is appropriate, and that there is quite a large uncertainty in this value.

5.2.1 Fitting methodology

The MATLAB code was used to methodically step through the possible values of α_{mean} and σ_α, to find the values which best fit the datasets using a restricted nonlinear least square fit. The results of running this code are shown in figures 5.6 and 5.7 for the RT-only and RCT clinical trials data respectively (both from Plataniotis and Dale [61]).

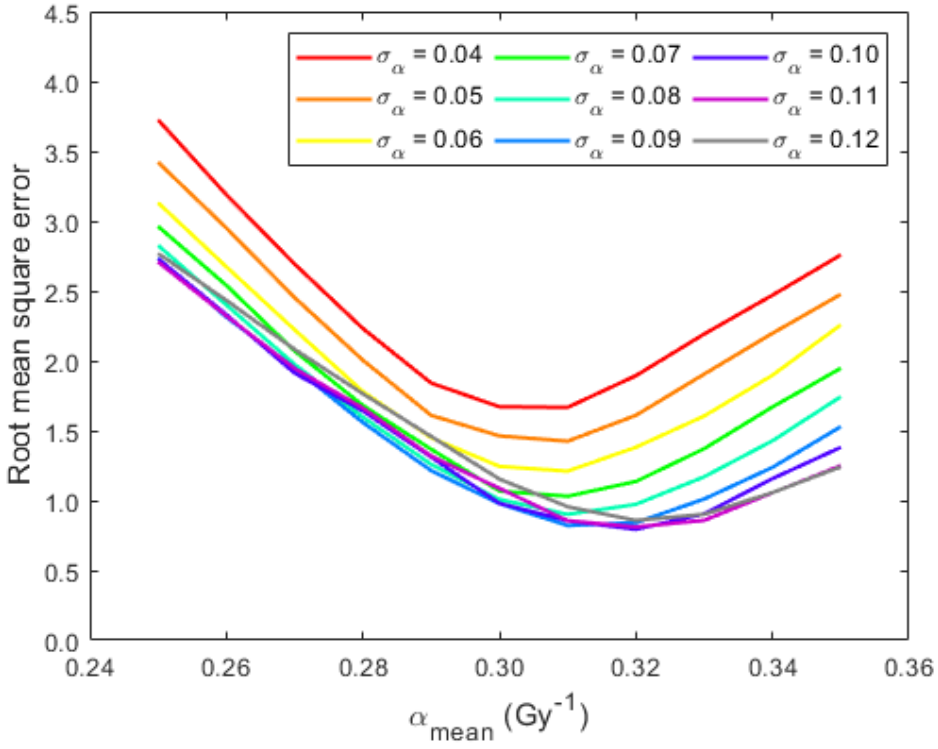

Figure 5.6: Graph showing how changing α_{mean} and σ_α affects the root mean square error (RMSE) when fitting RT-only clinical trials data from Plataniotis and Dale [61] with the Poisson model.

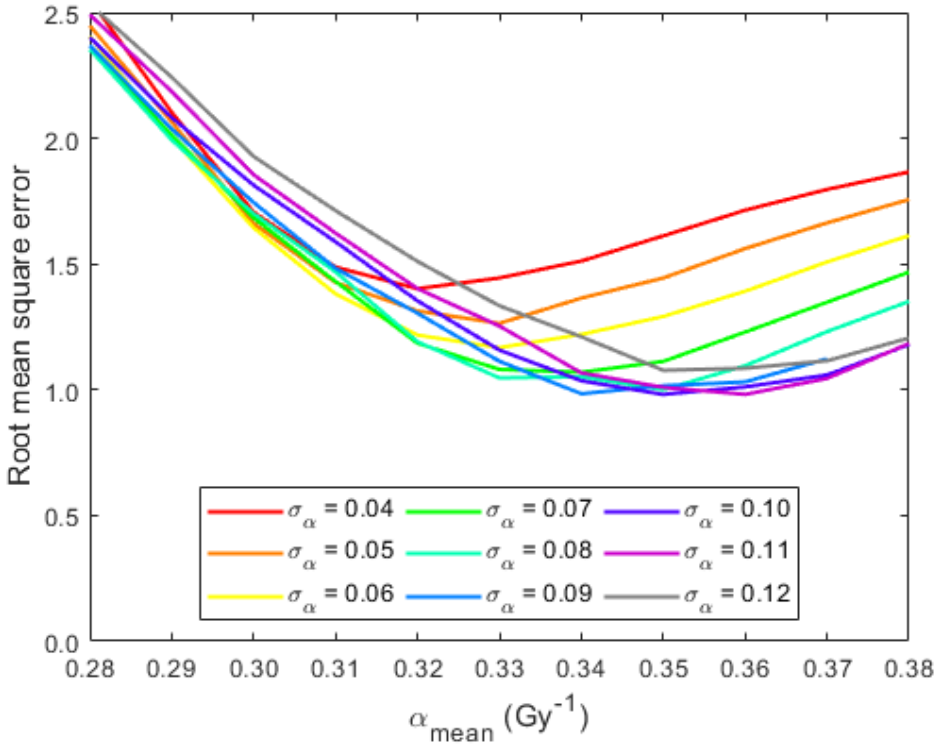

Figure 5.7: Graph showing how changing α_{mean} and σ_α affects the root mean square error (RMSE) when fitting radiochemotherapy (RCT) data from Plataniotis and Dale [61] with the Poisson model.

Figure 5.6 shows how varying α_{mean} and σ_α affects the root mean square error (RMSE) when fitting the RT-only data from Plataniotis and Dale [61] using the Poisson model. There is a wide plateau in the RMSE for the fits produced with α_{mean} in the range 0.31 - 0.33 Gy^{-1} and σ_α in the range 0.09 - 0.11 Gy^{-1}. The minimum RMSE produced was a value of 0.811 which occured when $\alpha_{mean} = 0.32$ and $\sigma_\alpha = 0.10$. As these values are approximately central within the plateau region, this appears reasonable. The values are similar to those found by Wright *et al.* ($\alpha_{mean} = 0.29$ and $\sigma_\alpha = 0.08$ respectively), although the endpoint used within that study was 3 year local control, rather than 2 year local control as used here.

Figure 5.7 similarly shows how the RMSE varies with change in α_{mean} and σ_α but instead when fitting the RCT dataset from Plataniotis and Dale using the Poisson model. There is again a wide plateau in values of α_{mean} and σ_α which produce the lowest RMSEs (approximately α_{mean} between 0.34 - 0.36 and σ_α 0.09 - 0.11). The minimum RMSE of 0.981 was produced when $\alpha_{mean} = 0.35$ and $\sigma_\alpha =$

0.10. Again, these values are approximately central within the plateau region.

5.2.2 Estimation of model uncertainties

TCP models in the literature frequently do not estimate the uncertainty in the model produced (for example Wright *et al.* report no estimate). This is perhaps partly because it is understood that the data used to produce the models are incomplete, and only exist in the range which is clinically acceptable to deliver to patients. Hence there is inherently a wide uncertainty in any model.

In order to estimate a 95 % confidence interval for the models produced here, the following method was used. The datapoints for both RT-only and RCT were closely clustered in terms of the values on the x-axis (EQD2), as shown in figures 5.1 and 5.2. Therefore, the mean EQD2 over all the clinical trials in each case (RT-only and RCT) was calculated, and assumed representative in this direction. The mean and standard deviation in the TCP (i.e. y-direction) was then calculated, and the combination used to produce points lying at mean EQD2 and mean TCP $\pm$ 2 s.d. These points are listed in table 5.1.

Table 5.1: Points calculated for 95 % confidence interval (CI) curves to pass through for RT-only and RCT data. Assuming no variation in dose and using spread in TCP of trials datapoints to estimate mean $\pm$ 2 s.d. in TCP. Points stated as (EQD2 (Gy), TCP (%)).

95% CI curve	**RT-only**	**RCT**
Upper	(58.55, 98.33)	(57.82, 84.41)
Lower	(58.55, 62.18)	(57.82, 44.27)

The same MATLAB code used to fit the data was then reused to manually generate curves which would pass through each of the points in table 5.1 by varying α_{mean} but keeping σ_α fixed. In this way, curves approximating the expected 95 % confidence interval curves were generated. The best fits and 95 % confidence interval curves are shown in figures 5.8 and 5.9 in section 5.3 for RT-only and RCT data respectively.

5.3 Results and discussion: Fitting the Poisson model to TCP data

5.3.1 Fit of Poisson model to RT-only data

Figure 5.8 shows the results of fitting the Poisson model as described to the RT-only dataset used by Plataniotis and Dale. The graph shows the RT-only clinical trials data (black circles) and Plataniotis and Dale's logistic fit (black line) as previously shown in figure 5.1 as well as the fit using the Poisson model with $\alpha_{mean} = 0.32$ and $\sigma_\alpha = 0.10$ (thick green line). The 95 % confidence interval in the Poisson fit is shown also (green shading).

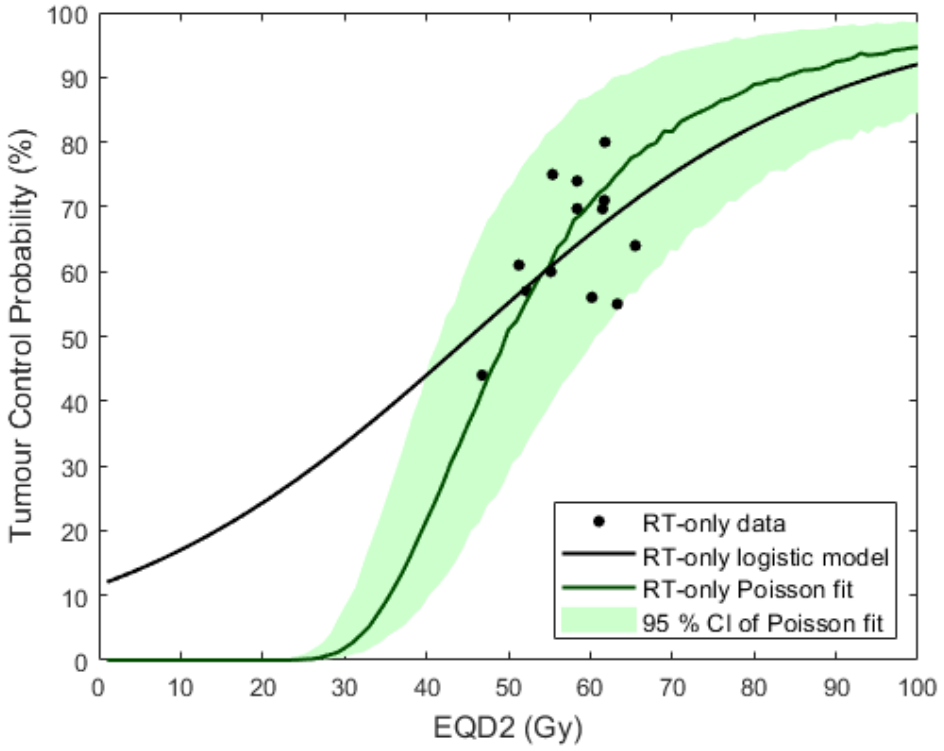

Figure 5.8: RT-only clinical trials data (black circles) and logistic fit (black line) reproduced from Plataniotis and Dale [61], along with the best fit using the Poisson model (green line) produced using the MATLAB script and $\alpha = 0.32$, $\sigma_\alpha = 0.10$. The 95 % confidence interval in the Poisson fit is also shown (green shading).

Figure 5.8 shows large differences in the fits for doses below ~45 Gy. This is not unexpected and is inherent to the models used (as discussed by Bentzen and

Tucker [60]). These doses, however, are below those usually used for radiotherapy treatments and therefore there are no clinical data in this region. The region of interest for the purpose of this thesis lies from around 50 Gy and above. In this region the maximum difference in TCP predicted by the logistic and Poisson models is 7 %.

5.3.2 Fit of Poisson model to RCT data

Using the same approach as in section 5.3.1 for the RCT data, the results shown in figure 5.9 were obtained. In this figure, the RCT trials data are shown by red triangles and Plataniotis and Dales fits are shown by the dark red (sensitizer model) and light red (fixed chemotherapy response model) solid lines. The best fit found using the Poisson model with $\alpha_{mean} = 0.35$, $\sigma_\alpha = 0.10$ is shown (purple line). The 95 % confidence interval in the Poisson fit is also shown (purple shading).

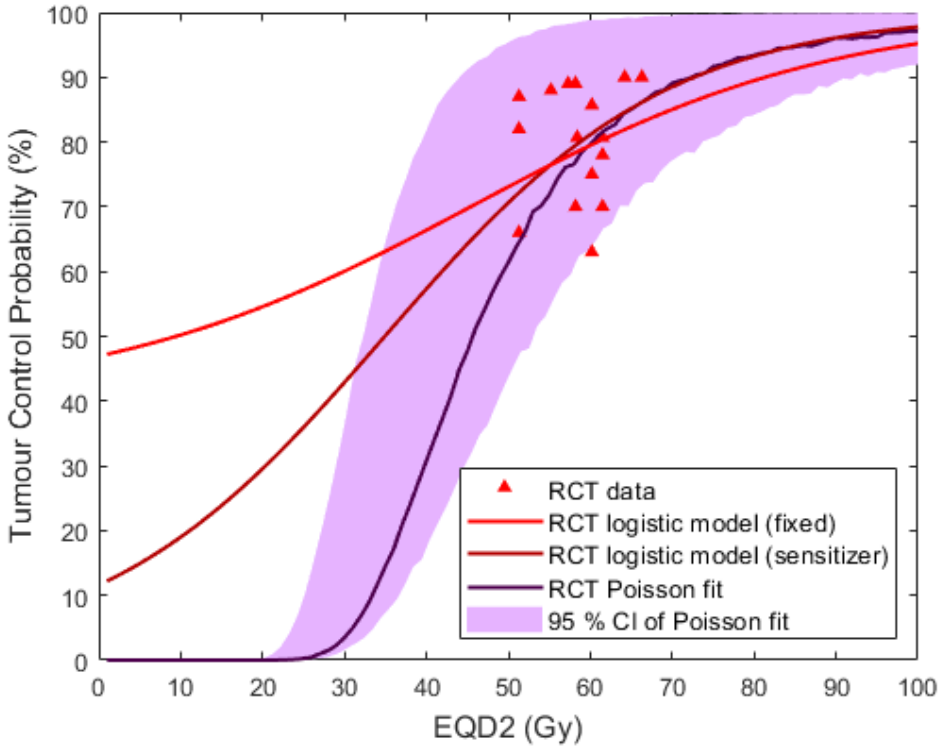

Figure 5.9: RCT trials data (red triangles) and both logistic fits reproduced from Plataniotis and Dale [61] (dark and light red lines), along with the best fit using the Poisson model produced using the MATLAB script with $\alpha_{mean} = 0.35$, $\sigma_\alpha = 0.10$ (purple line). The 95 % confidence interval in the Poisson fit is also shown (purple shading).

The upper limit for the 95 % confidence interval shown in figure 5.9 for the RCT Poisson fit appears large, in comparison to the other estimates. This is probably due to the method used to estimate the curve, as the best fit curve itself does not go quite through the mean value of the TCP datapoints at the location of the mean dose of the datapoints; it lies further to the right than this point. This makes the high estimate of the 95 % confidence interval appear to be overestimated relative to the lower estimate of the 95 % confidence interval. Also, the large TCP value that is required (98.3 % at a dose of 58.55 Gy) is such that a very steep sigmoid curve is generated. Nevertheless, these curves serve to highlight a reasonable estimate for the uncertainty involved in estimating TCP.

Figure 5.9 again shows large differences in the fits between logistic and Poisson models for doses below ∼45 Gy. In the region above 50 Gy the maximum

differences in TCP predicted by the logistic and Poisson models are ∼5 %. For the RCT (sensitizer) model the differences in predicted TCP using the Poisson model are <2 %.

5.3.3 Confidence in the models

Figure 5.10 shows all results for doses above 40 Gy, and the datapoints which correspond to the clinical trial BC2001 [7] are highlighted. This trial used two fractionation schemes which were shown in table 3.1 and were found to have equivalent TCP and toxicities and are two of the most commonly-used fractionation schemes in the UK. The trial compared RT-only and RCT for both fractionation schemes; in figure 5.10 both RT-only (green circles) and RCT (purple circles) datapoints can be seen to lie on either side of the relevant Poisson-fitted curves. This adds confidence that the fits are reasonable at these doses.

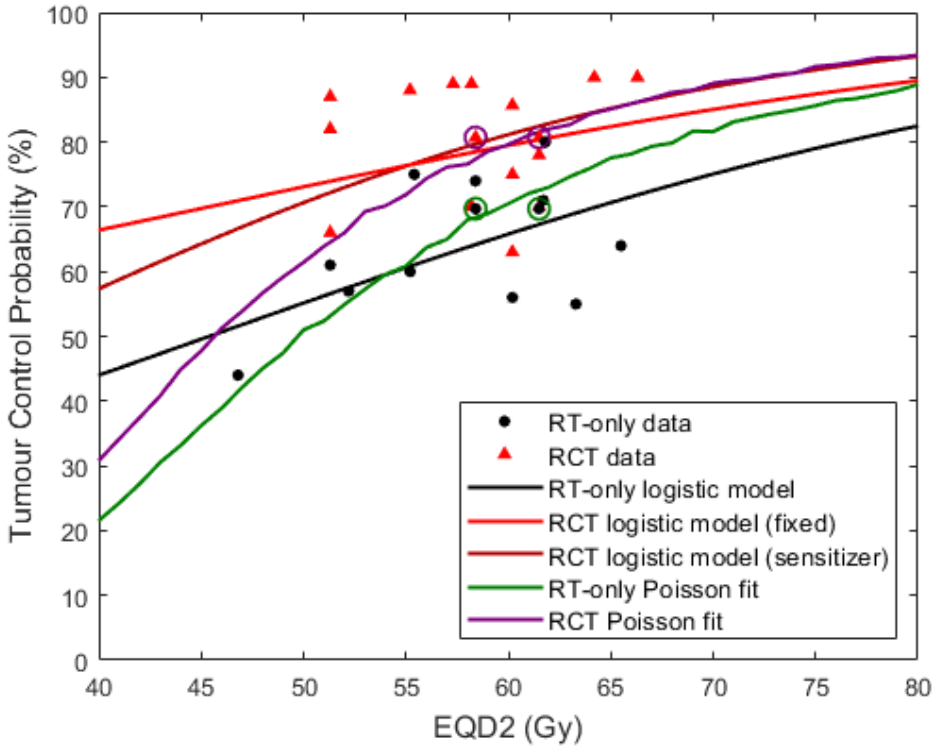

Figure 5.10: Graph showing all trials data and all fits, with the 4 datapoints from BC2001 [7] highlighted. Green circles indicate RT-only and purple indicates RCT. The points for 55 Gy/20# and 64 Gy/32# fractionation schemes lie either side of the appropriate Poisson-fitted curve in both cases.

The use of the Poisson model to fit the RT-only clinical trials data from Plataniotis and Dale is a standard approach, and produced fitting parameters which are similar to those found by others for other datasets. The appropriateness of the use of the Poisson model to fit the RCT dataset is less certain, however. For the purposes of this work it is certainly useful to have a 'best guess' of the increase in TCP which might be expected from the use of chemotherapy as well as RT, provided this is done with the caveat that the approach is simply in addition to the standard method, in order to gauge a reasonable estimate.

The data on which both TCP models (RT-only and RCT) are based is all for patients who received RT (without/with chemotherapy) after a 'maximal TURBT' had been performed. This is the standard care for patients with MIBC at present, however, the patients within the BladderPath trial will not receive the TURBT procedure. At present, there are no data to indicate the TCP following neoadjuvant chemotherapy without TURBT, followed by RT with or without chemotherapy - this is part of what the BladderPath trial aims to test. Hence, there may well be differences in outcome following the BladderPath protocol, and this is an inherent limitation to any model used for this purpose.

5.3.4 Use of these models to calculate TCP

Having produced the two Poisson models via fitting to clinical trials data for both RT-only and RCT, the next step was to alter the code to use treatment dose distributions to predict TCP. This would use the parameters of α_{mean} and σ_α which were found in section 5.2, and adapt the MATLAB code to read in the relevant dose information from calculated dose distributions. The RayStation TPS can produce text files which are generated by a Python script to produce differential dose volume histograms (DVHs). These files contain information about how many voxels receive each given dose, and the resolution of dose and voxel size can be chosen.

Firstly, the MATLAB script was adapted for the simple case where a 10 cm^3 tumour volume was treated to a uniform dose of 64 Gy in 32 fractions (i.e. EQD2 = 61.5 Gy using equation 5.2). This enabled testing that the script produced the expected result (72.6 % and 81.5 % for RT-only and RCT respectively), as this volume had been used to produce the fitted curve. Several further tests were performed to ensure that the code worked as expected, for example that 10 x 1 cm^3 tumour voxels produced the same result as a single voxel of 10 cm^3 receiving the same dose; and that a large decrease in dose for a small number of tumour voxels had a noticeable (and expected) effect.

The code was then further developed to produce several results depending

on the density of clonogens within the bladder wall. As for all previous work, it was assumed that tumour clonogenic cell density was 10^7 cm^{-3}, but the bladder wall clonogenic cell density was allowed to vary between zero and 10^7 cm^{-3} (i.e. the best and worst extremes) in logarithmic steps to see what effect this might have on overall TCP.

The code was checked using a standard 64 Gy uniform plan to the whole bladder within RayStation TPS, and which produced a text file containing the dDVH data for the tumour and bladder wall. This file was used by the MATLAB code and produced a predicted TCP within 1 % of the best fit curves in figure 5.8 (RT-only) and figure 5.9 (RCT), i.e the Poisson best-fit curves. The code was also adapted to produce estimates of the 95 % confidence intervals of these estimates, using the parameters from the work discussed in section 5.2.2. All results subsequently generated using this code are shown and discussed in Chapter 6 and 7.

5.4 Summary and conclusions

The approach used by Wright *et al.* [58] to fit a dataset of clinical outcomes data using the Poisson model was used to re-fit the datasets previously fitted by Plataniotis and Dale using the logistic model [61]. The parameters required to best fit the data were $\alpha_{mean} = 0.32$ and $\sigma_\alpha = 0.10$ for the RT-only dataset, and $\alpha_{mean} = 0.35$ and $\sigma_\alpha = 0.10$ for the RCT dataset. These values were then included within two MATLAB scripts (one for RT-only and one for RCT) which calculated predicted TCP from an input differential DVH such as those produced by a treatment planning system for a particular radiotherapy dose distribution. The functionality of these scripts was tested with simulated DVH files and the DVH text file from RayStation from a standard clinical dose distribution. Additional code produced estimates of the 95 % confidence interval TCP results for both RT-only and RCT models. Multiple combinations of clonogenic cell density were tested; with the standard 10^7 clonogens cm^{-3} within the GTV and varying between 0 and 10^7 cm^{-3} in the bladder wall.

The work presented in this chapter was intended to facilitate the calculation of TCP for a range of dose distributions, in order to predict the ability to escalate doses to MIBC tumour volumes. This use of the TCP models is discussed in chapter 6.

Chapter 6

Isotoxic dose escalation of simulated tumours

6.1 Introduction

The work presented in this chapter was inspired by a report by Warren *et al.* [69] in which 21 patients with mid-oesophageal cancer were retrospectively selected following conventional treatment, and a theoretical dose escalation study performed. Warren *et al.* used radiobiological modelling to calculate the required magnitude of a boost dose to the tumour (plus a 0.5 cm margin) such that a clinically significant increase in local control would be expected. The authors then calculated dose distributions on this basis in all patients, as well as standard distributions for comparison. They found that the dose escalation was achievable whilst continuing to meet existing dose constraints for nearby OARs for 16 out of 21 patients, with significant improvements in TCP and small increases in predicted toxicity.

The appproach taken in this chapter was similar to that of Warren *et al*, but involved a systematic increase in escalation dose until acceptable OAR doses were unachievable, followed by the calculation of the expected TCP. This meant that it was possible to determine the dose at which escalation became unfeasible in a variety of scenarios, rather than calculating a single dose for escalation based upon a specific intended increase in TCP.

The Warren paper studied dose escalation to tumours which are visible on CT, unlike post-TURBT bladder tumours. Therefore, in the work described in this chapter, tumours were first simulated in a range of possible locations within the bladder and with a range of volumes. The intention was to mimic a situation in which tumour positional information would originate from DW-MRI and be trans-

ferred to CT via image registration. Chapter 4 had separately sought to investigate the accuracy with which such information might be transferred, using phantom studies. Initial results in Chapter 4 produced a conservative estimate of 5 mm for the accuracy of such image data transfer, and subsequent work reduced this estimate to 2 mm. These values were each used within the study presented in this chapter, with initial work using the former value of 5 mm and subsequent testing using 2 mm.

6.2 Development of a method to simulate tumours

The planning CT and daily CBCT imaging from a previously treated MIBC patient was compiled and used for this section of work. The existing clinically-defined delineations of bladder (i.e. outer bladder wall), bowel, rectum, and femoral heads were retained. An internal 3 mm margin was created inside the bladder delineation to grow a 'bladder wall' volume (the value of 3 mm was chosen as representative of the values found by Jequier *et al.* [34]). When simulating a tumour volume post 'maximal TURBT' the volume was assumed to be 10 cm^3 as used by Wright *et al.* [58]. Simulations of such post-TURBT tumour volumes were created in six locations in the bladder (anterior, posterior, left, right, superior and inferior). The delineated volumes were chosen such that their extents were approximately symmetrical in each direction (see figures 6.1 and 6.2). All post-TURBT tumour volumes were 10 cm^3 and their thickness extended internally to 4 mm at the thickest point. These simulated tumours were designed to represent post-TURBT tumours such as those that would currently be treated in the standard way; an example schematic is shown in figure 6.1. The figure shows the inner and outer surface of the delineated bladder wall in yellow, and the simulated post-TURBT tumour volume delineated in orange. This example shows a tumour located inferiorly in the bladder, with noted symmetrical extent in the lateral (left and right) and anterior-posterior directions.

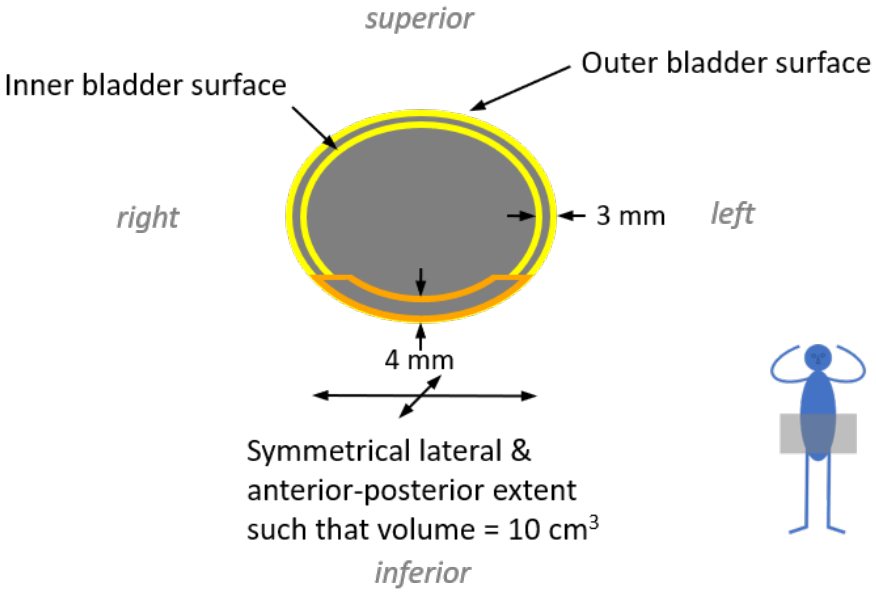

Figure 6.1: Schematic showing the coronal view of a simulation of an inferior post-TURBT (10 cm^3) tumour. Tumour extent is symmetrical as indicated in the lateral and anterior-posterior directions.

A second group of tumours were then simulated, based on the first, but in which an internal margin of 1 cm was used to increase their volume. Minor adjustments (<1 cm^3) were made to the volumes generated in each case so as to ensure the volume of all six tumours was exactly 20 cm^3. A third group of tumours were simulated in the same way, but by growing the internal margin by a further 0.5 cm and manually adjusting the tumour volumes generated to be exactly 30 cm^3. A schematic diagram of one of the third group of tumours can be seen in figure 6.2. In this figure, the inner and outer surfaces of the bladder wall are delineated in yellow, and the large simulated tumour in blue. This example shows a tumour located posteriorly in the bladder, with symmetrical extent (as far as is possible within the shape of the bladder itself) in the lateral and superior-inferior directions.

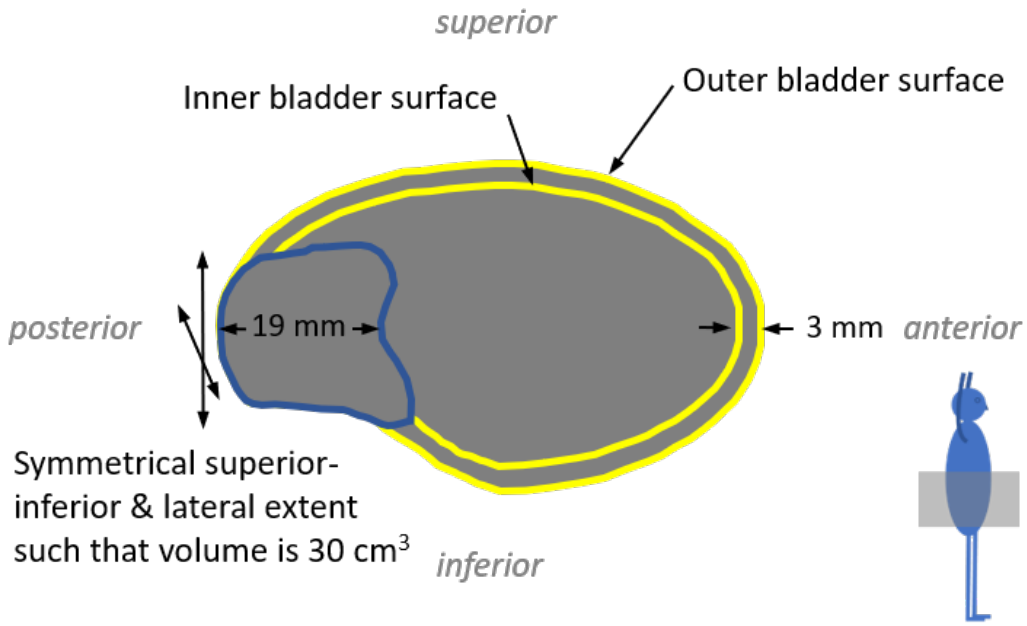

Figure 6.2: Schematic showing the sagittal view of a simulation of a posterior large (30 cm^3) tumour. Tumour extent is shown to be approximately symmetrical in the lateral and superior-inferior directions.

Following the described tumour simulation method, 18 tumours were simulated in total, with three in each location (anterior, posterior, left, right, superior and inferior). The three tumours in each location corresponded to small, i.e. post-TURBT (10 cm^3), medium (20 cm^3) and large (30 cm^3). Although it is possible that some MIBC tumours could be larger than 30 cm^3 at the time of presentation, the purpose of this work was to model what might be possible using the Bladder-Path pathway. In this pathway, patients receive neoadjuvant chemotherapy prior to radiotherapy treatment. It is expected that the tumours will therefore shrink between presentation and radiotherapy treatment, due to response to chemotherapy. As there is not yet any information available to show the degree to which shrinkage occurs, the range of tumour volumes was chosen to cover the existing, small post-TURBT volume, and two larger volumes in order to study the effect of variations in tumour volume at the time of radiotherapy treatment.

6.3 Radiotherapy treatment planning of simulated tumours

The aim of this section of work was to determine how far dose escalation could be driven without significant increase in toxicity, and to calculate the corresponding increase in TCP. The approach taken was similar to that of the RAIDER clinical trial (discussed in section 3.2.2). In RAIDER, the standard plan involves the whole bladder receiving 64 Gy in 32 fractions (WBRT) and this is compared with 2 trial arms. In both trial arms there are two PTVs, one incorporating the tumour (GTV) which receives the highest dose, and one incorporating the rest of the bladder, which is prescribed a lower dose of 52 Gy in 32 fractions. In the SART (standard dose adaptive radiotherapy) arm the high dose PTV (containing the tumour volume) still receives 64 Gy, and in the DART (dose escalated adaptive radiotherapy) arm it receives an escalated dose of 70 Gy.

The work presented here proceeds in a similar manner, however with the following differences:

- Reduced doses of 48, 52 and 56 Gy to the bladder wall are all studied, rather than 52 Gy only
- A range of dose escalations to the tumour (high dose PTV) are studied rather than only 70 Gy. The dose reached depends upon the achievability of that particular treatment plan
- The expected TCP resulting from the dose escalation was also calculated.

To this end, the standard plan (in which a uniform dose of 64 Gy in 32 fractions was prescribed to cover the whole bladder volume) was compared with systematically increased doses to the 18 simulated tumour volumes and reduced doses to the rest of the bladder wall. The organ at risk (OAR) dose limits used for this study were those used within the RAIDER trial and are shown in table 6.1. These values were chosen as they come from a current clinical trial and are therefore accepted to be safe clinically. Values within the table are expressed in terms of Vx where x is the dose in Gy which may be received by the volume in the adjacent column. The last line of the table shows the dose constraint to normal tissue (expressed as 'body - PTV') in terms of an optimal constraint of 105 % of the prescription dose, and a mandatory constraint of 110 % of the prescription dose. As the maximum prescription dose intended within RAIDER was 70 Gy, the corresponding values of 73.5 Gy and 77 Gy were adopted as the maximum absolute doses used for this work.

Table 6.1: Organ at risk (OAR) dose constraints for 32 fraction schedule of RAIDER (from Table 6a of RAIDER RT Guidelines [9]). Values given in terms of Vx where x is the dose in Gy which may be received by the volume given in the adjacent column of the table. For the bowel, two values of absolute volume are provided for each dose - these are the optimal and mandatory levels.

Organ at risk (OAR)	**Vx (Gy)**	**% Volume of OAR**	
Rectum	V30	80 %	
	V50	60 %	
	V60	50 %	
	V65	30 %	
	V70	15 %	
Femoral Heads	V50	50 %	
CTV - PTV2	V60	80 %	
	V65	50 %	
		Optimal (cm^3)	Mandatory (cm^3)
Bowel	V45	116	139
	V50	104	127
	V55	91	115
	V60	73	98
	V65	23	40
	V70	0	10
	V74	0	0
	Dx (cm^3)	**% of prescription dose (PD) to OAR**	
Body - PTV	D1	$\leq$ 105 % of PD	$\leq$110 % of PD

The margins used to expand the bladder wall (CTV) and tumour (GTV) to create PTVs were also taken from the RAIDER guidelines and are shown in table 6.2. These margins correspond to those used in RAIDER for the standard plans and the smallest of the adaptive plans, as they are the closest to relevance for the 'empty' bladder technique used here. The CTV is the volume of bladder wall receiving the reduced dose and this is expanded to produce the PTV. The GTV is the simulated tumour volume, which is expanded to produce PTV2 which receives the escalated dose. Mandatory and optimal dose limits for OARs as indicated in tables 6.1 and 6.2 were used directly as defined in RAIDER. Where possible the optimal dose limits were achieved, but mandatory limits were the backstop - if these

could not be reached, this implied the dose escalation chosen was not possible. The maximum dose escalation permitted was therefore found iteratively for each tumour volume in each location.

Table 6.2: Table showing RAIDER expansion margins in mm for creation of PTVs from GTV and CTV (taken from Tables 1 and 2 in RAIDER RT Guidelines [9]). PTV refers to the reduced dose volume of the bladder and PTV2 refers to the dose escalated volume containing the simulated tumour.

	Lateral	Anterior	Posterior	Superior	Inferior
Standard plans (CTV to PTV)	8	15	12	15	8
Dose escalated plans (GTV to PTV2)	5	5	5	5	5

The margins used to expand the tumour (GTV) to high dose PTV (PTV2) in RAIDER vary depending on the bladder volume. The margins are larger for partially-filled bladders to accommodate the variability in bladder filling expected during the course of treatment. The technique in use at this centre at the time of this project was not based on the RAIDER technique, and involved uniform treatment of a recently voided 'empty' bladder. Therefore only 'empty' bladder images were available for this project. A GTV-to-PTV margin of 10 mm was initially used for this study, within which 5 mm originated from the RAIDER recommendation for GTV-to-PTV margin for empty bladders, and a further 5 mm from the initial work in Chapter 4 which had shown tumour positional information from DW-MRI could be transferred via registration to CT within this accuracy. It could be argued that these values could have been added in quadrature, or some other margin recipe from the literature used (for example [70]). However, it was recognised that as larger, partially-filled bladders would require larger margins than these 'empty' bladders in any case, it was decided that this work would be best performed using the most conservative estimate (of a total margin of 10 mm). All other parameters used, including CTV (bladder wall) to PTV (low dose PTV) expansion were taken from RAIDER requirements. This latter value remained unchanged from RAIDER requirements and was not increased to incorporate positional uncertainties from DW-MRI, as the delineation of the external extents of the bladder would still originate from the planning CT not the DW-MRI.

The work in Chapter 4 using phantom II had shown an accuracy of <2 mm was achievable for transfer of positional data from DW-MRI to a registered CT.

Hence, a subset of plans were generated in which a GTV to PTV margin of 7 mm was used (i.e. 5 mm margins from RAIDER were retained, with an additional 2 mm included, reduced from 5 mm). This allowed the effect of variation in margin to be assessed as well as variations in tumour volume, dose to bladder wall and dose to tumour (GTV).

Table 6.3: Table showing target dose objectives (taken from RAIDER table 5 of RTGuidelines [9]) in terms of a percentage of the prescribed dose (PD). Dose constraints are provided in the form D_x where x is the percentage of the volume to receive this dose.

Volume	**Dose Constraint D_x (%)**	**Optimal**	**Mandatory**
PTV - PTV2	D_{98}	$\geq$ 95 % of PD	$\geq$ 90 % of PD
	$D_{50\%}$	$\pm$ 1 % of PD	-
PTV2	D_{98}	$\geq$ 95 % of PD	$\geq$ 90 % of PD
	D_{50}	-	$\pm$ 1 % of PD
	D_2	$\leq$ 105 % of PD	$\leq$ 107 % of PD

The doses prescribed to generate each radiotherapy treatment plan were based on those listed in table 6.3. This table indicates the two dose constraints used for the reduced dose part of the bladder (48, 52 or 56 Gy). For example, for the plans in which the bladder wall should receive 52 Gy, it was required that 50 % of the PTV received between 51.48 - 52.52 Gy, and that 98 % received $\geq$49.4 Gy (ideally) or, if that was not achievable then $\geq$46.8 Gy was acceptable. The three dose constraints for the dose escalated volume (PTV2) were calculated in the same way.

The reduction in dose to bladder wall was chosen so that the bladder wall dose of 52 Gy (as used in RAIDER), was compared with a lower (48 Gy) and higher (56 Gy) dose to investigate the effects of doing so. This was to assess the effect on TCP, and also regarding the ease of generation of the various dose distributions. Escalation doses to tumours were increased from the standard 64 Gy in steps of 4 Gy until a constraint was unachievable. The maximum dose possible was then individually determined to the nearest 1 Gy. For example, for anterior tumours the dose was increased from the standard 64 Gy to 68 Gy, then 72 Gy. This latter dose was not achievable and so 71 Gy was tested and found to be achievable.

Methodology used for generation of dose distributions (treatment planning)

The calculation of dose distributions for all 18 tumour volumes and multiple dose levels for low dose (PTV) and high dose PTV (PTV2) respectively was performed in RayStation. Within this TPS, the assessment of treatment plans can be performed via the use of clinical goals. These are essentially criteria to enable the user to rapidly ascertain whether the current dose distribution meets the required parameters (i.e. OAR and PTV dose ranges). The clinical goals are set via a maximum or minimum percentage or absolute dose to a percentage or absolute volume. For example 'no more than 2 % of the high dose PTV may receive $\geq$74.9 Gy'. If this requirement was not met by the dose distribution, it would be highlighted for the user. The clinical goals do not directly drive the optimization of the dose distribution; this is performed manually by the user via the selectable optimization functions. Table 6.1 informed the clinical goals used for all OARs, and table 6.3 those for the PTVs.

Export of DVHs and TCP calculations

Following creation of all dose distributions, the differential dose volume histograms (DVHs) were exported using a Python script in RayStation, for each plan in which all mandatory clinical goals had been met. This script generated a text file in which the number of voxels in the bladder wall and tumour receiving each dose was recorded. Doses were set to be binned in 0.1 cGy steps, and voxel volumes were $2 \times 2 \times 2$ mm^3. The files were used by the MATLAB code developed in Chapter 5 to calculate the expected TCP for a range of clonogen densities within the bladder wall, and with a density of 10^7 cm^{-3} within the simulated tumour. Both the RT-only and RCT Poisson-based TCP models were used to predict TCP, as discussed in Chapter 5.

6.4 Results and discussion

The results are discussed here for the following sections of work:

- Dose escalation using 10 mm margins (5 mm RAIDER plus 5 mm from work presented in chapter 4) and RT-only TCP calculations,
- Dose escalation using reduced (7 mm) margins (5 mm RAIDER plus 2 mm from chapter 4) and RT-only TCP calculations,
- All results following RCT TCP calculations.

6.4.1 Dose escalation for simulated tumours with 10 mm margins and RT-only TCP calculations

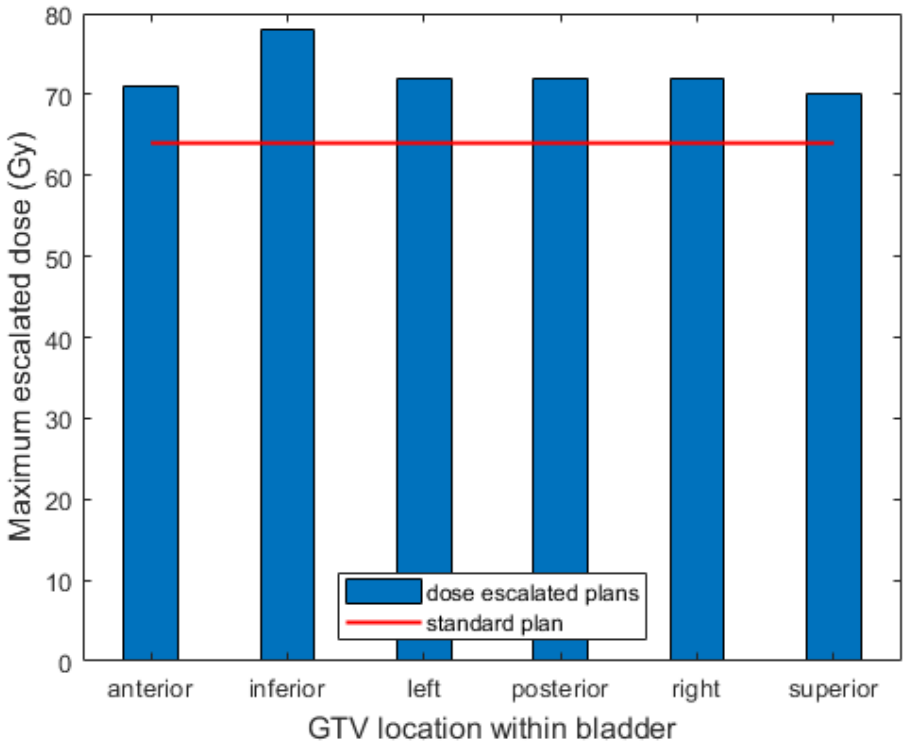

Figure 6.3: Effect of tumour (GTV) location within the bladder upon maximum achievable dose escalation. The standard plan is indicated by a red line for comparison.

Using margins of 10 mm in total for the GTV to high dose PTV expansion, a set of results was obtained in which the bladder wall was prescribed either 48, 52 or 56 Gy. PTV2, containing the simulated tumour, was prescribed increasing doses from the standard 64 Gy, in 4 Gy steps. When a dose became unachievable whilst meeting the required constraints, steps of 1 Gy were used to determine the highest possible dose for which all mandatory clinical goals remained achievable. It was found that this maximum dose was dependent on tumour location within the bladder, and was largely unaffected by either the reduced bladder dose value, or the volume of the tumour. Figure 6.3 shows this effect, with the maximum dose achieved for each tumour location, which remains constant for all bladder wall prescription doses and all tumour volumes. In this figure, the red line indicates for comparison, the dose prescribed in a standard plan of 64 Gy regardless of tumour location. It can be

seen that the dose escalation to anterior and superior tumours is more limited than for the inferior tumours in particular. This is due to the proximity of the bowel to tumour in the superior and anterior regions of the bladder, and so the dose to this OAR is higher for the same prescribed tumour dose. Nevertheless, these results show that dose escalation beyond the 70 Gy prescribed in RAIDER is possible if tumours are located anywhere other than in the most superior region of the bladder, and escalation to 78 Gy is possible for inferior tumours.

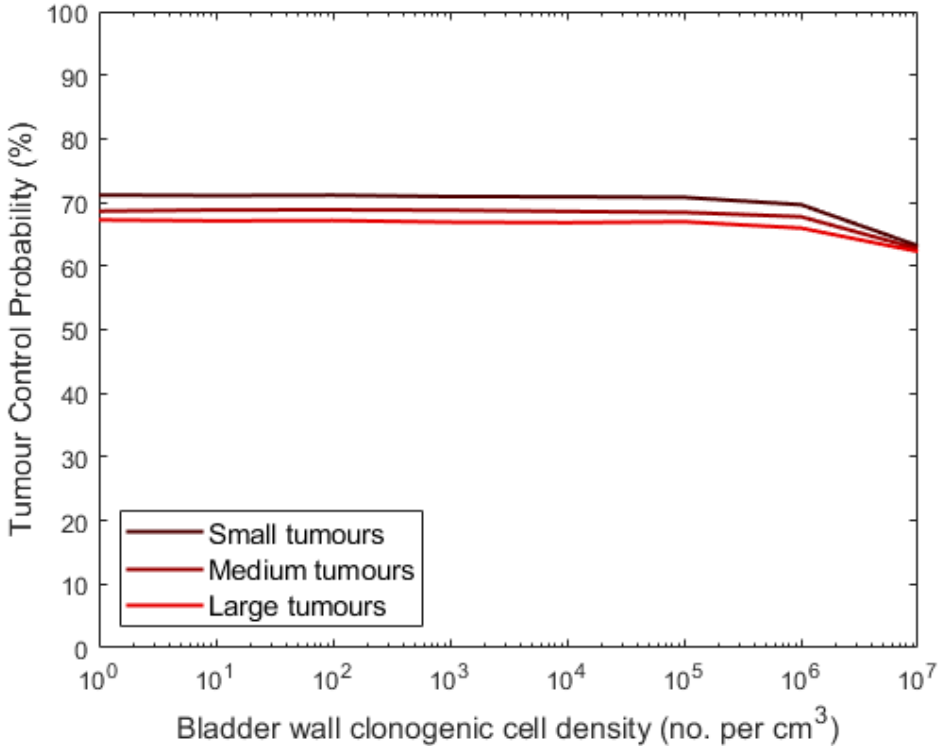

Figure 6.4: Effect of tumour volume on TCP using the standard technique of uniform irradiation of the whole bladder to 64 Gy in 32 fractions. For the standard dose distribution, the TCP is shown as a mean for small tumours (10 cm^3) in dark red, medium tumours (20 cm^3) in red and large tumours (30 cm^3) in pale red. Tumour clonogen density was kept constant at 10^7 cm^{-3}, whilst bladder wall clonogen density was varied from 10^0 - 10^7 cm^{-3} as the true value is not known but will lie within this range. The mean TCP for all small tumours (dark red) is consistently ~4% higher than for large tumours (pale red).

Figure 6.4 shows the effect of tumour volume on TCP when using the standard technique of uniform irradiation of the whole bladder to 64 Gy in 32 fractions.

The clonogen density within the tumour was kept constant (at 10^7 cm^{-3}, as previously in Chapter 5 and by Wright *et al.* [58]) in all cases. The graph shows the effect of varying the clonogen cell density within the bladder wall from 1 to 10^7 cm^{-3} in logarithmic steps. TCP can be seen to remain reasonably constant for all clonogen densities, and varies by around 4 % between small (dark red) and large (pale red) tumours. This was 71 % for small and 67 % for large tumours respectively on average for all tumour locations. The effect is due to the increased total number of clonogens within the larger tumour volume, even though the density remains constant. Only when the clonogen density in the bladder wall is 10^7 cm^{-3} does the TCP begin to decrease, although the effect is small (the average TCP for clonogen density of 10^7 cm^{-3} is 63 % across all volumes). This is probably due to a small proportion of the bladder wall receiving the lowest dose within the range permitted. Inspection of the DVH shows that 100 % of the bladder wall receives 63 Gy, 72.02 % receives 64 Gy, and 0.5 % receives 65 Gy. The $\sim$28 % of the bladder wall which receives slightly less than 64 Gy therefore begins to limit the TCP when the clonogen density is so high.

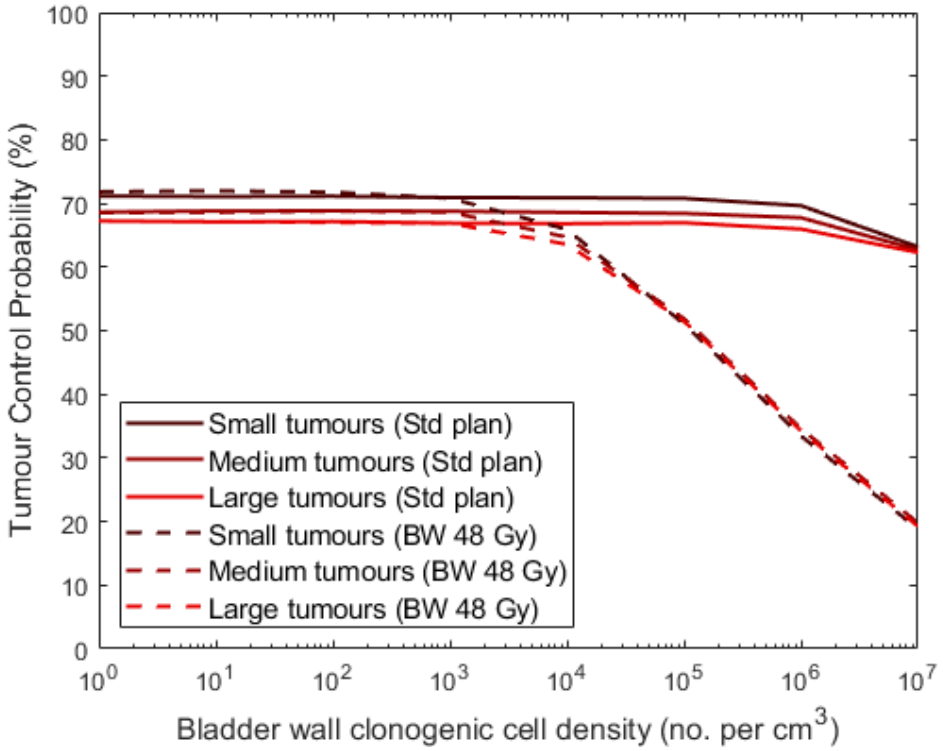

Figure 6.5: Effect of reducing dose to the bladder wall (BW) to 48 Gy (dashed lines), with dose to tumour maintained at 64 Gy and compared to the standard uniform dose of 64 Gy to the whole bladder (solid lines). All lines show the mean TCP calculated for the displayed tumour volumes. Tumour clonogen density was kept constant at 10^7 cm^{-3}, whilst bladder wall clonogen density was varied from 10^0 - 10^7 cm^{-3} as the true value is not known but will lie within this range.

Figure 6.5 shows the effect of reducing the planned dose to the bladder wall (BW) to 48 Gy whilst maintaining the 64 Gy prescription to the tumour (dashed lines), with the results for the standard plan from figure 6.4 also shown for comparison (solid lines). All lines show the mean TCP for the relevant tumour volume, as the effect is consistent for all tumour locations. In figure 6.5 the TCP predicted for the treatment plans with reduced dose to the bladder wall remains the same as for the standard plans, provided the bladder wall clonogen density is less than $\sim 10^4$ cm^{-3}. When the bladder wall clonogen density is greater than $\sim 10^4$ cm^{-3}, the TCP decreases significantly as it is dominated by the effect of the reduced dose to the bladder wall. The TCP in this latter region is also no longer affected by the size of the tumour, whereas for clonogen densities below 10^4 cm^{-3} the effect shown first in

figure 6.4 is maintained (where TCP is ∼4 % higher for small tumours than large tumours).

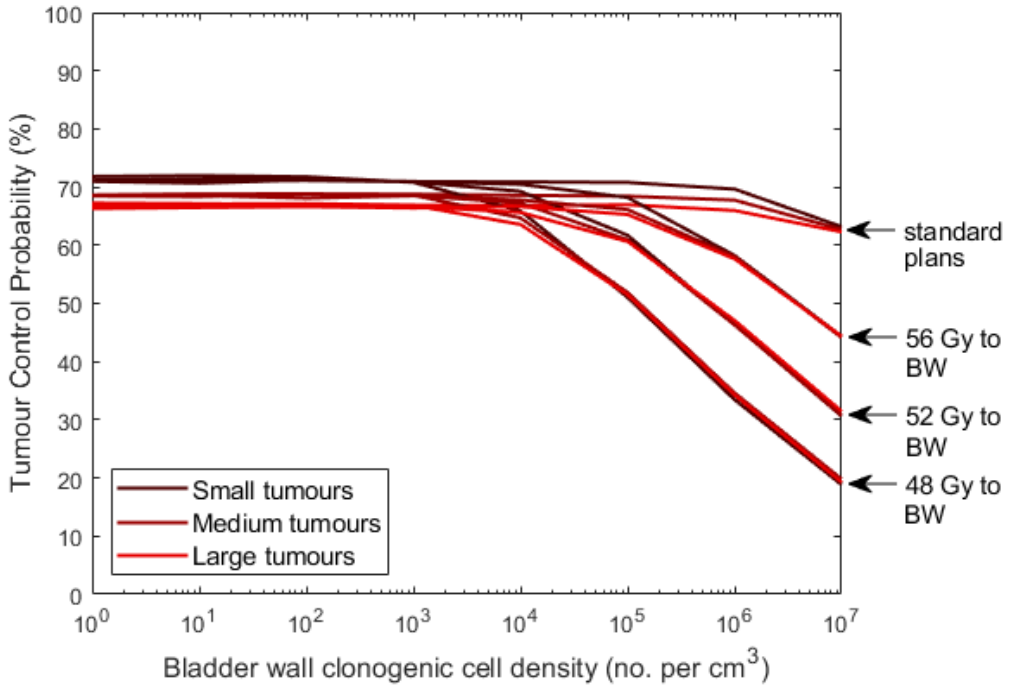

Figure 6.6: Effect of reducing dose to the bladder wall (BW) to 48, 52 or 56 Gy respectively, with dose to tumour maintained at 64 Gy and compared to the standard uniform dose of 64 Gy to the whole bladder. The effect of the reduced doses to bladder wall of 48, 52 or 56 Gy respectively is indicated via the annotations. Tumour clonogen density was kept constant at 10^7 cm^{-3}.

Figure 6.6 shows the effect of varying the magnitude of the permitted reduction in dose to the bladder wall, i.e. to 48 Gy, 52 Gy and 56 Gy respectively whilst maintaining the dose of 64 Gy to the tumour. As previously in figures 6.4 and 6.5, the tumour clonogen density was kept constant at 10^7 cm^{-3} whilst bladder wall clonogen density was varied from 10^0 - 10^7 cm^{-3} as the true value is not known but will lie within this range. It can be seen that these results follow the same pattern as seen in figures 6.4 and 6.5 regarding the effect of tumour volume. The effect dominates in the region where bladder wall clonogen cell density is below ∼10^4 cm^{-3} and TCP is ∼4% higher for small tumours than large tumours. Where the bladder wall clonogen density is above ∼10^4 cm^{-3} the magnitude of the prescribed dose to the bladder wall again begins to dominate, and the effect of tumour volume is no

longer visible. These effects occur at slightly greater clonogen densities for higher doses to bladder wall (i.e. $\sim 10^5$ cm^{-3} for the plans delivering 56 Gy to the bladder wall).

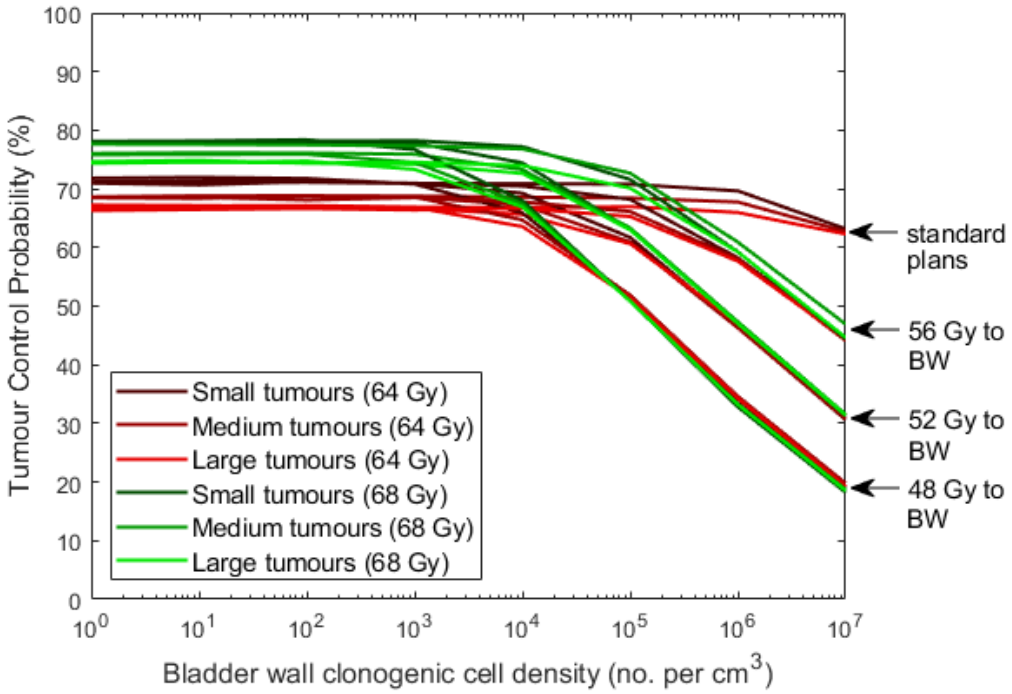

Figure 6.7: Effect of increase in tumour dose to 68 Gy compared with the 64 Gy plans. The effect of the reduced doses to bladder wall of 48, 52 or 56 Gy respectively is indicated via the annotations. Tumour clonogen density was kept constant at 10^7 cm^{-3} and bladder wall clonogen density was varied from 10^0 - 10^7 cm^{-3}.

Figure 6.7 highlights how increasing the dose to the tumour impacts upon the portion of the curve where clonogen density is below 10^4 cm^{-3}. In this graph, the TCP is seen to increase from 67-71 % at 64 Gy to 74-78 % at 68 Gy (in both cases the range in dose is due to the range in tumour volumes). The plateau value of TCP increases with the increase in dose as would be expected, but at greater clonogen densities in the bladder wall, the reduced dose to the bladder wall continues to dominate as already seen in figures 6.5 and 6.6. Similar TCP values are seen regardless of tumour dose and are instead dependent on bladder wall dose. Indeed, a similar pattern of results to those shown in figures 6.6 and 6.7 were found for all tumour dose escalation values. Figure 6.8 shows tumour doses of 64 Gy, 68 Gy and 78 Gy. The same pattern is seen in which the TCP plateau region when bladder

wall clonogen density is $<10^4$ cm^{-3} increases with tumour dose, and the effect of bladder wall dose is dominant where bladder wall clonogen density is $>10^4$ - 10^5 cm^{-3}.

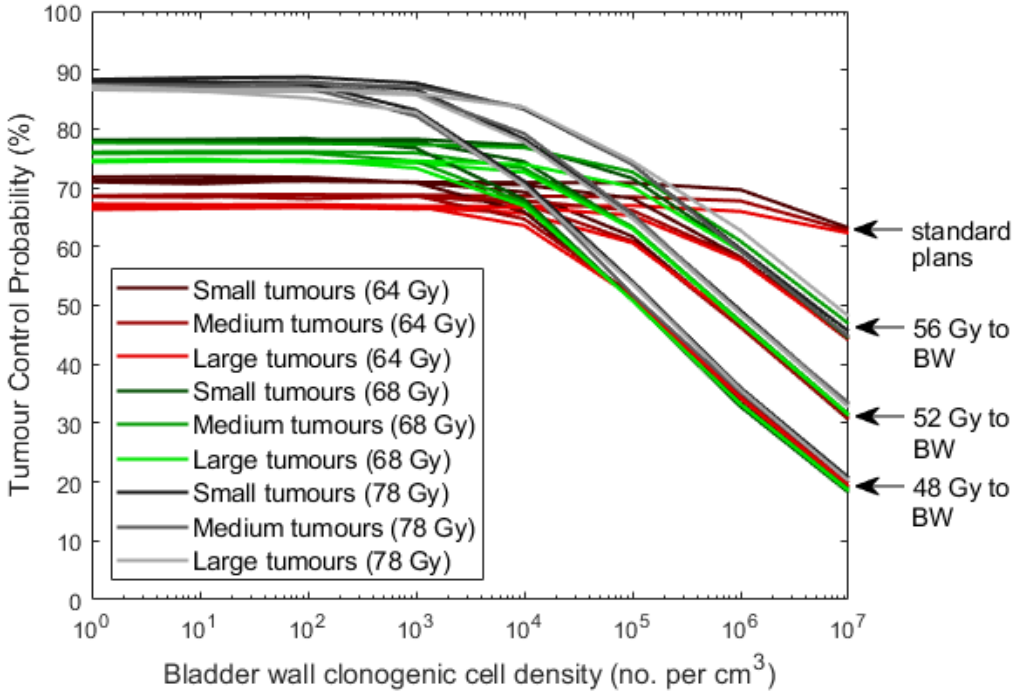

Figure 6.8: Tumour dose escalations of 64, 68 and 78 Gy. The effect of the reduced doses to bladder wall of 48, 52 or 56 Gy respectively is indicated via the annotations. Tumour clonogen density was kept constant at 10^7 cm^{-3}, and bladder wall clonogen density was varied from 10^0 - 10^7 cm^{-3}.

The increase in the predicted TCP within the plateau region with systematically escalated tumour dose is shown in figure 6.9. The points marked show the mean predicted TCP over the plateau region (bladder wall clonogen density 1 - 10^3 cm^{-3}) for the various tumour escalation doses investigated. Tumour escalation doses achieved were dependent on tumour location within the bladder, as seen in figure 6.3. For example, maximum tumour dose achievable for superior tumours of all volumes was limited to 70 Gy (owing to their proximity to the bowel). The corresponding predicted TCP using the RT-only Poisson model was 78.4 - 80.9 %, with the lower TCP value predicted for the large tumour and higher TCP predicted for the small tumour. Similarly, for the anterior tumours the maximum achievable dose was 71 Gy, for posterior, left and right tumours 72 Gy, and for inferior tumours

78 Gy. These doses were converted to EQD2 using equations 5.2 and 5.3 and can be seen in figure 6.9 plotted in relation to the RT-only Poisson model produced in chapter 5.

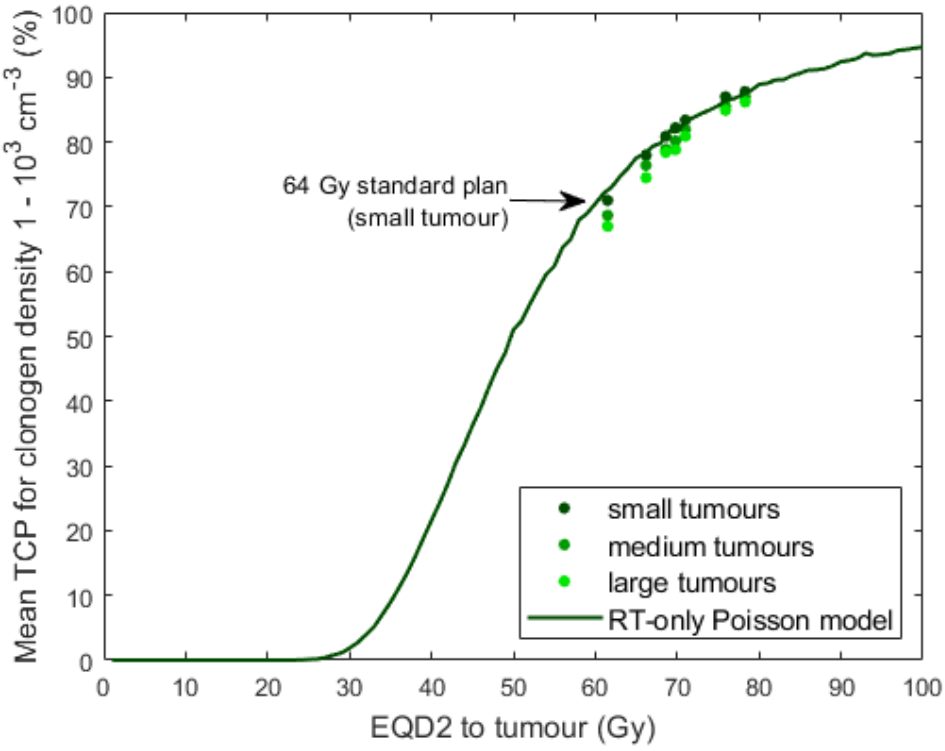

Figure 6.9: Mean predicted TCP using the RT-only Poisson model for small, medium and large tumours for the range of doses with EQD2 of 61.5 - 78.3 Gy (corresponding to prescribed doses 64 - 78 Gy) and compared with the RT-only Poisson model curve developed in chapter 5.

Figure 6.9 shows that the results predicted by the use of the RT-only Poisson model behave as expected. For standard treatment plans generated for small tumours (i.e. post-TURBT with a volume of 10 cm^3) receiving 64 Gy in 32 fractions, the model predicts a TCP of 71.0 %, which agrees well with the RT-only curve itself (TCP of 72.1 % at 61.5 Gy EQD2, i.e. 64 Gy/32 fractions). As planned doses were increased to the small tumours, the predictions remained along the RT-only curve (indeed, the point at EQD2 61.5 Gy showed the maximum difference of 2.1 %, with a mean difference of 0.1 % across all points). These small differences are likely to originate from two sources. Firstly, both the RT-only curve itself and the data-points plotted, are generated using calculations in which a Gaussian is sampled 10^4

times. Therefore there may be limited variability in the results obtained between one calculation and another (this was ∼0.2 % when tested).

Secondly, and more importantly, the individual voxels of the treatment plans will receive slightly different doses than the prescription (planned) dose. The treatment planning method used allowed specified proportions of a volume to receive certain ranges in dose via the setting of clinical goals. For example, where tumour dose escalation to 70 Gy was required, the dose to 50 % of the tumour PTV was set to lie within ± 1 % of 70 Gy (i.e. 69.3 - 70.7 Gy). In addition, the dose to 98 % of this volume must be ≥ 90 % of 70 Gy (63 Gy) and no more than 2 % of the volume is to receive ≥ 74.9 Gy. Similar ranges of acceptable doses were used to generate all of the plans (as discussed in section 6.2 and according to the values quoted in table 6.3). This variation in the voxel doses underlying the TCP predictions will cause small deviations from the values expected, when compared with the quoted prescription dose alone.

At all points marked on figure 6.9, the predicted TCP for large tumours remains ∼2 - 4 % lower than for the small tumours (and similarly below the RT-only curve which assumed a post-TURBT tumour volume of 10 cm^3).

Bladder wall prescribed dose

The results presented in figures 6.5 to 6.9 indicate that the reduced dose to bladder wall (of 48, 52 or 56 Gy), only impacts upon the predicted TCP if clonogen cell density in the bladder wall lies above $\sim 10^4$ cm^{-3}. However, in terms of the ability to escalate dose to the tumour, the prescribed bladder wall dose is not particularly important, as these plans were achievable regardless (it is noted, however, that the 52 Gy plans were more readily achievable).

Tumour location within the bladder and limiting OARs

When tumours were located in the superior region of the bladder, it was not possible to escalate doses above 70 Gy (as shown in figure 6.3). This was the case regardless of the dose prescribed to the bladder wall. The dose was limited by the requirement to deliver less than 70 Gy to a maximum volume of 10 cm^3 of the bowel, although in general for most plans the other dose constraints from table 6.1 were still achievable. Similar effects were found for anterior tumours of all volumes when the dose to tumour was escalated beyond 71 Gy. These results are unsurprising, as the bowel lies closest to the superior and anterior portions of the bladder. Figure 6.10 shows how close the bowel (shown in purple) lies in relation to a simulated superior tumour

(shown in bright green). PTV2 (dark green), which contains the tumour, overlaps with the bowel.

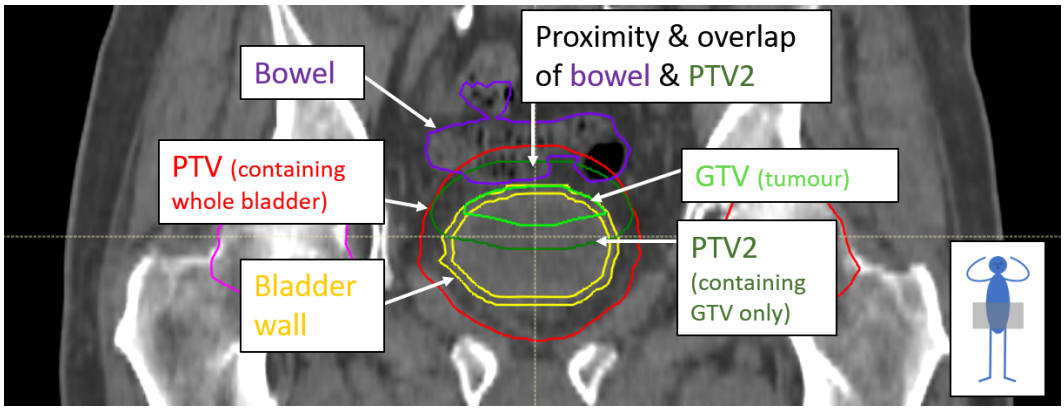

Figure 6.10: The location of a superior tumour close to the bowel results in lower achievable maximum dose escalations than for tumours in other locations within the bladder.

For tumours located in the posterior, left and right regions of the bladder, the maximum dose escalation achieved was 72 Gy. Again, this was regardless of tumour volume or dose prescribed to the bladder wall. As previously discussed for superior and anterior tumours, the limitation was the dose constraint of 70 Gy to $<$10 cm^3 of the bowel. These tumours were able to receive a slightly increased dose than the superior and anterior tumours before this requirement was breached, as they are further from the bowel.

Further illustrating the effect of proximity to the bowel, dose escalation to 78 Gy was achievable for the inferior tumours before dose constraints became unachievable. These tumours lie the furthest from the bowel, which lies superior and anterior of the bladder. For these dose distributions, the limiting dose constraint was that of 1 cm^3 of all normal tissue ('body - PTV' in table 6.1) to not receive more than 110 % of the prescription dose. This had been limited to a maximum of 77 Gy as is used within RAIDER.

These results show that the potentially achievable TCP varied between 67 - 71 % if there was no dose escalation to the GTV (i.e. for a standard plan with a uniform 64 Gy to the whole bladder), to 86 - 88 % for inferior tumours escalated to 78 Gy. Doses (and hence TCP) for tumours located within other regions of the bladder fell within this range, as can be seen in sections *'Tumours with 10 mm GTV to PTV margins'* and *'Standard plan'* within table 6.4.

Overall, these results show that the current clinical trials such as RAIDER,

Table 6.4: The maximum dose to which tumours located in the various regions of the bladder were escalated whilst continuing to meet all mandatory clinical goals. Also shown is the corresponding calculated TCP using the RT-only Poisson TCP model developed in chapter 5. Results for plans with reduced GTV to PTV margins and for tumours with reduced superior extent are included. The increases in TCP are shown between small tumours compared to the standard plan. All TCP values shown were calculated using the plateau region of TCP averaged over bladder wall clonogen density 10^0 - 10^3 cm^{-3}.

Tumour Location	**Maximum Prescribed Dose (Gy)**	**RT-only TCP (%)** large - small tumour (increase)
Standard plan for comparison		
Any	64	67.0 - 71.0 (N/A)
Tumours with 10 mm GTV to PTV margins		
Anterior	71	78.8 - 82.2 (11.8)
Posterior	72	
Left	72	80.9 - 83.4 (13.9)
Right	72	
Superior	70	78.4 - 80.9 (11.4)
Inferior	78	86.2 - 87.8 (19.2)
Tumours with reduced GTV to PTV margins (7 mm)		
Anterior	73	
Posterior	73	81.9 - 84.9 (14.9)
Left	73	
Superior	71	79.5 - 82.8 (12.5)
Inferior	84	90.0 - 91.2 (23.0)
Tumours with reduced superior extent and 7 mm margins		
Posterior	74	80.9 - 85.6 (13.9)
Left†	74	83.5 (16.5)

†only medium sized tumour investigated in this case.

in which doses to tumour volume are escalated to 70 Gy, are perhaps the realistic limit of current techniques for superior and anterior tumours. However, tumours located in other parts of the bladder may be escalated to higher doses whilst meeting the same OAR dose constraints, producing greater increases in TCP. In particular, inferior tumours could be escalated furthest, with doses of 78 Gy producing increased TCPs of 86 - 88 % compared to 67 - 71 % for standard plans of 64 Gy.

6.4.2 Dose escalation for simulated tumours with 7 mm margins and RT-only TCP calculations

Initial work presented in section 6.4.1 used the original estimate from chapter 4 of 5 mm for geometrical distortion in DW-MRI data. This was interpreted as an uncertainty in image positional information from registered DW-MRI to CT of up to 5 mm, hence resulting in a total GTV to PTV (PTV2) margin of 10 mm. The additional 5 mm was that shown in table 6.2 and taken from RAIDER recommendations [9] to account for variations in bladder position and movement.

The work using phantom II in Chapter 4 sections 4.2.7 - 4.2.9 showed that margins of 2 mm can account for the residual positional uncertainties involved in the use of DW-MRI for imaging bladder tumours, if additional image acquisition and processing is performed using software such as FSL. Therefore, a further subset of work was repeated using GTV to PTV margins of 7 mm (where 2 mm accounts for DW-MRI distortion and the previous margin of 5 mm from the RAIDER clinical trial accounts for bladder variations). The results of this work are shown in the third section of table 6.4 (*'Tumours with reduced GTV to PTV margins (7 mm)'*). They show that the dose to which each tumour can be escalated is slightly increased with the margin reduction, as might be expected. The dose increases are mostly very modest (70 to 71 Gy for superior tumours, 71 to 73 Gy for anterior tumours, and 72 to 73 Gy for posterior and left tumours)[1]. However, the final dose achieved for inferior tumours of all volumes was 84 Gy before the normal tissue dose constraint of <1 cm^3 to receive 77 Gy was breached. This is a very high dose and greater than that used clinically for most treatment sites, however it does serve to illustrate the degree to which the location of the tumour in the bladder is the central issue of importance in dose escalation of bladder tumours.

[1] As previous results for all lateral tumours were equivalent, only the left tumours were repeated with smaller margins.

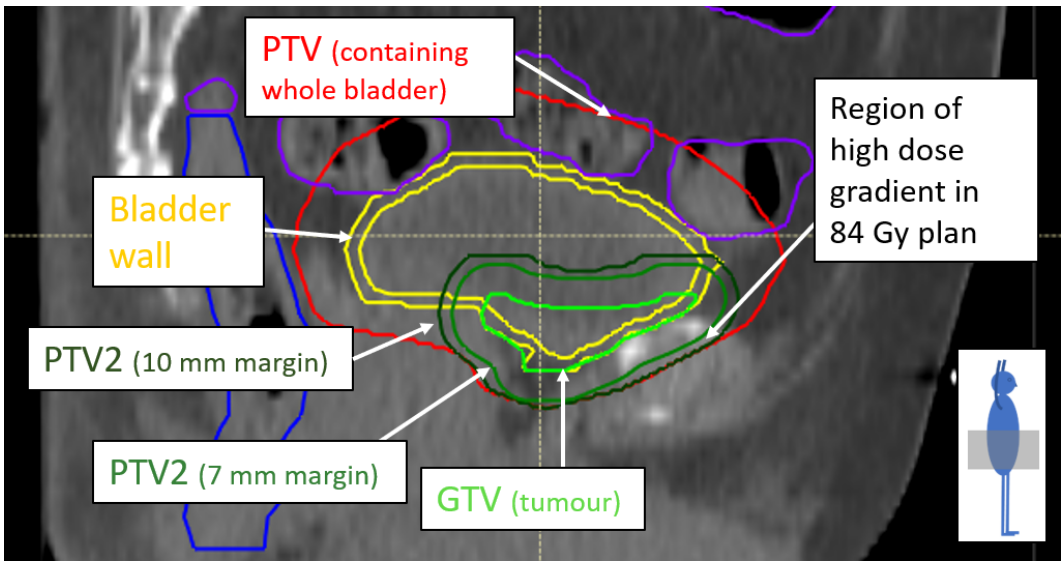

Figure 6.11: Inferior tumour shown in bright green, with mid-green PTV2 (7 mm margin) and dark green PTV2 (10 mm margin). The indicated region falling between PTV2 (7 mm margin) and the red PTV (containing whole bladder) is where high dose gradients are located in the 84 Gy plans.

Figure 6.11 indicates the reason for the large increase in dose that was possible for the inferior plans with reduced GTV to PTV2 margins. This figure shows a sagittal view of the bladder (yellow), containing simulated inferior tumour (bright green). The two PTV2s used are shown in dark green (10 mm margin) and mid-green (7 mm margin) respectively. The indicated region lying between PTV2 (7 mm margin) and the PTV covering the whole bladder (shown in red) allows a rapid decrease in dose to occur within a PTV region, rather than outside it (as when the 10 mm margin is used). Figure 6.12 compares the generated dose distributions of (a) the 78 Gy plan using a 10 mm margin with the whole bladder shown, and (b) the same 78 Gy plan shown magnified with just the high dose region, and (c) high dose region only of 84 Gy plan using the 7 mm margin. The region of high dose gradient in (b) occurs just outside the whole bladder PTV (red), rather than just inside as in (c). This difference was the reason that the normal tissue dose constraint of <1 cm^3 to receive 77 Gy was achievable at a much higher prescribed dose for the reduced GTV margin.

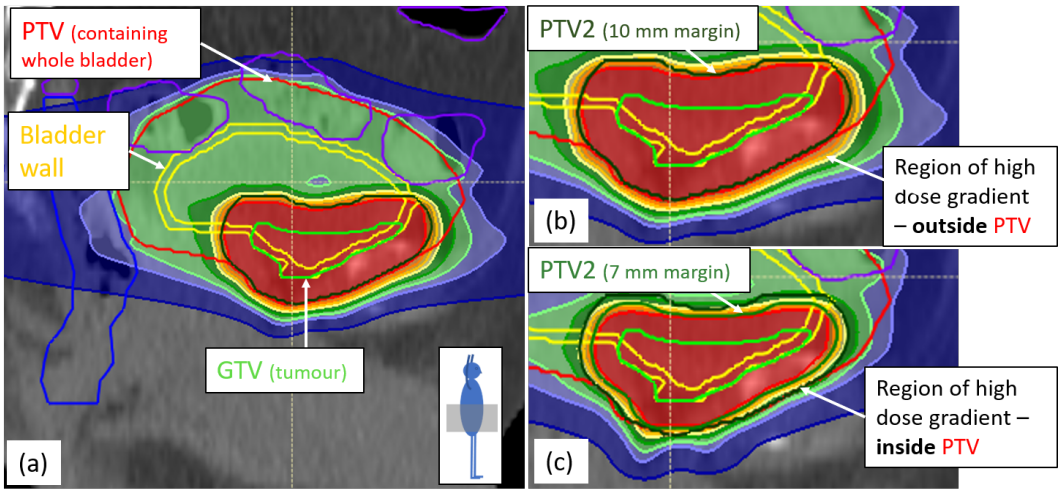

Figure 6.12: (a) 78 Gy plan to inferior tumour (whole bladder shown), (b) 78 Gy plan to inferior tumour (only high dose region shown magnified), (c) 84 Gy plan to the same inferior tumour also magnified. Inferior tumour shown in bright green, with mid-green PTV2 (7 mm margin) and dark green PTV2 (10 mm margin). The indicated region falling between PTV2 (7 mm margin) and the red PTV (containing whole bladder) contains a high dose gradient in (c), but this gradient is outside the whole bladder PTV in (b). The effect leads to a higher achievable dose to PTV2 using 7 mm margins before the normal tissue dose constraint of <1 cm^3 to receive 77 Gy is breached.

Tumour simulation and superior extent of tumours

Owing to the similar results for superior, anterior, posterior and lateral tumours, with very different results for the inferior tumours, the methodology used for simulating tumours was reassessed. It was noted that the simulated tumours had been produced such that the volumes, although located in the required regions of the bladder tended to extend towards the superior-inferior directions for the anterior, posterior and lateral tumours. As the superior-inferior location of the tumours had been found to be so influential in the dose to which the high dose PTV might be escalated, a subset of results were repeated for posterior and left GTVs, with reduced extent in the superior direction. Anterior tumours were themselves already located very close to the bowel regardless of superior extent, and so were not investigated further. All previous results for left and right tumours were equivalent and therefore only left tumours were repeated. In these further tests, the tumour volumes were altered to reposition the most superior 1 cm onto more inferior CT

slices, as illustrated in figure 6.13. In this figure a left tumour is shown as originally simulated in green, and after the most superior 1 cm was removed and added to the inferior edge (purple).

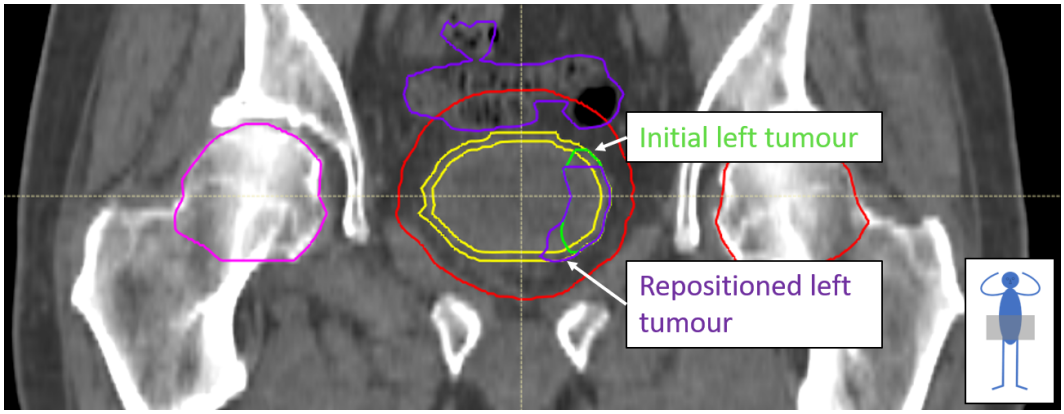

Figure 6.13: Left tumour shown re-simulated with reduced superior extent. Original location shown in green, with re-simulated tumour shown in purple.

The results of this repeated subset of plans are shown in the final section of table 6.4 *'Tumours with reduced superior extent and 7 mm margins'* in which it can be seen that doses of 74 Gy were achieved for all tested plans and GTVs, resulting in TCPs of 80 - 84 %. This meant that the maximum tumour escalation doses of 72 Gy found for posterior, left and right tumours are very dependent upon the degree to which those tumours extend superiorly, and hence their proximity to the bowel. This would of course also vary between patients owing to variations in internal anatomy. The original left tumours were approximately 0.2 cm from the most inferior portions of the bowel, whereas in these latter plans with altered GTVs, the left tumours were approximately 0.7 cm from the most inferior extent of the bowel. The equivalent figures for the posterior tumours were 0 cm and 0.3 cm respectively.

6.4.3 TCP calculations using the RCT Poisson model

All results discussed so far have referred only to those produced using the RT-only Poisson model to calculate expected TCP. This section discusses the effect using the RCT Poisson model instead. The model sought to provide a best estimate for the expected increased TCP when patient treatment involved the use of chemotherapy in addition to radiotherapy. The same dose distributions were used as in sections 6.4.1 and 6.4.2, but TCP calculations were performed using the RCT model.

The trends seen using the RCT model were similar to those already discussed regarding the RT-only model, but with higher calculated TCP as would be expected. For example, in figure 6.14 the results of tumour doses of 64 Gy and either 48, 52 or 56 Gy planned to the bladder wall, along with those from the standard plan show patterns similar to those seen in figure 6.6. The plateau values using the RCT model are 77-80 % compared to 67-71 % for the RT-only model. As before, the higher TCP values within the range relate to small tumours and the lower to the large tumours. The TCPs seen for bladder wall clonogen densities of 10^5 - 10^7 cm^{-3} follow the same pattern, with the bladder wall doses of 48, 52 or 56 Gy dominating the TCP although the absolute values of TCP are ∼10 % higher using the RCT model.

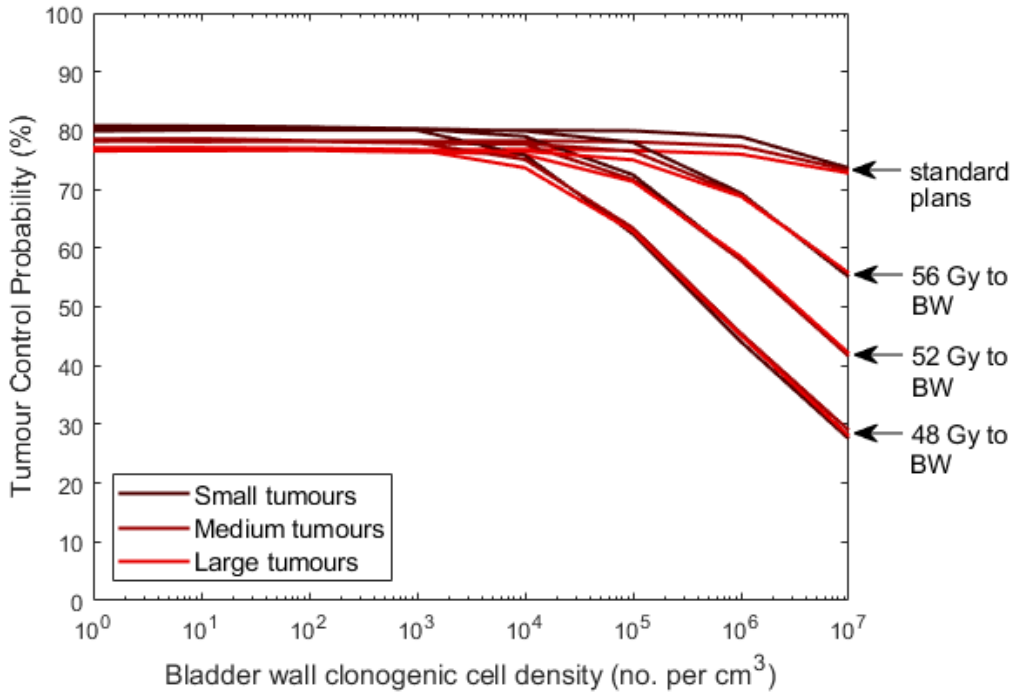

Figure 6.14: Effect of reducing bladder wall (BW) dose to 48, 52 or 56 Gy respectively, with dose to tumour maintained at 64 Gy and compared to the standard uniform dose of 64 Gy to the whole bladder (see annotations). TCP was calculated using the RCT Poisson model and tumour clonogen density was kept constant at 10^7 cm^{-3}, whilst bladder wall clonogen density was varied from 10^0 - 10^7 cm^{-3}.

The effect of increasing the tumour dose from 64 Gy to 78 Gy was again seen to affect the plateau region of the curves, and can be seen in figure 6.15.

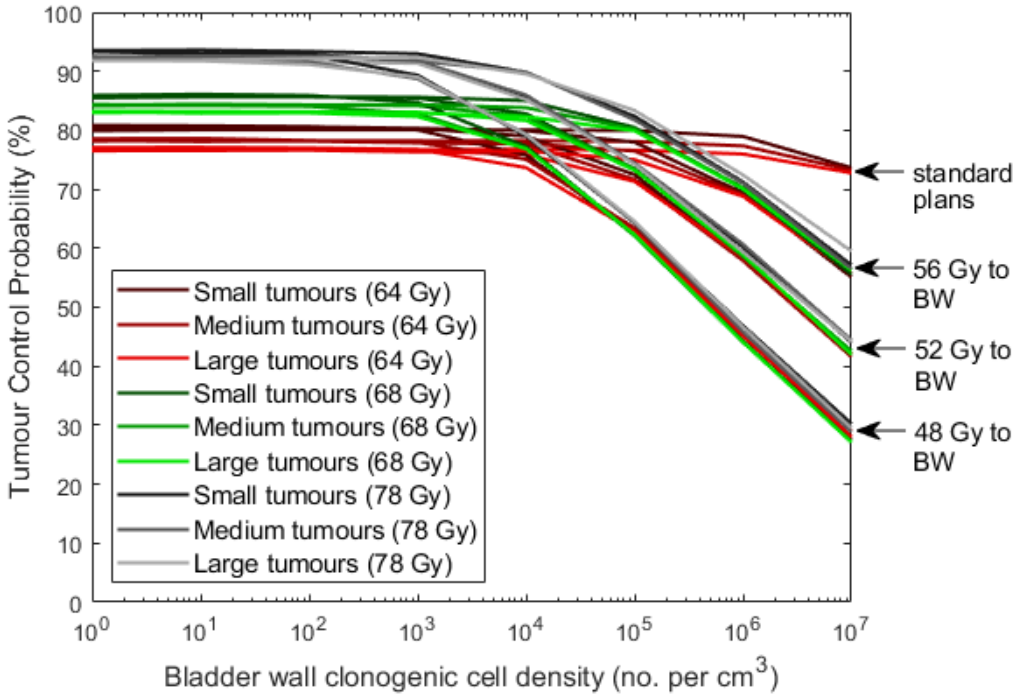

Figure 6.15: Effect of increase in tumour dose from 64 to 68 and 78 Gy compared with the standard plan (64 Gy) (see annotations). TCP was calculated using the RCT Poisson model and tumour clonogen density was kept constant at 10^7 cm^{-3}, whilst bladder wall clonogen density was varied from 10^0 - 10^7 cm^{-3}.

Figure 6.16 shows the impact on dose escalation beyond 68 Gy on the TCP in the region with bladder wall clonogen density of 1 - 10^3 cm^{-3} using both the RT-only model (as seen in figure 6.9) and RCT Poisson models. As previously, doses were converted to EQD2 using equations 5.2 and 5.3. The TCPs calculated for small tumours using the RCT model follow the original RCT curve produced in chapter 5 as would be expected. The largest difference between the datapoints plotted and the original RCT curve is 1.8 % and the mean difference is 0.1 %.

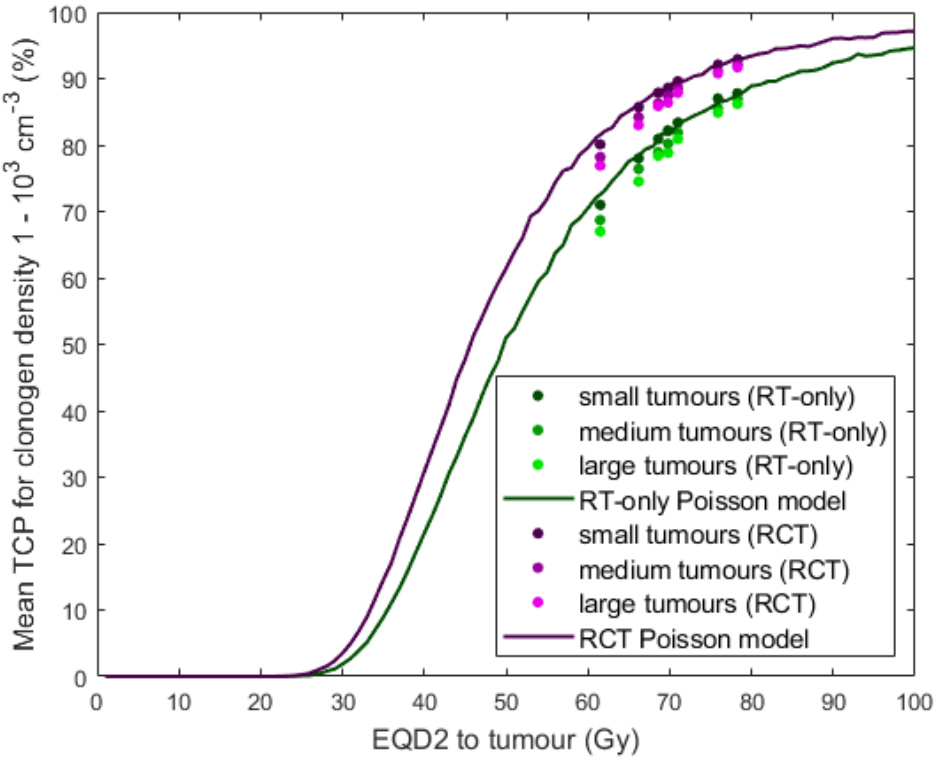

Figure 6.16: Mean TCP predicted using the RT-only and RCT Poisson models for small, medium and large tumours for the range of doses with EQD2 of 61.5 - 78.3 Gy (corresponding to prescription doses 64 - 78 Gy) and compared with both the RT-only and RCT Poisson model curves.

A summary of all the data presented in this chapter is given in table 6.5, which shows the maximum doses achievable within the various regions of the bladder, and the corresponding calculated TCPs using both the RT-only and RCT Poisson TCP models. The effects of reducing the margins required to accurately map tumour location from DW-MRI to CT from 5 mm to 2 mm is shown in the sections 'Tumours with 10 mm GTV to PTV margins' and 'Tumours with reduced GTV to PTV margins (i.e. 7 mm)' respectively. The effect of reducing the superior extent of tumours located in the posterior and left regions of the bladder are shown in the section 'Tumours with reduced superior extent and 7 mm margins'.

Table 6.5 shows all results for TCPs calculated using the RCT model alongside those already presented in table 6.4 using the RT-only model. This shows that the TCP calculated using the RT-only model for standard plans and is 67.0 - 71.0 %, which rises to 76.9 - 80.1 % using the RCT model. For the tumours which received

Table 6.5: The maximum dose to which tumours located in the various regions of the bladder were escalated whilst continuing to meet all mandatory clinical goals. Also shown is the corresponding calculated TCP using both TCP models developed in chapter 5. Results for plans with reduced GTV to PTV margins and for re-positioned tumours (reduced superior extent) are included. The increases in TCP are shown between small tumours compared to the standard plan and using the same TCP model. All TCP values shown were calculated using the plateau region of TCP averaged over bladder wall clonogen density 10^0 - 10^3 cm^{-3}.

Tumour Location	**Maximum Prescribed Dose (Gy)**	**RT-only TCP (%)** large - small tumour (increase)	**RCT TCP (%)** large - small tumour (increase)
Standard plan for comparison			
Any	64	67.0 - 71.0 (N/A)	76.9 - 80.1 (N/A)
Tumours with 10 mm GTV to PTV margins			
Anterior	71	78.8 - 82.2 (11.8)	86.4 - 88.6 (9.5)
Posterior	72		
Left	72	80.9 - 83.4 (13.9)	87.9 - 89.6 (11.0)
Right	72		
Superior	70	78.4 - 80.9 (11.4)	85.9 - 87.9 (9.0)
Inferior	78	86.2 - 87.8 (19.2)	91.7 - 92.9 (14.8)
Tumours with reduced GTV to PTV margins (i.e. 7 mm)			
Anterior	73		
Posterior	73	81.9 - 84.9 (14.9)	88.8 - 90.8 (11.9)
Left	73		
Superior	71	79.5 - 82.8 (12.5)	86.8 - 89.2 (9.9)
Inferior	84	90.0 - 91.2 (23.0)	94.2 - 95.0 (17.3)
Tumours with reduced superior extent and 7 mm margins			
Posterior	74	80.9 - 85.6 (13.9)	87.9 - 91.5 (11.0)
Left[†]	74	83.5 (16.5)	90.0 (13.1)

[†]only medium sized tumour investigated in this case.

the lowest dose escalation (superior tumours), these results rose to 78.4 - 80.9 % and 85.9 - 87.9 % respectively using the RCT model. For tumours located in the left, right or posterior portions of the bladder, the results using the RT-only and RCT models were 80.9 - 83.4 % and 87.9 - 89.6 % respectively, although these were quite variable, depending both upon the GTV-PTV margin used and the degree to which the tumours were allowed to extend in the superior direction.

When the margins used to create the high dose PTVs from the GTVs were reduced from 10 mm to 7 mm, the dose could be increased by a further 1 Gy whilst meeting the same clinical goals. This led to TCPs of 81.9 - 84.9 % and 87.9 - 89.6 % using the RT-only and RCT models respectively. A subset of these volumes (posterior small, medium and large, and left medium) were also adjusted to extend 1 cm less far in the superior direction, with the volume kept constant (i.e. repositioned over the other CT slices). These results showed that dose could again be escalated by a further 1 Gy (74 Gy total), producing calculated TCPs of 80.9 - 85.6 % and 87.9 - 91.5 % for the RT-only and RCT models respectively.

The highest TCP was consistently found for the inferior tumours, as the doses to which they could be escalated were the greatest. For GTV to PTV margins of 10 mm these doses were 78 Gy resulting in TCPs of 86.2 - 87.8 % and 91.7 - 92.9 % using the RT-only and RCT models respectively. When the GTV to PTV margin was reduced to 7 mm, the achievable dose escalation rose to 84 Gy resulting in increases in TCP to 90.0 - 91.2 % and 94.2 - 95.0 % respectively (although it is recognised that this is above the doses usually used clinically).

6.4.4 Toxicity

For OARs such as the femoral heads, the doses received even with these high dose escalations are still quite low, as the dose to the rest of the bladder is reduced compared with the standard technique. For example, the dose to 50% of the femoral heads was consistently within the range 18.5 - 25.5 Gy for all plans including standard and dose escalated (84 Gy) plans. This compares well with the maximum accepted in table 6.1 of 50 % of femoral heads to receive <50 Gy.

The doses which were most limiting to dose escalation were twofold:

1. Bowel: Maximum volume receiving 70 Gy (where the optimal constraint was 0 cm^3 and mandatory was 10 cm^3)

2. Normal tissue: No more than 1 cm^3 of the volume Body - PTV should receive 73.5 Gy (optimal) or 77 Gy (mandatory).

Dose escalation was limited by (1) for superior, anterior, posterior and lateral tumours. For inferior tumours the limitation was (2).

Owing to the large (>200) number of plans generated for the results presented in this chapter, the plans were unlikely to be of the high standard required for clinical use, particularly as parameters other than purely meeting dose constraints are considered when determining clinical acceptability. For example, the visible appearance of the dose distribution and the presence of any regions of high dose outside the target volume are considered, and these aspects were not part of the analysis included here. It is also arguable that these plans would not be truly 'isotoxic', that is that the likelihood of complications arising from treatment would not necessarily be the same for all discussed dose distributions including the standard plan, as there is such variation in the location of doses delivered. Nevertheless, all of the plans met the basic requirements for plans produced within a current clinical trial, and the general trends discussed remain.

Doses of 78 Gy (as found to be achievable for inferior tumours), are high compared with general clinical fractionation schemes within the pelvis. Standard fractionation schemes for the prostate, for example, are 60 Gy in 20 fractions or 74 Gy in 37 fractions. Therefore, although this dose appeared feasible from the perspective of meeting OAR dose constraints, from the perspective of clinical use, further work would be required to establish safety and toxicity at lower doses first.

6.5 Summary and conclusions

Dose escalation to a partial bladder volume incorporating the GTV plus margin could increase local control for MIBC by 9.0 - 19.2 % compared to the standard uniform treatment depending on tumour location and TCP model used for calculation. The increase is lowest for superior tumours and when using the RCT model (although for the latter the absolute values of TCP achieved are higher).

Chapter 7

Clinical verification and feasibility study

7.1 Introduction

In the previous chapter we saw that it was possible to escalate radiotherapy doses to some bladder tumours in such a way as to significantly increase the predicted TCP. This was possible without requiring the surrounding organs at risk to receive greater doses than would be acceptable within the RAIDER clinical trial. Ideally, the next step of work would be to determine the feasibility of delivery of such escalated doses in practice. This is not a straightforward task, however, as shall be discussed within this chapter.

The work reported here uses patient CBCTs acquired at the time of (standard) bladder radiotherapy delivery to infer the doses that would have been received had the escalated doses been delivered instead. It is recognised that there are many caveats in terms of the ability to use these images for this purpose, as shall be discussed. Nevertheless, this work is in essence a blueprint using the technology currently available to highlight the methodology required for future work using improved technology. Such technology would include the use of MR via an MR-linac rather than CBCT, to enable accurate assessment of soft tissue structures such as the bladder and bowel immediately prior to treatment delivery.

7.2 Calculation of accrued doses on CBCTs

Within the RayStation TPS there is a module ('Treatment Adaptation') which is intended to enable assessment of doses delivered to the patient based on CBCT(s)

acquired of that patient. The clinical use of this module largely concerns changes to the patient anatomy (for example weight loss) during the course of radiotherapy treatment. If these concerns arise, then a CBCT may be imported into the TPS and the planned dose distribution recalculated using the image intensities (HU) within the CBCT rather than the original planning CT. A DR is used to map the CBCT to the original planning CT, and then the doses calculated using the CBCT can also be mapped back to the original planning CT and doses to the various organs compared with those intended.

There are several sources of uncertainty involved in the standard clinical use of this technique:

- The increased scatter due to the cone-beam acquisition of the CBCTs means that the HU on CBCT images are not as accurate as for CT. This is accommodated partially within RayStation by assigning bulk densities to air, lung, adipose tissue, soft tissue and bone which are then used within dose calculations.

- The increased scatter and resulting poorer image quality of the CBCTs means that it is more difficult (and sometimes not possible) to distinguish soft tissue details corresponding to delineated organs on CT.

- Owing to these difficulties in determining soft tissue details and also limitations of DR algorithms, knowing the location of OARs and corresponding doses they receive is subject to uncertainty.

In clinical use at the centre this work was performed at, this technique is used only for assessment of absolute doses for tumours treated within the head and neck. In particular, the dose to the PTV is checked, and locations of the relevant OARs (spinal cord and brainstem) with respect to the PTV are assessed, along with the calculated delivered dose to these OARs. As the uncertainties listed above are greater within the pelvis, this technique is only currently routinely used for the assessment of relative dose differences within the pelvis.

Although the intended use of the Treatment Adaptation module is for mid-treatment assessment (and hence resulting treatment adaptation), it is also possible to use the toolkit to assess the doses that would have been received had other dose distributions been delivered instead. It is possible to accumulate doses on multiple CBCTs and then sum these doses to infer the delivered dose distribution from the whole treatment course, in order to compare with the original planned dose distribution. This is the approach that has been taken within this chapter, in order to infer the feasibility of delivery of the technique.

7.3 Methods of data extraction and analysis

Daily CBCT images were acquired for the patient whose planning CT was used for the work reported in chapter 6 during the course of their standard treatment. These images were imported into RayStation TPS, and RR was performed using the shifts applied at the time of treatment delivery by the radiographers based on their pre-treatment image registration.

As the CBCTs were acquired using smaller FOVs than the planning CT, some geometrical tools were used to recreate the external contour of the patient for the missing parts of the patient anatomy. These volumes were set to the density of water. DRs were created from each CBCT to the CT; this used the hybrid DR and included the use of image intensities (i.e. this is the expected clinical use of the algorithm studied in chapter 4).

This resulted in 10 DRs of daily CBCTs to the planning CT, with mapped delineations of all organs including the bladder, and simulated internal tumours. Delivered doses were then calculated on each CBCT and deformed back using the DRs to the planning CT for comparison with the planned dose distribution. This was performed for a subset of treatment plans - these were chosen to be representative of the variations covered in chapter 6. Therefore medium volume tumours and a planned dose of 52 Gy to the whole bladder were used in all cases (other than the standard plan), as neither tumour volume nor dose to the rest of the bladder had significantly affected the escalation dose achievable and these were the middle values used. The extremes of findings in chapter 6 were included, i.e. inferior and superior tumours with the relevant maximum achievable doses in each case (i.e. 78 Gy and 70 Gy respectively). As the results for superior and anterior were very similar, this was not repeated for an anterior tumour, but a posterior tumour with reduced margins (7 mm) was also tested as representative of right/left and posterior tumours (the results of which were similar in chapter 6). Therefore the following plans were used in addition to the standard plan of 64 Gy to the whole bladder, to accumulate dose on CBCTs:

- Superior medium tumour - 70 Gy planned to tumour and 52 Gy to whole bladder,
- Inferior medium tumour - 78 Gy planned to tumour and 52 Gy to whole bladder,
- Posterior medium tumour with reduced (7 mm) margins - 73 Gy to tumour and 52 Gy to bladder.

The DVHs for these inferred dose distributions were extracted and used for calculation of delivered TCP following the same methodology and MATLAB codes as described in chapters 5 and 6.

7.4 Results and discussion

This section reports the various different dose distributions recalculated on CBCTs using the shifts were applied at the time of treatment delivery (and are hence hereafter referred to as 'delivered' - as they were not delivered in reality, but the best estimate of what would have been delivered). The standard plan with 64 Gy to the whole bladder is the most similar to the dose distribution which would have actually been delivered to the patient, although the technique in use at the time of treatment used different margins to expand the bladder into the PTV.

7.4.1 Standard plan - 64 Gy to whole bladder

Figure 7.1 shows the original 64 Gy standard plan calculated on the planning CT for (a) a transaxial, (b) sagittal and (c) coronal view of the patient. Doses are shown as a percentage of a single fraction delivery of 2 Gy.

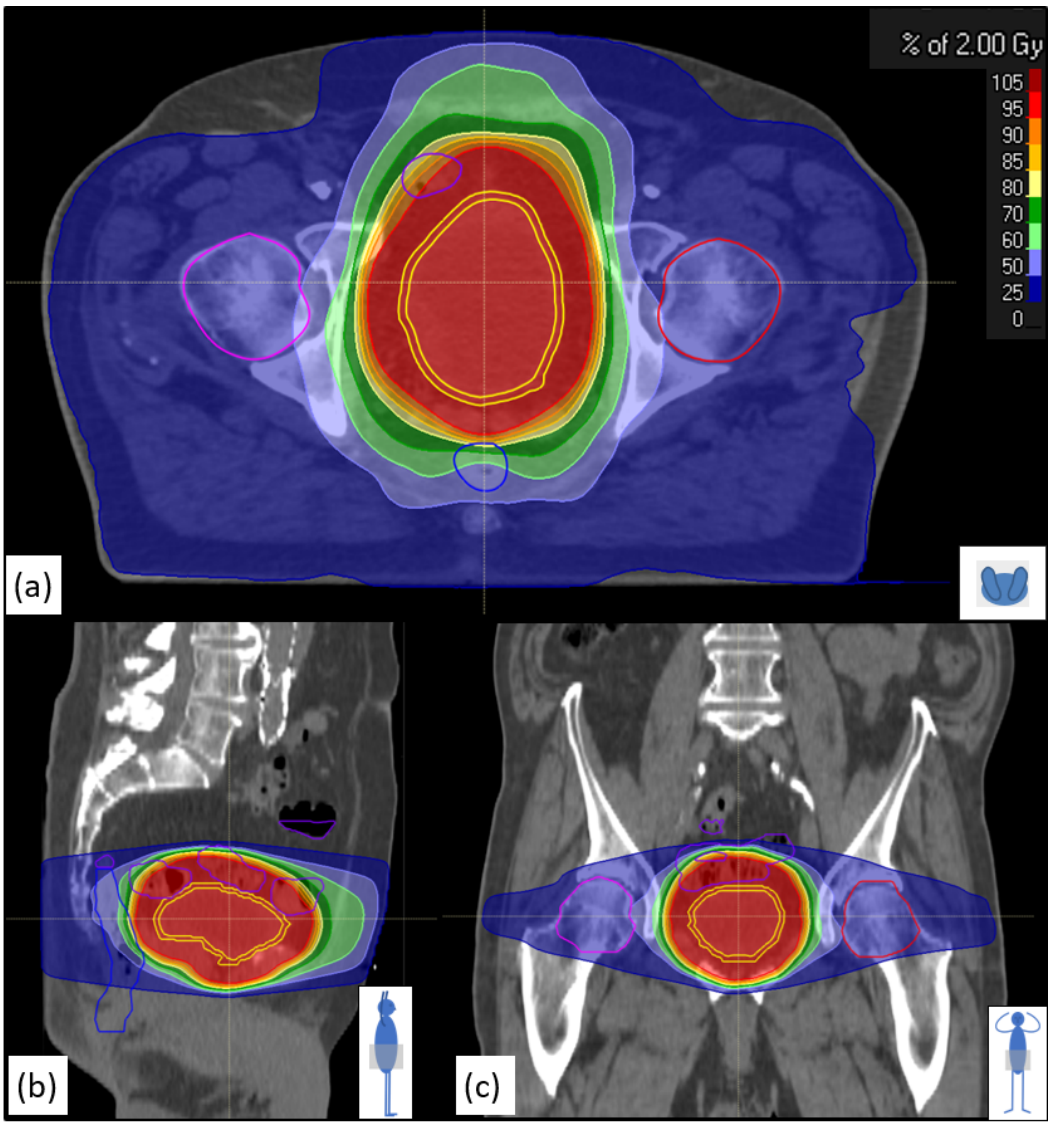

Figure 7.1: Original planned dose distribution calculated on the planning CT for a single (2 Gy) fraction using the standard 64 Gy plan. Images show (a) transaxial, (b) sagittal and (c) coronal views.

For comparison, the re-calculation of the fraction dose on a CBCT image is shown in figure 7.2. As in figure 7.1, the three orthogonal views of the patient are shown. Note that the images are of poorer quality, and that a smaller volume of the patient was imaged.

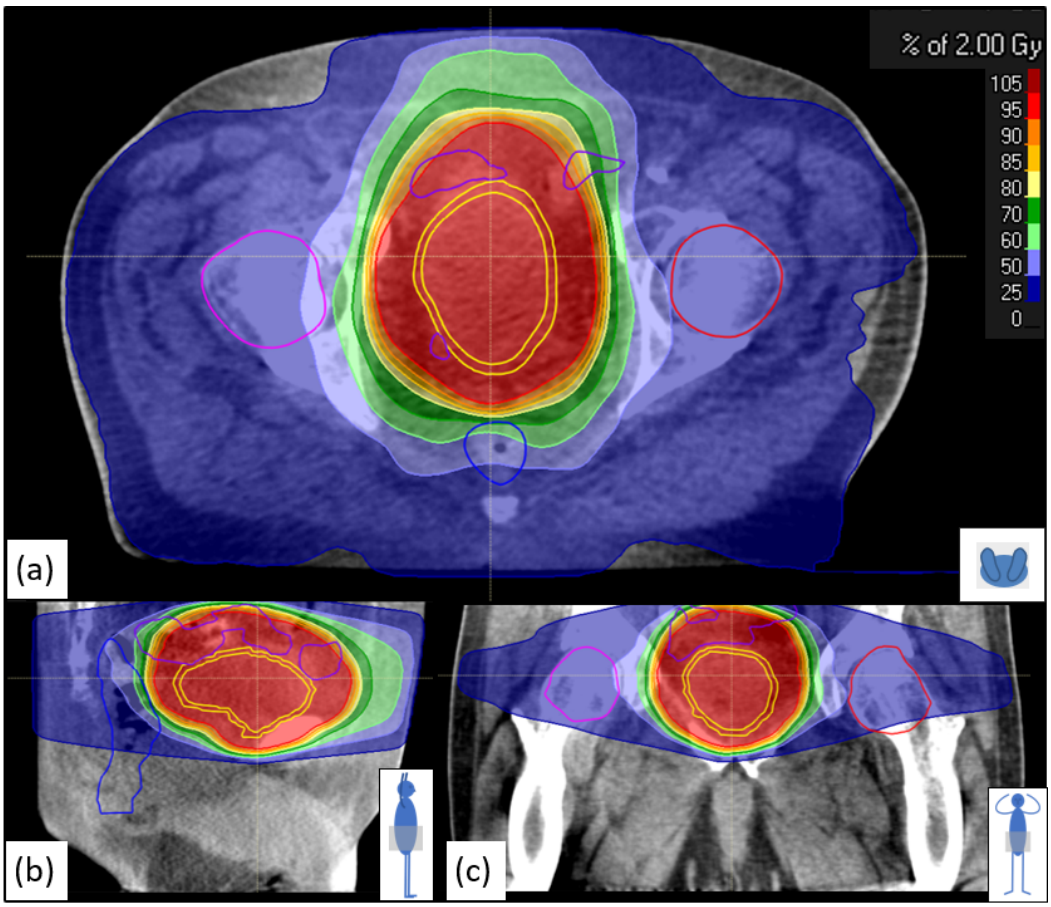

Figure 7.2: Re-calculated dose distribution on the CBCT for a single (2 Gy) fraction using the standard 64 Gy plan. Images show (a) transaxial, (b) sagittal and (c) coronal views.

Figure 7.3 shows the differences between the planned standard (64 Gy) dose distribution and the 'delivered' standard (64 Gy) dose distribution, in (a) transaxial, sagittal and (c) coronal views. The dose differences are those generally expected: around the edges of the patient anatomy small differences between patient anatomy at the time of original planning CT and the daily imaged anatomy cause surface dose differences, which are most clearly seen in (a) the transaxial view. Often patients experience weight loss during the treatment, and this and any other small differences in positioning will be visualised in this way. The positional differences in the treatment couch are also seen and highlighted in (a) and (b).

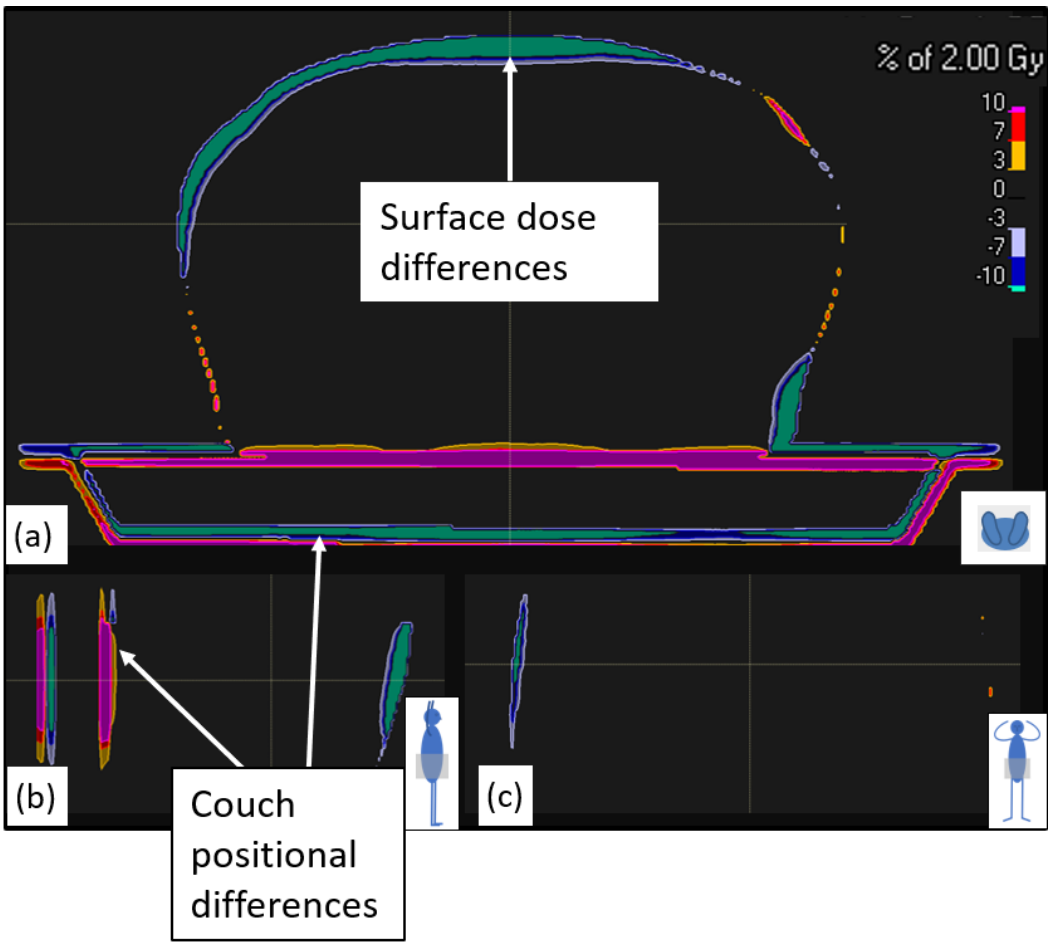

Figure 7.3: Differences between original planned dose distribution and the dose distributions which would have been delivered using the standard 64 Gy plan, based on re-calculation on a CBCT image acquired immediately prior to treatment. Differences shown for (a) transaxial, (b) sagittal and (c) coronal views of the patient. Discrepancies are indicated owing to surface variations of the patient and couch.

Figure 7.4 shows the differences between the recalculated dose distribution from figure 7.2 mapped back onto the planning CT via the DR, and compared with the original planned dose distribution.

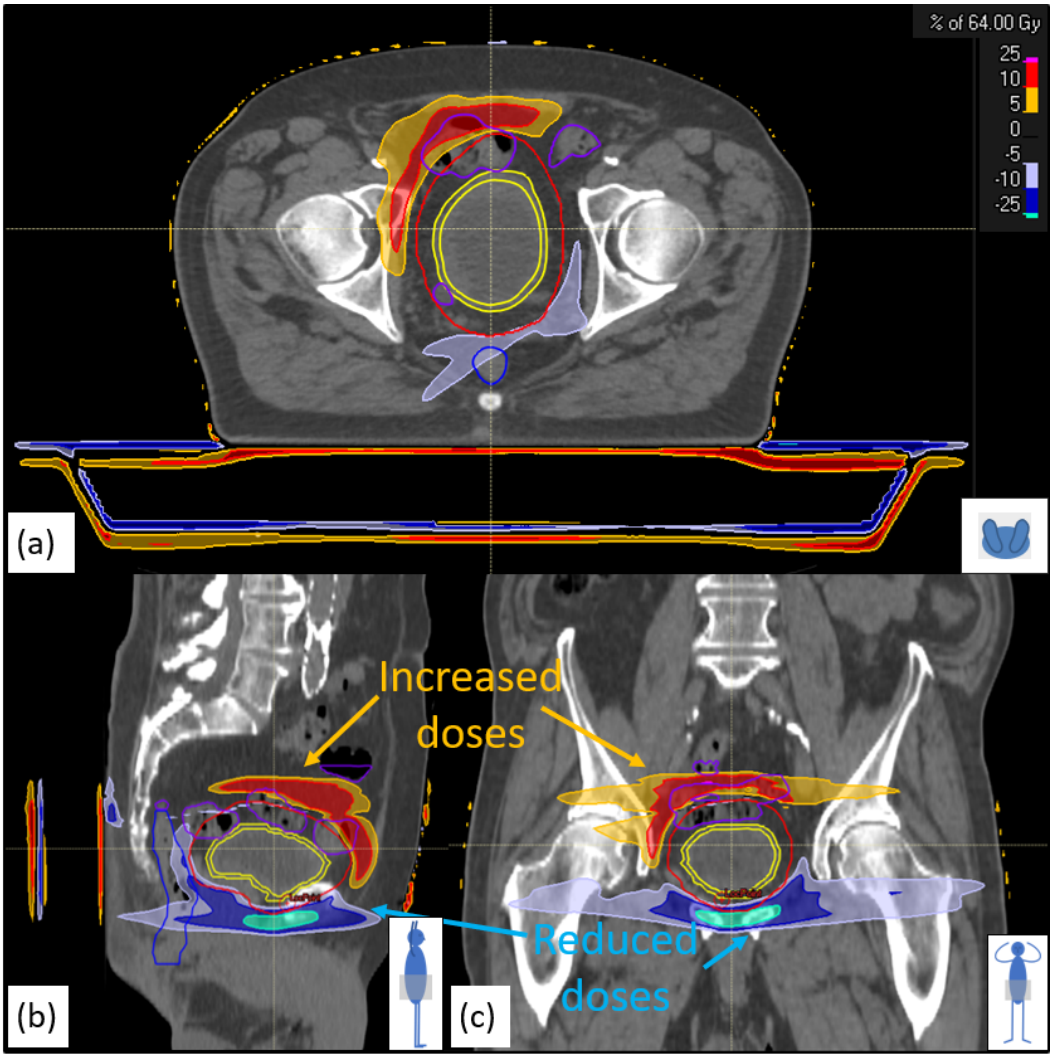

Figure 7.4: Differences between original planned dose distribution and the dose distributions which would have been delivered using the standard 64 Gy plan, based on re-calculation on a CBCT image acquired immediately prior to treatment which are then mapped back onto the orignal planning CT using the DR. Differences shown for (a) transaxial, (b) sagittal and (c) coronal views of the patient.

The dose differences seen within the patient CT volume are much greater than would be expected from the images seen in figures 7.1, 7.2 and 7.3. There is an increased dose to the region superior and slightly anterior to the PTV (shown delineated in red), and a corresponding decrease to the region inferior of the PTV as indicated in the figure. This appears to show that the DR is incorrectly mapping the dose back onto the planning CT. Figure 7.5 shows an overlay of the DR mapping

vectors onto the planning CT. Vectors are colour coded with red corresponding to a shift of 1 cm and yellow 0.5 cm, as indicated in the key. There are several regions showing large vectors, as annotated in the figure.

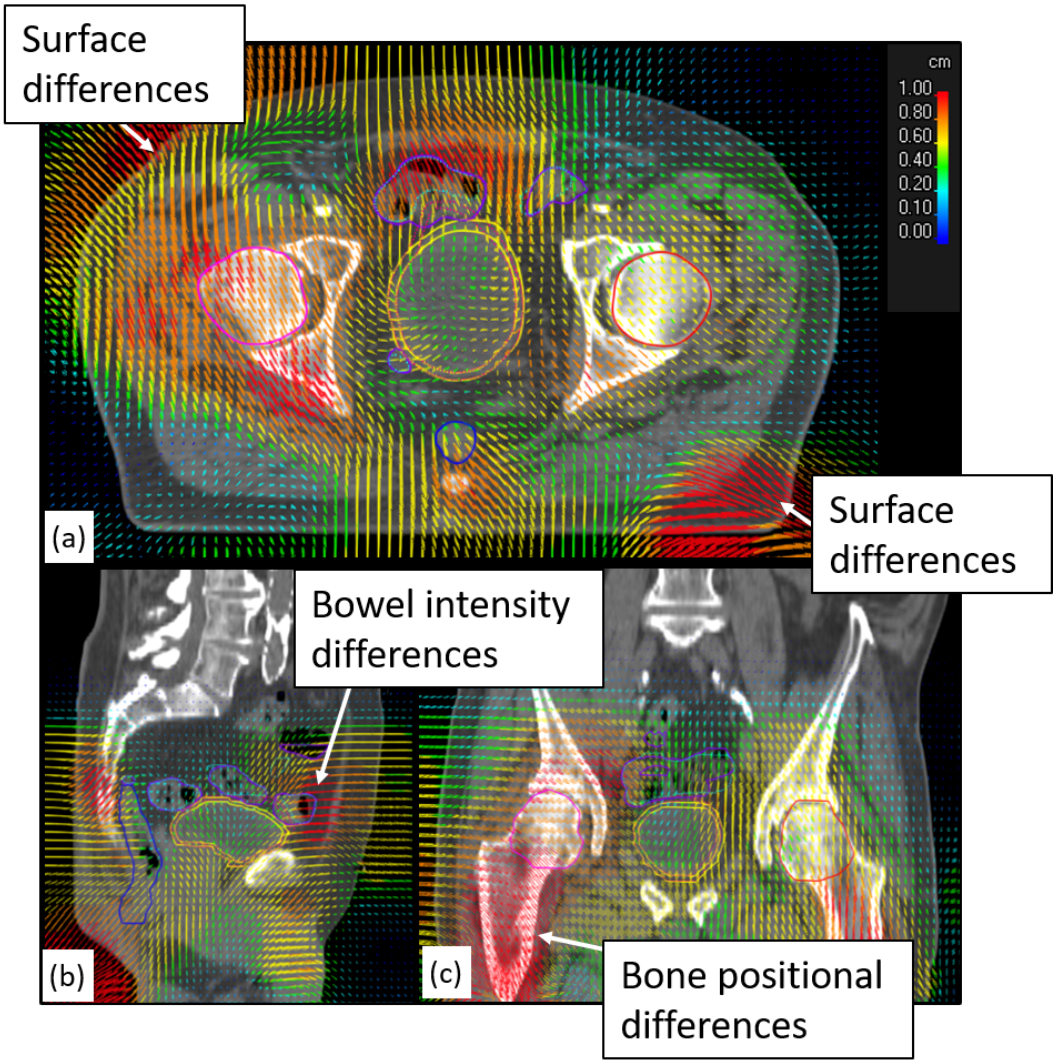

Figure 7.5: Deformable registration (DR) mapping vectors between CBCT and CT shown overlaid upon the planning CT for (a) transaxial, (b) sagittal and (c) coronal views.

Where there were known to be differences in the location of the patient surface owing to weight loss, these vectors are not surprising. There are also large vectors in the regions of bones, which may be due to small differences in position or rotational changes in leg positions. Neither of these would be likely to affect the doses mapped to the bladder or nearby OARs as they are not close to these structures.

There are, however, large vectors close to the bowel and in particular regions of bowel gas that have moved between the planning CT and CBCT. Obviously, these regions should not need to be shifted as they are in fact part of the same organ, but as the DR algorithm is designed to map intensities this is a difficulty in the use of such as algorithm for this part of the anatomy. The magnitude of the DR vectors in the region of the bladder wall is approximately 0.5 cm (yellow). This is not correct when the two datasets are visualised, for example, as can be seen in figure 7.6. In this figure, the delineations from the planning CT are shown overlaid onto the CBCT and show good agreement with the anatomy seen on the image, apart from the superior and anterior parts of the bladder and neighbouring bowel.

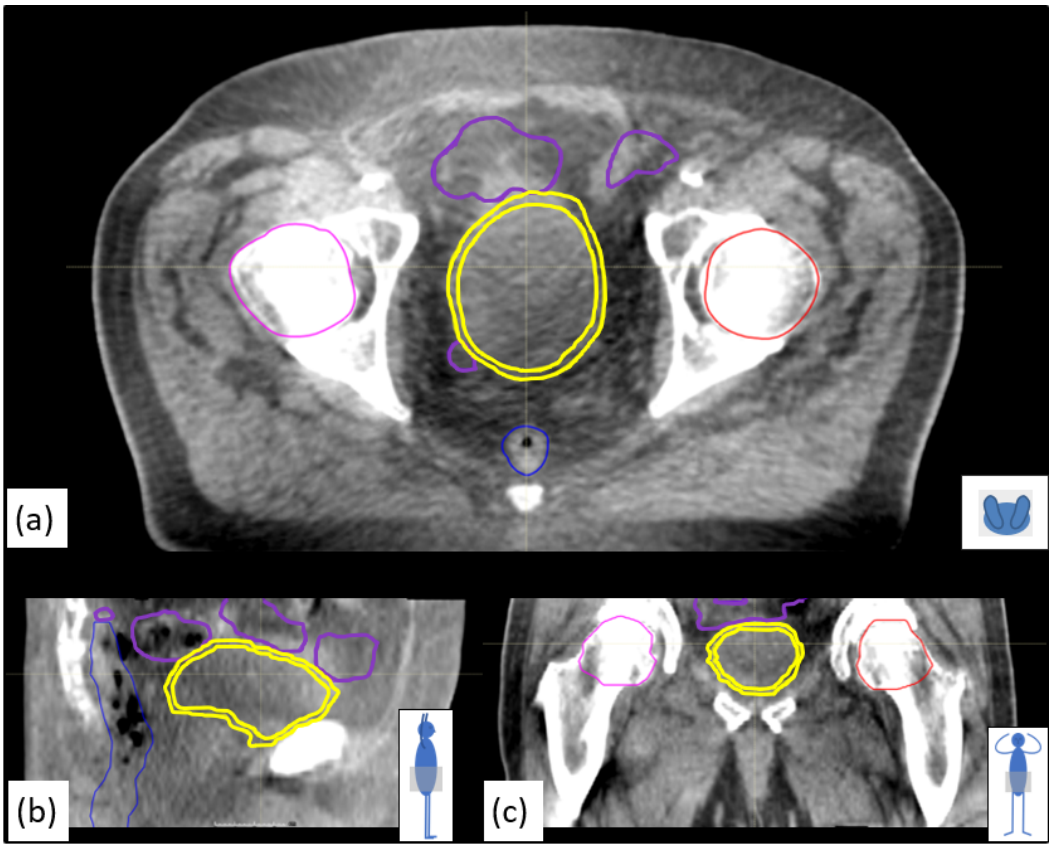

Figure 7.6: CBCT in (a) transaxial, (b) sagittal and (c) coronal views. The delineated volumes are overlaid from the original planning CT and are as follows: right femur (pink), left femur (red), bowel (purple), rectum (blue) and bladder wall (yellow). Most delineations are in good agreement with the image intensities seen in the CBCT image, apart from the superior and anterior parts of the bladder and neighbouring parts of the bowel.

Analysis of the CBCT images shows that the bladder filling is greater in general on the CBCTs than the planning CT, and this shifts the overlying bowel also. This difference is shown in figure 7.7.

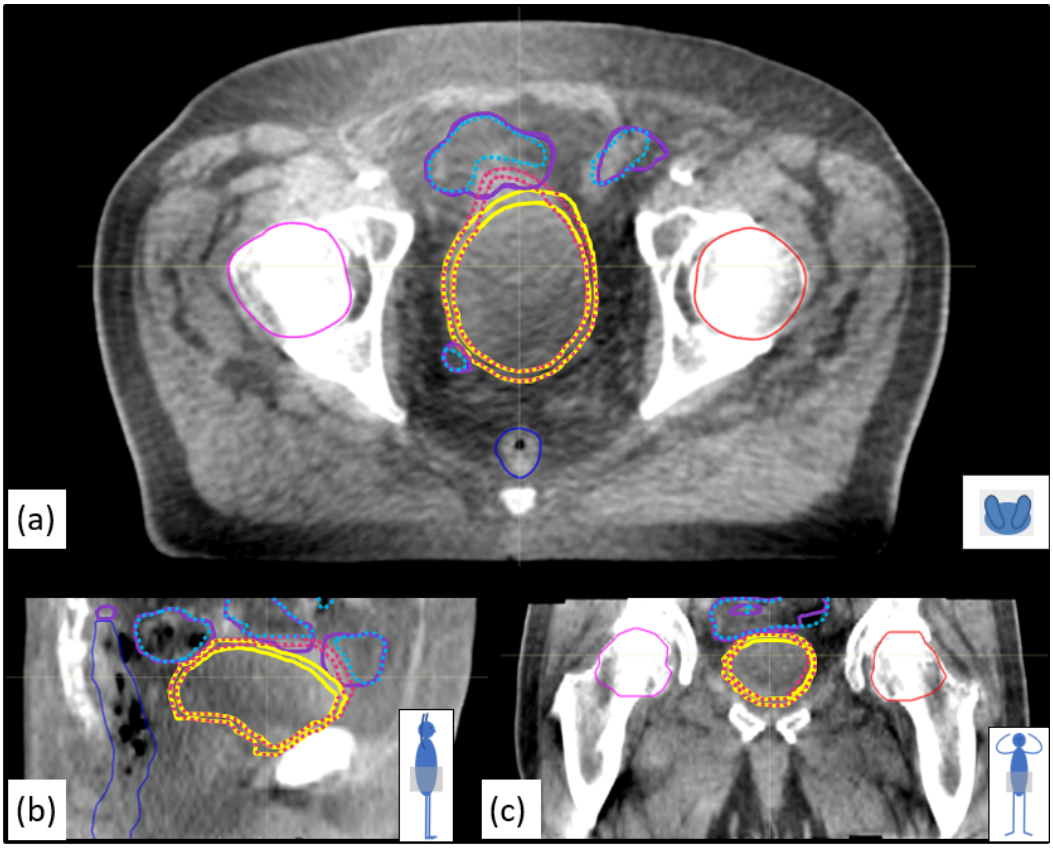

Figure 7.7: CBCT in (a) transaxial, (b) sagittal and (c) coronal views. The delineated volumes are mostly overlaid from the original planning CT and are as follows: right femur (pink), left femur (red), bowel (purple), rectum (blue) and bladder wall (yellow). Delineations on the CBCT of the bladder and bowel are shown in dotted magenta and dotted pale blue respectively.

Bladder filling was seen to be greater on all of the CBCTs acquired of this patient than on the planning CT. Large variations in filling are expected, and is the historical reason for the requirements for relatively large CTV-PTV margins for the bladder. The difference in bladder shape was not, however, picked up by the DR. Increased bladder filling pushes the overlying bowel superiorly and anteriorly, and this was also not picked up by the DR, although the DR did try to map parts of the bladder onto other parts of the bladder owing to movement of bowel gas.

For these reasons, the assessment of the feasibility of delivery of the dose

distributions calculated in chapter 6, cannot be accurately assessed by directly using the 'Treatment adaptation' functionality of RayStation as it requires the use of the DR. Instead, a single CBCT was used in which manual alteration of the bladder and bowel delineations was performed. As was seen in figure 7.7, the bladder is readily visible on the daily CBCT and the differences in filling are apparent between those from the original CT (yellow), and those visible by eye (magenta). The bowel is not, however, as readily visible owing to the poorer image quality using CBCT. Therefore, rather than attempting to delineate it manually, the only alterations made to the bowel were to remove it from the regions which were distinguished as bladder, and ensure that all volumes of gas (which are readily visibile owing to the low density) were included in the bowel contour. Otherwise, the existing structure from the planning CT was retained.

The DVHs corresponding to the various volumes delineated were calculated using the CBCT and compared with those originally planned. Figure 7.8 shows the DVH for the standard 64 Gy plan.

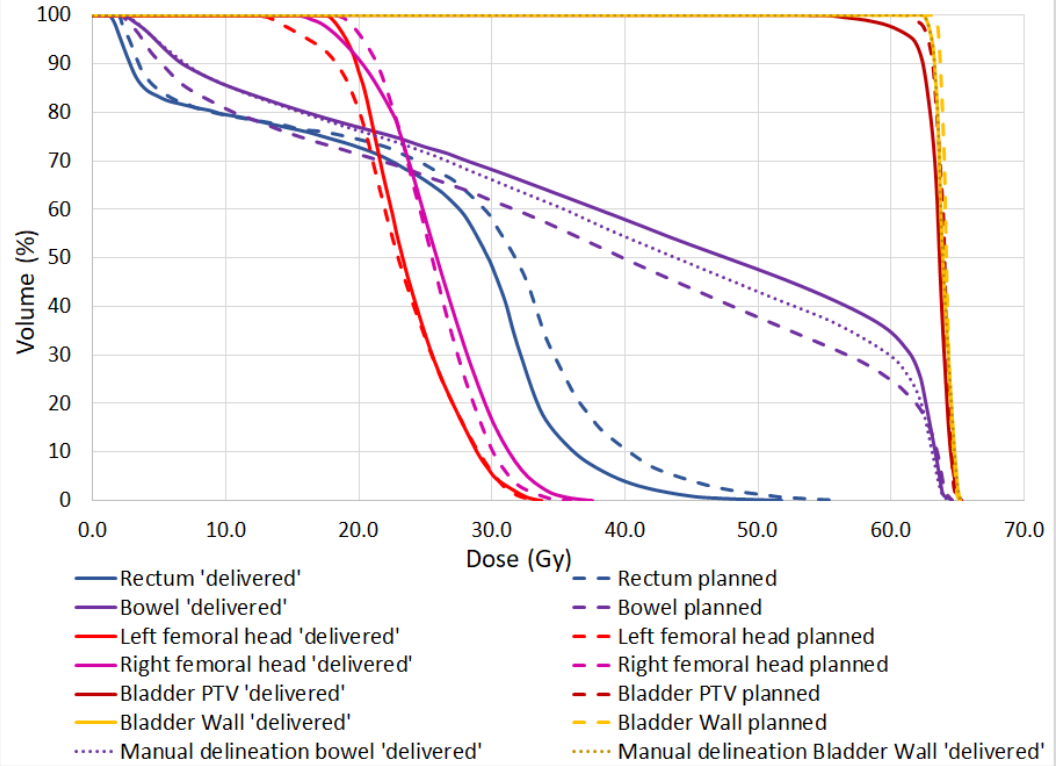

Figure 7.8: Cumulative dose-volume histograms for femoral heads (red and magenta), rectum (blue), bowel (purple), bladder wall (yellow) and bladder PTV (dark red). Planned and 'delivered' doses are shown as dashed and solid lines, respectively; where manual delineations were performed these are shown dotted.

The pairs of coloured lines in figure 7.8 show the various delineated structures, with solid lines indicating the 'delivered' dose, and dashed indicating the planned dose. The femoral heads (red and magenta) receive doses similar to those expected, and the rectum (blue) receives a slightly lower dose than expected. The bowel (purple) appears to receive a higher dose (solid line) than planned (dashed), but the manually altered delineation (dotted purple) falls between the two. It is difficult to be confident that this is an accurate representation of the doses received, owing to the uncertainties in delineation of the bowel volume on CBCT, but it does give confidence that the apparent overdose of the bowel indicated by the solid line is probably not correct, as this structure includes volume that is in fact the bladder. Although the PTV (dark red) receives lower doses than planned in part, the bladder wall (yellow) itself still receives the planned dose (this is the intention of the relatively large margins used to produce the PTV). The manual delineation of the bladder wall (dotted yellow) overlays the planned (solid) line, showing the bladder wall receives the planned dose even taking into account the change in bladder filling.

7.4.2 Superior tumour - 70 Gy

This section relates to the use of the planned dose distribution in which 70 Gy was prescribed to a medium tumour in the superior region of the bladder, with 52 Gy to the rest of the bladder. The same methodology as discussion in section 7.4.1 was used for the analysis of the feasibility of delivery of this dose distribution.

As this simulated tumour was in the superior region of the bladder, and it had already been established that the superior and anterior portion of the bladder had moved between the planning CT and CBCT, the delineation of the superior simulated tumour was adjusted, so that it included the superior portion of the bladder wall that had been altered manually. The inferior edge of the tumour was adjusted similarly towards the superior direction such that the total volume of the tumour was unchanged.

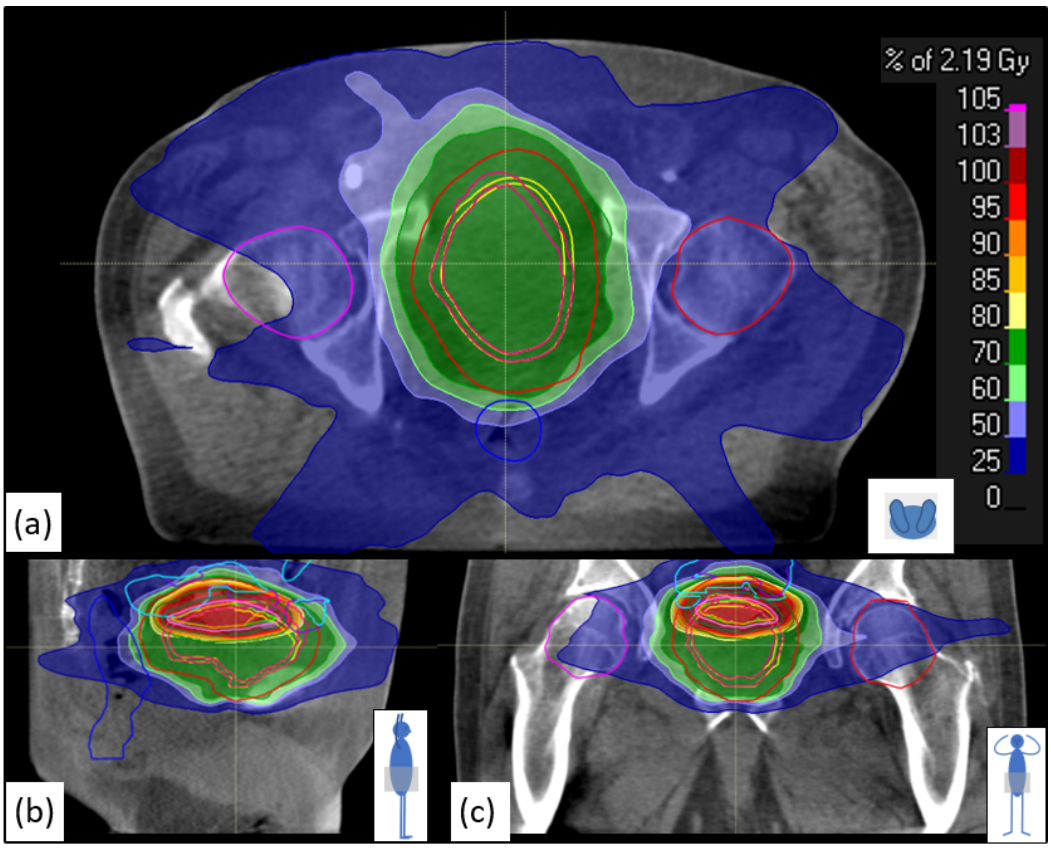

Figure 7.9: Dose distributions which would have been delivered using the 70 Gy to medium superior GTV plan, based on re-calculation on a CBCT image acquired at the time of treatment for (a) transaxial, (b) sagittal and (c) coronal views. Simulated superior tumour is shown in green.

Figure 7.10 shows the resulting differences between planned and 'delivered' doses via cumulative DVHs for the various organs. As discussed for the standard plan, most organs such as the femoral heads again receive doses similar to those expected, with the rectum receiving a slightly reduced dose. The manual alterations in the bowel resulted in a calculated bowel dose closer to that predicted, as shown by the overlaying purple dashed (planned) and dotted ('delivered' manually delineated) bowel curves. The bladder wall curves (yellow) show similar doses for planned (dashed) and manually delineated 'delivered' (dotted). The simulated superior GTV (pale green) shows similar results for planned (dotted) and 'delivered' (solid) doses, although the 'delivered' is around 1 Gy lower at its' furthest deviation.

The curves in figure 7.10 denoted by 'GTV+2mm' and 'GTV+5mm' show the doses 'delivered' to volumes produced by isotropic expansion of the GTV (i.e.

superior medium tumour volume). This was done to assess what dose would have been received by the actual tumour volume if the volume modelled had originated from DW-MRI, and been inaccurate by either 2 or 5 mm (corresponding to the results from Chapter 4 regarding geometric uncertainties in DW-MRI). As these curves both closely overlay that of the delineated GTV, this implies that the margin used (10 mm in this case) was sufficient to ensure coverage of the required volume.

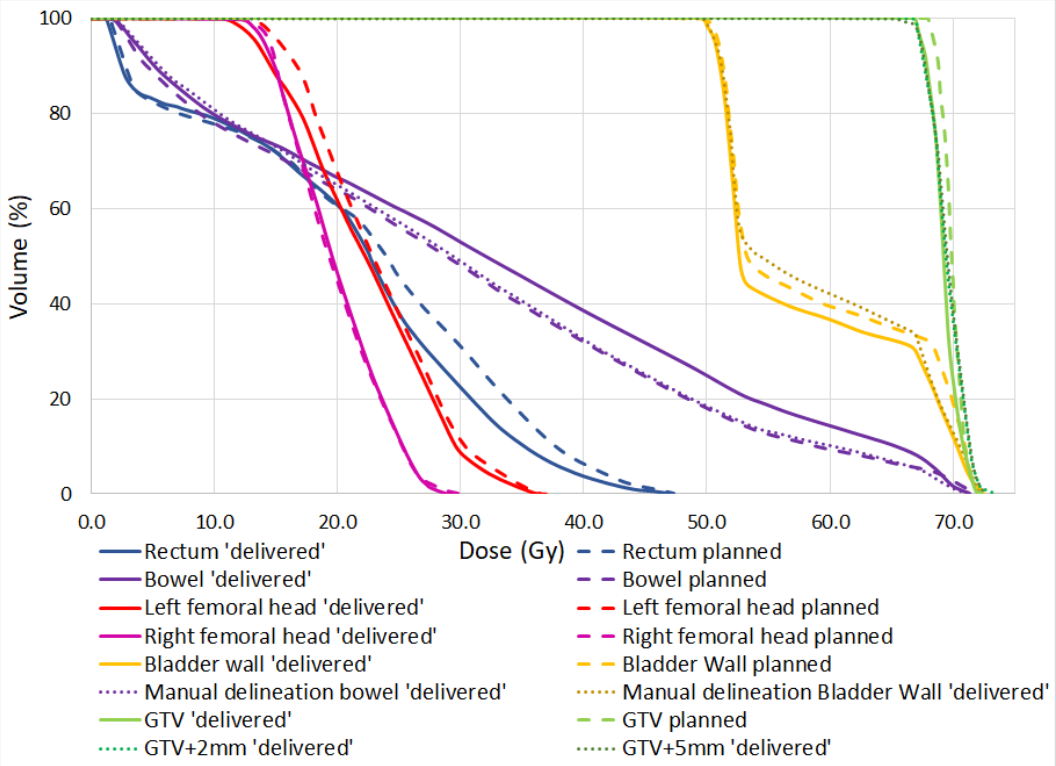

Figure 7.10: Cumulative dose volume histograms for femoral heads (red and magenta), rectum (blue), bowel (purple), bladder wall (yellow), and simulated superior tumour (i.e. GTV) (green). Planned doses are shown dashed, 'delivered' doses are solid lines and where delineations have been performed manually on the CBCT these are shown dotted for an improved estimate of 'delivered' doses. Expanded GTVs to assess the potential 'worst case' effect of geometric distortion in GTV delineation are shown for GTV+2mm and 5mm in dotted bright green and green, respectively.

Table 7.1 shows the resulting change in TCP using the 'delivered' DVHs for calculation for the RT-only and RCT models developed in chapter 4. In both cases these results are 0.3 % lower than predicted in chapter 6.

Table 7.1: Expected and 'delivered' (i.e. what would have been delivered had this plan been used clinically) TCPs according to the RT-only and RCT models developed in chapter 4.

	TCP (%) RT only model		**TCP (%) RCT model**	
Plan	Planned	'Delivered'	Planned	'Delivered'
Superior 70 Gy	78.6	78.3 *(-0.3 %)*	86.2	85.9 *(-0.3 %)*
Inferior 78 Gy	87.3	87.2 *(-0.1 %)*	92.3	92.5 *(0.2 %)*
Posterior 73 Gy	83.4	82.6 *(-0.9 %)*	89.7	88.9 *(-0.9 %)*

7.4.3 Inferior tumour - 78 Gy

The procedures previously described in section 7.4.1 were performed for the planned dose distribution in which 78 Gy was prescribed to an inferior simulated medium-sized tumour. Figure 7.11 shows a sagittal view of the calculated dose distribution on the CBCT.

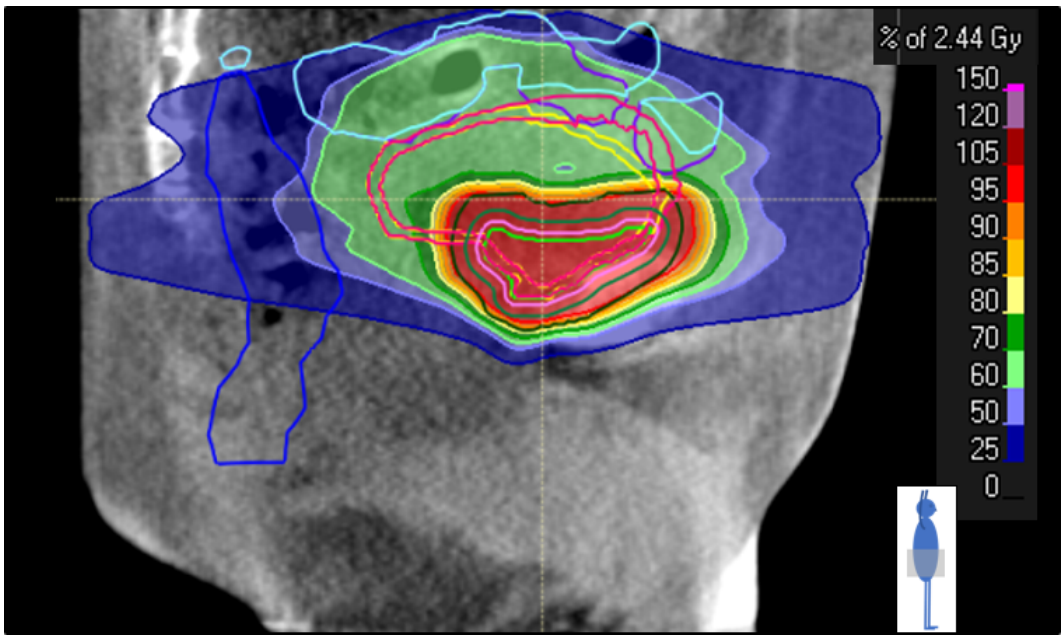

Figure 7.11: Dose distributions which would have been delivered using the 78 Gy to medium inferior GTV plan, based on re-calculation on a CBCT image acquired at the time of treatment. Dose distribution shown on sagittal views with simulated inferior tumour shown in green.

Figure 7.12 shows the resulting differences between planned and 'delivered'

doses via cumulative DVHs for the various organs. As previously seen, 'delivered' doses are similar to planned, although the delivered dose to the right femoral head is slightly higher than planned in this case. Again, the manually delineated bladder and bowel show results more closely matched with those planned than the volumes produced by the deformable registration. The simulated inferior GTV and expanded volumes (GTV+2mm and GTV+5mm) all receive very similar doses to those planned to the tumour volume. Table 7.1 shows the resulting TCP was calculated within 0.2 % of original predicted values.

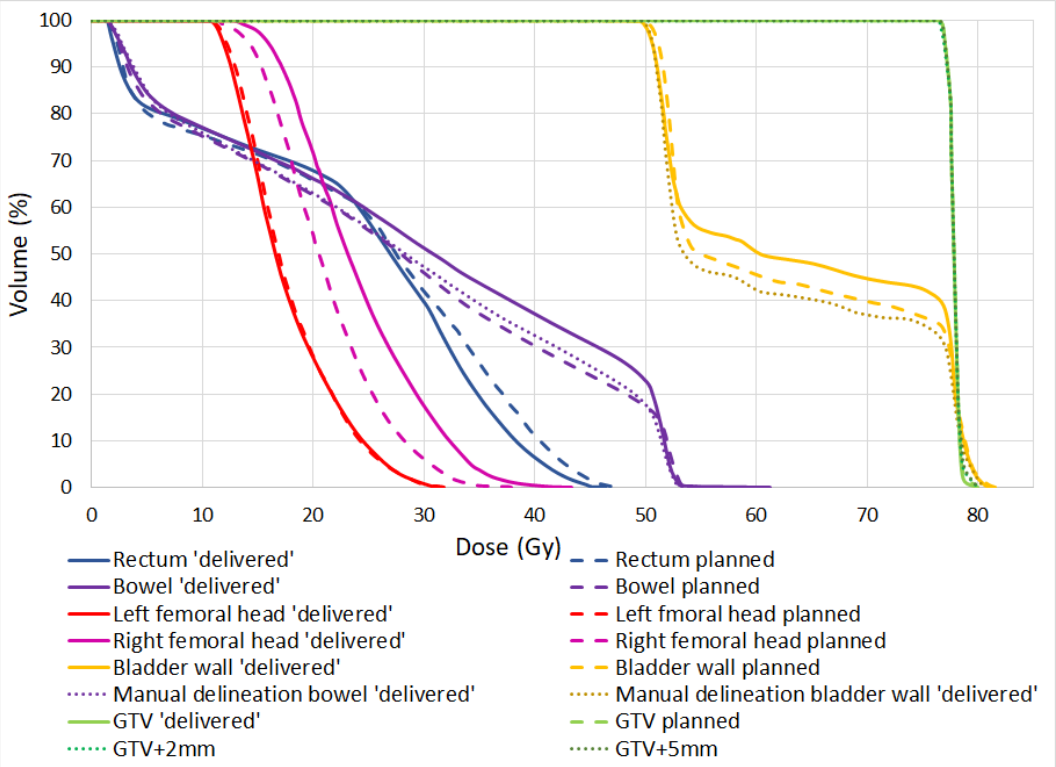

Figure 7.12: Cumulative dose volume histograms for femoral heads (red and magenta), rectum (blue), bowel (purple), bladder wall (yellow), simulated medium inferior tumour (green). Planned doses are shown dashed, 'delivered' doses are solid lines and where delineations were performed manually on the CBCT for an improved estimate of 'delivered' doses, these are shown dotted. Expanded GTVs to assess the potential 'worst case' effect of geometric distortion in GTV delineation are shown by dotted lines for GTV+2mm and 5mm in bright green and green respectively, although as these closely overlay the GTV the lines are indistinguishable from each other.

7.4.4 Posterior tumour with 7 mm margins - 73 Gy

The planned dose distribution in which 73 Gy was prescribed to the simulated posterior medium-sized tumour was analysed in the same way as previously described in section 7.4.1. This plan had been produced using reduced margins for GTV to PTV expansion, of 7 mm rather than 10 mm, i.e. incorporating a predicted geometric uncertainty within DW-MRI of 2 mm rather than 5 mm. Figure 7.13 shows the sagittal view of the 'delivered' dose distribution.

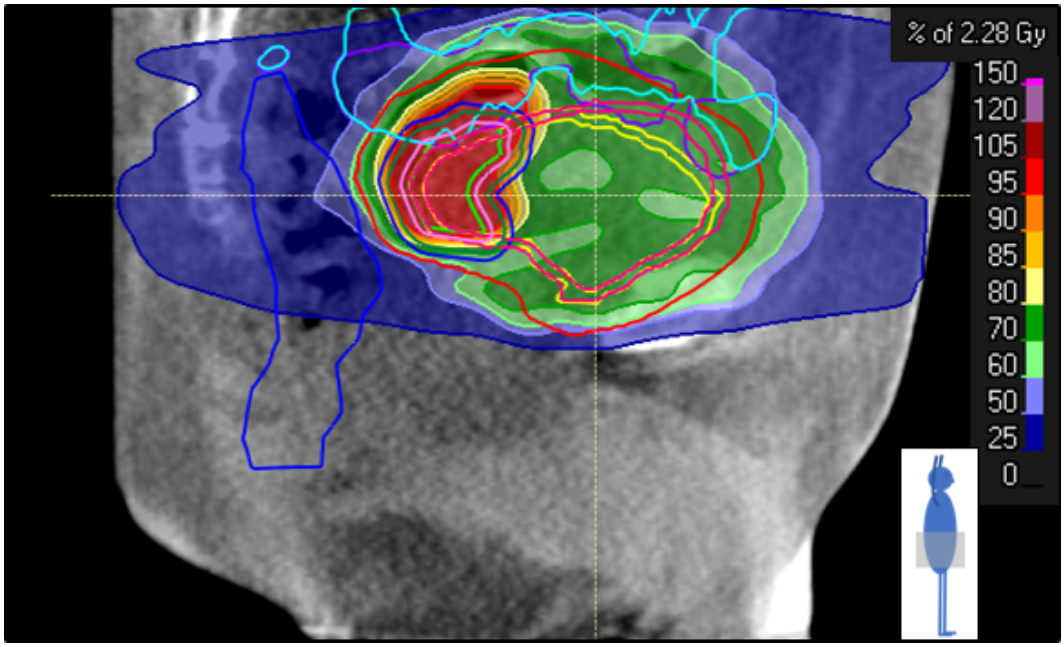

Figure 7.13: Dose distribution which would have been delivered using the 73 Gy to medium superior GTV plan, based on recalculation on a CBCT image acquired at the time of treatment. This plan used reduced margins (7 mm compared to previous 10 mm) to create the PTV containing the tumour. Dose distribution shown in sagittal view with simulated posterior GTV in green.

Figure 7.14 shows the resulting differences between planned and 'delivered' doses via cumulative DVHs for the various organs. The femoral heads received doses similar to those expected, and the rectum a slightly reduced dose as for previous plans. The bowel doses were higher using the DR mapped bowel volume, but the manually altered volume was again closer to the planned curve. The bladder wall planned and 'delivered' doses are similar, although this is reduced slightly when the bladder was manually delineated. The simulated posterior GTV shown in green receives a very similar dose to that planned, although the expanded GTV

(GTV+2mm, shown in bright green) receives a slightly lower dose than planned. Table 7.1 shows the resulting changes to TCP calculation: as expected using the reduced PTV margins this produced the greatest change in TCP; however this was only -0.9 % using both models.

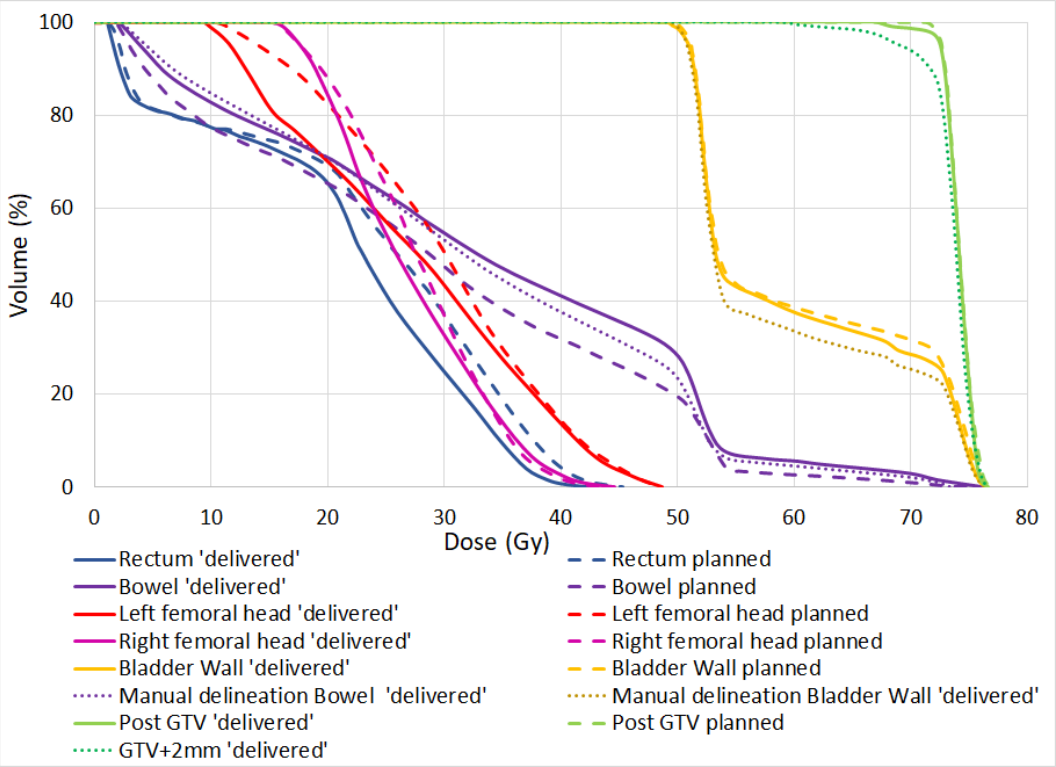

Figure 7.14: Cumulative dose volume histograms for rectum (blue), femoral heads (red and magenta), bowel (purple), bladder wall (yellow), simulated posterior GTV (green). Planned doses are shown dashed and 'delivered' by solid lines; where delineations were performed manually on the CBCT for an improved estimate of 'delivered' doses, these are shown dotted. An expanded GTV is shown to assess the potential 'worst case' effect of geometric distortion in GTV delineation and is shown by a dotted bright green line (GTV+2mm).

7.4.5 Limitations of this method

The method described in this chapter which was used to assess the feasibility of delivery of dose escalated radiotherapy used simulated tumours. In the case of the inferior and posterior tumours, the location inferred for the daily positioning of these simulated tumours was likely to be reasonably accurate, as there was little movement of the bladder wall in these regions. However, for the simulated superior tumour

there is greater uncertainty whether the inferred position at time of treatment would be correct, as this had required manual adjustment. Nevertheless, it appears that the margins used in all cases to produce the relevant PTVs were sufficient that the tumours themselves would have received similar doses to those intended.

The method used a coarse test of growing a margin around the original simulated tumour to attempt to assess whether the tumour would still have received the intended dose had the inferred position from DW-MRI been incorrect by the maximum predicted by the bladder phantom work report in Chapter 4 (i.e. 5 mm and 2 mm respectively). It is obviously unlikely that the tumour would be uniformly larger by this amount, however, the results from the plans using 10 mm GTV-PTV margins all produced very similar DVHs for the expanded GTVs to the original GTVs. The posterior plan using reduced margins of 2 mm showed a slightly reduced dose to part of this expanded GTV volume, but this had a <1 % effect on the calculated TCP.

The positioning of the bowel was difficult to assess, as again this is not well visualised on the CBCT. The method used involved removal of bowel from regions manually delineated as bladder, but added obvious volumes of bowel gas. This produced results in which doses were similar to those planned. Therefore the 'delivered' doses appear similar to those accepted within the RAIDER clinical trial, however this is still subject to some degree of uncertainty.

The simulated tumours and the positions they were manually deformed to would not necessarily be those expected by the deformation of the outside wall of the bladder. Perhaps less deformation of a tumour would in fact be expected, as Lotz *et al.* found that tumours tend to be more rigid than the bladder itself [71].

All results were based upon the positioning chosen by the radiographers treating the patient - and using the treatment plan and PTV margins in clinical use at that time. Therefore it is possible that different positioning would have been chosen had these different plans been in use instead, or with the knowledge for example that the tumour was in the inferior/superior/posterior portion of the bladder. Certainly, should this be tested using MR imaging at the time of treatment, the ability to visualise the tumour itself would be expected to improve dose delivery to closer match the intended distribution. Therefore it could be argued that these results indicate a worst case rather than realistic estimate of the dose that would be delivered in that case.

Developments to build upon the work outlined in this chapter would benefit greatly from the ability to assess bladder and tumour location immediately prior to or during radiotherapy treatment delivery using MRI, owing to its superior soft

tissue contrast. Many of the uncertainties relating to positional information are not possible to improve using the currently available technologies of CT and CBCT, but with the development of MR-linacs these issues should be possible to overcome.

7.5 Summary and conclusions

The approach taken in this chapter, of using treatment adaptation assessment within RayStation TPS to assess the feasibility of delivery of dose escalated treatments was limited by the ability of CBCT to visualise soft tissue, as well as the need for simulation of tumours. However, it sets outs a blueprint for what could be done using the same approach but using MR-sim of real tumours and an MR-linac.

Within the limitations stated, the delivery of the prescribed doses developed in chapter 6 appear feasible. Further work is necessary using MR to visualise tumour at the time of treatment delivery and to assess the impact upon organ at risk doses, in particular the bowel.

Chapter 8

Summary and Vision

The original aim of this work was to study the use of DW-MRI and resulting ADC maps with regard to their application for use within the radiotherapy treatment of MIBC. It was intended that the project would investigate the magnitude and effects of geometric distortion within DW-MRI upon the uncertainties in positional information of bladder tumours. The ways these uncertainties might be mitigated or accommodated in the design of radiotherapy dose distributions was to be investigated. The idea lying behind this project, was the potential to ultimately improve treatment outcomes for patients with MIBC. This would be achieved by increasing the radiotherapy dose prescribed, but without additional toxicity from such treatment because the use of DW-MRI would enable improved targeting of the tumour volume.

There is growing interest and investment in the use of MRI within radiotherapy imaging and treatment planning, as well as at the time of treatment delivery via hybrid systems such as MR-linacs. Several such systems are already in clinical use in many centres across the world [72], although at present much of the use of MRI is still in the realms of conventional T_1- and T_2-weighted imaging, rather than the 'functional' or 'multi-parametric' MRI that this thesis addresses. However, there are already the beginnings of investigations into the clinical use of MRI sequences for adaptation of radiotherapy treatments to various types of response [27, 28, 46]. The work in this thesis aims to add to this area of endeavour, and highlight what could be achieved with such technology for the particular tumour site of the bladder.

8.1 Summary of the work

Chapter 4 showed in principle that positional information acquired in DW-MRI of bladder tumours could be transferred to CT with a conservative estimate of 5 mm accuracy if the only attempt to correct for geometric distortion is made within the treatment planning system itself using deformable registration algorithms.

Subsequent work, also reported in chapter 4, tested how well an established method within the diagnostic MR setting worked to correct for geometric distortion in DW-MRI performed for the purposes of radiotherapy treatment planning. The results of this investigation found that the positional information could be transferred from DW-MRI to CT with a conservative estimate of 2 mm accuracy, although the workflow involved is not at present suitable for clinical use.

Chapter 5 used data from a paper by Plataniotis and Dale [61] in which patients with MIBC had received treatment only with radiotherapy and which the authors had fitted using a logistic TCP model. The chapter reported on the refitting of this data with the Poisson model following Wright *et al.*'s approach [58]. A second fit was also produced, to a further dataset from Plataniotis and Dale's paper in which patients had received chemotherapy as well as radiotherapy. This was done in order to produce a model which may better estimate outcomes for patients receiving both radiotherapy and chemotherapy.

The results from Chapters 4 and 5 were then used to predict TCP for a range of simulated bladder tumours with different volumes and locations within the bladder. It was found that the tumour location was of primary importance for the extent to which dose could be escalated, as proximity to the bowel was the main limitation. Variations in tumour volume were of secondary importance, although an effect was seen (as expected), in which larger tumours resulted in slightly lower TCP. Results using the model in which only the effects of radiotherapy were included, showed that TCP could be expected to increase by at least 9 % (for superior tumours, in which the dose escalation was the most limited), and up to >19 % for the most inferior tumours (owing to their greater distance from the bowel). The corresponding figures using the TCP model which incorporated the additional effects of chemotherapy showed smaller relative increases in TCP, but the absolute values of TCP were around 10 % higher.

The effects of variations in margin sizes used to produce PTVs from GTVs, showed some minor differences for most tumour locations, but a large effect for inferior tumours. Also, the effect of small changes in tumour location (i.e. shifting the superior border of lateral or anterior/posterior tumours inferiorly by 1 cm)

showed small effects on the dose to which tumours could be escalated (an increase of around 1 Gy).

Finally, work reported in chapter 7 using the CBCT daily imaging, attempted to ascertain the doses the treatment volumes might have received in practice. This work showed that the tumour received similar doses to those planned, and would have resulted in similar calculated TCPs to those originally predicted. There was some uncertainty in bowel location using the CBCT images, owing to the poorer image quality, and this could mean that the bowel received higher doses than originally planned, although manual delineations indicated that this was not likely the case. As the dose escalation was already pushing OAR doses close to tolerance, this is however an important finding which indicates that further work should be done to assess the effect prior to a clinical trial for such dose escalation techniques. This would ideally be performed using MRI which would show the required soft tissue contrast as well as tumour location.

Overall, this work set out to explore the possibility of the use of DW-MRI within the radiotherapy pathway. It addressed and quantified one of the main potential limitations in the use of DW-MRI (i.e. geometric distortion) and its' accommodation within radiotherapy treatment planning. The probability of local control of the tumour in MIBC was modelled and then used to infer the magnitude of potential increase should this change of treatment technique be used clinically. A blueprint for assessment of the feasibility of delivery of the treatment was developed, which showed that delivery of the change in technique appears feasible, as far as can be assessed using this available technology. Further work using a similar approach with MR rather than CT is the next step in developing this work.

8.2 Vision

The work within this thesis has indicated that it should be possible to improve the local control of MIBC, by at least 9 %, and up to 19 % depending upon tumour location and TCP model used. This is a large potential improvement in outcomes for patients given that there have been minimal improvements in outcomes for MIBC over several decades. The next steps required to enable the implementation of this work into clinical practice are detailed in section 8.3. This section aims to first paint a picture of how the technique could be implemented.

There are three main possibilities for the application of the work reported in this thesis. Firstly, using DW-MRI in the same manner as shown here to design radiotherapy dose distributions but only using the additional information from

DW-MRI alongside conventional CT scans via image registration. In this way, there would be a minor change in the methodology of radiotherapy treatments for MIBC, and which would not require any additional technology beyond that already widely available but there would likely be some degree of increased tumour control, particularly for those tumours which happened to lie towards the inferior portion of the bladder. A shortcoming of this approach is that the tumour may not be visible on CBCT at the time of treatment delivery, particularly towards the end of a course of treatment owing to response.

A second possible way to incorporate the findings within this thesis into clinical practice, would be to largely use the described methodology, but without the additional acquisition of CT for planning purposes. Instead, an anatomic MRI using standard MRI sequences could be performed along with the DW-MRI, and these images could be processed to enable direct radiotherapy planning on these images. This full MR-sim approach would mean that some uncertainty in the initial patient set-up could be reduced, as all images for treatment planning would be acquired in a single imaging session and the uncertainties involved in image registration (which propagate through the treatment process) would be minimised. Since many radiotherapy departments are beginning to use MR-sim, this is an approach which is likely to be possible in the near future, although the same shortcomings as previously noted would apply.

Thirdly, in addition to the use of MR-sim, the patient could also be treated on an MR-linac. In this scenario, the daily positioning for treatment could incorporate the acquisition of DW-MRI as well as conventional T1/T2 imaging. This could potentially allow the further reduction of margins for expansion of GTV to high dose PTV, as the GTV would now be directly visible at the time of treatment. Indeed, it would also be possible that the daily adaptation of treatment could incorporate tumour positional variations, variations in bladder filling, and also individual patient response to treatment via assessment of the quantitative information contained within ADC maps. This potential scenario was the original vision for exploration through the work in this thesis.

8.3 Future work

This section aims to outline the further work required to enable clinical implementation of the technique developed in this thesis. The main areas of work are:

1. Technical developments in image processing - either in-house, by TPS manufacturers, MR scanner and/or MR-linac manufacturers,

2. MR-sim and ideally MR-linac use for visualization of real MIBC tumours pre-treatment,

3. Further investigation of radiotherapy dose escalation of MIBC tumours using real MR images and assessing resulting OAR doses,

4. Outcomes from BladderPath trial showing the effect of removing TURBT from the treatment pathway would ideally be required to assure that this is at least non-inferior to the current standard pathway.

The workflow required to use ADC maps within the radiotherapy treatment planning process is at present cumbersome and unsuitable for clinical use. As noted in (1), this problem could be addressed by (a) in-house development of appropriate software, (b) TPS manufacturers incorporating distortion correction of DW-MRI within the TPS, much as they have deformable registration algorithms, or (c) MRI manufacturers directly addressing the issue via their scanner software. Any or all of these methods could enable the safe and robust transfer of DW-MRIs via DICOM, and for validated software within the radiotherapy department to then enable the clinical use of such images. Such software would also be highly desirable within an MR-linac platform, to enable the DW-MRI to be performed, and a distortion-corrected image registered with pre-treatment images for daily treatment adaptation prior to treatment delivery.

Radiotherapy dose escalation to MIBC should be further investigated, using images of actual tumours and multi-parametric MRI for radiotherapy treatment planning and pre-treatment positioning assessment where possible. Further work is necessary to ascertain the potential effect on OAR doses resulting from any dose escalation. Initial work could involve planning studies of those patients accrued through the BladderPath clinical trial, to see whether

(a) similar results are obtained across a wider patient cohort,

(b) plans can be generated upon MRI scans directly,

(c) a full (theoretical) workflow for the treatment process can be achieved, ideally leading to

(d) a clinical trial in which patients receive escalated doses based on their MRI without TURBT within the patient pathway.

A further step would involve follow-up of patients during and after treatment in which the response of tumours on DW-MRI and ADC maps would be seen. The

outcomes could then facilitate design of a clinical trial using an MR-linac which would enable on-treatment adaptation of radiotherapy treatment plans.

This vision of radiotherapy treatments based on tumour response as well as location within the bladder represents a major shift towards fully individualized treatments with the aim of minimising side effects whilst maximally improving outcomes.

Bibliography

[1] CRUK. Bladder cancer survival statistics, April 2018. URL www.cancerresearchuk.org/health-professional/cancer-statistics/statistics-by-cancer-type/bladder-cancer/survival#heading-Two.

[2] Bladder cancer statistics. http:/www.cancerresearchuk.org//health-professional/cancer-statistics/statistics-by-cancer-type/bladder-cancer#heading-Zero, Sep 2018.

[3] H. B. Grossman, R. B. Natale, C. M. Tangen, R. W. White, M. F. Sarosdy, D. P. Wood, D. Raghavan, and E. D. Crawford. Neoadjuvant Chemotherapy plus Cystectomy Compared with Cystectomy Alone for Locally Advanced Bladder Cancer. *New England Journal of Medicine*, pages 859–867, 2003.

[4] B. R. Konety and S. S. Chang. *Management of Bladder Cancer*. Springer-Verlag New York, 2016. ISBN 978-1-4939-1881-2. doi: 10.1007/978-1-4939-1881-2.

[5] NICE Guidance and guidelines. Improving outcomes in urological cancers. URL https://www.nice.org.uk/guidance/csg2.

[6] M. Quaresma, M. P. Coleman, and B. Rachet. 40-year trends in an index of survival for all cancers combined and survival adjusted for age and sex for each cancer in England and Wales, 1971-2011: A population-based study. *The Lancet*, 385(9974):1206–1218, 2015. ISSN 1474547X. doi: 10.1016/S0140-6736(14)61396-9. URL http://dx.doi.org/10.1016/S0140-6736(14)61396-9.

[7] N. D. James, S. A. Hussain, E. Hall, P. Jenkins, J. Tremlett, C. Rawlings, M. Crundwell, B. Sizer, T. Sreenivasan, C. Hendron, R Lewis, R. Waters, and R. A. Huddart. Radiotherapy with or without Chemotherapy in Muscle-Invasive Bladder Cancer. pages 1477–1488, 2012.

[8] C. Rödel, C. Weiss, and R. Sauer. Trimodality treatment and selective organ preservation for bladder cancer. *Journal of Clinical Oncology*, 24(35):5536–5544, 2006. doi: 10.1200/JCO.2006.07.6729. URL https://doi.org/10.1200/JCO.2006.07.6729. PMID: 17158539.

[9] RAIDER: a randomised phase II trial of adaptive image guided standard or dose escalated tumour boost radiotherapy in the treatment of transitional cell carcinoma of the bladder, Nov 2018. URL https://www.icr.ac.uk/our-research/centres-and-collaborations/centres-at-the-icr/clinical-trials-and-statistics-unit/clinical-trials/raider.

[10] N. James. Bladderpath clinical trial, October 2018. URL https://www.birmingham.ac.uk/research/activity/mds/trials/crctu/trials/Bladder-Path/investigators.aspx.

[11] P. Mayles, A. E Nahum, and J.-C. Rosenwald. *Handbook of radiotherapy physics: theory and practice*. CRC Press, 2007.

[12] J. R. Williams and D. I. Thwaites. *Radiotherapy physics in practice*. Oxford University Press, 2004.

[13] D. I. Thwaites and J. Malicki. Physics and technology in ESTRO and in Radiotherapy and Oncology: Past, present and into the 4th dimension. *Radiother. Oncol.*, 100(3):327–332, 2011. ISSN 01678140. doi: 10.1016/j.radonc.2011.09.014. URL http://dx.doi.org/10.1016/j.radonc.2011.09.014.

[14] T. R. Munro and C. W. Gilbert. The relation between tumour lethal doses and the radiosensitivity of tumour cells. *The British Journal of Radiology*, 34(400):246–251, 1961. doi: 10.1259/0007-1285-34-400-246. URL https://doi.org/10.1259/0007-1285-34-400-246. PMID: 13726846.

[15] M. Joiner and A. van der Kogel. *Basic Clinical Radiobiology*. Hodder Arnold, 2009. ISBN 978 0 340 929 667.

[16] M. Maqbool. *An introduction to medical physics*. Springer, 2017. ISBN 978-3-319-61538-7. doi: 10.1007/978-3-319-61540-0.

[17] International Commission on Radiation Units and Measurements. 4. Definition of Volumes. *J. ICRU*, 10(1):41–53,

2010. ISSN 1473-6691. doi: 10.1093/jicru/ndq009. URL http://jicru.oxfordjournals.org/cgi/doi/10.1093/jicru/ndq009.

[18] D. W. Robbie and E. A. Moore. *MRI From Picture to Proton.* University Press, 2003.

[19] P. Dirix, K. Haustermans, and V. Vandecaveye. The Value of Magnetic Resonance Imaging for Radiotherapy Planning, 2014. ISSN 15329461.

[20] J. M. Pollard, Z. Wen, R. Sadagopan, J. Wang, and G. S. Ibbott. The future of image-guided radiotherapy will be MR guided. *British Journal of Radiology*, 90(1073), 2017. ISSN 00071285. doi: 10.1259/bjr.20160667.

[21] H. H. Schild. *MRI Made Easy.* Schering AG, 1990.

[22] A. Allen Li. *Adaptive Radiation Therapy.* CRC Press, 2011.

[23] T. Maurer, T. Horn, M. Heck, J. Gschwend, and M. Eiber. Current staging procedures in urinary bladder cancer. *Diagnostics*, 3:315–324, 2013.

[24] E. O. Stejskal and J. E. Tanner. Spin diffusion measurements: spin echoes in the presence of time-dependent field gradient. *J Chem Phys*, 42(1):288 – 292, 1965.

[25] D. Le Bihan, E. Breton, D. Lallemand, P. Grenier, E. Cabanis, and M. Laval-Jeantet. Mr imaging of intravoxel incoherent motions: application to diffusion and perfusion in neurologic disorders. *Radiology*, 161(2):401 – 407, 1986.

[26] Woo Hyun Shim, Ho Sung Kim, Choong-Gon Choi, and Sang Joon Kim. Comparison of apparent diffusion coefficient and intravoxel incoherent motion for differentiating among glioblastoma, metastasis, and lymphoma focusing on diffusion-related parameter. *PLOS ONE*, 10(7):1–13, 07 2015. doi: 10.1371/journal.pone.0134761. URL https://doi.org/10.1371/journal.pone.0134761.

[27] N. Shaverdian, Y. Yang, P. Hu, S. Hart, K. Sheng, J. Lamb, M. Cao, N. Agazaryan, D. Thomas, M. Steinberg, D. A. Low, and P. Lee. Feasibility evaluation of diffusion-weighted imaging using an integrated MRI-radiotherapy system for response assessment to neoadjuvant therapy in rectal cancer. *British Journal of Radiology*, 90(1071), 2017. ISSN 00071285. doi: 10.1259/bjr.20160739.

[28] Y. Yang, M. Cao, K. Sheng, Y. Gao, A. Chen, M. Kamrava, P. Lee, N. Agazaryan, J. Lamb, D. Thomas, D. Low, and P. Hu. Longitudinal diffusion MRI for treatment response assessment: Preliminary experience using an MRI-guided tri-cobalt 60 radiotherapy system. *Medical Physics*, 43(3):1369–1373, 2016. ISSN 00942405. doi: 10.1118/1.4942381.

[29] S. M. Smith, M. Jenkinson, M. W. Woolrich, C. F. Beckmann, Timothy E. J. Behrens, H. Johansen-Berg, P. R. Bannister, M. De Luca, I. Drobnjak, D. E. Flitney, R. K. Niazy, J. Saunders, J. Vickers, Y. Zhang, N. De Stefano, J. M. Brady, and P. M. Matthews. Advances in functional and structural MR image analysis and implementation as FSL. *NeuroImage*, 23(SUPPL. 1):208–219, 2004. ISSN 10538119. doi: 10.1016/j.neuroimage.2004.07.051.

[30] J. L.R. Andersson, S. Skare, and J. Ashburner. How to correct susceptibility distortions in spin-echo echo-planar images: Application to diffusion tensor imaging. *NeuroImage*, 20(2):870–888, 2003. ISSN 10538119. doi: 10.1016/S1053-8119(03)00336-7.

[31] M. L. Kessler. Image registration and data fusion in radiation therapy. *Br. J. Radiol.*, 79(SPEC. ISS.):99–108, 2006. ISSN 00071285. doi: 10.1259/bjr/70617164.

[32] L. R. Dice. Measures of the Amount of Ecologic Association Between Species. *Ecology*, 26(3):297–302, 1945. ISSN 00129658. doi: 10.2307/1932409. URL `http://doi.wiley.com/10.2307/1932409`.

[33] E. S. Lukacz, C. Sampselle, M. Gray, S. MacDiarmid, M. Rosenberg, P. Ellsworth, and M. H. Palmer. A healthy bladder: a consensus statement. *International Journal of Clinical Practice*, 10(65):1026–1036, 2011.

[34] S. Jequier and O. Rousseau. Sonographic measurements of the normal bladder wall in children. *American Journal of Roentgenology*, 149(3):563–566, 1987. ISSN 0361803X. doi: 10.2214/ajr.149.3.563.

[35] P. Symonds, C. Deehan, J. Mills, C. Meredith, J. Walter, and C. K. Bomford. *Walter and Millers textbook of radiotherapy*. Elsevier Ltd., 2012.

[36] J. N. Kulkarni and G. K. Bakshi. Staging of transitional cell carcinoma: Has anything changed? *Indian J Urol.*, 1(24):68–71, 2008.

[37] N. G. Zaorsky, J. D. Palmer, M. D. Hurwitz, S. W. Keith, A. P. Dicker, and R. B. Den. What is the ideal radiotherapy dose

to treat prostate cancer? A meta-analysis of biologically equivalent dose escalation. *Radiotherapy and Oncology*, 115(3):295–300, 2015. ISSN 18790887. doi: 10.1016/j.radonc.2015.05.011. URL http://dx.doi.org/10.1016/j.radonc.2015.05.011.

[38] R. A. Huddart, E. Hall, S. A. Hussain, P. Jenkins, C. Rawlings, J. Tremlett, M. Crundwell, F. A. Adab, D. Sheehan, I. Syndikus, C. Hendron, R. Lewis, R. Waters, and N. D. James. Randomized noninferiority trial of reduced high-dose volume versus standard volume radiation therapy for muscle-invasive bladder cancer: Results of the BC2001 Trial (CRUK/01/004). *International Journal of Radiation Oncology Biology Physics*, 87(2):261–269, 2013. ISSN 03603016. doi: 10.1016/j.ijrobp.2013.06.2044. URL http://dx.doi.org/10.1016/j.ijrobp.2013.06.2044.

[39] M. Takeuchi, S. Sasaki, M. Ito, S. Okada, S. Takahashi, T. Kawai, K. Suzuki, H. Oshima, M. Hara, and Y. Shibamoto. Urinary Bladder Cancer: Diffusion-weighted MR ImagingAccuracy for Diagnosing T Stage and Estimating Histologic Grade. *Radiology*, 251(1):112–121, 2009. ISSN 0033-8419. doi: 10.1148/radiol.2511080873. URL http://pubs.rsna.org/doi/10.1148/radiol.2511080873.

[40] H. J. Wang, M. H. Pui, Y. Guo, S. R. Li, J. Guan, X. L. Zhang, and H. S. Cai. Multiparametric 3-T MRI for differentiating low-versus high-grade and category T1 versus T2 bladder urothelial carcinoma. *American Journal of Roentgenology*, 204(2):330–334, 2015. ISSN 15463141. doi: 10.2214/AJR.14.13147.

[41] R. J. De Haas, M. J. Steyvers, and J. J. Fütterer. Multiparametric MRI of the bladder: Ready for clinical routine? *American Journal of Roentgenology*, 202 (6):1187–1195, 2014. doi: 10.2214/AJR.13.12294.

[42] S. M. Bentzen. Theragnostic imaging for radiation oncology : dose-painting by numbers. *Lancet Oncol.*, 6:112–117, 2005.

[43] J. F. Fowler. Development of radiobiology for oncology - a personal view. *Phys. Med. Biol.*, 51:R263–R286, 2006.

[44] A. Malayeri, R. H. El Khouli, A. Zaheer, M. Jacobs, C. P. Corona-Villalobos, I. R. Kamel, and K. J. Macura. Principles and applications of diffusion-weighted imaging in cancer detection, staging, and treatment follow-up. *Radiographics*, 31(6):1773–91, 2011. doi: 10.1148/rg.316115515. URL http://www.ncbi.nlm.nih.gov/pubmed/21997994.

[45] A. R. Padhani. Imaging in Cancer Patient Management. *YSRAO*, 21(2): 119–140, 2011. ISSN 1053-4296. doi: 10.1016/j.semradonc.2010.10.004. URL http://dx.doi.org/10.1016/j.semradonc.2010.10.004.

[46] C. Grau, M. Hoyer, M. Alber, J. Overgaard, J. C. Lindegaard, and L. P. Muren. Biology-guided adaptive radiotherapy (BiGART)-more than a vision? *Acta Oncologica*, 52(7):1243–1247, 2013. ISSN 0284186X. doi: 10.3109/0284186X.2013.829245.

[47] A. R. Padhani, G. Liu, D. Mu-Koh, T. L. Chenevert, H. C. Thoeny, T. Takahara, A. Dzik-Jurasz, B. D. Ross, M. Van Cauteren, D. Collins, D. A. Hammoud, G. J.S. Rustin, B. Taouli, and P. L. Choyke. Diffusion-Weighted Magnetic Resonance Imaging as a Cancer Biomarker: Consensus and Recommendations. *Neoplasia*, 11(2): 102–125, 2009. ISSN 14765586. doi: 10.1593/neo.81328. URL http://linkinghub.elsevier.com/retrieve/pii/S1476558609800249.

[48] S. Kobayashi, F. Koga, S. Yoshida, H. Masuda, C. Ishii, H. Tanaka, Y. Komai, M. Yokoyama, K. Saito, Y. Fujii, S. Kawakami, and K. Kihara. Diagnostic performance of diffusion-weighted magnetic resonance imaging in bladder cancer: Potential utility of apparent diffusion coefficient values as a biomarker to predict clinical aggressiveness. *Eur. Radiol.*, 21(10):2178–2186, 2011. ISSN 09387994. doi: 10.1007/s00330-011-2174-7.

[49] C. C. Ling, J. Humm, S. Larson, H. Amols, Z. Fuks, S. Leibel, and J. A. Koutcher. Towards multidimensional radiotherapy (MD-CRT):biological imaging and biological conformality. *Int. J. Radiat. Oncol. Biol. Phys.*, 47(3):551–560, 2000.

[50] A. W. Beavis, P. Gibbs, R. A. Dealey, and V. J. Whitton. Radiotherapy treatment planning of brain tumours using mri alone. *The British Journal of Radiology*, 71(845):544–548, 1998. doi: 10.1259/bjr.71.845.9691900. URL https://doi.org/10.1259/bjr.71.845.9691900. PMID: 9691900.

[51] V. S. Khoo, A. R. Padhani, S. F. Tanner, D. J. Finnigan, M. O. Leach, and D. P. Dearnaley. Comparison of mri with ct for the radiotherapy planning of prostate cancer: a feasibility study. *The British Journal of Radiology*, 72(858):590–597, 1999. doi: 10.1259/bjr.72.858.10560342. URL https://doi.org/10.1259/bjr.72.858.10560342. PMID: 10560342.

[52] Y. K. Lee, M. Bollet, G. Charles-Edwards, M. A. Flower, M. O. Leach, H. McNair, E. Moore, C. Rowbottom, and S. Webb. Radiotherapy treatment planning of prostate cancer using magnetic resonance imaging alone. *Radiotherapy and Oncology*, 66(2):203 – 216, 2003. ISSN 0167-8140. doi: https://doi.org/10.1016/S0167-8140(02)00440-1. URL http://www.sciencedirect.com/science/article/pii/S0167814002004401.

[53] ACR. Phantom Test Guidance for the ACR MRI Accreditation Program. *American College of Radiology*, page 5, 2005. URL http://www.acr.org/ /media/ACR/Documents/Accreditation/MRI/LargePhantomGuidance.pdf.

[54] I. Lavdas, M. E. Miquel, D. W. McRobbie, and E. O. Aboagye. Comparison between diffusion-weighted MRI (DW-MRI) at 1.5 and 3 tesla: A phantom study. *Journal of Magnetic Resonance Imaging*, 40(3):682–690, 2014. ISSN 15222586. doi: 10.1002/jmri.24397.

[55] I. Lavdas, K. C. Behan, A. Papadaki, D. W. McRobbie, and E. O. Aboagye. A phantom for diffusion-weighted MRI (DW-MRI). *Journal of Magnetic Resonance Imaging*, 38(1):173–179, 2013. ISSN 10531807. doi: 10.1002/jmri.23950.

[56] I. Delakis, E. M. Moore, M. O. Leach, and J. P. De Wilde. Developing a quality control protocol for diffusion imaging on a clinical MRI system. *Physics in Medicine and Biology*, 49(8):1409–1422, 2004. ISSN 00319155. doi: 10.1088/0031-9155/49/8/003.

[57] I. Mano, H. Goshima, M. Nambu, and M. Iio. New Polyvinyl Alcohol Gel Material for MRI Phantoms. *Magnetic Resonance in Medicine*, 3:921–926, 1986.

[58] P. Wright, L. P. Muren, M. Høyer, and E. Malinen. Evaluation of adaptive radiotherapy of bladder cancer by image-based tumour control probability modelling. *Acta Oncol.*, 49(7):1045–51, 2010. ISSN 1651-226X. doi: 10.3109/0284186X.2010.498431. URL http://www.ncbi.nlm.nih.gov/pubmed/20831494.

[59] C. Rorden and M. Brett. Stereotaxic display of brain lesions. *Behavioural Neurology*, 12(4):191–200, 2000. ISSN 09534180. doi: 10.1155/2000/421719.

[60] S. M. Bentzen and S. L. TUCKER. Quantifying the position and steepness of radiation dose-response curves. *Int. J. Radiat. Biol.*, 71(5):531–

542, 1997. ISSN 0955-3002. doi: 10.1080/095530097143860. URL http://www.tandfonline.com/doi/full/10.1080/095530097143860.

[61] G. A. Plataniotis and R. G. Dale. Radio-chemotherapy for bladder cancer : Contribution of chemotherapy on local control Assessment of the Radiation-Equivalent of Chemotherapy Contributions in 1-Phase Radio-chemotherapy Treatment of Muscle-Invasive Bladder Cancer. (August 2013), 2016. doi: 10.4329/wjr.v5.i8.267.

[62] F. J. Pos, G. Hart, C. Schneider, and P. Sminia. Radical radiotherapy for invasive bladder cancer: What dose and fractionation schedule to choose? *Int. J. Radiat. Oncol. Biol. Phys.*, 64(4):1168–1173, 2006. doi: 10.1016/j.ijrobp.2005.09.023.

[63] W. Majewski, B. MacIejewski, S. Majewski, R. Suwinski, L. Miszczyk, and R. Tarnawski. Clinical radiobiology of stage T2-T3 bladder cancer. *International Journal of Radiation Oncology Biology Physics*, 60(1):60–70, 2004. ISSN 03603016. doi: 10.1016/j.ijrobp.2004.02.056.

[64] A. Horwich, D. Dearnaley, R. Huddart, J. Graham, E. Bessell, M. Mason, and J. Bliss. A randomised trial of accelerated radiotherapy for localised invasive bladder cancer. *Radiotherapy and Oncology*, 75(1):34–43, 2005. ISSN 01678140. doi: 10.1016/j.radonc.2004.11.003.

[65] C. Grassberger and H. Paganetti. Methodologies in the modeling of combined chemo-radiation treatments. *Physics in Medicine and Biology*, 61(21): R344–R369, 2016. ISSN 13616560. doi: 10.1088/0031-9155/61/21/R344. URL http://dx.doi.org/10.1088/0031-9155/61/21/R344.

[66] H. D. Suit, R. J. Shalek, and R. Wette. Radiation response of c3h mouse mammary carcinoma evaluated in terms of cellular radiation sensitivity. univ. of texas, 18th ann. symp. fund. cancer res., 1965. 1965.

[67] A. E. Nahum and D. M. Tait. Maximizing local control by customized dose prescription for pelvic tumours. In A. Breit, A. Heuck, P. Lukas, P. Kneschaurek, and M. Mayr, editors, *Tumor Response Monitoring and Treatment Planning*, pages 425–431, Berlin, Heidelberg, 1992. Springer Berlin Heidelberg. ISBN 978-3-642-48681-4.

[68] S. Webb and A. E. Nahum. A model for calculating tumour control probability in radiotherapy including the effects of inhomogeneous distributions of dose and clonogenic cell density. *Phys. Med. Biol.*, 38(6):

653, 1993. ISSN 0031-9155. doi: 10.1088/0031-9155/38/6/001. URL http://iopscience.iop.org/0031-9155/38/6/001%5Cnhttp://iopscience.iop.org/0031-9155/38/6/001/pdf/0031-9155_38_6_001.pdf.

[69] S. Warren, M. Partridge, R. Carrington, C. Hurt, T. Crosby, and M. A. Hawkins. Radiobiological determination of dose escalation and normal tissue toxicity in definitive chemoradiation therapy for esophageal cancer. *International Journal of Radiation Oncology Biology Physics*, 2014. ISSN 1879355X. doi: 10.1016/j.ijrobp.2014.06.028.

[70] M. Van Herk. Errors and Margins in Radiotherapy. *Seminars in Radiation Oncology*, 14(1):52–64, 2004. ISSN 10534296. doi: 10.1053/j.semradonc.2003.10.003.

[71] H. T. Lotz, F. J. Pos, M. C. C. M. Hulshof, M. Van Herk, J. Lebesque, J. C. Duppen, and P. Remeijer. Tumour motion and deformation during external radiotherapy of bladder cancer. (5):1551–1558. doi: 10.1016/j.ijrobp.2005.12.025.

[72] C. Menard and U. A. van der Heide. Introduction: Magnetic Resonance Imaging Comes of Age in Radiation Oncology. *Semin. Radiat. Oncol.*, 24(3):149–150, 2014. doi: 10.1016/j.semradonc.2014.02.001. URL http://dx.doi.org/10.1016/j.semradonc.2014.02.001.